

**UNIVERSITY OF THE WITWATERSRAND
JOHANNESBURG**



UNIVERSITY OF THE
WITWATERSRAND,
JOHANNESBURG

**SYNTHESIS AND CHARACTERIZATION OF HETEROATOM-
DOPED CARBON NANO-ONIONS SUPPORTED BIMETALLIC
NANOPARTICLES FOR APPLICATION IN BOTH DIRECT
ALCOHOL AND AMMONIA FUEL CELLS**

by

Ludwe Luther Sikeyi

Student Number: 2303563

**A thesis submitted to the Faculty of Science, University of the
Witwatersrand, Johannesburg, in fulfilment of the requirements
for the degree of Doctor of Philosophy**

SUPERVISORS: Dr M.S. Maubane-Nkadimeng

Prof N.J. Coville

Prof N.W. Maxakato

Johannesburg, January 2023

DECLARATION

I declare that this thesis is my own, and unaided work under the supervision of Dr Manoko S. Maubane-Nkadimeng, Prof Neil J. Coville, and Prof Nobanathi W. Maxakato. It is being submitted for the degree of Doctor of Philosophy at the University of the Witwatersrand, Johannesburg. It has not been submitted for any degree or examination in any other university.



_____ on this 12th day of May 2023

(Candidate)

ABSTRACT

The pressing demand for inexpensive, highly active and operational stability electrocatalyst materials for direct alcohol fuel cells (DAFC) and direct ammonia fuel cells (AFC) has inspired remarkable research and growing interest in this field. The main pressing concerns related with the commercial use of these fuel cells (FCs) are their significant expense, low activity and the insufficient long-term stability of the commonly used Pt/C electrocatalysts due to facilitate the intrinsic slow kinetics for the alcohol and ammonia oxidation reaction. As such, the substitution of Pt/C with novel and more successful nanocatalyst materials is critical. The high activity and long-term operational stability of the nanocatalysts rely to a large extent upon the attributes and properties of the carbon support material.

In this work, unique support materials were designed from onion-like carbon nanoparticles (OLCNs) for Pt and Pd catalysts to enhance their activity in FCs. OLCNs and the sulphur doped OLCNs were synthesized by a flame pyrolysis (FP) method to give p-OLCNs and S-OLCNs (S = 1.6 %) respectively. The synthesis of nitrogen doped (N-OLCNs) and oxygen functionalized nano-onions was achieved using chemical vapour deposition and reflux methods, respectively. Various Pd and Pt based electrocatalysts were then prepared for pristine, doped and functionalized OLCNs using a microwave-assisted synthesis method and their electrocatalytic activity was evaluated for the ethanol oxidation reaction (EOR). Based on a half-cell electrochemical investigation of the ethanol oxidation reaction in alkaline electrolyte, nitrogen and sulphur doped electrocatalysts demonstrated enhanced EOR catalytic activity and better stability, as well as fast electron transfer when compared to the equivalent undoped and commercial Pd/C electrocatalysts.

To further explore the use of OLCNs as support material, bimetallic (Pd/Ag and Pd/Zn) electrocatalysts supported on N-OLCNs were prepared by a one pot synthesis method using sodium borohydride as a reducing agent. The Pd/N-OLCN, Pd/Ag/N-OLCN, Pd/Zn/N-OLCN and Pd/C electrocatalysts were studied in

the methanol oxidation reaction (MOR). The bimetallic (Pd/Ag/N-OLCN and Pd/Zn/N-OLCN) electrocatalysts exhibited superior anti-poisoning tolerance, better electrocatalytic stability and fast charge transfer resistance when compared to monometallic (Pd/N-OLCN and Pd/C) electrocatalysts in the methanol electro-oxidation in alkaline media. The improved catalytic performance could be attributed to the strong metal–support interaction.

Overall, the FP method offered a facile synthesis route for the production of nanocarbons. The Pt or Pd nanoparticles supported on the surface of the modified OLCNs resulted in enhanced electrocatalytic activity in both alcohol and ammonia FCs.

DEDICATION

The research work is dedicated to God Almighty for his protection and guidance throughout my doctoral studies.

I would also like to dedicate this research work to;

My mother: Monica Sikeyi, for her outmost trust, love and motivation that inspired me to give my very best in everything I do.

My partener and kids: Sinomhlobo, Minentle and Ndalwentle for their prayers, immense support and encouragement.

My brother and sister: Luniko and Lisakhanya, for listening, understanding, encouraging and supporting my journey.

ACKNOWLEDGEMENTS

I would like to acknowledge the work of several individuals for their contribution, support, guidance, and assistance in the research project leading to the redaction of this thesis.

First and foremost, I would like to express my deepest gratitude to my supervisor, Dr. M.S. Maubane-Nkadimeng, for her constant encouragement, guidance, and support to the success of this research. She did a great job in guiding me throughout those four years.

I would like to express my deep and sincere gratitude to my co-supervisor Prof. N.J. Coville. His wide knowledge and his logical way of thinking have been of great value for me. His understanding, encouragement, guidance and financial support have provided a good basis for the present thesis.

I would like to express my great appreciation to my (former MSc supervisor and present co-supervisor) Prof. N.W. Maxakato for her guidance, encouragement, insight and great support in accomplishing this task. She did a great job in guiding me throughout those six years.

I would like to thank my co-workers who helped me with my work. Thank you Themba Ntuli, Thomas Mongwe and Laercia Bila; it has been a pleasure to work with you. I truly appreciate all the help you have given me. Thank you for your support.

This research would not be complete without the research facilities provided by the technical support and training by the Microscopy and Microanalysis unit at the University of the Witwatersrand. Special thanks to Prof. Alexander Ziegler, Dr. Ella Langaniso, Dr. Zikhona Tetana, Mrs Tutuzwa Zuma and Mr Jacques Gerber for their patience and help.

To the Catalysis and Materials (CATMAT) and Carbocatalysis group members; your positive criticism and valuable suggestions have encouraged me to work hard as well as to always give my best at everything I do.

In addition this research work would not have been possible without the major financial assistance of a PhD Postgraduate Merit Award (University of the Witwatersrand) and a NRF-DAAD Scholarship, from the German Academic Exchange Service.

PRESENTATIONS, PUBLICATIONS AND MEMBERSHIPS

Conference Presentations:

- ❖ Ludwe Luther Sikeyi, Nobanathi Wendy Maxakato, Neil John Coville and Manoko Stephina Maubane-Nkadimeng “Title Palladium nanoparticles supported on carbon nano onions-titanium dioxide composites as electrocatalysts for alcohol oxidation reactions in alkaline medium”, 2019 International Conference on 30th Catalysis Society of South Africa (CATSA 2019) Cape Town, South Africa, November 10 – 13, 2019 (Poster).
- ❖ Ludwe Luther Sikeyi, Nobanathi Wendy Maxakato, Neil John Coville and Manoko Stephina Maubane-Nkadimeng “Title Microwave assisted synthesis of nitrogen doped and oxygen functionalized carbon nano onions supported palladium nanoparticles as hybrid anodic electrocatalysts for direct alkaline ethanol fuel cells”, 2021 72nd Annual Meeting of the International Society of Chemistry, Jeju Island, Korea, 29 August - 03 September, 2021 (Virtual; Poster).
- ❖ Ludwe Luther Sikeyi, Nobanathi Wendy Maxakato, Neil John Coville and Manoko Stephina Maubane-Nkadimeng “Title Platinum nanoparticles loaded on pristine and boron oxide modified carbon nano-onions for enhanced ammonia electrooxidation in alkaline direct ammonia fuel cells”, 2021 10th Edition of the Nanosciences Young Researcher’s Symposium (NYRS 2021) Johannesburg, South Africa, October 7 – 8, 2021 (Virtual; Poster).
- ❖ Ludwe Luther Sikeyi, Nobanathi Wendy Maxakato, Neil John Coville and Manoko Stephina Maubane-Nkadimeng “Title Platinum nanoparticles loaded on pristine and boron oxide modified carbon nano-onions for enhanced ammonia electrooxidation in alkaline direct ammonia fuel cells”, 2022 NanoAfrica Conference Cape Town, South Africa, October 26 – 28, 2022 (Oral).

- ❖ Ludwe Luther Sikeyi, Nobanathi Wendy Maxakato, Neil John Coville and Manoko Stephina Maubane-Nkadimeng “Title Efficient electrooxidation of ammonia using platinum supported on titania/sulfur-doped onion like carbon nanoparticles in direct ammonia fuel cells”, 2022 International Conference on 32nd Catalysis Society of South Africa (CATSA 2021) Kwazulu Natal, South Africa, November 13 – 16, 2022 (Oral).

Publications related to this work:

- ❖ **L.L. Sikeyi**, T.D. Ntuli, T.H. Mongwe, N.W. Maxakato, E. Carleschi, B.P. Doyle, N.J. Coville, M.S. Maubane-Nkadimeng, Microwave assisted synthesis of nitrogen doped and oxygen functionalized carbon nano onions supported palladium nanoparticles as hybrid anodic electrocatalysts for direct alkaline ethanol fuel cells, *Int. J. Hydrogen Energy*. 46 (2021) 10862–10875. <https://doi.org/10.1016/j.ijhydene.2020.12.154>.
- ❖ **L.L. Sikeyi**, T.D. Ntuli, T.H. Mongwe, N.W. Maxakato, N.J. Coville, M.S. Maubane-Nkadimeng, Platinum Nanoparticles Loaded on Pristine and Boron Oxide Modified Carbon Nano-Onions for Enhanced Ammonia Electrooxidation in Alkaline Direct Ammonia Fuel Cells, *J. Electroanal. Chem.* 917 (2022) 116411. <https://doi.org/10.2139/ssrn.3982297>.
- ❖ **L.L. Sikeyi**, L.R. Bila, T.D. Ntuli, C.T. Selepe, N.W. Maxakato, N.J. Coville, M.S. Maubane-Nkadimeng, Efficient electrooxidation of ammonia using platinum supported on titania / sulfur-doped onion like carbon nanoparticles in direct ammonia fuel cells, *Diam. Relat. Mater.* 132 (2023) 109612. <https://doi.org/10.1016/j.diamond.2022.109612>.
- ❖ **L.L. Sikeyi**, T.D. Ntuli, L.R. Bila, N.W. Maxakato, N.J. Coville, M.S. Maubane-Nkadimeng, Ag and Zn promoted Pd-based electrocatalyst for enhanced methanol oxidation in alkaline direct methanol fuel cells, **(To be submitted)**.

Publications arising from collaborations:

- ❖ T.D. Ntuli, T.H. Mongwe, **L.L. Sikeyi** (Data curation, Formal analysis, Investigation), O. Mkhari, N.J. Coville, E.N. Nxumalo, M.S. Maubane-Nkadimeng, Removal of hexavalent chromium via an adsorption coupled reduction mechanism using olive oil derived carbon nano-onions, *Environ. Nanotechnology, Monit. Manag.* 16 (2021) 100477. <https://doi.org/10.1016/j.enmm.2021.100477>.
- ❖ C.T. Selepe, S.S. Gwebu, T. Matthews, T.A. Mashola, **L.L. Sikeyi** (Software), M. Zikhali, N.W. Maxakato, Effect of Sn doping on Pd electro-catalysts for enhanced electro-catalytic activity towards methanol and ethanol electro-oxidation in direct alcohol fuel cells, *Nanomaterials*. 11 (2021). <https://doi.org/10.3390/nano11102725>.
- ❖ T.H. Mongwe, T.D. Ntuli, **L.L. Sikeyi** (Formal analysis), N.J. Coville, M.A. Mamo, J.P.M. Serbena, M.S. Maubane-nkadimeng, The use of ex-situ nitrogen-doped olive oil-derived carbon nano-onions for application in chemi-resistive gas sensors to detect acetone at room temperature, *South African J. Chem.* 76 (2022) 38–48. <https://journals.co.za/content/journal/chem/>
- ❖ C.T. Selepe, S.S. Gwebu, T. Matthews, T.A. Mashola, **L.L. Sikeyi** (Software), M. Zikhali, S.P. Mbokazi, T.S. Makhunga, K.A. Adegoke, N.W. Maxakato, Electro Catalytic Properties of Palladium and Palladium Alloy Electro-Catalysts Supported on Carbon Nanofibers for Electro-Oxidation of Methanol and Ethanol in Alkaline Medium, *Catalysts*. 12 (2022) 608. <https://doi.org/10.3390/catal12060608>
- ❖ M.S. Maubane-nkadimeng, T.H. Mongwe, T.D. Ntuli, **L.L. Sikeyi** (Formal analysis), N.J. Coville, J.P.M. Serbena, M.A. Mamo, Facile Use Of In-Situ Doped Onion-Like Carbon Nanoparticles For Detecting Toluene At Room Temperature, *IEEE Xplore*. 20 (2022) 3–6. <https://doi.org/10.1109/SENSORS52175.2022.996713>

Memberships:

South African Chemistry Institute (SACI) - June 2017 – present.

Catalysis Society of South Africa (CATSA) – June 2017 – present.

South African Nanotechnology Initiative (SANi) – June 2021 – present.

International Society of Electrochemistry (ISE) – June 2021 - present.

TABLE OF CONTENTS

DECLARATION	i
ABSTRACT.....	ii
ACKNOWLEDGEMENTS	v
PRESENTATIONS, PUBLICATIONS AND MEMBERSHIPS.....	vi
Conference Presentations:.....	vi
Publications related to this work:	vii
Publications arising from collaborations:	viii
Memberships:.....	ix
TABLE OF CONTENTS.....	x
LIST OF FIGURES.....	xx
LIST OF TABLES	xxv
CHAPTER 1	1
INTRODUCTION.....	1

1.1	Challenges and motivation.....	1
1.2	Hypothesis	6
1.3.	Aim and objectives.....	6
1.3.1.	Specific objectives	6
1.4.	Research questions.....	7
1.5.	Outline of the thesis	8
 CHAPTER 2.....		14
 LITERATURE REVIEW		14
2.1	Fuel cell overview	14
2.1.1	Components of fuel cell	15
2.1.2	Operating principle of fuel cell	15
2.1.3	Advantages of fuel cells over traditional engines and batteries.....	16
2.1.3.1	Specific advantages.....	17
2.1.3.2	Disadvantages to fuel cells commercialization.....	18
2.2	Applications of fuel cells	19
2.3	Types of fuel cells (FCs).....	20
2.3.1	Direct Alkaline Alcohol Fuel Cells (DAAFCs).....	20
2.3.1.1	Direct Methanol Fuel Cells (DMFCs)	21
2.3.1.2	Direct Ethanol Fuel Cells (DEFCs)	22
2.3.2	Alkaline Fuel Cells (AFCs).....	23
2.3.2.1	Direct Ammonia Fuel Cells (DAFCs)	25
2.4	Catalysts Support Materials for Fuel cells	28
2.4.1	Carbon as catalyst supports for fuel cells	28
2.4.1.1	Carbon nanoonions (CNOs)/Onion like carbon nanoparticles (OLCNs).....	29
2.4.1.4	Inorganic support materials.....	32
2.5.	Electrocatalysts in fuel cells.....	33
2.5.1	Electrocatalysts used in direct alcohol fuel cells (DAFCs).....	34
2.5.1.1.	Electrocatalysts used in direct methanol fuel cells (DMFCs)	34

2.5.1.2 Electrocatalysts used in direct ethanol fuel cells (DEFCs)	35
2.5.2. Electrocatalysts used in direct ammonia fuel cells (DAFCs).....	36
2.6. Electrocatatalyst preparation methods	37
2.6.1. Microwave synthesis method	38
2.6.2. Chemical vapour deposition method (CVD)	38
2.6.3. Alcohol reduction/Polyol method	39
2.7. Electrochemical Modification Techniques.....	39
2.7.1. Drop coating.....	39
2.7.2. Dip-dry	40
2.7.3. Spin coating	40
References	40
CHAPTER 3.....	60
Microwave assisted synthesis of nitrogen doped and oxygen functionalized carbon nano onions supported palladium nanoparticles as hybrid anodic electrocatalysts for direct alkaline ethanol fuel cells.....	60
Abstract.....	61
Keywords: Carbon nano onions; Cyclic voltammetry; Chronoamperometry; Direct ethanol fuel cells; Electrocatalysts; Electrochemical impedance spectroscopy.....	61
3. Introduction	61

3.1. Experimental Section.....	64
3.1.1. Materials and Methods	64
3.1.2. Synthesis of carbon nano onions (CNOs)	65
3.1.3. Purification and oxidation of the p-CNO	65
3.1.4. Nitrogen doping of the p-CNO	65
3.1.5. Synthesis of Pd/p-CNO, Pd/ox-CNO, and Pd/N-CNO electrocatalysts.....	66
3.1.6. Physical characterization.....	66
3.1.7. Electrochemical measurements	67
3.2. Results and Discussion	68
3.2.1. Transmission electron microscopy	68
3.2.2. Scanning electron microscopy and Atomic force microscopy	69
3.2.3. Fourier transform infrared spectroscopy.....	70
3.2.4. Raman spectroscopy.....	71
3.2.5. Thermogravimetric analysis.....	73
3.2.6. X-ray diffraction spectroscopy	74
3.2.7. X-ray photoelectron spectroscopy	75
3.2.8. Brunauer-Emmett-Teller Nitrogen adsorption (BET)	77
3.3. Electrochemical properties of the metal-free carbon and metal carbon-based catalysts: Ethanol oxidation reaction (EOR) activity	78
3.3.1. Ethanol electro-oxidation using cyclic voltammetry	78
3.3.2. The effect of scan rate on the current density	81
3.3.3. Ethanol electro-oxidation using chronoamperometry	83
3.3.4. Electrochemical impedance spectroscopy (EIS)	84
Conclusions.....	86
Acknowledgments.....	86
References	87

CHAPTER 4.....	97
Platinum Nanoparticles Loaded on Pristine and Boron Oxide Modified Carbon Nano-Onions for Enhanced Ammonia Electrooxidation in Alkaline Direct Ammonia Fuel Cells.....	97
Abstract.....	97
Keywords: Carbon nano onions; Cyclic voltammetry; Boron oxide; Direct ammonia fuel cell; Nanocatalysts.....	98
4. Introduction	98
4.1. Experimental	103
4.1.1. Materials and methods	103
4.1.2. Synthesis of carbon nano-onions (CNOs)	103
4.1.3. Boron oxide modification of the pristine carbon nano-onions (p-CNO).....	103
4.1.4. Synthesis of Pt/p-CNO, unwashed (uw) Pt/B-CNO, and washed (w) Pt/B- CNO electrocatalysts.....	104
4.1.5. Physicochemical characterization	105
4.1.6. Electrochemical characterization.....	105
4.2. Results and discussion.....	106
4.2.1. Structural and morphological analysis	106
4.2.2. Transmission electron microscopy (TEM)	107
4.2.3. Scanning electron microscopy (SEM)	108
4.2.4. Raman spectroscopy.....	109
4.2.5. Thermogravimetric analysis (TGA)	111
4.2.6. X-ray diffraction spectroscopy (XRD)	112

4.2.7. X-ray photoelectron spectroscopy (XPS).....	113
4.2.8. Brunauer-Emmett-Teller Nitrogen adsorption (BET)	115
4.2.9. Summary of findings.....	115
4.2.10. Electrocatalytic behaviour of the nanocatalysts.....	116
4.2.11. Electrochemical surface area (ECSA)	117
4.2.12. Chronoamperometry (CA)	120
4.2.13. Electrochemical impedance spectroscopy (EIS)	121
Conclusions.....	123
Acknowledgments.....	124
References	124
CHAPTER 5.....	136
Efficient electrooxidation of ammonia using platinum supported on titania/sulfur-doped onion like carbon nanoparticles in direct ammonia fuel cells	136
Abstract.....	Error! Bookmark not defined.
Keywords: Ammonia oxidation reactions; Cyclic voltammetry; Nano- catalysts; Onion-like carbon nanoparticles; Sulfur doping.....	137

5. Introduction	137
5.2 Experimental	Error! Bookmark not defined.
5.1.1. Materials.....	141
5.1.2. Synthesis of sulfur doped onion-like carbon nanoparticles (S-OLCNs)	141
5.1.3. Synthesis of titanium dioxide (TiO ₂) anatase.....	141
5.1.4. Synthesis of TiO ₂ /S-OLCN composite support material	142
5.1.5. Synthesis of Pt/S-OLCN, Pt/TiO ₂ , and Pt/TiO ₂ /S-OLCN electrocatalysts .	142
5.1.6. Material characterization	143
5.1.7. Electrochemical measurements	143
5.2 Results and Discussion	144
5.2.0. Physical characterization.....	144
5.2.1. Transmission electron microscopy (TEM)	144
5.2.2. Scanning electron microscopy (SEM)	147
5.2.3. Energy dispersive X-ray spectroscopy (EDS).....	148
5.2.4. Fourier transform infrared and Raman spectroscopy	148
5.2.5. Thermogravimetric analysis (TGA)	149
5.2.6. X-ray diffraction spectroscopy (XRD)	150
5.2.7. X-ray photoelectron spectroscopy (XPS).....	151
5.2.8. Brunauer-Emmett-Teller nitrogen adsorption (BET) data ...	Error! Bookmark not defined.
5.3. Electrocatalytic behaviour of the Pt based electrocatalysts.....	154
5.3.1. Electrochemical surface area (ECSA)	154
5.3.2. Cyclic voltammetry (CV)	156
5.3.3. Chronoamperometry (CA)	158
5.2.4. Electrochemical impedance spectroscopy (EIS)	159
Conclusions.....	161
Acknowledgments.....	161

References	162
CHAPTER 6	169
Ag and Zn promoted Pd-based electrocatalyst for enhanced methanol oxidation in alkaline direct methanol fuel cells	169
Abstract.....	169
Keywords: Cyclic voltammetry; Electrocatalysts; Direct methanol fuel cell; Nitrogen doping; Onion like carbon nanoparticles.	169
6. Introduction	170
6.1 Experimental	170
6.1.1. Materials and methods	173
6.1.2. Synthesis of nitrogen doped onion-like carbon nanoparticles (N-OLCNs)	173
6.1.3. Synthesis of Pd/N-OLCN, Pd/Ag/N-OLCN and Pd/Zn/N-OLCN electrocatalysts.....	173
6.1.4. Physicochemical characterization	174
6.1.5. Electrochemical characterization.....	174
6.2. Results and discussion.....	175
6.2.1. Transmission electron microscopy (TEM) and Energy dispersive X-ray spectroscopy (EDS) mapping.....	175
6.2.2. Thermogravimetric analysis (TGA).....	177
6.2.3. X-ray diffraction spectroscopy (XRD)	178
6.2.4. X-ray photoelectron spectroscopy (XPS).....	179
6.2.5. Brunauer-Emmett-Teller Nitrogen adsorption (BET)	183

6.3. Electrocatalytic behaviour of the nanocatalysts	Error! Bookmark not defined.
6.3.1. Electrochemical surface area (ECSA)	Error! Bookmark not defined.
6.3.2. The effect of scan rate on the current density	188
6.3.3. Chronoamperometry (CA)	189
6.3.4. Electrochemical impedance spectroscopy (EIS)	190
Conclusions	192
Acknowledgments	193
References	193
CHAPTER 7	200
CONCLUSIONS AND RECOMMENDATIONS	200
7.1. Conclusion	200
7.2. Recommendations for further work	202
Appendix A: Supplementary Information	204
CHAPTER 3	204

CHAPTER 4..... 210

CHAPTER 5..... 217

LIST OF FIGURES

Figure 1.1: Graphic illustration of the estimated world global energy and electricity demand (Millions of barrels per day of oil equivalent) [4].	2
Figure 2.1: Simplified fuel cell operation diagram [12].	16
Figure 2.2: Schematic representation of direct methanol fuel cells [37].	22
Figure 2.3: Schematic representation of direct ethanol fuel cells [38].	23
Figure 2.4: Schematic representation of alkaline fuel cells [12].	24
Figure 2.5: Schematic representation of direct ammonia fuel cells [52].	26
Figure 2.6: Schematic representation of the structural models of; (a, b) carbon nano-onions, and (c, d) onion-like carbon nanoparticles, Adapted from Mongwe et al [83].	31
Figure 2.7: Structural representations of TiO ₂ (a) anatase, (b) rutile, (c) brookite [23].	33
Figure 3.1: TEM images of (a) ox-CNO, (b) N-CNO, (c) Pd/ox-CNO, and (d) Pd/N-CNO nanomaterials.	69
Figure 3.2: SEM images of (a) p-CNO, (b) Pd/p-CNO, (c) Pd/ox-CNO and (d) Pd/N-CNO nanomaterials.	70
Figure 3.3: FTIR spectra of p-CNO, N-CNO and ox-CNO nanomaterials.	71
Figure 3.4: Raman spectra for p-CNO, N-CNO and ox-CNO nanomaterials.	72
Figure 3.5: (a) TGA and (b) TGA derivative data for the p-CNO, N-CNO and ox-CNO nanomaterials.	74
Figure 3.6: X-ray diffractograms of p-CNOs, ox-CNO, N-CNO, Pd/p-CNO, Pd/N-CNO, and Pd/ox-CNO nanomaterials.	75

Figure 3.7: (a) CV curves for p-CNO, ox-CNO, N-CNO, and (b) Pd/C, Pd/p-CNO, Pd/ox-CNO, Pd/N-CNO electrocatalysts in 1M C₂H₅OH + 1M KOH at a scan rate of 50 mV s⁻¹ 80

Figure 3.8: Cyclic Voltammograms of N-CNO and Pd/N-CNO electrocatalysts in 1M C₂H₅OH + 1M KOH at different scan rates (a and c) and the plots of peak current density vs. square root of scan rates (b and d)..... 83

Figure 3.9: (a) Chronoamperometric curves for (a) p-CNO, ox-CNO, N-CNO, and (b) Pd/C, Pd/p-CNO, Pd/ox-CNO, Pd/N-CNO electrocatalysts in 1M C₂H₅OH + 1M KOH at -0.25 V..... 84

Figure 3.10: Impedance plots of p-CNO, ox-CNO, N-CNO and (b) Pd/C, Pd/p-CNO, Pd/ox-CNO, Pd/N-CNO electrocatalysts on GC electrode in (a) 1 M (KOH + C₂H₅OH) (c) equivalent circuits utilized in the fitting of the electrochemical impedance spectra. 85

Figure 4.1: Schematic representation of the preparation of the B-CNO and Pt/B-CNO nanocatalysts using the chemical vapor deposition and alcohol reduction methods (O-B = BO bond on CNO surface).. 107

Figure 4.2: TEM micrographs of (a and c) p-CNO, (b and d) B-CNO (e) Pt/p-CNO and (f) Pt/B-CNO nanomaterials. 108

Figure 4.3: Typical SEM micrographs of (a) B-CNO (b) Pt/B-CNO and EDX profile of (c) B-CNO (d) Pt/B-CNO nanomaterials..... 109

Figure 4.4: Raman spectra for p-CNO and B-CNO nanomaterials..... 110

Figure 4.5: (a) TGA profile and (b) TGA derivatives of Pt/p-CNO and unwashed Pt/B-CNO (1:5) nanomaterials. 112

Figure 4.6: X-ray diffractograms of p-CNO, B-CNO, Pt/p-CNO and Pt/B-CNO, nanomaterials. 113

Figure 4.7: XPS spectra (a) C 1s of Pt/B-CNO (b), O 1s of Pt/B-CNO (c) B 1s of Pt/B-CNO and (d) Pt 4f of Pt/B-CNO..... 114

Figure 4.8: (a) CV curves of Pt/C, Pt/p-CNO, Pt/B-CNOuw and Pt/B-CNOw modified electrodes in 0.5 M NaOH solution at scan rate 50 mV s⁻¹. 118

Figure 4.9: (a) CV curves for Pt/C, Pt/p-CNO, Pt/B-CNOuw and Pt/B-CNOw modified electrodes in 0.5 M NaOH + 1M NH₄OH at a scan rate of 50 mV s⁻¹. 120

Figure 4.10: (a) chronoamperometric curves for Pt/C, Pt/p-CNO, Pt/B-CNOuw and Pt/B-CNOw modified electrodes in 0.5 M NaOH + 1M NH₄OH for an applied potential of -0.30 V. 121

Figure 4.11: Nyquist plots of Pt/C, Pt/p-CNO, Pt/B-CNOuw and Pt/B-CNOw modified GC electrode in (a) in 0.5 M NaOH + 1M NH₄OH and the equivalent circuit diagram. 123

Figure 5.1: High Magnification TEM micrographs of (a) S-OLCN, (b) Pt/S-OLCN and inset image of histogram representing Pt nanoparticle size is (1.93 ± 0.38 nm), (c) TiO₂/S-OLCN, (d) Pt/TiO₂/S-OLCN and inset image of histogram representing Pt nanoparticle size is (2.13 ± 0.52 nm), (e) high resolution TEM micrographs of Pt/TiO₂/S-OLCN, (f) HR-TEM image of selected area of Pt/TiO₂/S-OLCN and inset is corresponding EDX mapping represents the combination of elements in Pt/TiO₂/S-OLCN, (g) TEM-EDX elemental color mapping of the C, O, S, Ti, Pt elements..... 146

Figure 5.2: Typical SEM micrographs of (a) S-OLCN (b) TiO₂/S-OLCN, (c) Pt/S-OLCN (d) Pt/TiO₂/S-OLCN nanomaterials. 148

Figure 5.3: (a) FTIR spectrum and (b) Raman spectrum of the S-OLCN nanomaterials 149

Figure 5.4: (a) thermogravimetric analysis profiles and (b) differential thermogravimetric analysis curves of Pt/S-OLCN and Pt/TiO₂/S-OLCN nanomaterials..... 150

Figure 5.5: X-ray diffractograms of S-OLCN, Pt/S-OLCN, Pt/TiO ₂ /S-OLCN, and TiO ₂ anatase nanomaterials.	151
Figure 5.6: XPS (a) survey spectra of Pt/TiO ₂ /S-OLCN (b), C 1s of Pt/TiO ₂ /S-OLCN (c) O 1s of Pt/TiO ₂ /S-OLCN (d) S 2p of Pt/TiO ₂ /S-OLCN (e) Ti 2p of Pt/TiO ₂ /S-OLCN and (f) Pt 4f of Pt/TiO ₂ /S-OLCN.	153
Figure 5.7: (a) CV curves for the Pt/C, Pt/TiO ₂ , Pt/S-OLCN and Pt/TiO ₂ /S-OLCN nanocatalysts in 1 M KOH at a scan rate of 50 mV s ⁻¹	155
Figure 5.8: CV curves of the Pt/C, Pt/TiO ₂ , Pt/S-OLCN and Pt/TiO ₂ /S-OLCN modified electrodes in 1 M KOH + 1M NH ₄ OH at a scan rate of 50 mV s ⁻¹	158
Figure 5.9: CA curves for Pt/C, Pt/TiO ₂ , Pt/S-OLCN and Pt/TiO ₂ /S-OLCN electrocatalysts in 1 M KOH + 1M NH ₄ OH at the potential peak of the ammonia oxidation.	159
Figure 5.10: Nyquist plots of Pt/C, Pt/TiO ₂ , Pt/S-OLCN and Pt/TiO ₂ /S-OLCN electrocatalysts in 1 M KOH + 1M NH ₄ OH and along with the equivalent circuit (inset).	160
Figure 6.1: TEM micrographs, EDX mapping and average particle size of (a, c and e) Pd/Ag/N-OLCN, (b, d and f) Pd/Zn/N-OLCN nanomaterials.	177
Figure 6.2: (a) TGA profile and (b) TGA derivatives of Zn/N-OLCN, Ag/N-OLCN, Pd/Zn/N-OLCN and Pd/Ag/N-OLCN nanomaterials.	178
Figure 6.3: X-ray diffractograms of Ag/N-OLCN, Pd/Ag/N-OLCN, Zn/N-OLCN and Pd/Zn/N-OLCN nanomaterials.	179
Figure 6.4: XPS spectra of Pd/N-CNO-Zn and Pd/N-CNO-Ag for (a) C 1s (b), O 1s (c) N 1s, (d) Zn 2p, (e) Ag 3d and (f) Pd 3d.	182
Figure 6.5: (a) CV curves of Pd/C, Pd/N-OLCN, Pd/Ag/N-OLCN- and Pd/ Zn/N-OLCN modified electrodes in 1 M NaOH solution at scan rate 50 mV s ⁻¹	185

Figure 6.6: shows the CV curves for the Pd/C, Pd/N-OLCN, Pd/Ag/N-OLCN and Pd/Zn/N-OLCN electrocatalysts in 1 M NaOH + 1 M CH₃OH solution at a scan rate of 50 mV s⁻¹ 188

Figure 6.7: shows the CV curves for the Pd/Ag/N-OLCN and Pd/Zn/N-OLCN electrocatalysts in 1 M NaOH + 1 M CH₃OH at different scan rates (a and c) and the plots of peak current density vs. square root of scan rates (b and d). 189

Figure 6.8: chronoamperometric curves for Pd/C, Pd/N-OLCN, Pd/Ag/N-OLCN and Pd/ Zn/N-OLCN modified electrodes in 1 M NaOH + 1M CH₃OH for an applied potential of -0.30 V. 190

Figure 6.9: Nyquist plots of Pd/C, Pd/N-OLCN, Pd/Ag/N-OLCN and Pd/ Zn/N-OLCN modified electrodes in 1 M NaOH + 1M CH₃OH and the equivalent circuit diagram (insert). 192

LIST OF TABLES

Table 2.1: Comparison of different generation systems [16].....	17
Table 2.2: Types of fuel cells, electrolyte, operating temperature and charge carrier [29].....	20
Table 2.3: advantages, disadvantages, and applications of different fuel cells[13].	27
Table 3.1: Raman data showing peak positions, intensities, and intensity ratios for p-CNO, N-CNO, and ox-CNO.	72
Table 3.2: BET surface areas of p-CNO, N-CNO and ox-CNO nanomaterials. ...	77
Table 3.3: Comparison of the catalytic activity, as the current density for our synthesized CNO and Pd/CNO electrocatalysts, tested towards EOR in the alkaline electrolyte as compared to other electrocatalysts tested in the same fuels and electrolytes.....	79
Table 3.4: The EIS circuit parameters of p-CNO, ox-CNO, N-CNO, Pd/C, Pd/p-CNO, Pd/ox-CNO, and Pd/N-CNO electrocatalysts.	85
Table 4.1: Raman data showing peak positions, intensities, and intensity ratios for p-CNO and unwashed B-CNO.	110
Table 4.2: Elemental composition of B-CNO and Pt/B-CNO obtained from XPS data.....	115
Table 4.3: BET surface area of unwashed B-CNO and Pt/B-CNO nanomaterial.	115
Table 4.4: Charge for the hydrogen adsorption, platinum loading and the electrochemical active surface area.....	118
Table 4.5: Comparison of the current density for unwashed Pt/B-CNO, washed Pt/B-CNO and Pt/p-CNO against other Pt/C nanocatalysts reported for ammonia oxidation reactions.	119

Table 4.6: <i>The EIS circuit parameters of Pt/C, Pt/p-CNO, Pt/B-CNOuw and Pt/B-CNOw nanocatalysts.....</i>	123
Table 5.1: <i>Elemental composition of Pt/TiO₂/S-OLCN sample obtained from XPS data.....</i>	152
Table 5.2: <i>BET surface area of the platinum supported on sulfur-doped onion like carbon nanoparticles-titania nanomaterials.....</i>	154
Table 5.3: <i>Comparison of Pt/TiO₂, Pt/S-OLCN and Pt/TiO₂/S-OLCN to other Pt/C catalysts reported for ammonia oxidation reactions.</i>	157
Table 5.4: <i>Electrochemical impedimetric data of Pt/C, Pt/TiO₂, Pt/S-OLCN and Pt/TiO₂/S-OLCN electrocatalysts.</i>	160
Table 6.1: <i>Elemental composition of Pd/N-CNO-Ag and Pd/N-CNO-Zn obtained from XPS data.....</i>	Error! Bookmark not defined.
Table 6.2: <i>BET surface area of N-OLCN, Pd/N-OLCN, Pd/Ag/N-OLCN and Pd/Zn/N-OLCN nanomaterial.</i>	183
Table 6.3: <i>Comparison of Pd/N-OLCN, Pd/Ag/N-OLCN and Pd/Zn/N-OLCN to other Pd/C catalysts reported for AOR.....</i>	185
Table 6.4: <i>The EIS circuit parameters of Pd/C, Pd/N-OLCN, Pd/Ag/N-OLCN and Pd/Zn/N-OLCN nanocatalysts.....</i>	192

GLOSSARY OF TERMS AND ABBREVIATIONS

The following is the list of abbreviations as they appear in the thesis:

AFM	Atomic force microscopy
Ag/AgCl	Silver-silver chloride
Ag	Silver
B	Boron
BET	Brunauer-Emmett-Teller Nitrogen adsorption
CNOs	Carbon nano onions
CNTs	Carbon nanotubes
CNFs	Carbon nanofibers
CB	Carbon black
C	Carbon
CVD	Chemical vapour deposition
CE	Counter electrode
DAFC	Direct alcohol fuel cells
DAFC	Direct ammonia fuel cells
DEFC	Direct ethanol fuel cells
DMFC	Direct methanol fuel cells
EOR	Ethanol oxidation reaction
ECSA	Electrochemical active surface area
EIS	Electrochemical impedance spectroscopy
EDX	Energy-dispersive X-ray spectroscopy
FP	Flame pyrolysis
GO	Graphene oxide
GCE	Glassy carbon electrode
JCDPS	Joint Committee of Powder Diffraction Standards
MOR	Methanol oxidation reaction
MCFC	Molten carbon fuel cell
MW	Microwave
N	Nitrogen
NaOH	Sodium hydroxide

NPs	Nanoparticles
O	Oxygen
Pt/C	Platinum catalyst supported on carbon black
PGM	Platinum group metal
Pd	Palladium
Pt	Platinum
p	Pristine
PEMFC	Proton exchange membrane fuel cell
SOFC	Solid oxide fuel cell
SEM	Scanning electron microscopy
SMSI	Strong Metal-Support Interaction
TGA	Thermogravimetric analyzer
TEM	Transmission electron microscopy
TiO₂	Titanium dioxide
Zn	Zinc

CHAPTER 1

INTRODUCTION

1.1 Challenges and motivation

The increasing search for environmentally and economically sustainable energy sources as an alternative replacement for fossil fuels has become one of the most important projects to meet the growing global energy demand [1]. At present, non-renewable resources such as fossil fuels are the main source for power generation and this source supplies about 80 % of the world energy demand [2]. The three non-renewable resources (coal, natural gas and crude oil) are becoming insufficient worldwide and will be expected to be depleted in the decades/centuries ahead [3]. Coal is currently abundant, but the burning of coal produces harmful waste gases such as carbon dioxide, sulphur dioxide, nitrogen oxide, etc. which can/does lead to environmental air pollution. The cleanest energy source and most efficient non-renewable fuel is natural gas; however, its supply is limited by inadequate extraction and transportation infrastructure. It has been reported that the need for oil exceeds 1,000 barrels every second and today two litres of oil are required per day for each individual in the world [4]. This worldwide utilization is equivalent to 13×10^{12} watts of power demand. Around 66% of the world's oil is consumed in the energy industries especial in the transportation sector [4].

According to the BP statistical review (World Energy 2022) increasing shortages and growing prices for non-renewable resources will occur as crude oil reserves are used up (ca. predicted to be 50 years supply) [5]. In addition, the environmental problems in the world due to the exploitation of fossil fuels is resulting in the phenomena of climate change This is being caused by the increase emission of greenhouse gases (GHG) resulting in increased global temperatures and potentially the destruction of the ozone layer [6]. Economic development will almost probably continue to expand, and in 2050, the demand for energy services could rise by an order of magnitude while the demand for primary energy is predicted to rise by 1.5–3 times, as illustrated in Fig. 1.1.

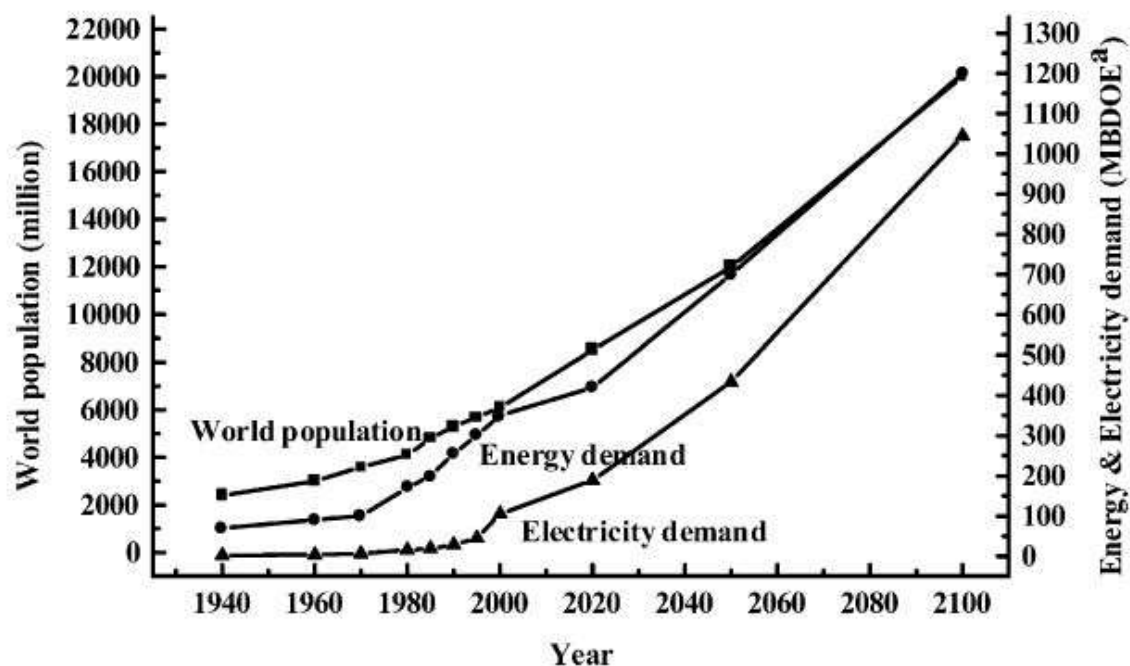


Figure 1.1: Graphic illustration of the estimated world global energy and electricity demand (Millions of barrels per day of oil equivalent) [4].

The substitution of non-renewable resources in South Africa (SA) has proven to be one of the greatest scientific challenges facing the future of the country. To solve the energy problems facing SA, scientists and engineers, in cooperation with government and industry, have been seeking to develop the use of alternative energy sources that are environmentally friendly, such as fuel cells and batteries [7]. Recently the SA government signed a carbon charge bill to reduce the high use of fuel sources. The SA government has targeted a zero-carbon economy, to be achieved between 2030-2050. This will require the use of non-carbon energy sources. The SA low-emission carbon development strategy (SALEDS 2050), similar to that of other countries in the world, focuses on low-carbon energy sources [8]. SA has situated itself to be engaged with the green economy by utilizing platinum group metals (PGMs). According to SFA Oxford, SA mines are the world's major supplier of many PGMs, which include 74% Pt, 39% Pd, 82% Rh, 90% Ru and 81% Ir (2021 data) [9]. These figures will be affected by the

Ukraine-Russia war since Russia is the world's largest producer of palladium metal [10]. PGMs are key electrocatalytic nanomaterials used in most types of fuel cells.

The Department of Science and Innovation (DSI) in SA has created three centres of competence to develop the use of Pt for use in fuel cells under the HySA (Hydrogen South Africa) umbrella. HySA falls within the National Hydrogen and Fuel Cell Technologies Research, Development and Innovation Strategy to develop technology, knowledge products (patents and publications), and human capital at tertiary education institutions (research projects) for the development of hydrogen as an energy source and Pt as the catalysts of choice for use in the fuel cell industry in the country. HySA has been in existence for over 15 years, since its endorsement by the government in 2007, with a key objective of advancing the use of domestic-based PGMs in the value chain as a catalyst in fuel cells. The expectation is to supply 25 % of the world's electrocatalyst demand for fuel cell technology (HFCT) by 2020.

Fuel cells offer a very attractive technology due to its environmental friendless as a power source. Fuel cells are believed to be one of the most promising solutions for producing energy since they can directly convert the chemical energy of a fuel directly into electricity via a redox reaction at the anode without emitting any greenhouse gases [11]. Amongst the energy technologies, fuel cells are a clean energy source that that have shown excellent energy conversion efficiency, silent operation, long operating times, and can operate under wide operating temperatures [12]. Hydrogen-powered fuel cells only generate water vapour and hot air at the outlet with no pollutant emissions, since they operate at temperatures that are much lower compared to internal combustion engines [13]. Hydrogen fuel cells do have their disadvantages but they still hold promise for our energy crisis [13]. The major challenges with using hydrogen as a fuel are its storage and transport because of the formation of explosive mixtures with air and its high flammability. In addition, hydrogen when utilized in fuel cells has a lower density than gasoline that creates issues of volatility [14]. In order to overcome these problems relating to high transportation costs and safe storage, hydrogen has

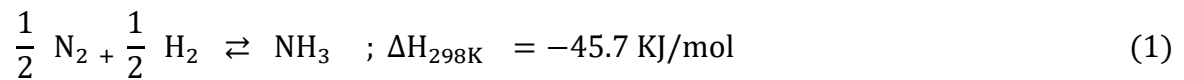
been 'stored' in liquid form in organic fuels such as in methanol, ethanol, and ammonia.

Direct alcohol fuel cells (DAFCs) use alcohols such as methanol, ethanol, ethylene glycol and glycerol rather than hydrogen as a source of the fuel [15]. In particular, methanol and ethanol can be easily made from various resources including natural gas, biomass, etc. [16]. The advantage of the direct alcohol fuel cell (DAFC) over the proton exchange membrane fuel cell (PEMFC) is that the oxidation of an alcohol molecule can hypothetically produce up to six electrons, three times more than hydrogen [17]. Alcohols also have a high-energy specific density, combined with easier transportation, and fuel storage. Like all fuel cells, DAFCs have disadvantages. These include electrode contamination by carbon monoxide, incomplete oxidation of alcohols on the electrocatalyst, fuel cell costs and the corrosion of carbon materials [18]. The Pd-based nanostructured electrocatalysts have been acknowledged as active catalysts in alcohol oxidation reactions in alkaline conditions [19]. The use of palladium in DAFC commercialization is limited due to its expense. Alloying Pd catalysts with cheaper metals like Zn, Fe, Ag, Co, and Ni has become a good approach to form bimetallic catalysts for the methanol electro-oxidation reaction in alkaline media [20,21]. Along these lines, combining Pd with Zn and Ag metals could not only change the properties of Pd, but also enhance its activity and resistance. In addition this would reduce the cost of the electrode.

Both carbon-based materials and metal oxides possess the required properties for their use as catalyst support materials [22]. These properties include: (i) high surface areas that are required for the dispersion of catalyst particles, (ii) the ability to conduct electricity, and (iii) the ability to maintain stability in reactions under alcohol and ammonia electrocatalytic oxidation conditions. Carbon nano-onions (CNOs) and heteroatom doped CNOs, as well as their related onion-like carbon nanomaterial (OLCNs) counterparts, are examples of support materials that can be used as catalyst supports in fuel cells [23]. CNOs and OLCNs are part of the fullerene family; the OLCNs (sometimes referred to as CNOs) are made up of

quasi-sphere shaped and polyhedral shaped nano-graphitic layers of carbon atoms [24].

Another way to produce and store clean electricity is to use ammonia as a fuel in a direct ammonia fuel cell. The electrochemical oxidation of ammonia as an efficient green method has attracted much attention for the application of ammonia as a transportation energy source and for mobile electricity generation without CO₂ emission [25]. Ammonia is a versatile hydrogen carrier that can be easily produced in the Haber-Bosch process, urea from animal/human waste, agricultural fertilizers, and industrial wastes [26]. The Haber–Bosch process is one of the most successful and economical industrial methods for the synthesis of ammonia. This chemical process was named after the German chemist Fritz Haber along with his assistant Carl Bosch, who used catalysts in the first decade of the 20th century. The process involves direct synthesis of ammonia by the reaction of atmospheric nitrogen (N₂) with hydrogen (H₂) using iron catalysts under high pressures and temperatures. The chemical reaction of nitrogen and hydrogen is reversible and the production of ammonia is an exothermic equilibrium reaction.



Liquid ammonia is a non-flammable chemical, which makes it a good choice for transportation and storage as compared to many other candidates [28]. Among other hydrogen carriers, ammonia is an excellent carbon-free chemical and only produces nitrogen and water as products on oxidation in alkaline media. Furthermore, ammonia has a high energy density and hydrogen content of ca. 130 kg H₂/m³ as compared to liquid hydrogen 70 kg H₂/m³, ethanol 105 kg H₂/m³ and methanol 95 kg H₂/m³ [29]. However, the electro-oxidation of the ammonia molecule into hydrogen and nitrogen is a very sluggish process, that also requires purification of products and elevated temperatures [30]. In terms of performance, platinum has been demonstrated as an excellent monometallic catalyst for the oxidation of ammonia in alkaline electrolyte but it is also susceptible to poisoning by nitrogen intermediates [31]. Since large-scale platinum catalysts are costly, nanocomposite materials are hence utilized for better reaction kinetics.

1.2 Hypothesis

In order to address the aforementioned problems, this research project will focus on the development of new electrocatalysts (metal free and metal based) for both direct alcohol and ammonia fuel cells. The high expense related to platinum (and palladium) as catalysts in the fuel cell has led to attempts to reduce the Pt loading and to alloy the Pt with cheaper metals. It is anticipated that the use of modified or heteroatom doped onion-like carbon nanoparticles and titanium dioxide as catalyst support materials will enhance platinum, palladium, silver, and zinc dispersion and improve their electrocatalytic activity. The benefits of employing the support (heteroatom-doped carbons, inorganic metal oxides, noble and non-noble metals) and the fuel (ethanol, methanol and ammonia) can only be realized if alcohol oxidation proceeds completely to CO₂ and the ammonia reaction kinetics are fast and by-products are minimized.

1.3. Aim and objectives

To develop a better understanding of the role that heteroatoms (O, N, B- and S) play in metal-carbon onion based electrocatalysts in alcohol and ammonia oxidation reactions in alkaline media.

1.3.1. Specific objectives

- ❖ To synthesize onion like carbon nanoparticles (OLCNs) using olive oil, coconut oil, thiophene, and acetonitrile as a carbon source.
- ❖ To synthesize oxidized OLCNs, nitrogen doped OLCNs, boron oxide modified OLCNs and sulfur doped OLCNs using different methods.
- ❖ To prepare palladium and platinum based electrocatalysts (Pd/p-OLCN, Pd/ox-OLCN, Pd/N-OLCN, Pt/p-OLCN, Pt/B-OLCN, Pt/S-OLCN, Pt/TiO₂, Pt/TiO₂/S-OLCN, Pd/Zn/N-OLCN and Pd/Ag/N-OLCN).

- ❖ To characterize the synthesized electrocatalysts using different techniques such as transmission electron microscopy (TEM), scanning electron microscopy (SEM), atomic force microscopy (AFM), Fourier-transform infrared (FTIR) spectroscopy, Raman spectroscopy, thermogravimetric analysis (TGA), X-Ray diffraction (XRD), X-ray photoelectron spectroscopy (XPS) and Brunauer-Emmett-Teller (BET) surface analysis methods.
- ❖ To investigate the performance of these electrocatalysts as electrodes for fuel cells under alkaline conditions using electrochemical techniques.

1.4. Research questions

- ❖ Can carbon nano-onions/onion like carbon nanoparticles act as a support materials for Pt?
- ❖ What is the role of the heteroatom doping in CNOs/OLCNs in making Pt/OLCNs and Pd/OLCNs catalysts?
- ❖ What is the role of the noble metals, non-noble metals and inorganic metal oxides in direct alcohol and ammonia fuel cells?
- ❖ Are there advantages to using bimetallic nanocomposite structures made from Pt or Pd with Ag and Zn?
- ❖ How can the catalytic performance of the electrocatalysts be further enhanced?
- ❖ How unique or novel are these electrocatalysts compared to those similar catalysts that have been prepared in previous research studies?

1.5. Outline of the thesis

Chapter 1: This chapter gives a brief description of the research background, challenges and motivation, hypothesis, research aim and objectives of the project.

Chapter 2: Literature is reviewed in this chapter and the focus is on an overview of fuel cells. This includes: components of a fuel cell, operating principle of a fuel cell, comparison of different generation systems, advantages and disadvantages, applications, types of fuel cells, catalyst support materials, electrocatalysis, electrocatalyst preparation methods and electrochemical modification techniques.

Chapter 3: This chapter details the synthesis and characterization of pristine carbon (p-CNO), nitrogen doped (N-CNO), oxygen functionalized (ox-CNO) nano onions and their Pd counterparts. Chapter 3 also provides the electrochemical activity of the metal free and metal carbon based electrocatalysts towards ethanol oxidation reactions (EOR) in alkaline electrolyte. **This part of the research work has been published in the International Journal of Hydrogen Energy.** <https://doi.org/10.1016/j.ijhydene.2020.12.154>

Chapter 4: This chapter reports the preparation and characterization of pristine and boron oxide modified carbon nano-onions supported platinum nanoparticles as electrocatalysts for ammonia oxidation reactions (AOR) in alkaline media. **This part of the research work was published in the Journal of Electroanalytical Chemistry.** <https://doi.org/10.2139/ssrn.3982297>.

Chapter 5: This chapter reports on the synthesis and characterization of platinum supported on titania oxide nanoparticles decorated on sulfur doped onion-like carbon nanoparticles (S-OLCNs) as highly efficient electrocatalysts for ammonia oxidation reactions in alkaline media. **This part of the research work was published in the Diamond and Related Materials Journal.** <https://doi.org/10.1016/j.diamond.2022.109612>.

Chapter 6: This chapter presents the synthesis and characterization of nitrogen doped onion-like carbon nanoparticles (N-OLCNs) and bimetallic (Pd/Ag/N-OLCN

and Pd/Zn/N-OLCN) electrocatalysts. The catalytic activity of the Pd based electrocatalysts for methanol oxidation reactions in alkaline conditions are discussed. **This part of the research work will be submitted for publication.**

Chapter 7: This chapter provides the general conclusions and fundamental perspectives of the overall discussed results of the synthesized nanocatalysts for the entire thesis. Future recommendations for the study are listed.

References: are listed at the end of each chapter.

Appendix section: selected prominent data is presented in this section.

References

- [1] M. Ilbas, B. Kumuk, M.A. Alemu, B. Arslan, Numerical investigation of a direct ammonia tubular solid oxide fuel cell in comparison with hydrogen, *Int. J. Hydrogen Energy*. 45 (2020) 35108–35117. <https://doi.org/10.1016/j.ijhydene.2020.04.060>.
- [2] J. Legemza, M. Fröhlichová, R. Findorák, Fossil fuels and renewable energy sources, *Biomass Carbon Fuels Metall.* (2020) 11–18. <https://doi.org/10.1201/9780429274039-2>.
- [3] S. Shafiee, E. Topal, When will fossil fuel reserves be diminished?, *Energy Policy*. 37 (2009) 181–189. <https://doi.org/10.1016/j.enpol.2008.08.016>.
- [4] A. Boudghene Stambouli, E. Traversa, Fuel cells, an alternative to standard sources of energy, *Renew. Sustain. Energy Rev.* 6 (2002) 295–304. [https://doi.org/10.1016/S1364-0321\(01\)00015-6](https://doi.org/10.1016/S1364-0321(01)00015-6).
- [5] R.M. Goss, BP statistical review of world energy 1982, (1983).
- [6] F. Barbir, Transition to renewable energy systems with hydrogen as an energy carrier, *Energy*. 34 (2009) 308–312. <https://doi.org/10.1016/j.energy.2008.07.007>.
- [7] R.A. Felseghi, E. Carcadea, M.S. Raboaca, C.N. Trufin, C. Filote, Hydrogen fuel cell technology for the sustainable future of stationary applications, *Energies*. 12 (2019). <https://doi.org/10.3390/en12234593>.
- [8] B. van der Zwaan, T. Kober, F.D. Longa, A. van der Laan, G. Jan Kramer, An integrated assessment of pathways for low-carbon development in Africa, *Energy Policy*. 117 (2018) 387–395. <https://doi.org/10.1016/j.enpol.2018.03.017>.

- [9] L. Thormann, B. Buchspies, C. Mbohwa, M. Kaltschmitt, PGE production in Southern Africa, part 1: Production and market trends, *Minerals*. 7 (2017). <https://doi.org/10.3390/min7110224>.
- [10] B.J. Glaister, G.M. Mudd, The environmental costs of platinum-PGM mining and sustainability: Is the glass half-full or half-empty?, *Miner. Eng.* 23 (2010) 438–450. <https://doi.org/10.1016/j.mineng.2009.12.007>.
- [11] D.K. Niakolas, M. Daletou, S.G. Neophytides, C.G. Vayenas, Fuel cells are a commercially viable alternative for the production of “clean” energy, *Ambio*. 45 (2016) 32–37. <https://doi.org/10.1007/S13280-015-0731-Z>.
- [12] A. John, S. Katkar, Revolution in renewable energy fuel cell, *Int. J. Comput. Sci. Technol.* 8 (2017) 46–50. <https://doi.org/ISSN:0976-849>.
- [13] B.C. Tashie-Lewis, S.G. Nnabuife, Hydrogen Production, Distribution, Storage and Power Conversion in a Hydrogen Economy - A Technology Review, *Chem. Eng. J. Adv.* 8 (2021) 100172. <https://doi.org/10.1016/j.ceja.2021.100172>.
- [14] R. Gupta, K. Pant, Fundamentals and Use of Hydrogen as a Fuel, *Hydrog. Fuel*. (2008) 2–32. <https://doi.org/10.1201/9781420045772.ch1>.
- [15] K.I. Ozoemena, Nanostructured platinum-free electrocatalysts in alkaline direct alcohol fuel cells: Catalyst design, principles and applications, *RSC Adv.* 6 (2016) 89523–89550. <https://doi.org/10.1039/c6ra15057h>.
- [16] R. Pogaku, *Horizons in bioprocess engineering*, Springer International Publishing, 2019. <https://doi.org/10.1007/978-3-030-29069-6>.
- [17] A.B. Delpéuch, Mechanistic study of the ethanol oxidation reaction on carbon supported Pt-, Rh- and SnO₂-based electrocatalysts in acidic medium, *Hal open science*. (2016) 191.
- [18] A.M. Sheikh, K. Ebn-Alwaled Abd-Alftah, C.F. Malfatti, On reviewing the catalyst materials for direct alcohol fuel cells (DAFCs), *J. Multidiscip. Eng. Sci. Technol.* 1 (2014) 3159–40.

- [19] Y. Yang, S. Yu, L. Gao, X. Wang, S. Yan, The properties of PdRu /C with respect to the electro-oxidation of methanol and ethanol, *Int. J. Electrochem. Sci.* 14 (2019) 1270–1282. <https://doi.org/10.20964/2019.02.50>.
- [20] V.F. Ruiz-Ruiz, R. González-Olvera, R. Díaz-Pardo, I. Betancourt, I. Zumeta-Dubé, D. Díaz, N. Farfán, M.J. Arellano-Jiménez, Mechanochemically obtained Pd–Ag nanoalloys. Structural considerations and catalytic activity, *Materialia*. 4 (2018) 166–174. <https://doi.org/10.1016/j.mtla.2018.09.031>.
- [21] X.L. Liang, X. Dong, G.D. Lin, H. Bin Zhang, Carbon nanotube-supported Pd-ZnO catalyst for hydrogenation of CO₂ to methanol, *Appl. Catal. B Environ.* 88 (2009) 315–322. <https://doi.org/10.1016/j.apcatb.2008.11.018>.
- [22] M.J. Lázaro, S. Ascaso, S. Pérez-Rodríguez, J.C. Calderón, M.E. Gálvez, M.J. Nieto, R. Moliner, A. Boyano, D. Sebastián, C. Alegre, L. Calvillo, V. Celorrio, Carbon-based catalysts: Synthesis and applications, *Comptes Rendus Chim.* 18 (2015) 1229–1241. <https://doi.org/10.1016/j.crci.2015.06.006>.
- [23] A. Shaikh, B.K. Singh, D. Mohapatra, S. Parida, Nitrogen-Doped Carbon Nano-Onions as a Metal-Free Electrocatalyst, *Electrocatalysis*.10 (2019) 222–231.
- [24] V. Dhand, M. Yadav, S.H. Kim, K.Y. Rhee, A comprehensive review on the prospects of multi-functional carbon nano onions as an effective, high-performance energy storage material, *Carbon N. Y.* 175 (2021) 534–575. <https://doi.org/10.1016/j.carbon.2020.12.083>.
- [25] Y. Guo, Z. Pan, L. An, Carbon-free sustainable energy technology: Direct ammonia fuel cells, *J. Power Sources.* 476 (2020) 228454. <https://doi.org/10.1016/j.jpowsour.2020.228454>.
- [26] S. Ghavam, M. Vahdati, I.A.G. Wilson, P. Styring, Sustainable Ammonia Production Processes, (n.d.). <https://doi.org/10.3389/fenrg.2021.580808>.
- [27] J.M. Modak, Haber process for ammonia synthesis, *Resonance.* 7 (2002) 69–77. <https://doi.org/10.1007/bf02836187>.

- [28] H. Kobayashi, A. Hayakawa, K.D.K.A. Somarathne, E.C. Okafor, Science and technology of ammonia combustion, *Proc. Combust. Inst.* 37 (2019) 109–133. <https://doi.org/10.1016/j.proci.2018.09.029>.
- [29] A. Klerke, C.H. Christensen, J.K. Nørskov, T. Vegge, Ammonia for hydrogen storage: Challenges and opportunities, *J. Mater. Chem.* 18 (2008) 2304–2310. <https://doi.org/10.1039/b720020j>.
- [30] N.M. Adli, H. Zhang, S. Mukherjee, G. Wu, Review—Ammonia Oxidation Electrocatalysis for Hydrogen Generation and Fuel Cells, *J. Electrochem. Soc.* 165 (2018) J3130–J3147. <https://doi.org/10.1149/2.0191815jes>.
- [31] V.A. Ribeiro, I.C. de Freitas, A.O. Neto, E. V. Spinacé, J.C.M. Silva, Platinum nanoparticles supported on nitrogen-doped carbon for ammonia electro-oxidation, *Mater. Chem. Phys.* 200 (2017) 354–360. <https://doi.org/10.1016/j.matchemphys.2017.07.088>.

CHAPTER 2

LITERATURE REVIEW

2.1 Fuel cell overview

A fuel cell is an electrochemical device that converts fuel chemical energy stored in a chemical bond e.g. in a hydrogen-hydrogen bond, directly into either mechanical or electrical power with the subsequent by-products as heat and water [1]. Hydrogen (H_2) can be produced from different sources; in particular, H_2 can be generated from water electrolysis, by the electrochemical splitting of water into H_2 and O_2 gases through passage of an electrical current. Hydrogen can also be generated from hydrocarbons with high hydrogen content, such as ethanol, methanol, ammonia, glycerol, and ethylene glycol. These molecules also produce electrical energy by oxidizing these liquid, hydrogen-rich molecules into protons (H^+) and electrons (current). The fuel cell oxidation reaction occurs on the surface of the anode (electrode catalyst). The electrode catalyst is one of the most important or crucial components of the fuel cell. Even though pure H_2 production is a target in a fuel cell environment, the energy safety storage, and transportation of H_2 have to be considered when the overall target use of fuel cells is considered.

Two of the fuel cells that are currently being studied and commercialized are the ammonia and direct alcohol fuel cells. Platinum (Pt) and the platinum group metals (PGMs) are the most widely used anode electrocatalysts used in these direct alcohol and ammonia fuel cells. An important issue preventing fuel cell commercialization is the carbon monoxide (CO) produced as a by-product specie from an organic liquid fuel during alcohol reaction and the nitrogen monoxide (NO) produced in the ammonia oxidation reaction (AOR) at the anode [2,3]. Fuel cell degradation can be caused by these CO and NO intermediates that can contaminate the Pt-electrocatalyst surface active sites, and prevent hydrogen adsorption and electrooxidation. Fundamental research to study these effects by taking into account parameters such as the metal electrode electrocatalyst, the type of fuel/electrolyte, and the operating temperature are

ongoing. Since platinum is expensive, there has been much research on the use of less noble metals to replace the Pt metal with a Pt-free catalyst or reduce the Pt loading by coupling it with less noble metals to form bimetallic electrocatalysts, which will lower the catalyst cost.

Ammonia as a fuel is one of the best carbon-free hydrogen carriers available, and when it is oxidized in an alkaline environment, the only byproducts are water and nitrogen. The direct ammonia fuel cell (DAFC), which has a conversion efficiency of above 50% to 60% at low temperatures (80 °C to 100 °C), is currently the most efficient fuel cell in use [4,5].

2.1.1 Components of fuel cell

The heart of a fuel cell is the membrane electrode assembly (MEA), which comprises of the gas diffusion layer (GDL), anode/cathode catalyst layer (CL), proton exchange membrane (PEM), and substrate [6]. The elimination of product water as well as the transfer of reactants into the catalyst layer is facilitated by the GDLs, which are located outside the catalyst layers. [7]. The oxidation reaction occurs at the anode in a fuel cell. Fuel cell membranes typically have a thickness of 10–100 μm and are made of an electrically insulating material. The membrane's function is to allow the transfer of protons from the anode side to the cathode side and water to the anode but it blocks the flow of oxygen from the cathode to the anode [8].

2.1.2 Operating principle of fuel cell

In a fuel cell an electrolyte is placed between two electrodes (an anode and a cathode) that are coated with a catalyst [9]. During a fuel cell's operation, oxygen, an oxidant supplied in the cathode compartment, combines with hydrogen fuel, in the anode compartment to produce electricity and water [10]. A platinum catalyst at the anode separates the hydrogen atoms into electrons (e^-) and protons (H^+). The electrons move from the anode side along an external circuit to the cathode side producing an electrical current. The catalyst at the cathode allows the protons to react with oxygen and

electrons to form water which is removed from the fuel cell with unused gases. A direct current can be produced as long as the fuel cell is supplied with both hydrogen and oxygen gases (Fig 2.1). In most fuel cell applications, air is typically employed instead of oxygen (ca. 21% of air) as it is cheaper to use [11]. The following electrochemical reactions take place at the anode and cathode:

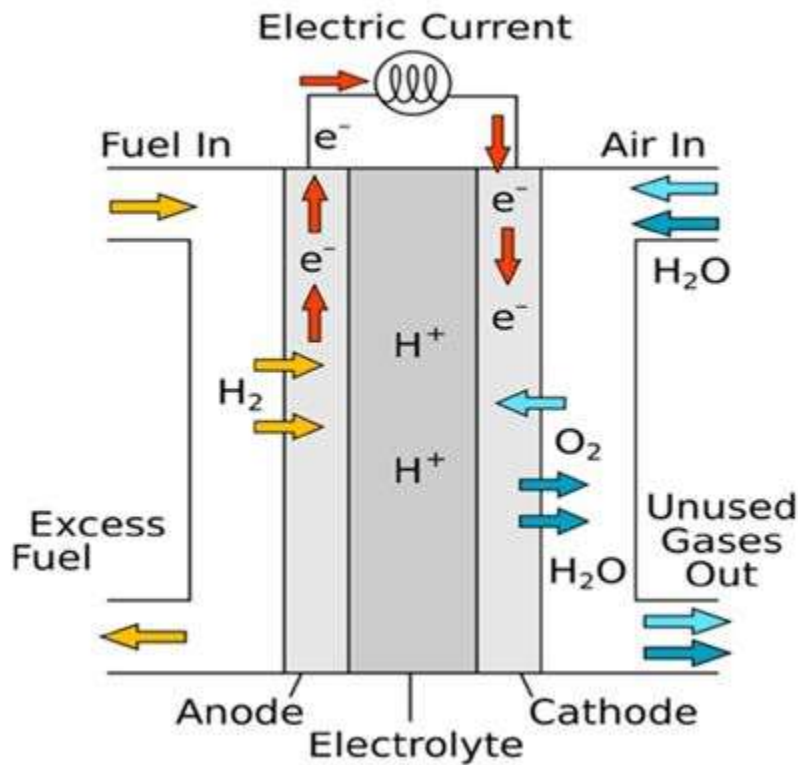
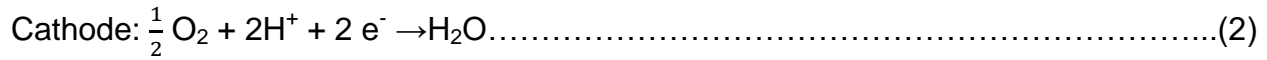
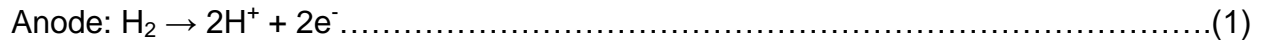


Figure 2.1: Simplified fuel cell operation diagram [12].

2.1.3 Advantages of fuel cells over traditional engines and batteries

Table 2.1 below provides a comparison of various energy generation systems [13]. Among traditional and other distributed generating systems, fuel cells are the only ones

with a high efficiency, as can be seen in Table 2.1 [14]. Fuel cells are about twice as effective at producing energy when compared to traditional internal combustion engines. This is due to the fact that fuel cells circumvent the thermal-mechanical-electric sequence with Carnot's cycle constraints utilized that is used in conventional indirect technologies. Fuel cells also offer many benefits when compared to other distributed generation technologies, including high energy conversion efficiency, modularity, zero-emission, scalability, and quick installation, as well as good opportunities for co-generation operations because they do not have moving parts and do not make noise [15].

Table 2.1: Comparison of different generation systems [16]

	Fuel cells	Photo voltaics	Turbine generator	Wind turbines	Reciprocating engine: diesel
Efficiency (%)	40 - 60	6 - 19	29 - 42	25	35
Capacity Range (kW)	200 - 2000	1 - 1000	500 - 25000	10 - 1000	500 - 5000
O & M Cost (\$/kW)	0.0019-0.0153	0.001-0.004	0.005-0.0065	0.01	0.005 - 0.015
Capital Cost (\$/kW)	1500 - 3000	6600	450 - 870	1000	200 - 350

2.1.3.1 Specific advantages

- ❖ High efficiency. This true particularly at low temperatures, since fuel cells are typically more effective than internal combustion engines (ICEs) and are not constrained by the Carnot cycle efficiency [17].
- ❖ Low or zero greenhouse emission. Despite the fact that hydrogen is not commonly found in its pure molecular form, technological advancements have

made it possible to manufacture it from renewable sources using electrolyzers that are powered by wind turbines or solar photovoltaics. At the point of usage, a hydrogen fuel cell produces no emissions; the only by product is water [18,19].

- ❖ Modular. Fuel cells are modular and so straightforward independent scaling between power and capacity. Conventional batteries cannot be utilized for large-scale applications, whereas fuel cells may be used for everything from 1 W application like mobile phones, to megawatt applications (power plants) [20].
- ❖ Easy refuelling. While fuel cells may be easily refuelled, batteries either need to be thrown away or recharged [21].
- ❖ No moving parts. Since fuel cells have no moving parts they are extremely durable and reliable systems [22].
- ❖ Flexibility. Fuel cell type and operating temperature have an impact on fuel cell flexibility. High-temperature fuel cells need less pure gases to operate than do fuel cells that operate at lower temperatures [23].

2.1.3.2 Disadvantages to fuel cells commercialization

- ❖ Storage and transportation problems. Distribution and storage of hydrogen in large quantities for industrial, domestic, and automotive uses present a significant challenge, which is complicated by its low volumetric energy density. Further, establishing the current infrastructure for the transportation, distribution, and storage of hydrocarbon fuels also posed challenges [13].
- ❖ High costs. Due to the need for materials with specialized properties, fuel cells are more expensive than traditional power systems. The challenge is to create low-cost replacements for essential components like the platinum metal catalyst and Nafion membrane used in Polymer Electrolyte Membrane Fuel Cell (PEMFCs) and Direct Methanol Fuel Cells (DMFCs), which operate at low temperatures. Much research work has been put into producing binary and ternary platinum-based alloy electro-catalysts as well as modifying Nafion membranes in order to cut costs [24].

- ❖ **Stability problems.** A disadvantage of fuel cell technology is the stability and durability of the fuel cell. Fuel cell systems must reach the current US Department of Energy lifetime specified target of 5 000 hours; 20 000 hours for bus application; and 40 000 hours of continuous operation for stationary applications. Despite significant advancement over the years, this target has not yet been met for fuel cell systems [25].

2.2 Applications of fuel cells

- ❖ **Portable Power.** Electronic devices like laptops, cell phones, camcorders, and other low-power appliances can be powered by a portable fuel cell. Fuel cells with power densities ranging from 25 W to 5 kW are used in portable electronic devices where low operating temperatures are needed [26].
- ❖ **Stationary Power.** Hospitals, apartments, office buildings, and small towns without electricity can all be powered by stationary fuel cell power systems that simultaneously provide heat and electricity. Fuel cells are being employed for a variety of purposes, including military applications, remote weather stations, and power sources for spacecraft. Compared to the traditional electric generators used to power homes, companies, and hospitals, stationary power fuel cells are much more dependable and durable [27].
- ❖ **Transportation Power.** For the purpose of generating electricity, transportation fuel cells are used in vehicles including buses, lorries, cars, and submarines. In comparison to battery-powered vehicles, hydrogen-oxygen fuel cell-powered electric vehicles generate no pollutants and are more efficient [28]. Because of the potential of this new form of technology, in comparison to traditional internal combustion engines, several major automakers, including Daimler-Chrysler, Ford, Nissan, Mazda, Toyota, Honda, and Hyundai, have developed vehicles using fuel cells with pure (gaseous or liquid) hydrogen.

2.3 Types of fuel cells (FCs)

The different fuel cell types are named and classified according to the operating temperatures and the type of electrolyte employed, as summarized in Table 2.2. The six primary fuel cell types are listed below.

- ❖ Polymer Electrolyte Membrane Fuel Cell (PEMFCs)
- ❖ Phosphoric Acid Fuel Cells (PAFCs)
- ❖ Solid Oxide Fuel Cells (SOFCs)
- ❖ Molten Carbonate Fuel Cells (MCFCs)
- ❖ Direct Alcohol Fuel Cells (DAFCs)
- ❖ Alkaline Fuel Cells (AFCs)

Table 2.2: Types of fuel cells, electrolyte, operating temperature and charge carrier [29]

FC type	Electrolyte	Fuel	Operating temperature	Charge carrier
PEMFCs	Polymer, PEM	Hydrogen	20-120 C	H ⁺
PAFCs	Liquid H ₃ PO ₄	Hydrogen	150-200 C	H ⁺
SOFCs	Stabilized zirconia	Natural gas or propane	500-1000 C	O ²⁻
MCFCs	Potassium carbonate	Hydrogen, propane	600-700 C	CO ₃ ²⁻
DAFCs	Liquid KOH	Methanol, ethanol	20 – 90 C	H ⁺
AFCs	Liquid KOH	Hydrogen, ammonia	90-120 C	OH ⁻

2.3.1 Direct Alkaline Alcohol Fuel Cells (DAAFCs)

DAAFCs are low-temperature fuel cells that use alcohol (ethanol or methanol) as the fuel and either an anion exchange membrane or an alkaline medium as the electrolyte

[30]. Additionally, they can be considered as liquid fuel cells. The advantages of high energy density and convenient storage that come with using alcohols as fuel in DAAFCs have drawn research attention to this type of fuel cell. Alcohol oxidation in an alkaline medium produces enhanced current densities, which are superior to those obtained when acid electrolytes are used [31]. In an effort to reduce that cost, efforts have been focused on the electrocatalysts, one of the main factors contributing to the high cost of fuel cells. Although precious metal catalysts are used in fuel cells, DAAFCs can use non-precious metal catalysts, which are less expensive than the catalysts that are typically used [32]. Reduced metal loading also lowers the catalyst's overall cost. Fuel cells that use an alkaline electrolyte experience less poisoning than those that use an acid electrolyte.

2.3.1.1 Direct Methanol Fuel Cells (DMFCs)

Cairns and Bartosik reported the development of the first alcohol fuel cell in 1964 and they operated the cell on methanol using alkaline conditions at 115–130 °C [33]. DMFCs are one of the most prevalent types of low-temperature fuel cells that generate electricity through electrochemical reactions by using liquid methanol as a fuel [34]. The electrolyte used in DMFCs is either potassium hydroxide or sodium hydroxide. Methanol has a high energy density and has been developed to address the infrastructural, distribution, and storage issues associated with the use of pure hydrogen [35]. Methanol (CH_3OH) dissolves in water on the anode side of the device during operation, producing hydrogen [25]. Protons and electrons from the anode recombine at the cathode side in an external circuit with oxidized air, producing water as a by-product. One of DMFC's key advantages is that the anode catalyst itself extracts hydrogen from methanol, eliminating the demand for a reformer and lowering total costs. It functions very similarly to the PEM fuel cell, but its activity is constrained by the anode's sluggish electrochemical oxidation of methanol, and the crossing of methanol from the anode to the cathode reduces the efficiency of the DMFCs [36]. Since a single DMFC can deliver 0.3 to 0.5 V when fully loaded, it is typically used to interchange with batteries in 1 W to 1 kW capacity notebook computers, cameras, and other portable electronics.

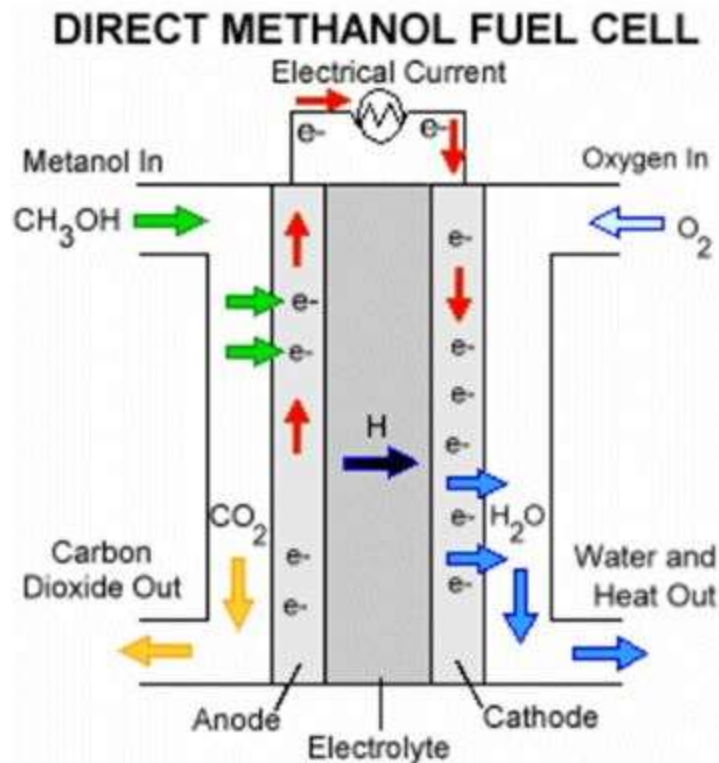


Figure 2.2: Schematic representation of direct methanol fuel cells [37].

2.3.1.2 Direct Ethanol Fuel Cells (DEFCs)

The DEFCs is one of the most suitable candidates for a low-temperature fuel cell that uses liquid ethanol as fuel to generate an electrical current [38]. In comparison to methanol, ethanol is a more desirable fuel for direct alcohol oxidation reactions. Similar to methanol, ethanol is simple to transport and store, but it is less hazardous, and large amounts of ethanol may be generated using renewable resources. Ethanol can be successfully produced from renewable sources through the fermentation process of biomass feed stocks originating from agriculture [39]. Ethanol has many advantages, including a hydrogen-rich liquid, high theoretical energy density, and no impact on greenhouse gas emissions. Ethanol is electrocatalytically transformed to protons, CO_2 , and water at the anode in a DEFC [40]. The main objective of a DEFC is to completely oxidize ethanol to produce carbon dioxide, which will result in the production of 12 electrons in a single reaction. This outperforms the original DMFC, which required 6 electrons to completely oxidize methanol to carbon dioxide. In contrast to the DMFC, the DEFC exhibits a smaller percentage of complete oxidation reactions. This reduced

rate is caused by drawbacks such the chain-like structure of ethanol, the type of catalyst, the structure of the fuel, the membrane employed, and physical parameters like concentration and temperature [41]. DEFCs are enticing when compared to conventional fuel cells for a variety of applications, including large-scale stationary power generation, portable power, distributed power, and transportation.

DIRECT ETHANOL FUEL CELL

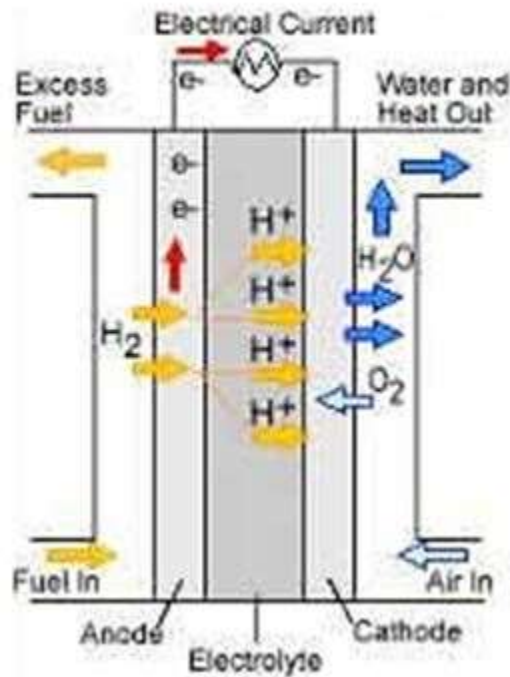


Figure 2.3: Schematic representation of direct ethanol fuel cells [38].

2.3.2 Alkaline Fuel Cells (AFCs)

One of the oldest fuel cell technologies is the alkaline fuel cell (AFC), sometimes known as the bacon fuel cell, which dates to the 1960s and 1970s [42]. These are one of the fuel cell systems that Allis-Chalmers and National Aeronautics and Space Administration (NASA) used as early as the 19th century [43]. This device works at a low temperature of 100 °C and employs a potassium hydroxide (KOH) and sodium hydroxide (NaOH) aqueous solution as an electrolyte [44]. Due to their simplicity, ease

of mobility at the cathode and anode ability to employ non-noble metals, and low cost relative to other fuel cell types, interest in AFCs has grown since their development. Instead of positive ions, the negative ions move through the electrolyte to the anode where they react with hydrogen to produce water as a byproduct of the reaction [45]. AFC's popularity has increased as a result of the use of an alkaline medium because of its high efficiency, reduced fuel crossover and larger range of fuels and electrocatalysts [46]. However, due to its longer reaction time and sensitivity to carbon dioxide, as well as the fact that it consumes the alkali in the electrolyte, which lowers the concentration of hydroxide ions during chemical reactions. Due to these limitations, its commercial applications are limited. The additional drawback is the use of a corrosive electrolyte, which limits its lifespan [47]. AFCs have been used in space shuttles and transportation. Direct Ammonia Fuel Cells (DAFCs) is a subcategory of AFCs.

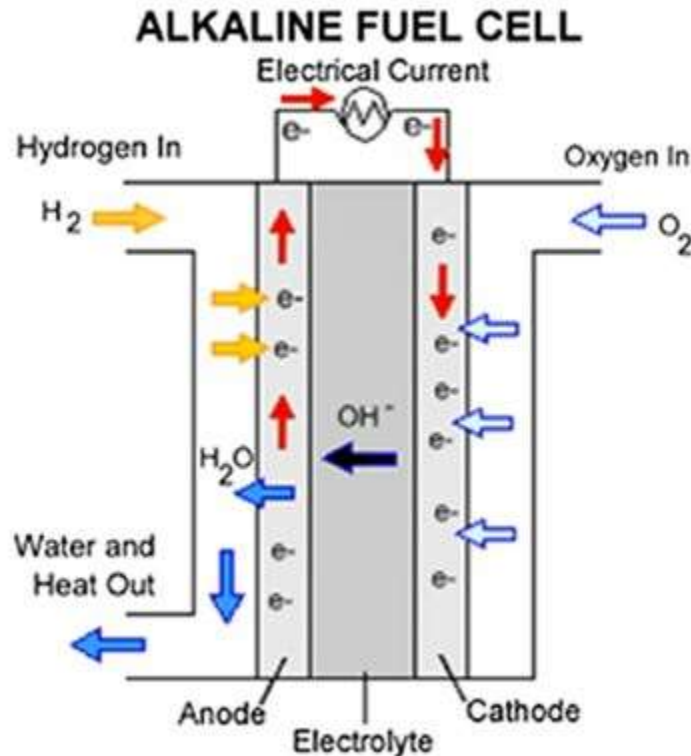


Figure 2.4: Schematic representation of alkaline fuel cells [12].

2.3.2.1 Direct Ammonia Fuel Cells (DAFCs)

The first alkaline fuel cells (AFCs) with a KOH electrolyte and a typical operating temperature of 50–200°C were researched as direct ammonia fuel cells in the 1960s [48]. Direct ammonia fuel cells are a significant technology that can be used to efficiently harvest the chemical energy contained in small ammonia molecules and convert it to electricity [49]. Ammonia was initially studied as a fuel cell source for energy generation and as a source for generating nitrogen oxide, an important chemical. Ammonia does not contain carbon, hence when used as a fuel in a fuel cell or gas turbine, it does not produce CO₂, making it an efficient indirect hydrogen storage source. Liquid ammonia has a theoretical energy density of 11.5 MJ/L, which is greater than the energy densities of 8.491 MJ/L for liquid hydrogen and 4.5 MJ/L for compressed H₂ at 690 pressure and 15°C. The production, storage, and delivery of hydrogen as NH₃ are far more cost-effective and energy-efficient as compared to cryogenic hydrogen [50]. Ammonia's infrastructure is already in place, while building new fueling stations for hydrogen would need a significant investment. To recover the energy contained in ammonia, technologies such as gas turbines, combustion engines, and fuel cells using ammonia as the fuel are being developed [51]. The main disadvantage of employing ammonia as the fuel, however, is considered to be safety. It is possible that the ammonia produced from an ammonia tank during a vehicle accident will pose a safety risk, however this can be avoided by using metal amines with low ammonia partial pressure. Ammonia is harmful; humans can still detect it at amounts as low as 1 ppm. Since anhydrous ammonia is less dense than air, it spreads naturally in the atmosphere. DAFCs were developed to be used in practical applications such as decentralized energy supply, vehicles, energy storage and spacecraft [51]. In DAFCs, ammonia is fed directly to the fuel cell anode where it is broken electrochemically into hydrogen, nitrogen and electrons with water and heat produced as the by-products [52].

DIRECT AMMONIA FUEL CELL

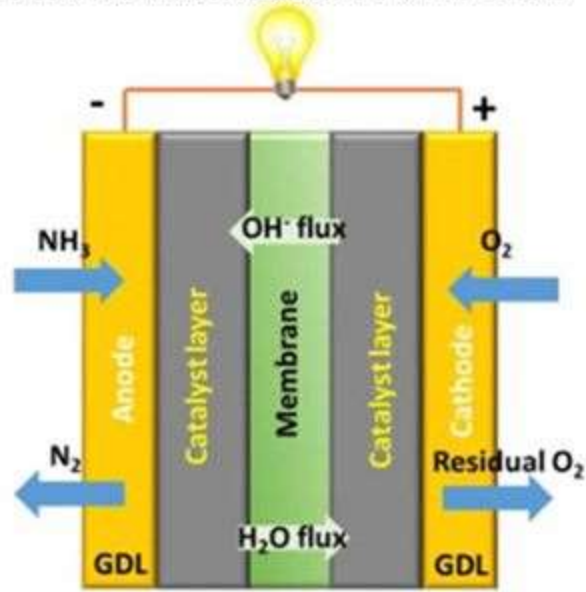


Figure 2.5: Schematic representation of direct ammonia fuel cells [52].

Table 2.3: advantages, disadvantages, and applications of different fuel cells[13]

FC types	Advantages	Disadvantages	Application	Efficiency (%)
PEMFC	Low temperature Rapid start-up High power density	Expensive electrolyte Expensive metal catalyst Catalyst poisoning	Stationary Transport Portable	[53,54]
PAFC	Cheap electrolyte Developed technology Good reliability	Frequent electrolyte change Low CO tolerance (2%) Expensive catalyst	Stationary	[39,55]
SOFC	Solid electrolyte Fuel flexibility Cheap catalyst	Expensive materials Sealing issues	Stationary	[56,57]
DMFC	Rapid initiation Easy fuel handling Low temperature	Fuel crossover Low efficiency High catalyst cost	Portable	[58]
DEFC	High fuel utilization Fuel transport/storage Low temperature Renewable and safe fuel	Catalyst poisoning Anode and cathode performance Water management Noble metal catalysts	Portable Transport	[59]
MCFC	High-quality waste heat Fuel flexibility Cheap catalyst	Expensive materials Corrosive, molten electrolyte Lifetime issue	Stationary	[60,61]
AFC	Low-cost electrolyte Enhanced oxygen reduction Cheap catalyst	Progressive carbonization Water management	Transport Stationary	[62]

2.4 Catalysts Support Materials for Fuel cells

Support materials for fuel cell catalysts play an essential role, mechanically and texturally, in the electrocatalytic activity of the electrode [63]. In addition to having corrosion resistance, it should also be stable in both alkaline and acidic conditions. The support material enhances the dispersion degree, particle size distribution, morphology, alloyed degree, mass transport, and electrical conductivity, which improves the catalytic performance and durability of the catalysts [64]. The perfect support material should have the following properties: (1) large specific surface area, which is necessary for enhancing the dispersion of catalytic materials; (2) suitable porosity to boost gas flow; (3) high electrical conductivity to allow the support to serve as an electron flow channel; (4) excellent electrochemical stability under alcohol and ammonia oxidation reactions; and (5) a successful catalyst support interaction.

2.4.1 Carbon as catalyst supports for fuel cells

Among the elements in the periodic table, carbon is interesting because it can take on a wide range of shapes, different allotropic forms and have numerous micro-textures [65]. This makes carbon a desirable material that can be used in a variety of electrochemical applications. In fuel cells, carbon is frequently utilized as a support for metal nanocatalyst particles due to its superior electrical conductivity, high surface area, and pore structure [66]. Pt is typically supported on a large surface area carbon in the form of nano-dispersed particles to minimize the amount of precious metal catalyst utilized [67].

The commonly employed catalyst support materials for direct alcohol and ammonia fuel cells include carbon-based materials such as carbon black (CB) [68], graphene (G) [69], carbon nanotubes (CNTs) [70], carbon nanodots (CNDs) [71], carbon nanofibers (CNFs) [72], carbon nanoonions (CNOs)/onion like-carbon nanoparticles (OLCNs) [73] and hollow carbon spheres (HCSs) [74]. Among the newer used carbon supports, carbon nano-onions (CNOs) and onion-like carbon nanoparticles (OLCNs) have received much attention due to their excellent properties [75].

2.4.1.2 Carbon nanoonions (CNOs)/Onion like carbon nanoparticles (OLCNs)

Recently, CNOs have received a great deal of attention as a carbon support material for metal nanoparticles in energy storage and conversions [76]. Carbon nano onions (CNOs) as well as their related onion-like carbon counterparts (OLCNs) are examples of support materials that can be used as catalyst supports in fuel cells [77]. CNOs and OLCNs are part of the multi-fullerene family; the OLCNs (sometimes referred to as CNOs) are made up of quasi-sphere shaped and polyhedral shaped nano-graphitic layers of carbon atoms [78]. Onion like carbon nanoparticles with spherical carbon structure can be synthesized by a simple flame pyrolysis (FP) method [79] when a hydrocarbon source is burned partially in the air. This particular variety of FP-produced spherical carbon has a closed-cage structure and a cross-sectional appearance that shows concentric multi-layers. These carbon structure layers are idealized to resemble those of an onion and are referred as carbon nano-onions (CNOs) (see Fig. 6 (a) and (b)). As seen in Fig. 6 (c) and (d), these materials more frequently contain incomplete shells with varied quantities of patchwork carbons. According to Baranov et al., the majority of spherical carbons are composed of varying-sized, short-range, organized, and curved graphene sheets that lead to quasi-spherical multi-layered nanoparticles [80]. These spherical constructions can also be divided into groups depending on whether their cores are solid, hollow, or filled with metal and can have a variety of shells [81,82]. The synthesis method employed to produce the carbon determines the type of carbon that is produced. Any carbon source will yield carbonaceous nanomaterials when it is incompletely burned in a flame, including gases like CO, liquids like poly-aromatic hydrocarbons, and solids like carbon soot. This reaction has been induced by the use of catalysts, various hydrocarbon sources, various reactors, and a range of reaction parameters. This technique produces OLCNs in the gram scale by using a flammable hydrocarbon as a carbon source, such as biodiesel, wood wool, diesel, liquefied petroleum gas, and lycopene (from tomatoes) etc. [83].

2.4.1.3 Heteroatom-doping and functionalization of Onion-like carbon nanoparticles (OLCNs)

One of the limitations in employing OLCNs in different applications is their low ability to disperse in aqueous and organic solvents, which causes the nanoparticles to aggregate [84,85]. Doping and functionalization are two methods that have been employed to address this issue. The most frequent heteroatom dopants that have been incorporated into OLCNs are N and B [77,86]. These have the suitable sizes and electronegativities to be introduced to the edge of a carbon platelet as well as be inserted into a carbon matrix. An OLCN platelet can also have additional heteroatoms like P, O, and S added to its periphery [87–89]. It is to be noted that the difference in size of N (67 pm) and S (88 pm) does not allow the S to be incorporated into the plane of the graphite layer [90]. It thus will only dope at the carbon edges to give thiophene like structures.

In-situ and ex-situ doping are the two main types of heteroatom doping procedures to make OLCNs [91,92]. In the in-situ heteroatom introduction, the initial material may already include the heteroatom (such as N in acetonitrile and pyridine) or may be combined with a heteroatom complex such as diboron trioxide [93,94]. In the ex-situ doping procedure, the heteroatoms are added after the OLCN has already been synthesized. Various C-N heteroatom bonds such as pyridinic- and pyrrolic-nitrogen bonds can be developed when N is introduced into a carbon matrix [95,96]. The majority of doped OLCNs made by FP are made in-situ using a variety of different precursors [97,98]. Also, ammonia has been used as a nitrogen source to synthesize ex-situ N-doped OLCNs.

In addition to heteroatom doping, well-known organic synthesis techniques can be used to modify the structural properties of the as-prepared OLCNs through various functionalization processes [99,100]. The functionalization procedure can be utilized to enhance the surface area of the carbon structure and to increase the dispersibility of OLCNs in both organic and aqueous solutions [101]. The OLCN can be functionalized to produce novel hydrogen bonds and van der Waals interactions [102]. The covalent surface that can be produced by the functionalization methods can also improve the dissolvability of OLCNs [103]. The sp^2 hybridized surface of OLCNs can undergo a variety of chemical reactions,

such as oxidation, fluorination, and cyclopropanation [83]. Supramolecular architectures may result from this kind of functionalization. Several polar solvents, including water and methanol, can disperse functionalized OLCNs (f-OLCNs). Due to their improved biocompatibility, minimal toxicity, and large surface area, f-OLCNs can thus be viable carbon materials for biomedical applications [104]. It should be emphasized, nevertheless, that their reactivity is dependent on the size of the f-OLCN particles and the structural strain, with a larger particle size causing a reduction in reactivity.

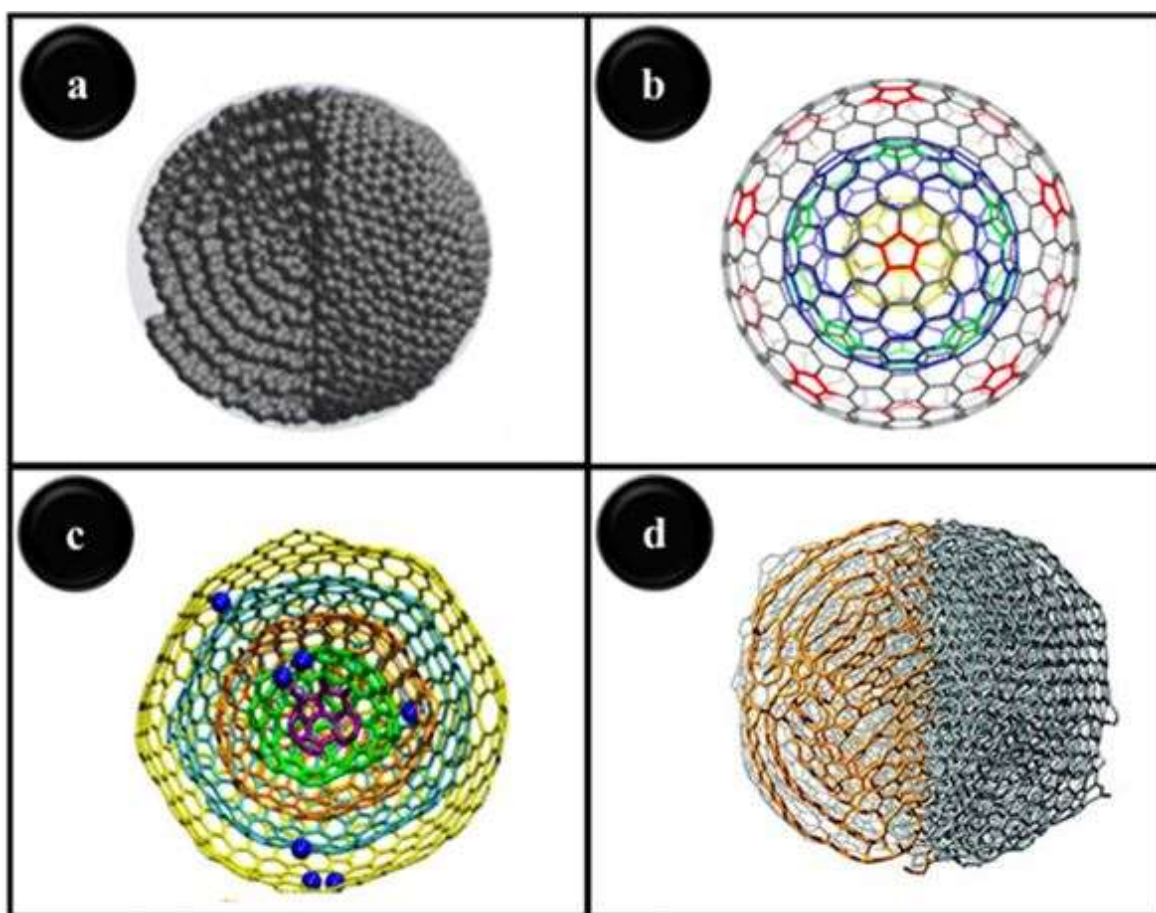


Figure 2.6: Schematic representation of the structural models of; (a, b) carbon nano-onions, and (c, d) onion-like carbon nanoparticles, Adapted from Mongwe et al. [83].

2.4.1.4 Inorganic support materials

Among the numerous inorganic supports used in catalysis, metal oxides play a prominent part due to their ease of preparation in the necessary sizes and shapes. Further, they are inexpensive to produce and may not be toxic. Inorganic metal oxides such WO_3 , CeO_2 , Al_2O_3 , NiO , MnO_2 , SnO_2 , Mn_3O_4 and TiO_2 have been employed as support materials for metal catalysts for direct alcohol and ammonia fuel cells [105–107].

2.4.1.4.1 Titanium dioxide (TiO_2)

Among the various transition metal oxides, TiO_2 is the most desirable because of its superior electrochemical characteristics and long-term stability in a fuel cell environment [108]. The three main crystallographic forms of titanium are anatase and rutile which are the most common polymorphs as well as brookite [109]. The microwave synthesis method can be used to synthesize titania and produce small particles with a limited size distribution and high purity in a short amount of time. Titania has been used in various applications such as photovoltaics and photocatalysis, photo-electrochromism and in sensors because of its distinctive physical characteristics [110]. TiO_2 is an excellent photocatalyst due to its large specific surface area, strong chemical stability, reusability, and stable photocatalytic activity under UV light, which can be extended to the visible light spectrum when doped. The combination of a TiO_2 semiconductor with carbon nanomaterials is one of the most efficient ways to enhance the low electrical conductivity of TiO_2 [110]. Badam et al. synthesized Pt NPs on a hybrid CNT- TiO_2 using a photochemical method, but the electrocatalysts showed lower $E_{1/2}$ and ECSA values than commercial Pt/C catalysts for fuel cells [110]. The positive influence, due to the incorporation of TiO_2 , altered the Pt d orbital electronic properties and this resulted in the contraction of Pt-Pt bonds which impacted on the electrocatalytic oxidation of alcohols and ammonia in fuel cells.

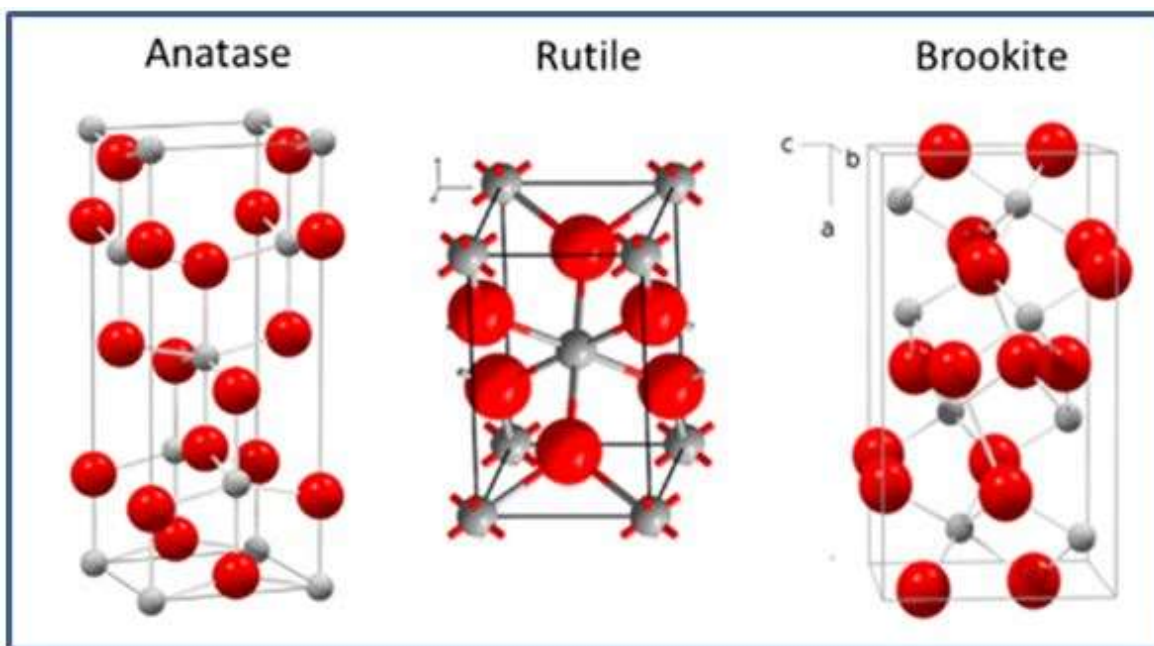


Figure 2.7: Structural representations of TiO_2 (a) anatase, (b) rutile, (c) brookite [23].

2.5. Electrocatalysts in fuel cells

An electrocatalyst by definition is a catalyst that takes part in electrochemical reactions and is employed to accelerate the rate of reaction mechanisms at electrode surface. Platinum group metals (PGMs), have drawn a lot of interest in the field of electrocatalysis because of their distinctive properties [111]. Platinum (Pt) and Palladium (Pd) are the two PGMs that are most commonly employed as catalysts because of their excellent catalytic efficiency and long term stability in a fuel cell environment. However, their usage has been restricted by their scarcity and high price [111]. In large part, platinum and palladium catalysts have similar physiochemical properties, such as the atomic size, fcc crystal structure, d-block nature, melting point, electronegativity, oxidation states, Van der Waals forces, and ionization energies. In a fuel cell, the electrocatalyst is essential because it speeds up electro-oxidation reactions at the electrode surface where fuel and electrolyte come into contact [112]. Due to its greater activity in an alkaline media than platinum, palladium is a preferred electrocatalyst for use in alkaline fuel cells [113]. In the majority of oxidation reduction reactions, Pd and Pd alloys performed

better than alloys of Pt and Pt alloys, particularly in the oxidation of alcohols in an alkaline media. This common metal is preferable and the most recently researched metal because it is less harmed or poisoned when used as an electrocatalyst in a fuel cell by reformat made from alcohols and hydrocarbons [7].

2.5.1 Electrocatalysts used in direct alcohol fuel cells (DAFCs)

DAFCs can be classified as alkaline or acid-based depending on the kind of membrane utilized inside the cell. Fuel cells with alkaline membranes are more popular as a result of the failure of fuel cells with acid membranes, which have a sluggish kinetics for oxidizing alcohol. In addition to having faster kinetics, alkaline direct alcohol fuel cells (ADAFc) also offer an advantage when it comes to using catalysts since they are not restricted to using only precious metals. These kinds of cells can make use of non-precious metals. The types of electrocatalysts utilized for DAFCs have been expanded to include binary and ternary electrocatalysts by the inclusion of transition metals and metal oxides as promoters of the mono electrocatalysts. The ADAFCs that are of interest for this thesis study are the direct methanol fuel cells (DMFC) and direct ethanol fuel cells (DEFC).

2.5.1.1. Electrocatalysts used in direct methanol fuel cells (DMFCs)

DMFCs are categorized as PEMFCs due to the usage of a proton exchange membrane (PEM) [25,114]. Only Pt-based materials, have been demonstrated to be able to adsorb methanol in acid conditions, and have sufficient stability and activity to be desirable as fuel cell electrocatalysts [115]. The main problem with platinum metal as an electrocatalyst is carbon monoxide (CO) poisoning that can block catalyst active sites. On the surface of Pt, carbon monoxide, an intermediary of methanol oxidation, is significantly adsorbed [114]. To increase methanol's efficiency, various Pt-based alloys including PtRu, PtMo, PtW, PtSn, and PtOs have been researched [116]. Among the Pt-based catalysts, a PtRu alloy has been shown to have the best performance due to its appropriate structural composition, particle size, alloying degree, and morphology. When using binary catalysts in DMFCs, Ru has typically been employed as a promoter with Pt. When ruthenium and platinum combine, this enhances the adsorption of oxygen-

containing species at lower potentials and speeds up the conversion of carbon monoxide to carbon dioxide, mitigating the effects of platinum poisoning [117]. Ru atoms alter the electronic properties of Pt, making Pt metal more susceptible to OH adsorption [117]. Using platinum with the less noble metal can also help with cost reduction because alloying reduces the loading of the platinum metal. Reducing the metal loading has been the key focus in relation to the problems with catalysts in DMFCs, but it compromises the fuel cell's performance over time. Research has since switched to investigating potential alternatives, to palladium-based electrocatalysts and alkaline-based DMFC [118].

2.5.1.2 Electrocatalysts used in direct ethanol fuel cells (DEFCs)

Liquid ethanol can be readily oxidized in both acidic and in alkaline environment. Each environment employs a different electrooxidation mechanism. The problem with ethanol direct oxidation is its sluggish reaction kinetics, which involves a variety of reaction routes, intermediates, and products, as well as poisonous species [119]. The full oxidation of ethanol produces CO_2 and releases 12 electrons, and results in the greatest benefit from the perspective of DEFC performance. However, the most common end product is acetic acid, which only releases 4 electrons [38]. This presents a significant challenge as the stable sp^2 C-C bond of ethanol is difficult to break even with the most active Pt based electrocatalysts. Palladium based electrocatalysts have attracted attention because of their potential and capacity to oxidize ethanol [120]. Additionally, onset potentials for ethanol oxidation have reportedly been enhanced over those obtained when Pt is employed, resulting in the largest negative potentials and highest current densities. According to the findings, Pd is a better catalyst for ethanol oxidation than Pt. Several metals, such as Pb, Cu, Sn, Ru, Cd, and Au, among others, have been used to enhance the synthesis of binary Pd-based catalysts [121]. According to some of the literature, the binary electrocatalysts utilized most frequently in DEFCs include PdSn/C, PdBi/C, PdAg/C, PdTb/C, and PdAu/C, among others [122]. Other binary electrocatalysts incorporate metal oxides such as Co_3O_4 , CeO_2 , NiO, ZrO_2 , Mn_3O_4 , and MgO etc. [41]. One pattern that has been observed in both bimetallic and metal oxide-promoted Pd

electrocatalysts is that the catalyst is active at oxidizing ethanol in an alkaline media [123].

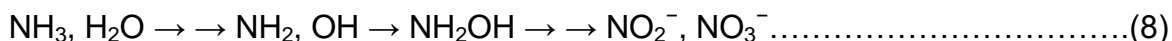
2.5.2. Electrocatalysts used in direct ammonia fuel cells (DAFCs)

The mechanism of ammonia oxidation reactions (AOR) has received a great deal of attention since ammonia is a fuel rich in hydrogen [124]. The primary challenges with AOR are brought on by the slow kinetic speeds of the electrooxidation of ammonia [124]. The construction of high-performance electrocatalysts for ammonia electrooxidation is crucial to resolving these problems. A suitable electrocatalyst should satisfy requirements that include high activity, stability, and an adequate cost. The majority of early investigations focused on selecting platinum-based anode materials and appropriate AOR experimental conditions [125]. In early research by Muller [126] on the ammonia oxidation process, the electrolysis of ammonia was done with a platinum modified electrode in a solution of sodium hydroxide (NaOH). The ideal conversion of NH₃ to N₂ should occur without further oxidation to nitrate ions. However, nitrogen and nitrate ions are among the oxidation products as shown in equations (4) and (5).



The ammonia oxidation occurs with excessive ammonia oxidation to nitrogen oxides at the anode. In a fuel cell, 3 M ammonia in KOH solution was electrolyzed by Katan and Galiotto [124], who prepared the anode using Pt on carbon black. Pure nitrogen was present in the gas released by the ammonia oxidation reaction when a current density of 10 to 100 mA cm⁻² was applied; this corresponded to an anode potential range of - 0.31 to - 0.11 versus SHE for the anode. Bunce et al. suggested that there is a water oxidation potential, which comprises the nitrogen produced from ammonia and oxygen produced from water [127]. Ammonia and water were simultaneously oxidized in this region of water, resulting in the cross-combination product NH₂OH. Subsequently, NO₂⁻ and NO₃⁻ were produced.





Platinum is associated with ammonia over-oxidation and chemical intermediates that are heavily adsorbed have a deactivating impact on platinum. Other noble metals and transition metals also show the same oxidation mechanism as platinum metal. Alloying with another metal is a popular alternative to using pure noble metals for the AOR [128]. Pt and Ir among the different metals show steady-state action to nitrogen production [129]. Other transition metals (Ru, Rh, and Pd) may not assist to the nitrogen production due to the intermediate hydrogenated adsorbate's propensity to generate more stable atomic nitrogen during the AOR [130]. Pt is the only metal with the highest AOR activity among these single metals. Numerous researches have been published on the use of Pt-based alloy electrocatalysts for the oxidation of ammonia in an alkaline electrolyte conditions [131]. In the past few years, bimetallic and multi-metallic platinum nanocatalysts were studied in direct ammonia fuel cells such as Pt₅Pd₅, Pt₇Pd₃, PtPdRh, Pt₇Ir₃, Pt-Ir-Rh, Pt-Ni, PtAu/C, PtRh/C, and Pt-Ru [131–135]. The bimetallic nanocatalyst shows dehydrogenation steps of ammonia at a lower potential (around - 0.6V) than the catalyst with the lowest ammonia oxidation potential (0.1V) on pure Pt. AOR catalysts modified with metal oxides, particularly rare earth oxides (CeO₂, Y₂O₃, La₂O₃, and Sm₂O₃), have been studied [52]. The findings showed that the CeO₂ additive had the biggest increase in current and that the metal oxide addition improved the supply capacity of OH- adsorption to the active sites on Pt [136].

2.6. Electrocatalyst preparation methods

The electrocatalysts used in fuel cells can be synthesized using a variety of techniques, such as microwave assisted synthesis, chemical vapor deposition, alcohol reduction, impregnation, spray pyrolysis, microemulsion, sol-gel, precipitation, colloidal, hydrothermal, and aerosol assisted deposition [137–141]. The methodology that can be employed to produce electrocatalysts has a significant impact on their structure, morphology, size, and consequently, their electrocatalytic properties. The following methods that are discussed below were used to synthesize our Pd and Pt based electrocatalysts.

2.6.1. Microwave synthesis method

Microwave synthesis is a widely used technique for the production of a wide range of inorganic metallic and bimetallic alloy nanoparticles since it is simple, quick, and energy-efficient and does not require high temperatures or high pressures [142]. Microwaves are oscillating electromagnetic radiation at frequencies between 300 MHz and 300 GHz and wavelengths between 1 mm and 1 m. In this technique, the heat is produced using a microwave to catalyze the desired chemical reaction. The reactants absorb microwave radiation, which is subsequently converted to heat. Additionally, microwave heating (irradiation) (MWI) has the advantage of being useful for controlled large-scale synthesis due to its ability to reduce the effects of thermal gradients [143]. Furthermore, the concentration of the precursor and the MWI time can be changed to adjust nanoparticle size, and the composition and concentration of the ligating solvents can be changed to control the shape of the produced nanostructures [144].

2.6.2. Chemical vapour deposition method (CVD)

The CVD technique is a process that is utilized for the production of solid materials with high purity and performance by the reaction of gaseous materials sources [145]. This technique is commonly used in the semiconductor industry to generate thin films of a wide range of materials. In a typical CVD procedure, a substrate is subjected to one or more volatile precursors, which react or disintegrate on the surface of the substrate to form the desired deposits. Volatile by-products are also regularly formed and eliminated by the reaction chamber's gas flow. This method can be used to deposit material in a variety of shapes, including polycrystalline, monocrystalline, epitaxial, and during unstructured, the microfabrication process [145]. Materials such as silicon, carbon nanofibers, carbon nanotubes, and filaments are also manufactured in this process. One of the main benefits is that thin films are frequently extremely conformal, meaning that the film thickness on the sidewalls of structures with high aspect ratios is comparable to the thickness on the top [146]. Another benefit is that the equipment can typically be changed to a wide range of process variations and does not typically require ultrahigh vacuum. Its adaptability enables for several compositional modifications during

deposition and the easily accomplished co-deposition of compounds or elements [147].

2.6.3. Alcohol reduction/Polyol method

The polyol process is another name for the alcohol reduction technique. It is the most used technique because it is straightforward and produces tiny particles with controlled loading in the 2–7 nm range. The alcohol reduction technique was developed in 1989 by Fievet et al. to produce well-defined metal nanoparticles, such as Co, Ni, and Cu particles in terms of size, shape, composition, and crystallinity [148]. It is a reliable method for developing supported nanoparticle catalysts by stabilizing the growth and aggregation of metal catalysts at high temperatures with a polymeric capping agent. It involves reducing metal precursors in ethylene glycol, which acts as a reducing agent in various ratios, in the liquid phase. Subsequently, hydrogen peroxide is added, and the mixture is then heated to a refluxing temperature of 473-593 K for several of hours. In the alcohol reduction process, metal ions receive electrons from ethylene glycol, which dissolves to produce glycolic acid, and are then reduced to form metal colloid (zero valent oxidation state) using ethylene solvent. The polyol technique has the benefit of stabilizing metal colloids in an alkaline solution by deprotonating glycolic acid to produce a glycolate anion [149,150]. In order to control particle size growth and facilitate the formation of nanoparticles, sodium hydroxide was essential in modifying the pH of the reaction solution [151].

2.7. Electrochemical Modification Techniques

2.7.1. Drop coating

Drop-coating is a straightforward, inexpensive, and adaptable method that involves dropping small droplets of a modifier solution in a volatile solvent on the electrode surface and letting them dry for a predetermined time period [152]. The solvent will begin to evaporate off the electrode's top surface, or the substrate will be heated to accelerate the process, and the modifier will then form a thin, irregular solid film in the dry pore space. However, the thickness of the film is

influenced by the electrode surface roughness, solvent type, rate of solvent evaporation, and casting solution concentration [153].

2.7.2. Dip-dry

Early in the 1980s, the dip dry method was developed to enhance high-index resistant lenses. This procedure involves slowly dipping the electrode into the modifier solution for a certain period of time to allow for enough interaction with an electrode moving at a constant speed to produce a uniform coating material for complete wetting [154]. The excess liquid will drain away once the electrode is dragged upwards in the solution at a consistent speed, leaving behind the dried thin coating on the electrode surface. Sintering or heat drying can be used to accelerate the formation of this thin film and burn out any associated chemical reactions, such as functional oxides.

2.7.3. Spin coating

The spin coating method is a simple and quick-growing method for depositing modifier solution on the electrode surface. In the conventional spin coating procedure, excess amounts of a solution are applied to the substrate and rotated quickly in order to disperse the liquid by centrifugal force and achieve the appropriate film thickness after drying [155]. The great surface-to-volume ratios, porous architectures, and extreme thinness of spin-coated films make them ideal for fuel cell and sensor applications. The concentration of both the solvent and the solution, however, determines the film's thickness. Spin coating is widely employed in microfabrication and photolithography, and the resulting film may have lower crystallite coverage than a film that is only evaporate [156].

References

- [1] O.Z. Sharaf, M.F. Orhan, An overview of fuel cell technology: Fundamentals and applications, *Renew. Sustain. Energy Rev.* 32 (2014) 810–853. <https://doi.org/10.1016/j.rser.2014.01.012>.
- [2] M.J. Janik, M. Neurock, A first principles analysis of the electro-oxidation of CO over Pt(1 1 1), *Electrochim. Acta.* 52 (2007) 5517–5528.

- <https://doi.org/10.1016/j.electacta.2007.01.060>.
- [3] E. Antolini, Pt-Ni and Pt-M-Ni (M = Ru, Sn) anode catalysts for low-temperature acidic direct alcohol fuel cells: A review, *Energies*. 10 (2017). <https://doi.org/10.3390/en10010042>.
- [4] Y. Zhao, B.P. Setzler, J. Wang, J. Nash, T. Wang, B. Xu, Y. Yan, An Efficient Direct Ammonia Fuel Cell for Affordable Carbon-Neutral Transportation, *Joule*. 3 (2019) 2472–2484. <https://doi.org/10.1016/j.joule.2019.07.005>.
- [5] G. Jeerh, M. Zhang, S. Tao, Recent progress in ammonia fuel cells and their potential applications, *J. Mater. Chem. A*. 9 (2021) 727–752. <https://doi.org/10.1039/d0ta08810b>.
- [6] S.M. Haile, Fuel cell materials and components, *Acta Mater*. 51 (2003) 5981–6000. <https://doi.org/10.1016/j.actamat.2003.08.004>.
- [7] S. Litster, G. McLean, PEM fuel cell electrodes, *J. Power Sources*. 130 (2004) 61–76. <https://doi.org/10.1016/j.jpowsour.2003.12.055>.
- [8] M. Gasik, Materials for fuel cells, *Mater. Fuel Cells*. (2008) 1–498. <https://doi.org/10.1533/9781845694838>.
- [9] C. Song, Fuel processing for low-temperature and high-temperature fuel cells: Challenges, and opportunities for sustainable development in the 21st century, *Catal. Today*. 77 (2002) 17–49. [https://doi.org/10.1016/S0920-5861\(02\)00231-6](https://doi.org/10.1016/S0920-5861(02)00231-6).
- [10] H. Shen, C. Choi, J. Masa, X. Li, J. Qiu, Y. Jung, Z. Sun, Electrochemical ammonia synthesis: Mechanistic understanding and catalyst design, *Chem*. 7 (2021) 1708–1754. <https://doi.org/10.1016/j.chempr.2021.01.009>.
- [11] Y. Zhao, Y. Liu, G. Liu, Q. Yang, L. Li, Z. Gao, Air and hydrogen supply systems and equipment for PEM fuel cells: a review, *Int. J. Green Energy*. 19 (2022) 331–348. <https://doi.org/10.1080/15435075.2021.1946812>.
- [12] H. Vaghari, H. Jafarizadeh-Malmiri, A. Berenjian, N. Anarjan, Recent

- advances in application of chitosan in fuel cells, *Sustain. Chem. Process.* 1 (2013) 1. <https://doi.org/10.1186/2043-7129-1-16>.
- [13] A. Kirubakaran, S. Jain, R.K. Nema, A review on fuel cell technologies and power electronic interface, *Renew. Sustain. Energy Rev.* 13 (2009) 2430–2440. <https://doi.org/10.1016/j.rser.2009.04.004>.
- [14] G.L. Soloveichik, Liquid fuel cells, *Beilstein J. Nanotechnol.* 5 (2014) 1399–1418. <https://doi.org/10.3762/bjnano.5.153>.
- [15] F. Alcaide, P.L. Cabot, E. Brillas, Fuel cells for chemicals and energy cogeneration, *J. Power Sources.* 153 (2006) 47–60. <https://doi.org/10.1016/j.jpowsour.2005.11.041>.
- [16] J. Li, X. Geng, J. Li, A comparison of electricity generation system sustainability among G20 countries, *Sustain.* 8 (2016) 1–11. <https://doi.org/10.3390/su8121276>.
- [17] E. Antolini, E.R. Gonzalez, Ceramic materials as supports for low-temperature fuel cell catalysts, *Solid State Ionics.* 180 (2009) 746–763. <https://doi.org/10.1016/j.ssi.2009.03.007>.
- [18] S. Mekhilef, R. Saidur, A. Safari, Comparative study of different fuel cell technologies, *Renew. Sustain. Energy Rev.* 16 (2012) 981–989. <https://doi.org/10.1016/j.rser.2011.09.020>.
- [19] A.M. Sheikh, K. Ebn-Alwaled Abd-Alftah, C.F. Malfatti, On reviewing the catalyst materials for direct alcohol fuel cells (DAFCs), *J. Multidiscip. Eng. Sci. Technol.* 1 (2014) 3159–40. www.jmest.org. JMESTN42350307 83.
- [20] A. Boudghene Stambouli, E. Traversa, Fuel cells, an alternative to standard sources of energy, *Renew. Sustain. Energy Rev.* 6 (2002) 295–304. [https://doi.org/10.1016/S1364-0321\(01\)00015-6](https://doi.org/10.1016/S1364-0321(01)00015-6).
- [21] R.A. Felseghi, E. Carcadea, M.S. Raboaca, C.N. Trufin, C. Filote, Hydrogen fuel cell technology for the sustainable future of stationary applications, *Energies.* 12 (2019). <https://doi.org/10.3390/en12234593>.

- [22] S.K. Dash, S. Chakraborty, M. Roccotelli, U.K. Sahu, Hydrogen Fuel for Future Mobility: Challenges and Future Aspects, *Sustain.* 14 (2022). <https://doi.org/10.3390/su14148285>.
- [23] A. Bach Delpuch, M. Jacquot, M. Chatenet, C. Cremers, The influence of mass-transport conditions on the ethanol oxidation reaction (EOR) mechanism of Pt/C electrocatalysts, *Phys. Chem. Chem. Phys.* 18 (2016) 25169–25175. <https://doi.org/10.1039/c6cp04294e>.
- [24] M. Yaldagard, M. Jahanshahi, N. Seghatoleslami, Carbonaceous Nanostructured Support Materials for Low Temperature Fuel Cell Electrocatalysts—A Review, *World J. Nano Sci. Eng.* 03 (2013) 121–153. <https://doi.org/10.4236/wjnse.2013.34017>.
- [25] H. Liu, C. Song, L. Zhang, J. Zhang, H. Wang, D.P. Wilkinson, A review of anode catalysis in the direct methanol fuel cell, *J. Power Sources.* 155 (2006) 95–110. <https://doi.org/10.1016/j.jpowsour.2006.01.030>.
- [26] C. Stone, A.E. Morrison, From curiosity to “power to change the world®,” *Solid State Ionics.* 152–153 (2002) 1–13. [https://doi.org/10.1016/S0167-2738\(02\)00315-6](https://doi.org/10.1016/S0167-2738(02)00315-6).
- [27] B. Braunschweig, D. Hibbitts, M. Neurock, A. Wieckowski, Electrocatalysis: A direct alcohol fuel cell and surface science perspective, *Catal. Today.* 202 (2013) 197–209. <https://doi.org/10.1016/j.cattod.2012.08.013>.
- [28] E.I. Ortiz-Rivera, A.L. Reyes-Hernandez, R.A. Febo, Understanding the history of fuel cells, 2007 IEEE Conf. Hist. Electr. Power, HEP 2007. (2007) 117–122. <https://doi.org/10.1109/HEP.2007.4510259>.
- [29] K.A.I.L. Wijewardena Gamalath, B.M.P. Peiris, Theoretical Approach to the Physics of Fuel Cells, *Int. Lett. Chem. Phys. Astron.* 2 (2013) 15–27. <https://doi.org/10.18052/www.scipress.com/ilcpa.2.15>.
- [30] B.C. Ong, S.K. Kamarudin, S. Basri, Direct liquid fuel cells: A review, *Int. J. Hydrogen Energy.* 42 (2017) 10142–10157. <https://doi.org/10.1016/j.ijhydene.2017.01.117>.

- [31] E. Antolini, E.R. Gonzalez, Alkaline direct alcohol fuel cells, *J. Power Sources*. 195 (2010) 3431–3450. <https://doi.org/10.1016/j.jpowsour.2009.11.145>.
- [32] J. Maya-Cornejo, R. Carrera-Cerritos, D. Sebastián, J. Ledesma-García, L.G. Arriaga, A.S. Aricò, V. Baglio, PtCu catalyst for the electro-oxidation of ethanol in an alkaline direct alcohol fuel cell, *Int. J. Hydrogen Energy*. 42 (2017) 27919–27928. <https://doi.org/10.1016/j.ijhydene.2017.07.226>.
- [33] Cairns, E.J.; Bartosik, D.C. A Methanol Fuel Cell with an Invariant Alkaline Electrolyte. *J. Electrochem. Soc.* 1964, 111, 1205–1210. <https://doi.org/10.1149/1.2425961>
- [34] M.P. Hogarth, G.A. Hards, Direct methanol fuel cells: Technological advances and further requirements, *Platin. Met. Rev.* 40 (1996) 150–159. <https://doi.org/10.1016/C2018-0-04199-7>.
- [35] Y. Na, F. Zenith, U. Krewer, Increasing fuel efficiency of direct methanol fuel cell systems with feedforward control of the operating concentration, *Energies*. 8 (2015) 10409–10429. <https://doi.org/10.3390/en80910409>.
- [36] B.L. García, V.A. Sethuraman, J.W. Weidner, R.E. White, R. Dougal, Mathematical model of a direct methanol fuel cell, *J Fuel Cell Sci Technol*. 1 2004. <https://doi.org/10.1115/1.1782927>.
- [37] P. Kotrbacek, N.V. Long, C.M. Thi, M. Nogami, T. Physical, Novel Pt and Pd Based Core-Shell Catalysts with Critical New Issues of Heat Treatment, Stability and Durability for Proton Exchange Membrane Fuel Cells and Direct Methanol Fuel Cells, *Heat Treatment*. 3 (2012). <http://dx.doi.org/10.5772/2798>
- [38] M.A.F. Akhairi, S.K. Kamarudin, Catalysts in direct ethanol fuel cell (DEFC): An overview, *Int. J. Hydrogen Energy*. 41 (2016) 4214–4228. <https://doi.org/10.1016/j.ijhydene.2015.12.145>.
- [39] S.P.S. Badwal, S. Giddey, A. Kulkarni, J. Goel, S. Basu, Direct ethanol fuel cells for transport and stationary applications - A comprehensive review,

- Appl. Energy. 145 (2015) 80–103.
<https://doi.org/10.1016/j.apenergy.2015.02.002>.
- [40] Y. Zheng, Advanced Catalytic Materials for Ethanol Oxidation, *Catalysts*. 10(2) (2020) 166. <https://doi.org/10.3390/catal10020166>.
- [41] E. Antolini, Catalysts for direct ethanol fuel cells, *J. Power Sources*. 170 (2007) 1–12. <https://doi.org/10.1016/j.jpowsour.2007.04.009>.
- [42] G. Merle, M. Wessling, K. Nijmeijer, Anion exchange membranes for alkaline fuel cells: A review, *J. Memb. Sci.* 377 (2011) 1–35. <https://doi.org/10.1016/j.memsci.2011.04.043>.
- [43] K. Kordesch, J. Gsellmann, M. Cifrain, S. Voss, V. Hacker, R.R. Aronson, C. Fabjan, T. Hejze, J. Daniel-Ivad, Intermittent use of a low-cost alkaline fuel cell-hybrid system for electric vehicles, *J. Power Sources*. 80 (1999) 190–197. [https://doi.org/10.1016/S0378-7753\(98\)00261-4](https://doi.org/10.1016/S0378-7753(98)00261-4).
- [44] C.A.C. Sequeira, D.S.P. Cardoso, M. Martins, L. Amaral, Novel materials for fuel cells operating on liquid fuels, *AIMS Energy*. 5 (2017) 458–481. <https://doi.org/10.3934/energy.2017.3.458>.
- [45] F. Bidault, D.J.L. Brett, P.H. Middleton, N.P. Brandon, Review of gas diffusion cathodes for alkaline fuel cells, *J. Power Sources*. 187 (2009) 39–48. <https://doi.org/10.1016/j.jpowsour.2008.10.106>.
- [46] T.B. Ferriday, P.H. Middleton, Alkaline fuel cell technology - A review, *Int. J. Hydrogen Energy*. 46 (2021) 18489–18510. <https://doi.org/10.1016/j.ijhydene.2021.02.203>.
- [47] A. Verma, S. Basu, Direct alkaline fuel cell for multiple liquid fuels: Anode electrode studies, *J. Power Sources*. 174 (2007) 180–185. <https://doi.org/10.1016/j.jpowsour.2007.07.077>.
- [48] R. Lan, S. Tao, Ammonia as a suitable fuel for fuel cells, *Front. Energy Res.* 2 (2014). <https://doi.org/10.3389/fenrg.2014.00035>.
- [49] O. Siddiqui, I. Dincer, A review and comparative assessment of direct

- ammonia fuel cells, *Therm. Sci. Eng. Prog.* 5 (2018) 568–578. <https://doi.org/10.1016/j.tsep.2018.02.011>.
- [50] S. Suzuki, H. Muroyama, T. Matsui, K. Eguchi, Fundamental studies on direct ammonia fuel cell employing anion exchange membrane, *J. Power Sources*. 208 (2012) 257–262. <https://doi.org/10.1016/j.jpowsour.2012.02.043>.
- [51] Y. Guo, Z. Pan, L. An, Carbon-free sustainable energy technology: Direct ammonia fuel cells, *J. Power Sources*. 476 (2020) 228454. <https://doi.org/10.1016/j.jpowsour.2020.228454>.
- [52] N.M. Adli, H. Zhang, S. Mukherjee, G. Wu, Review—Ammonia Oxidation Electrocatalysis for Hydrogen Generation and Fuel Cells, *J. Electrochem. Soc.* 165 (2018) J3130–J3147. <https://doi.org/10.1149/2.0191815jes>.
- [53] A. Jablonski, A. Lewera, Improving the efficiency of a direct ethanol fuel cell by a periodic load change, *Cuihua Xuebao/Chinese J. Catal.* 36 (2015) 496–501. [https://doi.org/10.1016/S1872-2067\(14\)60226-6](https://doi.org/10.1016/S1872-2067(14)60226-6).
- [54] J. Friedl, U. Stimming, Model catalyst studies on hydrogen and ethanol oxidation for fuel cells, *Electrochim. Acta.* 101 (2013) 41–58. <https://doi.org/10.1016/j.electacta.2012.12.130>.
- [55] A.M. Sheikh, P.S. Correa, E. Leal da Silva, I.D. Savaris, S.C. Amico, C.F. Malfatti, Energy conversion using pd-based catalysts in direct ethanol fuel cell, *Renew. Energy Power Qual. J.* 1 (2013) 342–345. <https://doi.org/10.24084/repqj11.300>.
- [56] S. Heysiattalab, M. Shakeri, M. Safari, M.M. Keikha, Investigation of key parameters influence on performance of direct ethanol fuel cell (DEFC), *J. Ind. Eng. Chem.* 17 (2011) 727–729. <https://doi.org/10.1016/j.jiec.2011.05.037>.
- [57] N. Li, Y.X. Zeng, S. Chen, C.W. Xu, P.K. Shen, Ethanol oxidation on Pd/C enhanced by MgO in alkaline medium, *Int. J. Hydrogen Energy.* 39 (2014) 16015–16019. <https://doi.org/10.1016/j.ijhydene.2013.12.122>.

- [58] L.K. Tsui, C. Zafferoni, A. Lavacchi, M. Innocenti, F. Vizza, G. Zangari, Electrocatalytic activity and operational stability of electrodeposited Pd-Co films towards ethanol oxidation in alkaline electrolytes, *J. Power Sources*. 293 (2015) 815–822. <https://doi.org/10.1016/j.jpowsour.2015.05.121>.
- [59] P. Saisirirat, B. Joommanee, Study on the Performance of the Micro Direct Ethanol Fuel Cell (Micro-DEFC) for Applying with the Portable Electronic Devices, *Energy Procedia*. 138 (2017) 187–192. <https://doi.org/10.1016/j.egypro.2017.10.148>.
- [60] J.S. Spendelow, A. Wieckowski, Electrocatalysis of oxygen reduction and small alcohol oxidation in alkaline media, *Phys. Chem. Chem. Phys.* 9 (2007) 2654–2675. <https://doi.org/10.1039/b703315j>.
- [61] R. Carrera-Cerritos, R. Fuentes-Ramírez, F.M. Cuevas-Muñiz, J. Ledesma-García, L.G. Arriaga, Performance and stability of Pd nanostructures in an alkaline direct ethanol fuel cell, *J. Power Sources*. 269 (2014) 370–378. <https://doi.org/10.1016/j.jpowsour.2014.06.161>.
- [62] E.H. Majlan, D. Rohendi, W.R.W. Daud, T. Husaini, M.A. Haque, Electrode for proton exchange membrane fuel cells: A review, *Renew. Sustain. Energy Rev.* 89 (2018) 117–134. <https://doi.org/10.1016/j.rser.2018.03.007>.
- [63] A. Chalgin, C. Song, P. Tao, W. Shang, T. Deng, J. Wu, Effect of supporting materials on the electrocatalytic activity, stability and selectivity of noble metal-based catalysts for oxygen reduction and hydrogen evolution reactions, *Prog. Nat. Sci. Mater. Int.* 30 (2020) 289–297. <https://doi.org/10.1016/j.pnsc.2020.01.003>.
- [64] S. yeong Lim, S.I. Kim, M.S. Lee, S.J. Bak, D.H. Lee, S.H. Kwon, T. Kim, Effect of uniformity and surface morphology of Pt nanoparticles to enhance oxygen reduction reaction in polymer electrolyte membrane fuel cells, *Int. J. Hydrogen Energy*. 47 (2022) 29456–29466. <https://doi.org/10.1016/j.ijhydene.2022.06.264>.
- [65] X.Y. Ding, C. Zhang, D.Q. Wang, B.S. Li, Q. Wang, Z.G. Yu, K.W. Ang, Y.W. Zhang, A new carbon allotrope: T5-carbon, *Scr. Mater.* 189 (2020) 72–77.

<https://doi.org/10.1016/j.scriptamat.2020.08.004>.

- [66] S. TANG, G. SUN, J. QI, S. SUN, J. GUO, Q. XIN, G.M. HAARBERG, Review of New Carbon Materials as Catalyst Supports in Direct Alcohol Fuel Cells, *Chinese J. Catal.* 31 (2010) 12–17. [https://doi.org/10.1016/s1872-2067\(09\)60034-6](https://doi.org/10.1016/s1872-2067(09)60034-6).
- [67] C. Prado-Burguete, A. Linares-Solano, F. Rodriguez-Reinoso, C.S.M. De Lecea, Effect of carbon support and mean Pt particle size on hydrogen chemisorption by carbon-supported Pt catalysts, *J. Catal.* 128 (1991) 397–404. [https://doi.org/10.1016/0021-9517\(91\)90298-1](https://doi.org/10.1016/0021-9517(91)90298-1).
- [68] L. Kaluža, M.J. Larsen, M. Zdražil, D. Gulková, Z. Vít, O. Šolcová, K. Soukup, M. Koštejn, J.L. Bonde, L. Maixnerová, M. Odgaard, Highly loaded carbon black supported Pt catalysts for fuel cells, *Catal. Today.* 256 (2015) 375–383. <https://doi.org/10.1016/j.cattod.2015.02.016>.
- [69] L. Cunci, C.V. Rao, C. Velez, Y. Ishikawa, C.R. Cabrera, Graphene-Supported Pt, Ir, and Pt-Ir Nanoparticles as Electrocatalysts for the Oxidation of Ammonia, *Electrocatalysis.* 4 (2013) 61–69. <https://doi.org/10.1007/s12678-012-0120-3>.
- [70] Z.Z. Jiang, Z.B. Wang, Y.Y. Chu, D.M. Gu, G.P. Yin, Carbon riveted microcapsule Pt/MWCNTs-TiO₂ catalyst prepared by in situ carbonized glucose with ultrahigh stability for proton exchange membrane fuel cell, *Energy Environ. Sci.* 4 (2011) 2558–2566. <https://doi.org/10.1039/C1ee01091c>.
- [71] S.S. Gwebu, T. Matthews, W.N. Maxakato, Pt Nanoparticles on Carbon Nanodots-Titania Composite for Enhanced Electro Oxidation of Alcohol Fuels, *J. Electrochem. Energy Convers. Storage.* 19 (2022) 1–8. <https://doi.org/10.1115/1.4050000>.
- [72] J. Guo, G. Sun, Q. Wang, G. Wang, Z. Zhou, S. Tang, L. Jiang, B. Zhou, Q. Xin, Carbon nanofibers supported Pt-Ru electrocatalysts for direct methanol fuel cells, *Carbon N. Y.* 44 (2006) 152–157. <https://doi.org/10.1016/j.carbon.2005.06.047>.

- [73] A. Shaikh, S. Parida, Facile sonochemical synthesis of highly dispersed ultrafine Pd nanoparticle decorated carbon nano-onions with high metal loading and enhanced electrocatalytic activity, *RSC Adv.* 6 (2016) 83711–83719. <https://doi.org/10.1039/c6ra18190b>.
- [74] V. Mashindi, P. Mente, N. Mporfu, T.N. Phaahlamohlaka, O. Makgae, A.I. Kirkland, R. Forbes, K.I. Ozoemena, P.B. Levecque, N.J. Coville, Platinum supported on pristine and nitrogen-doped bowl-like broken hollow carbon spheres as oxygen reduction reaction catalysts, *J. Appl. Electrochem.* (2021). <https://doi.org/10.1007/s10800-021-01554-0>.
- [75] O. Butsyk, P. Olejnik, E. Romero, M.E. Plonska-Brzezinska, Postsynthetic treatment of carbon nano-onions: Surface modification by heteroatoms to enhance their capacitive and electrocatalytic properties, *Carbon N. Y.* 147 (2019) 90–104. <https://doi.org/10.1016/j.carbon.2019.02.063>.
- [76] V. Dhand, M. Yadav, S.H. Kim, K.Y. Rhee, A comprehensive review on the prospects of multi-functional carbon nano onions as an effective, high-performance energy storage material, *Carbon N. Y.* 175 (2021) 534–575. <https://doi.org/10.1016/j.carbon.2020.12.083>.
- [77] A. Shaikh, B.K. Singh, D. Mohapatra, S. Parida, Nitrogen-Doped Carbon Nano-Onions as a Metal-Free Electrocatalyst as a Metal-Free Electrocatalyst, *Electrocatalysis.* 10 (2019). <https://doi.org/10.1007/s12678-019-00514-9>.
- [78] K. Bogdanov, A. Fedorov, V. Osipov, T. Enoki, K. Takai, T. Hayashi, V. Ermakov, S. Moshkalev, A. Baranov, Annealing-induced structural changes of carbon onions: High-resolution transmission electron microscopy and Raman studies, *Carbon N. Y.* 73 (2014) 78–86. <https://doi.org/10.1016/j.carbon.2014.02.041>.
- [79] T.H. Mongwe, B.J. Matsoso, B.K. Mutuma, N.J. Coville, Synthesis of chain-like carbon nano-onions by a flame assisted pyrolysis technique using different collecting plates *Diamond & Related Materials* Synthesis of chain-like carbon nano-onions by a flame assisted pyrolysis technique using di ff

- erent collecti, *Diam. Relat. Mater.* 90 (2018) 135–143. <https://doi.org/10.1016/j.diamond.2018.10.002>.
- [80] V.F.P. A. F. Baranov, and N. Taran, Early Soot Formation Stages In Low-Pressure Diffusional Counterflow Hydrocarbon Flames, *Combust. Explos. Shock Waves.* 29 (1993) 345–347. <https://doi.org/10.1007/BF00797656>.
- [81] A.T. Smith, A.M. LaChance, S. Zeng, B. Liu, L. Sun, Synthesis, properties, and applications of graphene oxide/reduced graphene oxide and their nanocomposites, *Nano Mater. Sci.* 1 (2019) 31–47. <https://doi.org/10.1016/j.nanoms.2019.02.004>.
- [82] A. Molina-Ontoria, M.N. Chaur, M.E. Plonska-Brzezinska, L. Echegoyen, Preparation and characterization of soluble carbon nano-onions by covalent functionalization, employing a Na–K alloy, *Chem. Commun.* 49 (2013) 2406–2408. <https://doi.org/10.1039/c3cc39077b>.
- [83] T.H. Mongwe, N.J. Coville, M.S. Maubane-Nkadimeng, Synthesis of onion-like carbon nanoparticles by flame pyrolysis, *Nanoscience.* 8 (2022) 198–220. <https://doi.org/10.1039/9781839167218-00198>.
- [84] M.E. Plonska-Brzezinska, A. Palkar, K. Winkler, L. Echegoyen, Electrochemical properties of small carbon nano-onion films, *Electrochem. Solid-State Lett.* 13 (2010). <https://doi.org/10.1149/1.3299252>.
- [85] A. Guo, K. Bao, S. Sang, X. Zhang, B. Shao, C. Zhang, Y. Wang, F. Cui, X. Yang, Soft-chemistry synthesis, solubility and interlayer spacing of carbon nano-onions, *RSC Adv.* 11 (2021) 6850–6858. <https://doi.org/10.1039/d0ra09410b>.
- [86] Y. Lin, Y. Zhu, B. Zhang, Y.A. Kim, M. Endo, D.S. Su, Boron-doped onion-like carbon with enriched substitutional boron: The relationship between electronic properties and catalytic performance, *J. Mater. Chem. A.* 3 (2015) 21805–21814. <https://doi.org/10.1039/c5ta03141a>.
- [87] M. Zeiger, N. Jäckel, V.N. Mochalin, V. Presser, Review: Carbon onions for electrochemical energy storage, *J. Mater. Chem. A.* 4 (2016) 3172–3196.

<https://doi.org/10.1039/c5ta08295a>.

- [88] D. Mohapatra, G. Dhakal, M.S. Sayed, B. Subramanya, J. Shim, S. Parida, Sulfur Doping: Unique Strategy To Improve the Supercapacitive Performance of Carbon Nano-onions, *ACS Appl. Mater. Interfaces*. 11 (2019) 8040–8050. <https://doi.org/10.1021/acsami.8b21534>.
- [89] M.P. Thomas, N. Wanninayake, M. De Alwis Goonatilleke, D.Y. Kim, B.S. Guiton, Direct imaging of heteroatom dopants in catalytic carbon nano-onions, *Nanoscale*. 12 (2020) 6144–6152. <https://doi.org/10.1039/d0nr00335b>.
- [90] S. Bag, B. Mondal, A.K. Das, C.R. Raj, Nitrogen and sulfur dual-doped reduced graphene oxide: Synergistic effect of dopants towards oxygen reduction reaction, *Electrochim. Acta*. 163 (2015) 16–23. <https://doi.org/10.1016/j.electacta.2015.02.130>.
- [91] E.Y. Choi, C.K. Kim, Fabrication of nitrogen-doped nano-onions and their electrocatalytic activity toward the oxygen reduction reaction, *Sci. Rep.* 7 (2017) 1–9. <https://doi.org/10.1038/s41598-017-04597-6>.
- [92] K. Mamtani, U.S. Ozkan, Heteroatom-Doped Carbon Nanostructures as Oxygen Reduction Reaction Catalysts in Acidic Media: An Overview, *Catal. Letters*. 145 (2015) 436–450. <https://doi.org/10.1007/s10562-014-1434-y>.
- [93] A.V. Ramya, R. Thomas, M. Balachandran, Mesoporous onion-like carbon nanostructures from natural oil for high-performance supercapacitor and electrochemical sensing applications: Insights into the post-synthesis sonochemical treatment on the electrochemical performance, *Ultrason. Sonochem.* 79 (2021) 105767. <https://doi.org/10.1016/j.ultsonch.2021.105767>.
- [94] G. Panomsuwan, S. Chiba, Y. Kaneko, N. Saito, T. Ishizaki, In situ solution plasma synthesis of nitrogen-doped carbon nanoparticles as metal-free electrocatalysts for the oxygen reduction reaction, *J. Mater. Chem. A*. 2 (2014) 18677–18686. <https://doi.org/10.1039/c4ta03010a>.

- [95] S. Sang, S. Yang, A. Guo, X. Gao, Y. Wang, C. Zhang, F. Cui, X. Yang, Hydrothermal Synthesis of Carbon Nano-Onions from Citric Acid, *Chem. - An Asian J.* 15 (2020) 3428–3431. <https://doi.org/10.1002/asia.202000983>.
- [96] J. Bartelmess, S. Giordani, Carbon nano-onions (multi-layer fullerenes): chemistry and applications, *BELSTEIN J. Nanotechnol.* 5 (2014) 1980–1998. <https://doi.org/10.3762/bjnano.5.207>.
- [97] D. Mohapatra, S.S. Nemala, M.S. Sayed, J.J. Shim, S. Mallick, P. Bhargava, S. Parida, Carbon nano-onion-powered optically transparent and economical dye-sensitized solar cells, *Nanoscale.* 12 (2020) 20621–20630. <https://doi.org/10.1039/d0nr04382f>.
- [98] M.R. Pallavolu, N. Gaddam, A.N. Banerjee, R.R. Nallapureddy, S.W. Joo, Superior energy-power performance of N-doped carbon nano-onions-based asymmetric and symmetric supercapacitor devices, *Int. J. Energy Res.* 46 (2022) 1234–1249. <https://doi.org/10.1002/er.7242>.
- [99] L.L. Sikeyi, T.D. Ntuli, T.H. Mongwe, N.W. Maxakato, E. Carleschi, B.P. Doyle, N.J. Coville, M.S. Maubane-Nkadimeng, Microwave assisted synthesis of nitrogen doped and oxygen functionalized carbon nano onions supported palladium nanoparticles as hybrid anodic electrocatalysts for direct alkaline ethanol fuel cells, *Int. J. Hydrogen Energy.* 46 (2021) 10862–10875. <https://doi.org/10.1016/j.ijhydene.2020.12.154>.
- [100] B. Shaku, T.P. Mofokeng, T.H. Mongwe, N.J. Coville, K.I. Ozoemena, M.S. Maubane-Nkadimeng, Physicochemical Properties of Nitrogen Doped Carbon Nano-onions Grown by Flame Pyrolysis from Grapeseed Oil for Use in Supercapacitors, *Electroanalysis.* 32 (2020) 2946–2957. <https://doi.org/10.1002/elan.202060383>.
- [101] V. Singh, Natural source derived carbon nano-onions as electrode material for sensing applications, *Diam. Relat. Mater.* 87 (2018) 202–207. <https://doi.org/10.1016/j.diamond.2018.06.007>.
- [102] N. Mamidi, A. González-Ortiz, I.L. Romo, E. V. Barrera, Development of functionalized carbon nano-onions reinforced zein protein hydrogel

- interfaces for controlled drug release, *Pharmaceutics*. 11 (2019). <https://doi.org/10.3390/pharmaceutics11120621>.
- [103] M. Frasconi, V. Maffei, J. Bartelme, L. Echegoyen, S. Giordani, Highly surface functionalized carbon nano-onions for bright light bioimaging, *Methods Appl. Fluoresc.* 3 (2015) 044005. <https://doi.org/10.1088/2050-6120/3/4/044005>.
- [104] S. Giordani, J. Bartelme, M. Frasconi, I. Biondi, S. Cheung, M. Grossi, D. Wu, L. Echegoyen, D.F. O'Shea, NIR fluorescence labelled carbon nano-onions: Synthesis, analysis and cellular imaging, *J. Mater. Chem. B*. 2 (2014) 7459–7463. <https://doi.org/10.1039/c4tb01087f>.
- [105] P. Munnik, P.E. De Jongh, K.P. De Jong, Recent Developments in the Synthesis of Supported Catalysts, *Chem. Rev.* 115 (2015) 6687–6718. <https://doi.org/10.1021/cr500486u>.
- [106] F. Chekin, S. Bagheri, S.B. Abd Hamid, Synthesis of Pt doped TiO₂ nanoparticles: Characterization and application for electrocatalytic oxidation of L-methionine, *Sensors Actuators, B Chem.* 177 (2013) 898–903. <https://doi.org/10.1016/j.snb.2012.12.002>.
- [107] C. Martín, G. Solana, P. Malet, V. Rives, Nb₂O₅-supported WO₃: A comparative study with WO₃/Al₂O₃, *Catal. Today*. 78 (2003) 365–376. [https://doi.org/10.1016/S0920-5861\(02\)00301-2](https://doi.org/10.1016/S0920-5861(02)00301-2).
- [108] N. Abdullah, S.K. Kamarudin, Titanium dioxide in fuel cell technology: An overview, *J. Power Sources*. 278 (2015) 109–118. <https://doi.org/10.1016/j.jpowsour.2014.12.014>.
- [109] M. Andrade-Guel, L. Díaz-Jiménez, D. Cortés-Hernández, C. Cabello-Alvarado, C. Ávila-Orta, P. Bartolo-Pérez, P. Gamero-Melo, Microwave assisted sol-gel synthesis of titaniumdioxide using hydrochloric and acetic acid ascatalysts, *Bol. La Soc. Esp. Ceram. y Vidr.* 58 (2018) 171–177. <https://doi.org/10.1016/j.bsecv.2018.10.005>.
- [110] R. Badam, R. Vedarajan, K. Okaya, K. Matsutani, N. Matsumi, Sacrificial

Reducing Agent Free Photo-Generation of Platinum Nano Particle over Carbon/TiO₂ for Highly Efficient Oxygen Reduction Reaction, *Sci. Rep.* 6 (2016) 1–7. <https://doi.org/10.1038/srep37006>.

- [111] A.E. Hughes, N. Haque, S.A. Northey, S. Giddey, Platinum group metals: A review of resources, production and usage with a focus on catalysts, *Resources*. 10 (2021) 1–40. <https://doi.org/10.3390/resources10090093>.
- [112] M. Winter, R.J. Brodd, What are batteries, fuel cells, and supercapacitors?, *Chem. Rev.* 104 (2004) 4245–4269. <https://doi.org/10.1021/cr020730k>.
- [113] M.L. Perry, T.F. Fuller, A Historical Perspective of Fuel Cell Technology in the 20th Century, *J. Electrochem. Soc.* 149 (2002) S59. <https://doi.org/10.1149/1.1488651>.
- [114] S. Sharma, B.G. Pollet, Support materials for PEMFC and DMFC electrocatalysts - A review, *J. Power Sources*. 208 (2012) 96–119. <https://doi.org/10.1016/j.jpowsour.2012.02.011>.
- [115] R.S. Amin, K.M. El-Khatib, R.M.A. Hameed, E.R. Souaya, M.A. Etman, Synthesis of Pt-Co nanoparticles on multi-walled carbon nanotubes for methanol oxidation in H₂SO₄ solution, *Appl. Catal. A Gen.* 407 (2011) 195–203. <https://doi.org/10.1016/j.apcata.2011.08.045>.
- [116] P.P. Patel, M.K. Datta, P.H. Jampani, D. Hong, J.A. Poston, A. Manivannan, P.N. Kumta, High performance and durable nanostructured TiN supported Pt₅₀-Ru₅₀ anode catalyst for direct methanol fuel cell (DMFC), *J. Power Sources*. 293 (2015) 437–446. <https://doi.org/10.1016/j.jpowsour.2015.05.051>.
- [117] S.J. Yoo, T.Y. Jeon, K.S. Kim, T.H. Lim, Y.E. Sung, Multilayered Pt/Ru nanorods with controllable bimetallic sites as methanol oxidation catalysts, *Phys. Chem. Chem. Phys.* 12 (2010) 15240–15246. <https://doi.org/10.1039/c0cp00737d>.
- [118] S.K. Kamarudin, F. Achmad, W.R.W. Daud, Overview on the application of

- direct methanol fuel cell (DMFC) for portable electronic devices, *Int. J. Hydrogen Energy*. 34 (2009) 6902–6916. <https://doi.org/10.1016/j.ijhydene.2009.06.013>.
- [119] Y. Wang, S. Zou, W. Bin Cai, Recent advances on electro-oxidation of ethanol on Pt- and Pd-based catalysts: From reaction mechanisms to catalytic materials, *Catalysts*. 5 (2015) 1507–1534. <https://doi.org/10.3390/catal5031507>.
- [120] C. Li, K. Wang, D. Xie, A review of approaches for the design of high-performance electrocatalysts for ethanol electrooxidation, *Surfaces and Interfaces*. 28 (2022) 101594. <https://doi.org/10.1016/j.surfin.2021.101594>.
- [121] D. Łukowiec, T. Wasiak, D. Janas, E. Drzymała, J. Depciuch, T. Tarnawski, J. Kubacki, S. Waclawek, A. Radoń, Pd decorated Co–Ni nanowires as a highly efficient catalyst for direct ethanol fuel cells, *Int. J. Hydrogen Energy*. 7 (2021). <https://doi.org/10.1016/j.ijhydene.2021.11.177>.
- [122] E. Antolini, Palladium in fuel cell catalysis, *Energy Environ. Sci.* 2 (2009) 915–931. <https://doi.org/10.1039/b820837a>.
- [123] C.V.S. Almeida, G. Tremiliosi-Filho, K.I.B. Eguiluz, G.R. Salazar-Banda, Improved ethanol electro-oxidation at Ni@Pd/C and Ni@PdRh/C core–shell catalysts, *J. Catal.* 391 (2020) 175–189. <https://doi.org/10.1016/j.jcat.2020.08.024>.
- [124] T. Katan, R.J. Galiotto, Current Efficiencies for the Anodic Oxidation of Ammonia in Potassium Hydroxide Solution, *J. Electrochem. Soc.* 110 (1963) 1022. <https://doi.org/10.1149/1.2425915>.
- [125] H. Gerischer, A. Mauerer, Untersuchungen Zur anodischen Oxidation von Ammoniak an Platin-Elektroden, *J. Electroanal. Chem.* 25 (1970) 421–433. [https://doi.org/10.1016/S0022-0728\(70\)80103-6](https://doi.org/10.1016/S0022-0728(70)80103-6).
- [126] E. Muller and F. Spitzer, Z. Uber anodische Oxydbildung und Passivitat. *Elektrochem.*, 11, 917 (1905).
- [127] N.J. Bunce, D. Bejan, Mechanism of electrochemical oxidation of ammonia,

Electrochim. Acta. 56 (2011) 8085–8093.
<https://doi.org/10.1016/j.electacta.2011.07.078>.

- [128] J.C.M. Silva, S.G. Da Silva, R.F.B. De Souza, G.S. Buzzo, E. V. Spinacé, A.O. Neto, M.H.M.T. Assumpção, PtAu/C electrocatalysts as anodes for direct ammonia fuel cell, *Appl. Catal. A Gen.* 490 (2015) 133–138. <https://doi.org/10.1016/j.apcata.2014.11.015>.
- [129] A.C.A. De Vooy, M.T.M. Koper, R.A. Van Santen, J.A.R. Van Veen, The role of adsorbates in the electrochemical oxidation of ammonia on noble and transition metal electrodes, *J. Electroanal. Chem.* 506 (2001) 127–137. [https://doi.org/10.1016/S0022-0728\(01\)00491-0](https://doi.org/10.1016/S0022-0728(01)00491-0).
- [130] M. Massetti, F. Jiao, A.J. Ferguson, D. Zhao, K. Wijeratne, A. Würger, J.L. Blackburn, X. Crispin, S. Fabiano, Unconventional Thermoelectric Materials for Energy Harvesting and Sensing Applications, *Chem. Rev.* 121 (2021) 12465–12547. <https://doi.org/10.1021/acs.chemrev.1c00218>.
- [131] T.L. Lomocso, E.A. Baranova, Electrochemical oxidation of ammonia on carbon-supported bi-metallic PtM (M = Ir, Pd, SnOx) nanoparticles, *Electrochim. Acta.* 56 (2011) 8551–8558. <https://doi.org/10.1016/j.electacta.2011.07.041>.
- [132] C.M. Hung, Electrochemical properties of PtPdRh alloy catalysts for ammonia electrocatalytic oxidation, *Int. J. Hydrogen Energy.* 37 (2012) 13815–13821. <https://doi.org/10.1016/j.ijhydene.2012.03.147>.
- [133] J.C.M. Silva, S.G. Da Silva, R.F.B. De Souza, G.S. Buzzo, E. V. Spinacé, A.O. Neto, M.H.M.T. Assumpção, PtAu/C electrocatalysts as anodes for direct ammonia fuel cell, *Appl. Catal. A Gen.* 490 (2015) 133–138. <https://doi.org/10.1016/j.apcata.2014.11.015>.
- [134] R. Lan, J.T.S. Irvine, S. Tao, Ammonia and related chemicals as potential indirect hydrogen storage materials, *Int. J. Hydrogen Energy.* 37 (2012) 1482–1494. <https://doi.org/10.1016/j.ijhydene.2011.10.004>.
- [135] M.H.M.T. Assumpção, R.M. Piasentin, P. Hammer, R.F.B. De Souza, G.S.

- Buzzo, M.C. Santos, E. V. Spinacé, A.O. Neto, J.C.M. Silva, Oxidation of ammonia using PtRh/C electrocatalysts: Fuel cell and electrochemical evaluation, *Appl. Catal. B Environ.* 174–175 (2015) 136–144. <https://doi.org/10.1016/j.apcatb.2015.02.021>.
- [136] Z.F. Li, Y. Wang, G.G. Botte, Revisiting the electrochemical oxidation of ammonia on carbon-supported metal nanoparticle catalysts, *Electrochim. Acta.* 228 (2017) 351–360. <https://doi.org/10.1016/j.electacta.2017.01.020>.
- [137] J.M.S. Ayoub, A.N. Geraldes, M.M. Tusi, E. V. Spinacé, A.O. Neto, Preparation of PtSnSb/C by an alcohol reduction process for direct ethanol fuel cell (DEFC), *Ionics (Kiel)*. 17 (2011) 559–564. <https://doi.org/10.1007/s11581-011-0574-y>.
- [138] M. Li, X. Wu, J. Zeng, Z. Hou, S. Liao, Heteroatom Doped Carbon Nanofibers Synthesized by Chemical Vapor Deposition as Platinum Electrocatalyst Supports for Polymer Electrolyte Membrane Fuel Cells, *Electrochim. Acta.* 182 (2015) 351–360. <https://doi.org/10.1016/j.electacta.2015.09.122>.
- [139] A. Esmailifar, M. Yazdanpour, S. Rowshanzamir, M.H. Eikani, Hydrothermal synthesis of Pt/MWCNTs nanocomposite electrocatalysts for proton exchange membrane fuel cell systems, *Int. J. Hydrogen Energy.* 36 (2011) 5500–5511. <https://doi.org/10.1016/j.ijhydene.2011.02.015>.
- [140] J. Mitzel, F. Arena, T. Walter, M. Stefener, R. Hempelmann, Direct methanol fuel cell - Alternative materials and catalyst preparation, *Zeitschrift Fur Phys. Chemie.* 227 (2013) 497–540. <https://doi.org/10.1524/zpch.2013.0341>.
- [141] X. Hu, P. Song, X. Yang, C. Wang, J. Wang, Y. Tang, J. Zhang, Z. Mao, One-step microwave-assisted synthesis of carbon-supported ternary Pt-Sn-Rh alloy nanoparticles for fuel cells, *J. Taiwan Inst. Chem. Eng.* 115 (2020) 272–278. <https://doi.org/10.1016/j.jtice.2020.10.008>.
- [142] R.M. Richards, N. Renewable, Nanoscopic Metal Particles – Synthetic Methods and Potential Applications MICROREVIEW Nanoscopic Metal Particles ∫ Synthetic Methods and Potential Applications Helmut

- Bönnemann * [a] and Ryan M . Richards [a], *Eur. J. Inorg. Chem.* 0682 (2019) 2455–2480. [https://doi.org/10.1002/1099-0682\(200109\)2001](https://doi.org/10.1002/1099-0682(200109)2001).
- [143] W. Chen, J. Zhao, J.Y. Lee, Z. Liu, Microwave heated polyol synthesis of carbon nanotubes supported Pt nanoparticles for methanol electrooxidation, *Mater. Chem. Phys.* 91 (2005) 124–129. <https://doi.org/10.1016/j.matchemphys.2004.11.003>.
- [144] A. Dehghan Banadaki, A. Kajbafvala, RHinda, Recent Advances in Facile Synthesis of Bimetallic Nanostructures: An Overview, *J. Nanomater.* 2014 (2014). <https://doi.org/10.3934/matersci.2019.2.17>.
- [145] J. Lu, J.W. Elam, P.C. Stair, Atomic layer deposition — Sequential self-limiting surface reactions for advanced catalyst “ bottom-up ” synthesis, *Surf. Sci. Rep.* 71 (2016) 410–472. <https://doi.org/10.1016/j.surfrep.2016.03.003>.
- [146] O.O. Abegunde, E.T. Akinlabi, O.P. Oladijo, Overview of thin film deposition techniques, *J. Mater. Sci.* 6 (2019) 174–199. <https://doi.org/10.3934/matersci.2019.2.174>.
- [147] D.A. Jameel, *Thin Film Deposition Processes*, (2015).
- [148] F. Fievet, J.P. Lagier, B. Blin, B. Beaudoin, M. Figlarz, Homogeneous and heterogeneous nucleations in the polyol process for the preparation of micron and submicron size metal particles, *Solid State Ionics.* 32–33 (1989) 198–205. [https://doi.org/10.1016/0167-2738\(89\)90222-1](https://doi.org/10.1016/0167-2738(89)90222-1).
- [149] J. Quinson, A. Dworzak, S.B. Simonsen, L. Theil Kuhn, K.M.Ø. Jensen, A. Zana, M. Oezaslan, J.J.K. Kirkensgaard, M. Arenz, Surfactant-free synthesis of size controlled platinum nanoparticles: Insights from in situ studies, *Appl. Surf. Sci.* 549 (2021). <https://doi.org/10.1016/j.apsusc.2021.149263>.
- [150] T.K. Lee, H.J. Park, M.K. Kwon, J.H. Jung, J. Kim, S.H. Hur, Polyol-free synthesis of uniformly dispersed Pt/graphene oxide electrocatalyst by sulfuric acid treatment, *J. Nanomater.* 2012 (2012). <https://doi.org/10.1155/2012/418737>.

- [151] A. Esmailifar, S. Rowshanzamir, M.H. Eikani, E. Ghazanfari, Synthesis methods of low-Pt-loading electrocatalysts for proton exchange membrane fuel cell systems, *Energy*. 35 (2010) 3941–3957. <https://doi.org/10.1016/j.energy.2010.06.006>.
- [152] Y. Wang, Y. Li, L. Tang, J. Lu, J. Li, Application of graphene-modified electrode for selective detection of dopamine, *Electrochem. Commun.* 11 (2009) 889–892. <https://doi.org/10.1016/j.elecom.2009.02.013>.
- [153] M. Aliofkhaezai, A.S.H. Makhlof, Handbook of nanoelectrochemistry: Electrochemical synthesis methods, properties, and characterization techniques, *Handb. Nanoelectrochemistry Electrochem. Synth. Methods, Prop. Charact. Tech.* (2016) 1–1451. <https://doi.org/10.1007/978-3-319-15266-0>.
- [154] M. Shateri-Khalilabad, M.E. Yazdanshenas, Fabricating electroconductive cotton textiles using graphene, *Carbohydr. Polym.* 96 (2013) 190–195. <https://doi.org/10.1016/j.carbpol.2013.03.052>.
- [155] P. Mele, T. Endo, S. Arisawa, C. Li, T. Tsuchiya, Oxide thin films, multilayers, and nanocomposites, *Oxide Thin Film. Multilayers, Nanocomposites*. (2015) 1–316. <https://doi.org/10.1007/978-3-319-14478-8>.
- [156] L. Xu, R.G. Karunakaran, J. Guo, S. Yang, Transparent, superhydrophobic surfaces from one-step spin coating of hydrophobic nanoparticles, *ACS Appl. Mater. Interfaces*. 4 (2012) 1118–1125. <https://doi.org/10.1021/am201750h>.

CHAPTER 3

Microwave assisted synthesis of nitrogen doped and oxygen functionalized carbon nano onions supported palladium nanoparticles as hybrid anodic electrocatalysts for direct alkaline ethanol fuel cells

L.L. Sikeyi, T.D. Ntuli, T.H. Mongwe, N.W. Maxakato, E. Carleschi, B.P. Doyle, N.J. Coville, M.S. Maubane-Nkadimeng, Microwave assisted synthesis of nitrogen doped and oxygen functionalized carbon nano onions supported palladium nanoparticles as hybrid anodic electrocatalysts for direct alkaline ethanol fuel cells, *Int. J. Hydrogen Energy*. 46 (2021) 10862–10875. <https://doi.org/10.1016/j.ijhydene.2020.12.154>. Impact factor: 7.139.

1. Sikeyi - Synthesis and characterization, Writing-Original Draft, Validation
2. Ntuli – Data Curation
3. Mongwe - Flame pyrolysis method
4. Carleschi - XPS analysis
5. Doyle - XPS analysis
6. Maxakato - Resources, Supervision
7. Coville - Reviewing and Editing, Resources, Supervision
8. Maubane-Nkadimeng- Conceptualization, Resources, Supervision

Ludwe L Sikeyi^a, Themba D Ntuli^{a,d}, Thomas H Mongwe^{a,d}, Nobanathi W Maxakato^b, Emanuela Carleschi^c, Bryan P Doyle^c, Neil J Coville^{a,d} and Manoko S Maubane-Nkadimeng^{a,d,e*}

^a Molecular Sciences Institute, School of Chemistry, University of the Witwatersrand, Braamfontein, 2050, South Africa, ^b Department of Chemical Science, University of Johannesburg, Doornfontein, 2021, South Africa. ^c Department of Physics, University of Johannesburg, Auckland Park, 2092, South Africa. ^d DSI-NRF Centre of Excellence in Strong Materials, University of the Witwatersrand, Braamfontein, 2050, South Africa. ^e Microscopy and Microanalysis Unit, University of the Witwatersrand, Braamfontein, 2050, South Africa

Abstract

In this study, we present the synthesis of pristine carbon (p-CNO), nitrogen doped (N-CNO) and oxygen functionalized (ox-CNO) nano onions, using flame pyrolysis, chemical vapour deposition, and reflux methods, respectively. Pd/p-CNO, Pd/N-CNO and Pd/ox-CNO electrocatalysts are prepared using a simple and quick microwave-assisted synthesis method. The various CNO and Pd/CNO electrocatalysts are fully characterized and the FTIR and XPS results reveal that the synthesized CNOs contain oxygen and nitrogen functional groups that facilitate the attachment and dispersion of the Pd nanoparticles. Electrochemical tests show that the N-CNO and Pd/N-CNO electrocatalysts exhibit high current density (4.2 mA cm^{-2} and 17.4 mA cm^{-2}), long-term stability (1.2 mA cm^{-2} and 6.9 mA cm^{-2}), and fast electron transfer when compared to the equivalent pristine and oxidized catalysts (and their Pd counterparts), and a commercial Pd/C electrocatalyst, towards ethanol oxidation reactions in alkaline medium.

Keywords: Carbon nano onions; Cyclic voltammetry; Chronoamperometry; Direct ethanol fuel cells; Electrocatalysts; Electrochemical impedance spectroscopy.

3. Introduction

Carbon nano onions (CNOs) are a new member of the multi-shell fullerene family [1]. CNOs consist of a spherical structure made up of concentric nano-graphitic layers of carbon atoms [2]. A diversity of methods has been reported for the preparation of CNOs including flame pyrolysis (FP), chemical vapour deposition (CVD), ion implantation, counter-flow diffusion flames, annealing of nano-diamonds, electron irradiation, and plasma spraying of nano-diamonds [3]. Depending on the synthesis methods used to make the CNOs, various sorts of carbon nanostructures can be accomplished with different sizes (5-20 nm), shapes (circular and polyhedral), and with different kinds of centers (dense and hollow).

Their interesting physical and chemical properties include biocompatibility, low toxicity, high carbon ordering which induces high electrical conductivity, a low density promoting a moderately high surface area, mesoporous nature, and high thermal stability [4]. Of all available methods for the production of CNOs, FP is receiving much attention as it uses single-step process, inexpensive hydrocarbon sources and produce CNOs in higher yields [5]. Recently, our group has reported a facile flame assisted ghee oil pyrolysis synthesis method for producing chain-like graphitic CNOs in bulk quantity [6]. The flame pyrolysis synthesis method reported in this current study is an alternative method that uses carbon containing liquids and/or oils as carbon source for growing of CNO under ambient temperatures.

CNOs have been actively studied as support material and metal free electrocatalyst for use in electrochemical energy-storage applications and for electrocatalytic performance in alkaline fuel cells [7–9]. Shaikh et al. reported Pd decoration of CNOs obtained from a simple sonochemical method for the formaldehyde oxidation reaction by only a cyclic voltammetry technique [8]. These CNOs were utilized in as-prepared condition with no further treatment (doping or functionalization). To expand the scope of CNOs usage, current research is focused on the functionalization and doping of CNOs to incorporate oxygen and nitrogen-containing groups that will increase their hydrophilicity and improve the catalyst-support interaction. Synthesis methods include impregnation, acid, and peroxide treatment (such as a mixture of HNO_3 and H_2O_2), microwave assisted synthesis, polyol process, ion-exchange and electrochemical deposition [10]. Heteroatom-doping is a constructive way to improve the catalytic performance of carbon material and to change their physical and chemical properties. Shaku et al. reported on nitrogen doping of CNOs for use in supercapacitor and observed an increased in specific capacitance as compared to pristine CNOs [11]. On the other hand, while studying the oxygen reduction reaction (ORR) on Pd/N-rGO Ejaz et al. revealed the individual influence of pyrrolic, pyridinic and graphitic-N on the synthesis, size, and extraordinary distribution of Pd NPs [12]. Zang et al. reported that nitrogen doping of CNOs provided better electrocatalytic activity and stability for the oxygen reduction reaction in alkaline condition [13]. The improvement in

ORR performance of N-CNOs can be ascribed to the effects of exposed catalytic sites, good electron transport, and CNO mesoporosity. Furthermore, the hydrogen peroxide generation or oxygen functionalization on Pd₃Fe/C showed enhanced performance for ORR with regard to surface inactivity against oxidation and adsorption of methanol [14]. These studies show that the introduction of these doping agents substantially modifies the architecture of carbon nanomaterials, providing better dispersion and distribution of the catalyst's nanoparticles.

The microwave assisted synthesis method is an industrial synthetic method used for the preparation of the metal carbon based electrocatalysts [15]. This method makes use of a microwave to generate heat energy that accelerates a desired chemical reaction. The main feature of the microwave heating of metal precursors and carbon nanomaterials in solution is that the reduction reaction occurs in the solution rather than in the solid state, the metal electrocatalyst is formed by nucleation and growth from solution [16]. In microwave synthesis, the polyol process (ethylene glycol) is the most common route used to produce metal carbon based electrocatalysts. Kumar et al. reported microwave-assisted synthesis of Pd nanoparticles intercalated nitrogen doped reduced graphene oxide for ethanol oxidation reaction (EOR) in alkaline media [17]. The Pd/N-rGO electrocatalyst showed enhanced catalytic activity for EOR when compared to Pd/rGO electrocatalyst.

Direct alcohol fuel cells (DAFCs) are attractive as power sources as they employ a low molecular weight and use cheap, green fuel [18]. They have fascinating advantages such as high efficiency, high energy density, low working temperature, greatly simplified design, and quiet operation without vibration or noise [19]. Ethanol as a liquid fuel has the advantage that it is renewable and non-toxic [20]. The commercialization of direct alcohol fuel cells (DAFCs) has however been limited by poor alcohol electro-oxidation reaction kinetics, the poisoning effect of the anode catalysts by CO intermediates, and the high cost of the platinum electrocatalyst [21]. Platinum is still considered to be the most active catalyst for DAFCs, but its cost makes it difficult to commercialize the DAFC technology [21]. These problems could be resolved by using less expensive palladium, palladium alloys, and/or palladium-free catalysts [22]. It has been observed that palladium

shows greater activity in alkaline media than platinum [23]. This suggests a focus on alkaline direct alcohol fuel cells (ADAFCS) which can utilize cheap Pd based electrocatalyst or Pd free electrocatalyst [14].

The performance of the electrocatalyst for alcohol oxidation depends on the dispersion of the catalyst and the particle size distribution and the characteristics of the support utilized [24]. Also, the support material for a fuel cell electrocatalyst must have enough electrical conductivity so that the support can act as a passage for the progression of electrons [25]. Supporting electrolytes such as sodium hydroxide, potassium hydroxide, and sulphuric acid play a vital role in determining the overall fuel cell performance [26]. Hence stability and corrosion resistance of the catalyst support material in the fuel cell environment is of great importance in the advancement of new catalyst support materials [27].

In this work, a green and simple flame pyrolysis method for synthesizing CNOs has been developed. We also present the use of CNOs produced as a support material and as a metal-free electrocatalyst for use in DAFCs. The CNOs supported palladium nanoparticles (obtained by reduction of Pd with sodium borohydride) were prepared using a microwave assisted synthesis method. To the best of our knowledge, a detailed study of the physicochemical properties of nitrogen doping and oxygen functionalization on CNOs supported palladium nanoparticles as electrocatalysts for ethanol oxidation in alkaline condition has not been reported or carried out. It was observed that the Pd/N-CNO (N = nitrogen doped) electrocatalyst exhibited higher electrocatalytic performance for ethanol oxidation in the alkaline electrolyte as compared to the Pd/ox-CNO (ox = oxidized) and Pd/p-CNO (p = pristine) electrocatalysts.

3.1. Experimental Section

3.1.1. Materials and Methods

The chemical reagents were used without purification to prepare the electrocatalysts and electrolyte solutions used in this research work: ethanol >

99.9% (Sigma-Aldrich), Nafion solution > 5 wt.% (Sigma-Aldrich), Pd/C commercial standard > 10% loading (Sigma-Aldrich), H_2PdCl_4 > 98.0% (Sigma-Aldrich), nitric acid > 99.9% (Sigma-Aldrich), hydrogen peroxide > 50% (Sigma-Aldrich), sodium borohydride > 99.5% (Sigma-Aldrich) and potassium hydroxide powder (Merck).

3.1.2. Synthesis of carbon nano onions (CNOs)

CNOs were synthesized using flame pyrolysis of olive oil as reported in the literature [6]. The wick immersed in olive oil was ignited to create a flame. The deep-black powder was produced by the flame because of the incomplete burning of the oil in the center zone of the flame. In a typical experiment, the prepared CNOs were gathered onto a brass collecting plate (BCP) for 60 minutes. The collected carbogenic black powder was then named as pristine carbon nano-onions (Yield: 5 g p-CNO).

3.1.3. Purification and oxidation of the p-CNO

The p-CNO were purified using 2M nitric acid and oxidized with 50% hydrogen peroxide as described by Siswana et al. [28]. The p-CNO (2 g) were transferred to a round bottom flask containing 50 mL of 2 M HNO_3 . The mixture was refluxed for 6 h. The acidified carbon nano-onions mixture was separated using a centrifuge (15 000 rpm) for 15 min and washed with double distilled water. The CNO sediment was thereafter treated with 40 mL of 50% hydrogen peroxide under stirring at 80 °C for 6 h to introduce carboxylic (COO^-) functional groups. The purified functionalized CNOs were filtered, rinsed several times with double distilled water, and then dried in an oven at 100 °C overnight to obtain the oxidized carbon nano onions (ox-CNO).

3.1.4. Nitrogen doping of the p-CNO

The p-CNO were purified using nitric acid as described in the section above. Nitrogen-doped CNOs were prepared by using a chemical vapor deposition method using argon as carrier gas and ammonia as nitrogen source[29]. Two grams of the purified p-CNO were transferred into a quartz boat which was placed at the center of the quartz tube and mounted inside an electric furnace and the system flushed with argon. The furnace temperature was raised to 600 °C under argon and the purified p-CNO were then heated at 600 °C under a stream of dilute gases (100 mL/min argon and 150 mL/min ammonia) for 60 min. The N-CNO formed were permitted to cool at ambient temperature under argon. After the heat-treatment at 600 °C, the N-CNO yield was 1.8 g.

3.1.5. Synthesis of Pd/p-CNO, Pd/ox-CNO, and Pd/N-CNO electrocatalysts

The Pd/CNO electrocatalysts were synthesized as follows: The three different CNOs (p-CNO, ox-CNO, and N-CNO) were dispersed in sodium borohydride in 100 mL water and an appropriate calculated amount of H_2PdCl_4 was added to the mixture to produce a 10% wt Pd loading on the CNOs. The resulting mixture was treated in an ultrasound bath for 60 minutes. The three solutions (90 mL) labelled Pd/p-CNO, Pd/ox-CNO and Pd/N-CNO nanomaterials were then placed into 100 mL Teflon reaction vessels and put in a microwave (M300) Anton Paar reactor set to 220 °C for 1 h. The microwave irradiated resulting suspensions were centrifuged (15 000 rpm) and then rinsed several times with double distilled water to eliminate residual chloride ions. The acquired black solids were dried at 100 °C for overnight to obtain the 200 mg Pd/CNO electrocatalysts.

3.1.6. Physical characterization

Transmission electron microscopy (TEM) (Jeol JEM-2100F 200 kV) was used to analyze the shape and morphology of the CNO and Pd/CNO materials. The morphology and characteristics of the CNO and Pd/CNO materials were studied by scanning electron microscopy (SEM) using a ZEISS GeminiSEM 560 instrument with sub 1 kV resolution below 1 nm. Topography of the CNO and

Pd/CNO materials was acquired using A Veeco Di-3100 atomic force microscopy (AFM). The infrared spectra of CNOs were obtained using Fourier transform infrared (FTIR) spectroscopy on a Perkin Elmer Spectrum 100 instrument. The quality and structural properties of CNOs were studied using a T64000 Raman spectrometer system from HORIBA scientific, Jobin Yvon Technology. The thermal stability of CNOs was monitored using a Perkin Elmer 6000 thermogravimetric analyzer. A Micromeritics Tristar 3000 surface area and porosity analyzer were used to determine the surface area and pore volume of the CNOs. Powder X-ray diffraction (PXRD) (Bruker D2 Phaser) with a monochromatic Cu $K\alpha$ radiation ($\lambda=0.15405$ nm) generated at 30 kV and 10 mA was used to explore the crystalline structure and particle size of the CNO and Pd/CNO nanomaterials. X-ray photoelectron spectroscopy (XPS) data of the CNO and Pd/CNO samples were acquired in an ultra-high vacuum (UHV) chamber equipped with a SPECS PHOIBOS 150 hemispherical electron energy analyzer (Al $K\alpha$ excitation line; $h\nu = 1486.71$ eV).

3.1.7. Electrochemical measurements

To study the electrochemical properties of the synthesized materials, electrocatalyst inks were prepared by dispersing 10 mg of the various CNOs or Pd/CNO electrocatalyst in the solution of 1 mL isopropyl alcohol and 1 drop of Nafion (5 wt.%) using ultrasonic stirring. Then 15 μ L of the electrocatalyst ink was deposited on the surface of a glassy carbon electrode using a micropipette. Thereafter the CNOs and Pd/CNO modified electrode was dried at ambient temperature for 30 min. The alkaline electrolyte solution was purged with argon 15 min before the experiment. Electrochemical studies were performed using Dropsens potentiostat. The potentials of the modified glassy carbon electrode were explored in 1 M KOH + 1M C₂H₅OH solution using platinum wire as a counter electrode and Ag/AgCl (saturated with 3M KCl solution) as a reference electrode. The surface area of the working electrode (GC) was calculated to be 0.196 cm². The current values were normalized against the geometrical area of the working electrode. All results were compared with a 10 % wt commercial Pd/C electrocatalyst tested under similar reaction conditions.

3.2. Results and Discussion

3.2.1. Transmission electron microscopy

Transmission electron microscopy (TEM) images of the ox-CNO, and N-CNO are shown in Fig. 3.1 (a and b). The images show that these materials have an onion-like nanostructure. As shown in Fig. 3.1(a and b), no conspicuous fracturing in the circular shell of ox-CNO and N-CNO was observed, showing the onion-like nanostructure was maintained during the oxidation and nitrogen doping steps. The p-CNO, ox-CNO, and N-CNO were observed to exhibit disordered concentric graphite multi-shells, all with an interplanar spacing close to 0.33 nm [9] (Fig. S1. (a-d)).

Fig. 3.1(c and d) presents TEM micrographs of Pd/ox-CNO, Pd/N-CNO, and Pd/p-CNO electrocatalysts. In contrast, Fig. 3.1(c) shows well distributed Pd nanoparticles on the ox-CNO surface demonstrating a better interaction between the Pd NPs and the oxygen functional groups of the CNOs. Moreover, the Pd particles appear larger and less spherical on the ox-CNO. Fig. 3.1 (d) shows that the palladium nanoparticles were well dispersed onto the surface of N-CNO. The incorporation of nitrogen functional groups onto the carbon structure facilitated a high palladium dispersion. The Pd particles appeared to be smaller and spherical. The Pd nanoparticles (Pd NPs) were highly agglomerated on the surface of the p-CNO support material. This indicates that there are very few binding sites on the unactivated surface area of the carbon support (see Fig. S1. (e) and Fig. S1. (f)). The dispersion of the Pd NPs is consistent with literature reports on Pd supported on carbon nanotubes (CNT) and nitrogen doped (N-CNT) [30]. Image J software was used to evaluate the mean Pd particle size in random regions. From TEM images, the mean Pd particle size of Pd/p-CNO, Pd/ox-CNO, and Pd/N-CNO was found to be 6.6, 7.6 nm, and 4.7 nm respectively (Fig. S1 (g), Fig. S1 (h) and Fig. S1. (i)). In comparison, the average Pd particle size on our synthesized Pd/CNO nanomaterials were smaller than the ones that was reported

by Corma et al. [31] and Nitze et al. [32] for Pd/CNT or Pd/C and Pd/CNF nanomaterials, respectively.

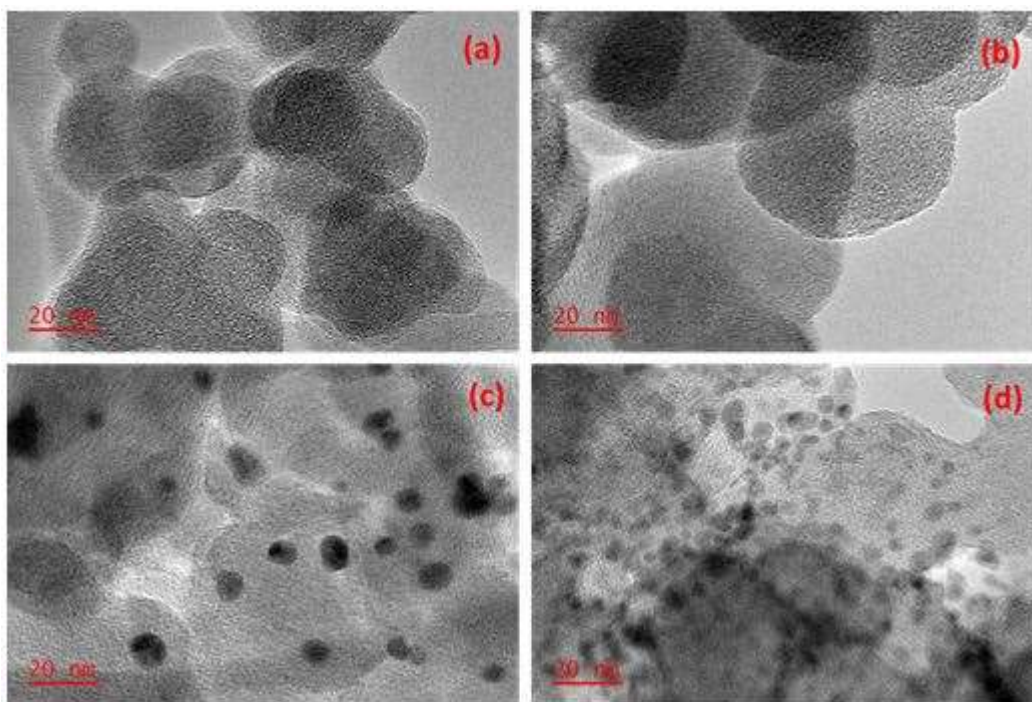


Figure 3.1: TEM images of (a) ox-CNO, (b) N-CNO, (c) Pd/ox-CNO, and (d) Pd/N-CNO nanomaterials.

3.2.2. Scanning electron microscopy and Atomic force microscopy

Scanning electron microscopy (SEM) images of the p-CNO, Pd/p-CNO, Pd/ox-CNO and Pd/N-CNO are illustrated in Fig. 3.2 (a-d). These images show the quasi-spherical morphology of the CNOs ($d = 20 - 70$ nm), with aggregation or conglomeration of nanoparticles as shown in Fig. 3.2 (a-d) and S2. (a and b). Fig. S2. (a-f) shows the atomic force microscopy (AFM) with the corresponding image surface areas of the p-CNO, ox-CNO, N-CNO, Pd/p-CNO, Pd/N-CNO, and Pd/ox-CNO nanomaterials.

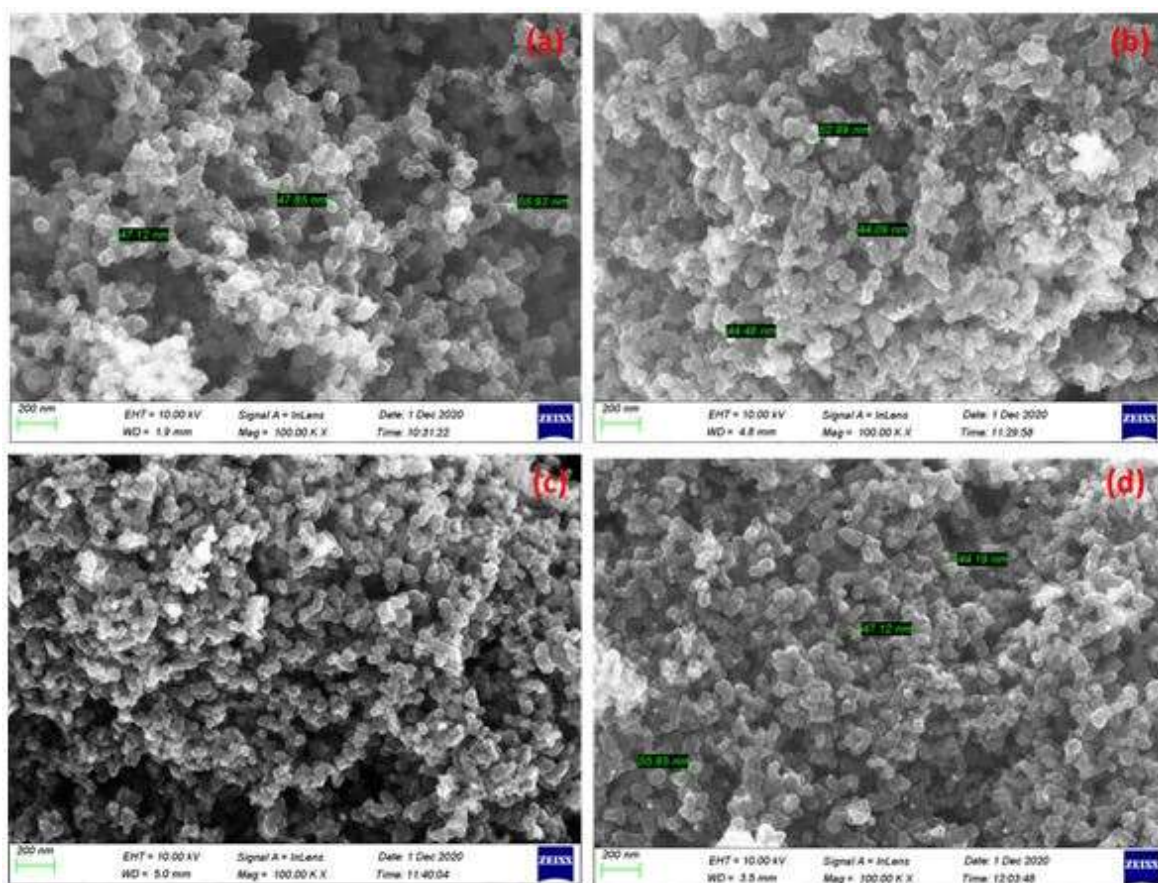


Figure 3.2: SEM images of (a) p-CNO, (b) Pd/p-CNO, (c) Pd/ox-CNO and (d) Pd/N-CNO nanomaterials.

3.2.3. Fourier transform infrared spectroscopy

The Fourier transform infrared (FTIR) spectra of the p-CNO, N-CNO, and ox-CNO are presented in Fig. 3.3. Five peaks of interest can be seen in the spectra of the p-CNO. The first and the second peaks at 3425 and 3142 cm^{-1} are due to OH stretching modes [33]. Normally the OH peak between 3000 to 3500 cm^{-1} is broad but in this case, the peak is split into two, which is attributed to the presence of alcohol OH groups and water present on the surface of the p-CNO [34]. The third peak at 1639 cm^{-1} can be due to the C=C stretching mode in aromatic rings. The fourth peak at 1400 cm^{-1} is attributed to the C-O-H stretching due to carboxylic groups. The fifth peak at 1043 cm^{-1} is ascribed to a C-O stretching mode.

The p-CNO were also functionalized with hydrogen peroxide to introduce oxygenated functional groups on the CNO surface and this resulted in the formation of a new peak at 1717 cm^{-1} that can be associated with the C=O stretching mode of carboxylic groups [35]. Interestingly the peak at 1043 cm^{-1} for the C-O group was split into three peaks (1134 , 1129 , and 1097 cm^{-1}) [33]. After the p-CNO was doped with nitrogen, a new peak formed at 2360 cm^{-1} for a C≡N stretching mode for a nitrile group. This suggests that nitrogen was incorporated into the structure of the p-CNO. The spectra for all three materials were similar indicating that the materials had a common backbone structure and that the nitrogen doping and the oxidation steps did not completely break/damage the carbon structure of the p-CNO [10]. The oxygen and nitrogen functional groups mentioned above are in good agreement with those found on CNO derived from the burning of acetonitrile and the functionalization of graphene with nitrile groups [35,36]. These functional groups facilitated the attachment of palladium nanoparticles on the surface of CNOs.

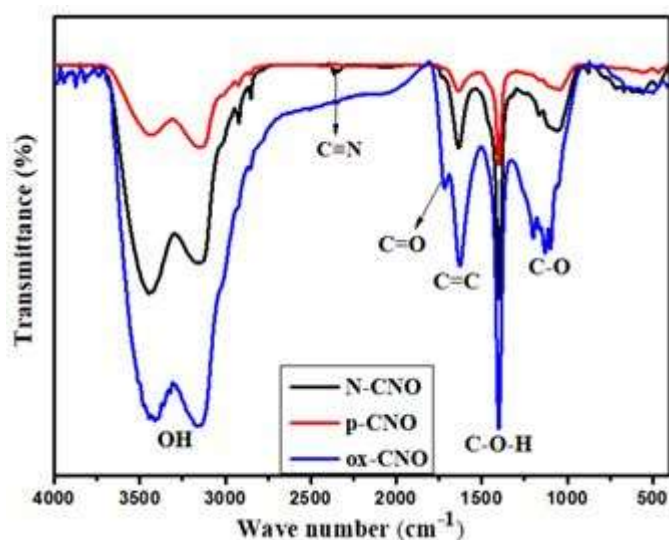


Figure 3.3: FTIR spectra of p-CNO, N-CNO and ox-CNO nanomaterials.

3.2.4. Raman spectroscopy

Fig. 3.4 shows the Raman spectra (D and G bands) of p-CNO, N-CNO, and ox-CNO. The defective graphene layers associated with D band were zone centered

at 1346 cm^{-1} (C atoms with sp^3 hybridization) for all three CNO samples [37]. This broad peak is assigned to a first-order scattering band. The G band is the characteristic peak of a C-C stretching mode in the graphite plane at 1588 cm^{-1} (C atoms with sp^2 hybridization) for the three CNO materials (see Table 3.1) [38]. This peak is ascribed to a second-order scattering band. The peak positions for the p-CNO, N-CNO and ox-CNO, showed a small upshift for the D and G bands (N-CNO > ox-CNO > p-CNO) indicating an electronic impact of both the nitrogen and oxygen incorporation on the carbon structure [13]. The peak areas of the D and G bands were used to calculate the D and G ratio (I_D/I_G) for the N-CNO, ox-CNO, and p-CNO (5.07, 4.36, and 3.22) respectively, which relates to the defect-rich nature of the CNOs after N and O addition (see Table 3.1) [39].

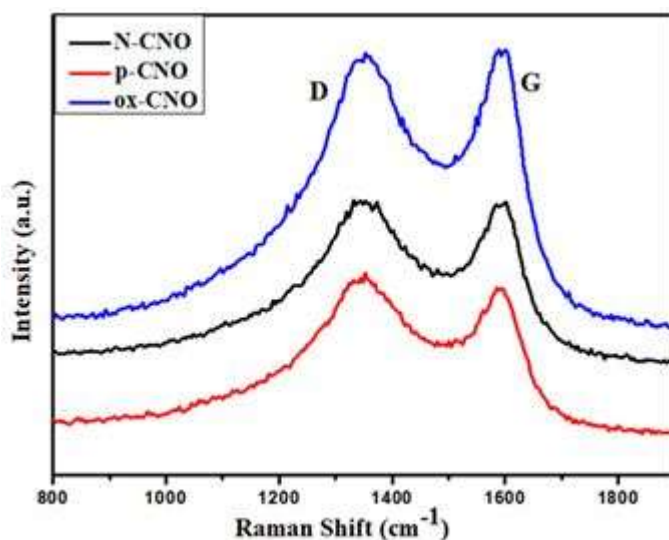


Figure 3.4: Raman spectra for p-CNO, N-CNO and ox-CNO nanomaterials.

Table 3.1: Raman data showing peak positions, intensities, and intensity ratios for p-CNO, N-CNO, and ox-CNO

Sample	D band		G band		Area ratio (I_D/I_G)
	Position (cm^{-1})	Area	Position/ (cm^{-1})	Area	
p-CNO	1346	10.5	1588	3.22	
N-CNO	1350	15.1	1588	5.07	
ox-CNO	1350	18.8	1588	4.36	

p-CNO	1346	119141	1588	36997	3.22
N-CNO	1346	69199	1588	13631	5.07
ox-CNO	1346	70631	1588	16168	4.36

3.2.5. Thermogravimetric analysis

Thermogravimetric (TG) and the derivative thermogravimetric (DTG) analysis was employed to compare the thermal stability of the p-CNO, ox-CNO, and N-CNO nanomaterials (Fig. 3.5). As shown in Fig. 3.5 (a) the TGA profiles of the p-CNO, ox-CNO and N-CNO reveals a major weight loss at 552 °C, 507 °C, and 534 °C, respectively. The decrease in the weight loss of ox-CNO at 507 °C is ascribed to the thermal decomposition of the oxygen functional groups and possibly some of the carbon core of the onion structure [40]. The loss of weight for N-CNO at 534 °C is due to both loss of nitrogen and oxygen-containing groups.

The DTG data (Fig. 3.5 b) showed that the N-CNO exhibited higher thermal stability (701 °C) than the p-CNO (670 °C) and the ox-CNO (650 °C). The higher decomposition temperature for N-CNO is due to the successful introduction of nitrogen atoms into the onion structure to form small and disarranged CNO as also shown by the broader derivative peak [41]. The lowered peak position for ox-CNO is due to the loss of oxygen-functional groups [42]. Fig. 3.5 (b) also shows a small weight loss peak for ox-CNO in the range from 150 to 250 °C. This can be ascribed to the incorporation of oxygen-functional groups on the onion structure surface e.g. C=O, -COOH, and C-O [43]. The TGA and DTG results are in good agreement with the Raman results.

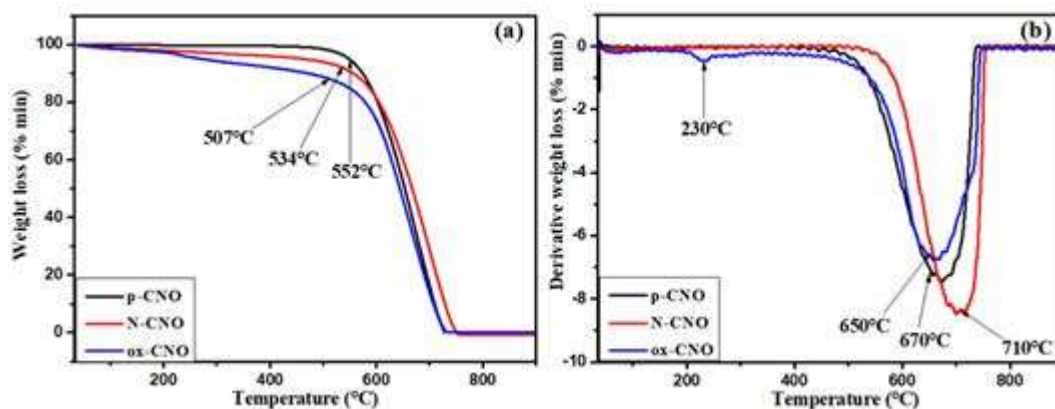


Figure 3.5: (a) TGA and (b) TGA derivative data for the p-CNO, N-CNO and ox-CNO nanomaterials.

The thermogravimetric (TGA) and differential thermogravimetric (DTA) analyses results for Pd/p-CNO, Pd/ox-CNO, and Pd/N-CNO are presented in Fig S3. (a) and (b) respectively. Fig S3. (a) reveals the TGA weight loss curves of the Pd/p-CNO, Pd/ox-CNO, and Pd/N-CNO at 525 °C, 516 °C and 504 °C, respectively. Notably, all the palladium electrocatalysts reveal lower onset decomposition temperature as compared to palladium free electrocatalysts. The residual weight of the Pd/p-CNO (9.8%), Pd/ox-CNO (8.7%), and Pd/N-CNO (9.8%) are close to the 10% nominal Pd loading.

3.2.6. X-ray diffraction spectroscopy

Fig. 3.6 shows X-ray diffractograms of the p-CNO, ox-CNO, N-CNO, Pd/p-CNO, Pd/N-CNO, and Pd/ox-CNO. A broad amorphous peak of at $2\theta = 25.7^\circ$ is due to the carbon (002) graphitic plane reflection [44]. The broad carbon signal is an indication of small disordered fragments of a carbon structure in line with the TEM images [2]. The XRD pattern for the three Pd/CNO presents strong 2θ diffraction peaks at 40.08° , 46.7° , 68.4° , and 82.0° . These characteristic diffraction peaks of Pd are assigned to (111), (200), (220) and (311) planes of palladium facets [45]. XRD peaks for all CNO and the catalysts did not show significant differences, showing that the onion-like nanostructure was maintained during the oxidation and nitrogen doping steps [46]. The average particle size of the strong diffraction signal

Pd(111) for Pd/p-CNO, Pd/N-CNO, and Pd/ox-CNO were found to be 12.97, 12.95, and 12.99 respectively, using the Debye Scherrer equation. From TEM images, the average particle size of Pd/p-CNO, Pd/N-CNO, and Pd/ox-CNO were found to be 6.6 nm, 4.7 nm, and 7.6 nm. The difference between XRD and TEM values relates to the method by which the two techniques determine the average Pd diameters [47]. These differences also relate to the observation that the Pd ensemble in the TEM images consist of well dispersed small polycrystalline nanoparticles as compared to the large Pd(111) monocrystalline nanoparticles in XRD [48].

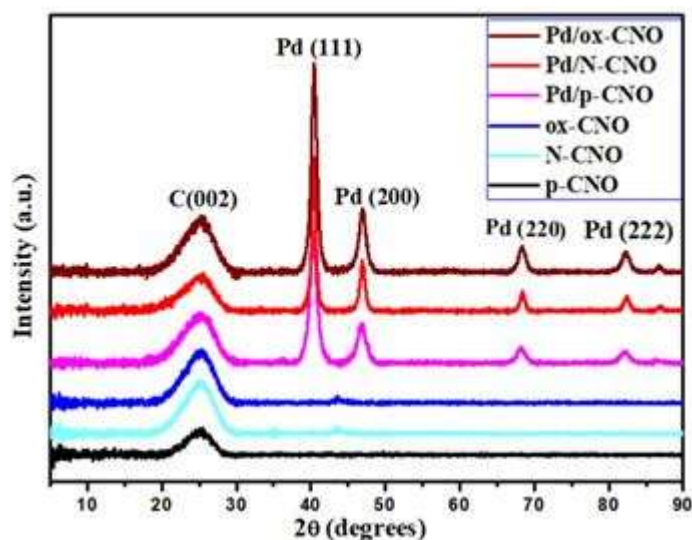


Figure 3.6: X-ray diffractograms of p-CNOs, ox-CNO, N-CNO, Pd/p-CNO, Pd/N-CNO, and Pd/ox-CNO nanomaterials.

3.2.7. X-ray photoelectron spectroscopy

Fig. S5 (a) shows the XPS survey scans of the CNO and the Pd/N-CNO nanomaterials in which O 1s, C 1s, N 1s, Pd 3d, and residual Si 2s and Si 2p were detected. Fig.4 S5 (b) reports the O 1s core-level spectra of the four CNO samples. The line shape of this core level peak shows good consistency for p-CNO, N-CNO, and ox-CNO, while it varies slightly for Pd/N-CNO. Following the relevant literature and the expected deconvolution of this core level, all four spectra could be fitted with five Voigt-type peaks and a Shirley background. The

fitted components, the background, and the overall fit are displayed in Fig. S5 (b). The overall fit shows very good agreement with the experimental data for all four samples. The BEs and the relative percentage areas of the five fitted components for O 1s are reported in Table S1. The full width at half maximum (FWHM) was consistently 1.3 eV for all peaks. Based on the relevant literature, we can assign the fitted components as follows: O1 to C-O; O2 to C=O, O3 to C-O-H, O4 to C-O-C, and finally O5 to COOH carboxylic group [49]. The values displayed in Table S3 (1) are generally consistent for p-CNO, N-CNO, ox-CNO, and Pd/N-CNO while that of O1 is lower.

Fig. S5 (c) displays the C 1s core-level spectra for the same four samples. The line shape is composed of several subcomponents and shows small changes only slightly for the four samples. We have used five Voigt-type peaks and a Shirley background to fit the experimental data. The parameters of the best fits are reported in Table S2. The FWHM was optimized to be 1.37 eV for all peaks. The identification of the components was done by comparing the observed BEs found here with the available literature [49,50], and it was found that C1 can be attributed to C-H, C2 to sp^2 hybridized carbon (C=C), C3 to sp^3 hybridized carbon (C-C), while C4 and C5 are ascribed to oxidized carbon atoms in forms of C-O and C=O respectively.

N 1s spectra for N-CNO and Pd/N-CNO are reported in Fig. S5 (d). The N% was found to be 3.7 % and 2.4 % for N-CNO and Pd/N-CNO, respectively. The best fit to the data was obtained by using three Voigt-type singlets (labelled N1, N2, and N3) and a Shirley background. The fitted parameters are reported in Table S3. The FWHM was 1.82 eV for all the peaks. A comparison with the available literature using fitted BEs allowed us to identify the origin of these components [49]. N1 is attributed to pyridinic nitrogen, N2 to pyrrolic nitrogen, and finally N3 to oxidized nitrogen in a -NO configuration. While Table S2 shows good consistency between the BEs of the fitted components, the spectral weights of N1 and N2 changed between the two samples, showing an increase in the pyrrolic nitrogen and a decrease in the pyridinic nitrogen in Pd/N-CNO with respect to N-CNO. This suggests that the Pd covers the pyridinic N atoms.

Finally, Fig. S5 (e) shows the Pd 3d spectrum for Pd/N-CNO. This BE region is composed of two sub-regions, one from 334 eV to 339 eV and one from 339 eV to 344 eV, corresponding to Pd 3d_{5/2} and Pd 3d_{3/2} spin-orbit components, respectively. Each sub-region is composed of an asymmetric main peak and a smaller peak on the higher BE side, which are a fingerprint of the different oxidation states for Pd in this compound. The best fit to the experimental data (thick solid line) was obtained by summing three spin-orbit doublets to a Shirley background, which are all appended in Fig. S5 (e). The spin-orbit energy splitting was set to 5.26 eV and the linewidth was set to 1.29 eV for all three components. The BEs of the 3d_{5/2} peaks for the three components are 335.45 eV, 336.39 eV, and 337.93 eV, which have been ascribed to Pd ions in a metallic state (Pd⁰⁺), Pd ions in a PdO-type oxide (or Pd²⁺), and Pd ions in a PdO₂ type oxide (or Pd⁴⁺) respectively, as labelled in the Fig. S5 (e) [51–53]. As far as relative percentage area is concerned, Pd⁰⁺ takes up 68% of the spectral weight of this core level, while Pd²⁺ and Pd⁴⁺ take up 20% and 12% respectively.

3.2.8. Brunauer-Emmett-Teller Nitrogen adsorption (BET)

Table 3.2: BET surface areas of p-CNO, N-CNO and ox-CNO nanomaterials

Sample	Surface area (m ² g ⁻¹)	Pore volume (cm ³ g ⁻¹)	Pore size (nm)
p-CNO	60	10.2	14.8
N-CNO	79	10.3	19.5
ox-CNO	80	10.7	34.9
Pd/p-CNO	49	20.3	6.1
Pd/N-CNO	52	19.7	5.8
Pd/ox-CNO	62	16.3	5.6

Table 3.2 shows a summary of the BET data. Nitrogen (N₂) adsorption-desorption isotherms acquired at 77 K have been utilized to evaluate the BET specific surface

area (SSA). The SSA of ox-CNO was $80 \text{ m}^2 \text{ g}^{-1}$ with a pore volume of $10.7031 \text{ cm}^3 \text{ g}^{-1}$ and a pore size of 34.9 nm. The surface areas ox-CNO and the N-CNO are equivalent. The increase in the BET surface area by oxidation is due to the corrosion of the external shell of carbon nano onions [54]. Notably, all the palladium electrocatalysts reveal lower surface areas, higher pore volumes and smaller pore sizes as compared to palladium free electrocatalysts indicating coverage of pores by the Pd. The pore-size distribution (PSD) was evaluated utilizing the Barrett, Joyner, and Halenda (BJH) technique applied to the desorption branch [55]. The PSD revealed that ox-CNO, N-CNO, and p-CNO has abundant mesopores and micropores with pore diameter (39.4 nm and 0.26 nm), (19.7 nm and 0.23 nm) and (17.0 nm and 0.19 nm), respectively. The existence of these micropores and mesopores for the three-carbon materials are beneficial for enhanced rate kinetics and quick dissemination of electrolyte ions [56].

3.3. Electrochemical properties of the metal-free carbon and metal carbon-based catalysts: Ethanol oxidation reaction (EOR) activity

3.3.1. Ethanol electro-oxidation using cyclic voltammetry

The cyclic voltammetry (CV) tests were done to analyze the performance of the metal-free carbon and metal-carbon electrocatalysts and to examine the effect of Pd nanoparticle addition to CNO in $1\text{M C}_2\text{H}_5\text{OH} + 1\text{KOH}$ electrolyte. Fig. 3.7 shows the CV curves of the p-CNO, ox-CNO, N-CNO, and Pd/C, Pd/p-CNO, Pd/ox-CNO, Pd/N-CNO modified electrodes towards the ethanol oxidation reaction (EOR) in alkaline media at a scan rate of 50 mVs^{-1} . The anodic current peak in the forward scan and a current peak in the backward scan was observed in the cyclic voltammograms for all electrocatalysts. The forward scan is ascribed to the oxidation peak of chemisorbed ethanol molecules and the backward scan is attributed to the removal of residual carbon species formed in the forward peak [57,58]. The redox response peaks in the CV curves clearly show the electrocatalytic activity of the prepared metal-free catalysts. As can be seen in Fig. 3.7 (a), the ethanol oxidation current densities of p-CNO, ox-CNO, and N-CNO

electrocatalysts are 3.3 mA cm^{-2} , 3.8 mA cm^{-2} and 4.2 mA cm^{-2} , respectively. It can be observed that the N-CNO electrocatalyst gives a better current density than the ox-CNO and p-CNO electrocatalysts and indicates a promoted electrochemical performance by the inclusion of N atoms on top of the onion structure [59]. Also, this high performance is ascribed to the high surface area, degree of graphitization and porous nature of N-CNO electrocatalyst [5]. In comparison with p-CNO (-0.28 V) and ox-CNO (-0.26 V), the N-CNO (-0.24 V) also displays a greater positive shift of the onset potential and improved electrocatalytic activity. Nitrogen doping plays a major role in promoting the catalytic activity of the electrocatalysts [60]. There are generally four types of N-dopants found in a carbon structure which are pyridinic-N, pyrrolic-N, nitrilic-N, and oxidized-N [61]. However, in these CNOs the major N-type species seen are pyridinic (63.1%), pyrrolic (32.4 %) and oxidized nitrogen (4.5 %). It has been shown that pyridinic and pyrrolic nitrogen atoms in N-doped CNO increase electrical conductivity and reduce the bandgap of CNOs because of an electron abundance in the delocalized π -framework [12]. The pyridinic and pyrrolic nitrogen atoms act as anchoring sites and enhance the net positive charge on neighbouring carbon atoms, encouraging oxygen adsorption on the anode side [62]. Moreover, nitrogen anchoring sites have elevated binding energy for interaction with electrolytic ions. The oxygen functional groups also perform as active sites for the dispersion and adsorption of palladium nanoparticles [63]. Table 3.3 shows the comparison of the current density for our synthesized electrocatalysts with other electrocatalysts tested with the same fuels and in the same electrolytes. It has been reported that higher current densities for N-CNO electrocatalysts towards oxygen reduction reaction were also observed by Zhang et al. [13] and Shaikh et al. [29] but with values less than found for our prepared electrocatalysts towards ethanol oxidation reaction.

Table 3.3: Comparison of the current density for our synthesized electrocatalysts, tested towards EOR in the alkaline electrolyte as compared to other electrocatalysts tested in the same fuels and electrolytes

Anode	Cathode	Fuel (M)	Electrolyte (M)	CD (mA cm ⁻²)	Ref.
ox-CNO		1 Ethanol	1 KOH	3.8	This work
N-CNO		1 Ethanol	1 KOH	4.2	This work
Pd/ox-CNO		1 Ethanol	1 KOH	14.5	This work
Pd/N-CNO		1 Ethanol	1 KOH	17.4	This work
	N-CNO		0.1 KOH	1.0	[13]
	N-CNO		0.1 KOH	0.2	[29]
CFCNT		1 Ethanol	1 NaOH	3.1	[22]
Pd/CNO		0.3 Formaldehyde	0.1 NaOH	9.6	[8]
Pd/MWCNT		1 Ethanol	0.5 NaOH	11.5	[64]
Pd/CFCNT		1 Ethanol	1 NaOH	16.9	[22]
Pd/HCNF		0.5 Ethanol	1 KOH	55.2	[65]

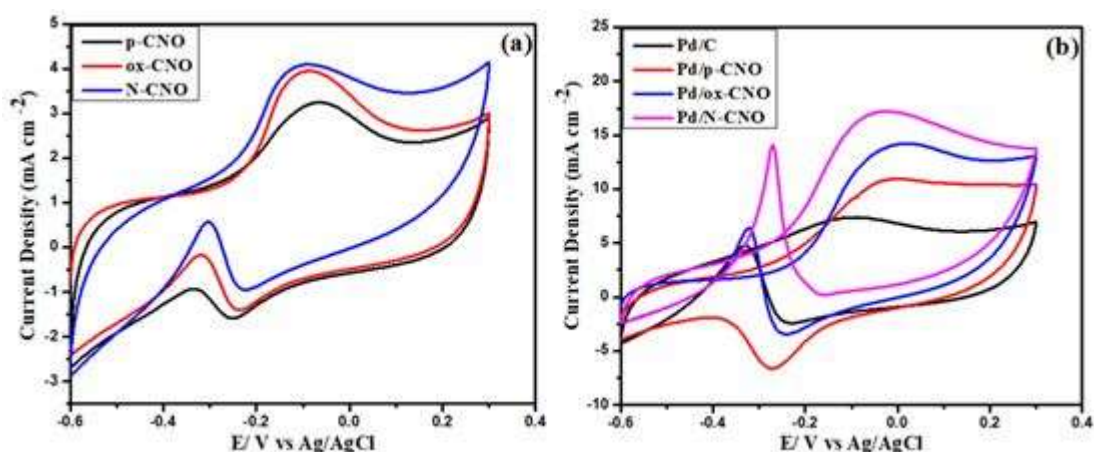


Figure 3.7: (a) CV curves for p-CNO, ox-CNO, N-CNO, and (b) Pd/C, Pd/p-CNO, Pd/ox-CNO, Pd/N-CNO electrocatalysts in 1M C₂H₅OH + 1M KOH at a scan rate of 50 mV s⁻¹.

The CV curves of the Pd/C, Pd/p-CNO, Pd/ox-CNO, and Pd/N-CNO in a solution of 1M C₂H₅OH + 1M KOH at a scan rate of 50 mV s⁻¹ are illustrated in Fig. 3.7 (b). Four ethanol oxidation current peaks were seen in the anodic sweep, which correlates to electrochemical processes materializing over the palladium surface. A wide ethanol oxidation current peak at a potential between -0.14 V and 0.09 V on the positive sweep is observed, which can be credited to the transformation of the Pd metal in the surface film into Pd(II) oxide and the corresponding peak in the range of -0.37 and -0.24 V is attributed to the reduction of PdO into Pd metal [64]. The anodic ethanol oxidation over Pd/C, Pd/p-CNO, Pd/ox-CNO, and Pd/N-CNO indicates that the catalytic activity of CNO metal-free catalysts has changed after Pd nanoparticles deposition. As depicted in Fig. 3.7 (a), the Pd/N-CNO (17.4 mA cm⁻²) exhibits a much larger ethanol oxidation current compared to the Pd/ox-CNO (14.5 mA cm⁻²), Pd/p-CNO (10.9 mA cm⁻²), and a commercial Pd/C (7.6 mA cm⁻²) electrocatalyst. This might be credited to the nitrogen functional groups of the CNOs which provides a strong interaction between the onion structure and the Pd nanoparticles resulting in a high Pd dispersion and electronic conduction [65]. Furthermore, the high specific surface area, degree of graphitization and the porous nature of N-CNOs improves the dispersion which can be related to smaller palladium particle size which enhances the catalytic activity of the electrocatalyst [66]. Moreover, nitrogen doping gives rise to structural defects resulting in strong electron transfer among Pd nanoparticles and CNOs [67].

3.3.2. The effect of scan rate on the current density

Since N-CNO and Pd/N-CNO performed better than other four electrocatalysts prepared in terms of high current density, low onset potential and stability, further studies were carried out using these electrocatalysts. Fig. 3.8 (a) and Fig. 3.8 (c) shows the cyclic voltammograms of the N-CNO and Pd/N-CNO electrocatalyst in 1M C₂H₅OH + 1M KOH electrolyte at different scan rates (20-100) mVs⁻¹ respectively. As depicted in Fig. 3.8 (a) and Fig. 3.8 (c), as the scan rate increases, the forward peak current occurs at higher peak potentials. A plot of the peak current density and the square root of the scan rate studied are displayed in the Fig. 3.8 (b) and Fig. 3.8 (d). Here it is seen that the current density is linearly

proportional to the square root of the scan rate, which implies that the ethanol oxidation on N-CNO and Pd/N-CNO electrocatalyst on the electrode is under control of a diffusion process [68]. For each electrocatalyst, the diffusion coefficient (D) was calculated using the Randles–Sevcik equation [69], $I_p = 2.69 \times 10^5 n^{3/2} A D^{1/2} \nu^{1/2} C$; where I_p is the peak current in amperes, n is the number of electrons transferred in the rate-determining step, A is the electrode surface area, ν is the scan rate in $V s^{-1}$, C is the solution concentration in mole cm^{-3} and D is the diffusion coefficient in $cm^2 s^{-1}$, which is found by plotting the relation between the square root of the scan rate and the current density. Diffusion coefficients for the N-CNO and Pd/N-CNO electrocatalysts were found to be 2.3×10^{-7} and 7.8×10^{-7} , respectively. This reveals that the charge-transport rate at the Pd/N-CNO electrocatalyst within the electrode–electrolyte interface is quicker as compared to the N-CNO electrocatalyst.

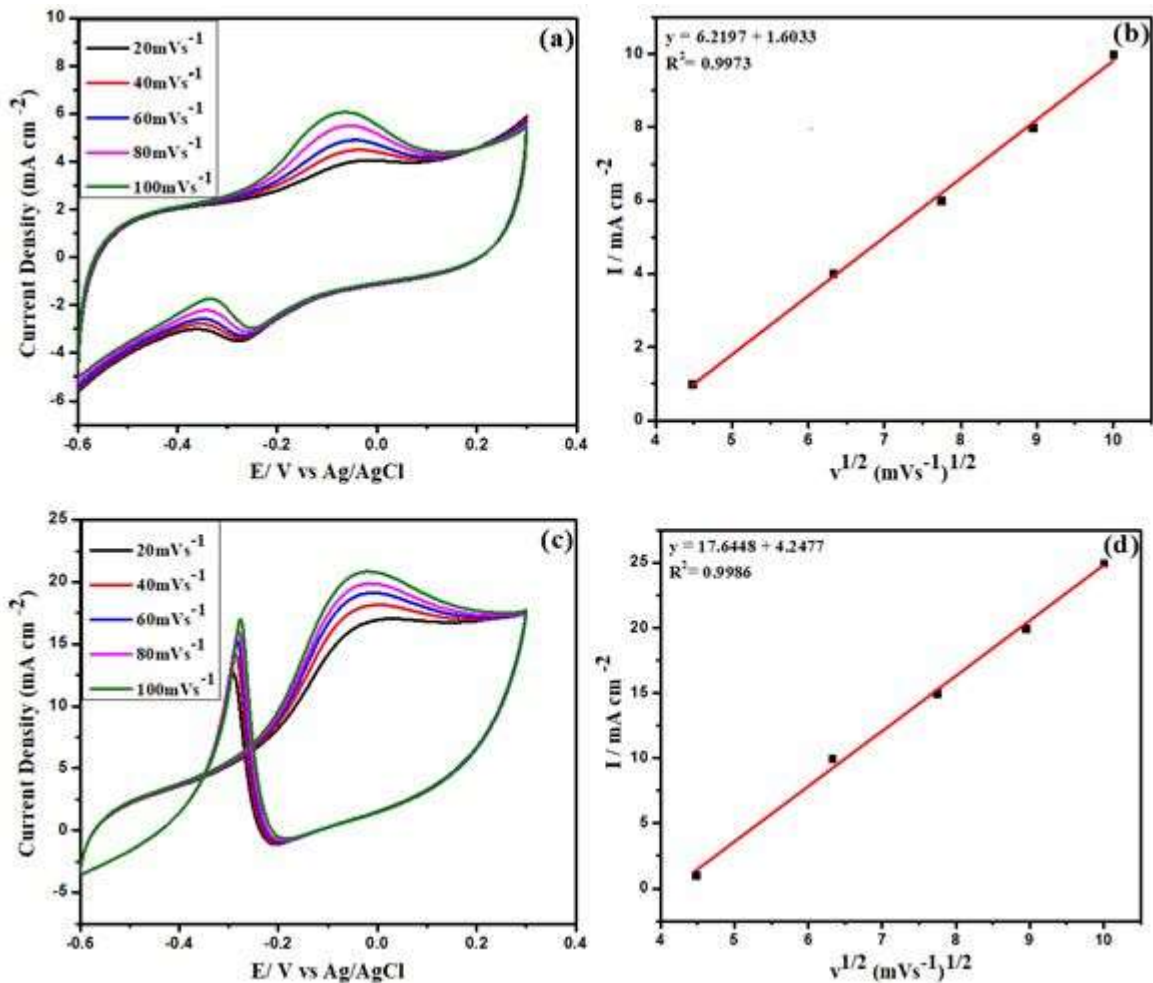


Figure 3.8: Cyclic Voltammograms of N-CNO and Pd/N-CNO electrocatalysts in 1M C₂H₅OH + 1M KOH at different scan rates (a and c) and the plots of peak current density vs. square root of scan rates (b and d).

3.3.3. Ethanol electro-oxidation using chronoamperometry

To evaluate the stability and poisoning tolerance of the metal-free carbon and metal carbon-based electrocatalysts, chronoamperometric measurements were carried out for the alkaline ethanol oxidation reaction for 2000 s. Fig. 3.9 (a) shows the chronoamperometric curves for p-CNO, ox-CNO and N-CNO modified electrodes in a solution of 1M C₂H₅OH + 1M KOH electrolyte in alkaline medium. The prepared N-CNO (1.19 mA cm⁻²) was observed to have a better oxidation current followed by the ox-CNO (0.75 mA cm⁻²) and p-CNO (0.47 mA cm⁻²) catalysts. It is evident that the N-CNO electrocatalyst degrades more slowly compared to the ox-CNO and p-CNO electrocatalysts, indicating that N-CNO electrocatalyst is the most stable one with a lower poisoning rate among all the synthesized electrocatalysts [70]. The enhanced electrocatalytic activity of N-CNO electrocatalyst towards EOR can be ascribed to its higher pyrrolic-N, pyridinic-N content, and mesoporous structure, which gives a high density of anchoring sites and mass diffusion enhancement for EOR [71]. These results confirm that the nitrogen doping produces nitrogen-containing species that bond strongly with the poisoning carbonaceous intermediates [72].

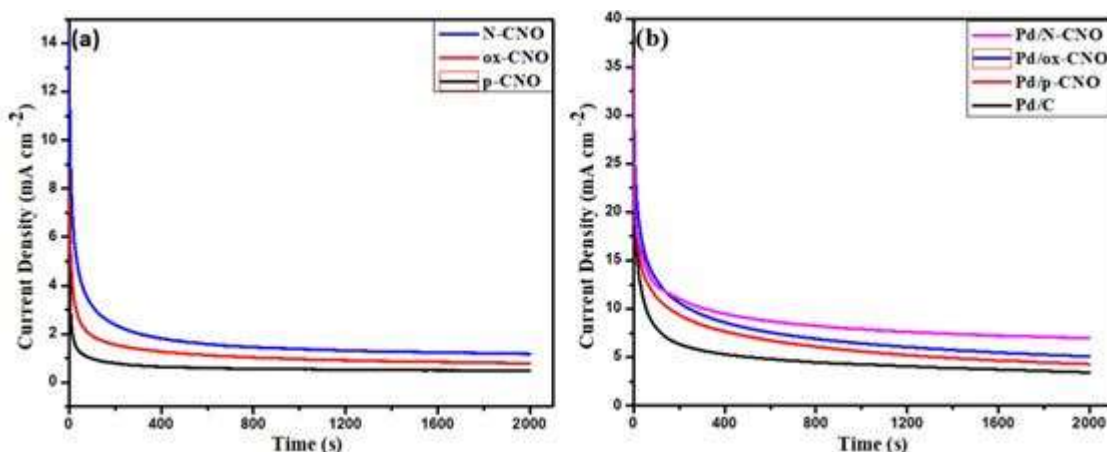


Figure 3.9: (a) Chronoamperometric curves for (a) *p*-CNO, *ox*-CNO, *N*-CNO, and (b) Pd/C, Pd/*p*-CNO, Pd/*ox*-CNO, Pd/*N*-CNO electrocatalysts in 1M C₂H₅OH + 1M KOH at -0.25 V.

Fig. 3.9 (b). presents the current–time curves of the four-palladium based electrocatalysts in a solution of 1M C₂H₅OH + 1M KOH electrolyte. The ethanol oxidation currents of Pd/C, Pd/*p*-CNO, Pd/*ox*-CNO, and Pd/*N*-CNO GC modified electrodes in the alkaline electrolyte are 3.4 mA cm⁻², 4.3 mA cm⁻², 5.1 mA cm⁻², and 6.9 mA cm⁻², respectively. The Pd/*N*-CNO electrocatalyst has long-term stability and lower poisoning tolerance compared to Pd/*p*-CNO, Pd/*ox*-CNO electrocatalysts. As observed in Fig. 3.9 (b), the ethanol oxidation current was in the steady-state for all electrocatalysts which are possibly due to the transformation of the Pd metal in the surface film into PdO [73]. The poisoning tolerance from these adsorbed species can be portrayed as the decay of the current density acquired from chronoamperometry after 2000 s [74].

3.3.4. Electrochemical impedance spectroscopy (EIS)

As shown in Fig. 3.10 (a) and 3.10 (b), the catalytic performance of each electrocatalyst for ethanol oxidation reaction in the alkaline electrolyte was analyzed by electrochemical impedance spectroscopy (EIS). Nyquist Impedance spectra of each anode catalyst in the frequency range from 0.005 Hz to 1000 kHz were recorded. The electrical equivalent circuit consists of the solution resistance (R_s), charge transfer resistance (R_{ct}), and constant phase element (CPE) of the ethanol oxidation reaction [75]. The radius of the impedance arc was used to assess the charge transfer resistance for various CNO and Pd/CNO electrocatalysts. The EIS circuit parameters are recorded in Table 3.4. In Fig. 3.10 (a) and 3.10 (b), the semi-circular diameter reflects the charge transfer resistance between the alkaline electrolyte and the surface of the working electrode when ethanol is oxidized on the surface of the GC electrode. The smaller the semi-circular diameter is, the smaller impediment to electron transfer, and the higher the electrocatalytic activity is [76]. The R_{ct} values of the two pairs (*N*-CNO and Pd/*N*-

CNO) is smaller as compared to (ox-CNO and Pd/ox-CNO), (p-CNO and Pd/p-CNO) and Pd/C electrocatalysts. This might be ascribed to the nitrogen atoms with overabundance electrons in the delocalized p-framework leads to enhanced electrical conductivity, which encourages the exchange of more electrons at the anode surface [77]. The electrocatalyst with small palladium size nanoparticles (Pd/N-CNO) had the lowest R_{ct} values, which is in accordance with the higher mass activities seen in both the cyclic voltammetry and chronoamperometric studies.

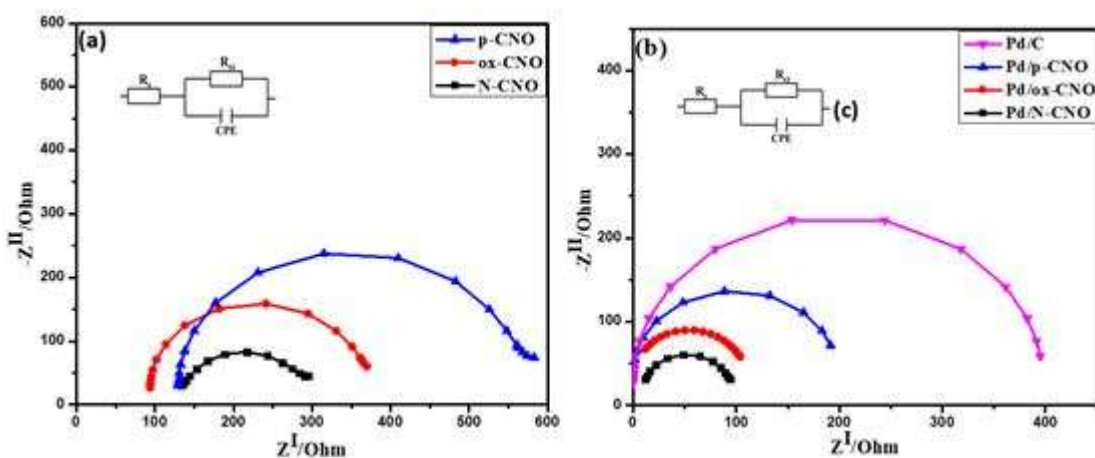


Figure 3.10: Impedance plots of p-CNO, ox-CNO, N-CNO and (b) Pd/C, Pd/p-CNO, Pd/ox-CNO, Pd/N-CNO electrocatalysts on GC electrode in (a) 1 M (KOH + C₂H₅OH) (c) equivalent circuits utilized in the fitting of the electrochemical impedance spectra.

Table 3.4: The EIS circuit parameters of p-CNO, ox-CNO, N-CNO, Pd/C, Pd/p-CNO, Pd/ox-CNO, and Pd/N-CNO electrocatalysts

2 M KOH + 2 M CH ₃ CH ₂ OH			
Electrocatalysts	R_s (Ohm)	R_{ct} (Ohm)	CPE (μF)
p-CNO	50.8	584.6	131.4
ox-CNO	48.6	372.5	155.9
N-CNO	41.4	296.8	170.8
Pd/C	46.3	396.5	184.2

Pd/p-CNO	45.8	195.3	212.5
Pd/ox-CNO	40.6	109.8	235.1
Pd/N-CNO	35.4	97.9	256.8

Conclusions

This research work provides an overview of synthesis methods and electrochemical applications of metal-free catalysts and metal carbon-based catalysts. The CNO were successfully synthesized utilizing flame pyrolysis followed by purification and chemical oxidation and nitrogen doping methods. Furthermore, the Pd/CNO electrocatalysts were prepared using a microwave synthesis method. Spectroscopic and microscopic examination of the new materials confirmed the successful modification of the CNO indicating the presence of oxygen and nitrogen functional groups on the CNO and the attachment of Pd NPs to the onion structure. N-CNO revealed lower thermal stability than ox-CNO and the p-CNO. The materials were all tested for electrochemical activity and the synthesized N-CNO (and Pd/N-CNO) nanocatalysts exhibited a significantly improved electrocatalytic performance and superior long-term stability when compared to the ox-CNO (and Pd/ox-CNO) as well as the p-CNO (and Pd/p-CNO) towards ethanol oxidation reaction in alkaline electrolyte. The results indicate how modification of CNOs with oxygen and nitrogen functional groups, as well as the synthesis of the equivalent Pd catalysts on the different CNOs, can provide a means for the facile synthesis of either Pd-free or Pd carbon-based catalysts by reasonable design and that will lead to catalysts with enhanced activity. The data are consistent with other reports in the literature and thus indicate a facile process for making electrocatalysts from CNO.

Acknowledgments

This work is based on the research supported in part by the National Research Foundation (NRF) of South Africa (Grant Numbers: 118137, 118148, 85364, 90698, 93205, 119314); the University of the Witwatersrand (Postgraduate Merit

Award, University Research Council and the Molecular Science Institute), and the NRF-DAAD (Grant number: 117841). The authors also acknowledge the efforts and support provided by the University of Johannesburg (Faculty of Science, University Research Council, and Centre for Nanomaterials Science Research). We also wish to acknowledge Mr. Siyasanga Mpelane at the University of Johannesburg (Auckland park) for the high magnification TEM analysis.

References

- [1] Dhand V, Prasad JS, Rao MV, Bharadwaj S, Flame synthesis of carbon nano onions using liquefied petroleum gas without catalyst, *Mat. Sci. Eng.* 2012; 33: 758-762.
- [2] McDonough JK, Gogotsi Y, Carbon Onions: Synthesis and Electrochemical Applications, *Electrochem Soc. interface* 2013; 12: 61–66.
- [3] Mykhailiv O, Zubyk H, Plonska-brzezinska ME, Carbon nano-onions: Unique carbon nanostructures with fascinating properties and their potential applications *Inorganica Chimica Acta* Carbon nano-onions: Unique carbon nanostructures with fascinating properties and their potential applications, *Inorganica Chim. Acta* 2017; 468: 49–66.
- [4] Bepete G, Khan L, Chiguvare Z, Coville NJ, (N-doped) Carbon Nanotube Nanostructuring of the Hole Transport Electrode for Reduced Space-Charge Accumulation in Polymer-Fullerene Solar Cells, *Physica Status Solidi* 2017; 214: 1–6.
- [5] Shaikh et al. Advances Facile sonochemical synthesis of highly dispersed ultra fine Pd nanoparticle decorated carbon nano- onions with high metal loading and enhanced, *RSC Adv.* 2016; 6: 83711–83719.
- [6] Mongwe TH, Matsoso BJ, Mutuma BK, Coville NJ, Maubane MS, Synthesis of chain-like carbon nano-onions by a flame assisted pyrolysis technique using different collecting plates *Diamond & Related Materials* Synthesis of chain-like

carbon nano-onions by a flame assisted pyrolysis technique using different collectors, *Diam. Relat. Mater* 2018; 90: 135–143.

[7] Zeiger M, Jäckel N, Mochalin VN, Presser V, Review: Carbon onions for electrochemical energy storage, *J. Mater. Chem. A* 2016; 4: 3172–3196.

[8] Shaikh et al. Advances Facile sonochemical synthesis of highly dispersed ultra fine Pd nanoparticle decorated carbon nano-onions with high metal loading and enhanced, *RSC Adv.* 2016; 6: 83711–83719.

[9] Chatterjee K, Ashokkumar M, Gullapalli H, Gong Y, Nitrogen-rich carbon nano-onions for oxygen reduction reaction, *Carbon N. Y.* 2018; 130: 645–651.

[10] Butsyk O, Olejnik P, Romero E, Plonska-brzezinska ME, Postsynthetic treatment of carbon nano-onions: Surface modification by heteroatoms to enhance their capacitive and electrocatalytic properties, *Carbon N. Y.* 2019; 147: 90–104.

[11] Shaku B, Mofokeng TP, Mongwe TH, Coville NJ, Physicochemical Properties of Nitrogen Doped Carbon Nano-onions Grown by Flame Pyrolysis from Grapeseed Oil for use in Supercapacitors, *Electroanalysis.* 2020;10: 1–13.

[12] Ejaz A, Jeon S, The individual role of pyrrolic, pyridinic and graphitic nitrogen in the growth kinetics of Pd NPs on N-rGO followed by a comprehensive study on ORR, *Int. J. Hydrogen Energy* 2018; 43: 5690–5702.

[13] Zhang et al. Nitrogen doped carbon nano-onions as efficient and robust electrocatalysts for oxygen reduction reactions, *Curr. Appl. Phys.* 2018; 18: 417–423.

[14] Neergat M, Gunasekar V, Rahul R, Carbon-supported Pd – Fe electrocatalysts for oxygen reduction reaction (ORR) and their methanol tolerance, *J. Electroanal. Chem.* 2011; 658: 25–32.

[15] Sakthivel M, Schlange A, Kunz U, Turek T, Microwave assisted synthesis of surfactant stabilized platinum/carbon nanotube electrocatalysts for direct methanol fuel cell applications, *J. Power Sources.* 2010; 195: 7083–7089.

- [16] Motshekga SC, Pillai SK, Sinha Ray S, Jalama K, Krause RWM, Recent trends in the microwave-assisted synthesis of metal oxide nanoparticles supported on carbon nanotubes and their applications, *J. Nanomater.* 2012; 2012: 15.
- [17] Kumar et al. Microwave-assisted synthesis of palladium nanoparticles intercalated nitrogen doped reduced graphene oxide and their electrocatalytic activity for direct-ethanol fuel cells, *J. Colloid Interface Sci.* 2018; 515: 160–171.
- [18] Ding K, Zhao Y, Liu L, Li Y, Liu L, Wang Y, Gu H , Wei H, Guo Z, Multi-walled carbon nanotubes supported Pd composite nanoparticles hydrothermally produced from technical grade PdO precursor, *Electrochim. Acta* 2015; 176: 1256–1265.
- [19] Cerritos RC, Guerra-balcázar M, Ramírez RF, Ledesma-garcía J, Arriaga LG, Morphological Effect of Pd Catalyst on Ethanol Electro-Oxidation Reaction, *Materials* 2012; 5: 1686–1697.
- [20] Shen SY, Zhao TS, Wu QX, Product analysis of the ethanol oxidation reaction on palladium-based catalysts in an anion-exchange membrane fuel cell environment, *Int. J. Hydrog. Energy* 2011; 7: 1–8.
- [21] Saipanya S, Lapanantnoppakhun S, Sarakonsri T, Electrochemical Deposition of Platinum and Palladium on Gold Nanoparticles Loaded Carbon Nanotube Support for Oxidation Reactions in Fuel Cell, *J. Chem.* 2014; 2014: 104514.
- [22] Mei Chen X, Jie Lin Z, Tian Jia T, Min Cai Z, Li Huang X, Qi Jiang Y, Chen X, Nan Chen G, A facile synthesis of palladium nanoparticles supported on functional carbon nanotubes and its novel catalysis for ethanol electrooxidation, *Anal. Chim. Acta* 2009; 650: 54–58.
- [23] Spinacé EV, Neto AO, Linardi M, Glycerol Electro-Oxidation In Alkaline Medium Using Pd / C And PdSn / C Electrocatalysts Prepared By Electron Beam Irradiation, *Electrochim. Acta* 2013; 25: 831–840.

- [24] Chen Y, Zhuang L, Lu J, Non-Pt Anode Catalysts for Alkaline Direct Alcohol Fuel Cells, *Chinese J. Catal.* 2007; 28: 870–874.
- [25] Wang J, Cheng N, Banis MN, Xiao B, Riese A, Sun X, Comparative study to understand the intrinsic properties of Pt and Pd catalysts for methanol and ethanol oxidation in alkaline media, *Electrochim. Acta* 2015; 185: 267–275.
- [26] Antolini E, Palladium in fuel cell catalysis, *Energy Environ. Sci.* 2009; 9: 915–931.
- [27] Sheikh AM, Correa PS, Silva EL, Savaris ID, Amico SC, Malfatti CF, Energy conversion using Pd-based catalysts in direct ethanol fuel cell, *RE&PQJ* 2013; 11: 1–4.
- [28] Siswana et al. Electrocatalysis of asulam on cobalt phthalocyanine modified multi-walled carbon nanotubes immobilized on a basal plane pyrolytic graphite electrode, *Electrochim. Acta* 2006; 50: 114–122.
- [29] Shaikh A, Singh BK, Mohapatra D, Parida S, Nitrogen-Doped Carbon Nano-Onions as a Metal-Free Electrocatalyst, *Electrocatalysis* 2019; 10: 222-231.
- [30] Prekob A, Muránszky G, Kocserha I, Fiser B, Kristály F, Halasi G, Kónya Z, Sonochemical Deposition of Palladium Nanoparticles Onto the Surface of N - Doped Carbon Nanotubes: A Simplified One - Step Catalyst Production Method, *Catal. Letters.* 2019; 150: 505-513.
- [31] Corma et al. Catalytic activity of palladium supported on single wall carbon nanotubes compared to palladium supported on activated carbon: Study of the Heck and Suzuki couplings, aerobic alcohol oxidation and selective hydrogenation, *J. Mol. Catal. A Chem.* 2005; 230: 97–105.
- [32] Nitze et al. Synthesis of palladium nanoparticles decorated helical carbon nanofiber as highly active anodic catalyst for direct formic acid fuel cells, *Electrochim. Acta.* 2012; 63: 323–328.

- [33] Rani UA, Ng LY, Ng CY, Mahmoudi E, A review of carbon quantum dots and their applications in wastewater treatment, *Adv. Colloid Interface Sci.* 2020 ; 278; 102124.
- [34] Croitoru A, Oprea O, Nicoara A, Trusca R, Radu M, Neacsu I, Ficai D, Ficai A, Andronescu E, Multifunctional platforms based on graphene oxide and natural products, *Med.* 2019; 55: 230.
- [35] Han TH, Mohapatra D, Mahato N, Parida S, Shim JH, Nguyen ATN, Nguyen VQ, Cho MH, Shim JJ, Effect of nitrogen doping on the catalytic activity of carbon nano-onions for the oxygen reduction reaction in microbial fuel cells, *J. Ind. Eng. Chem.* 2020; 81: 269–277.
- [36] Peng X, Li Y, Zhang G, Zhang F, Fan X, Functionalization of graphene with nitrile groups by cycloaddition of tetracyanoethylene oxide, *J. Nanomater* 2013; 2013: 1-5.
- [37] Bartelmess J, Giordani S, Carbon Nano-Onions: chemistry and applications, *Beilstein J Nanotechnol.* 2014; 5: 1980–1998.
- [38] Han F, Yao B, Bai Y, Preparation of Carbon Nano-Onions and Their Application as Anode Materials for Rechargeable Lithium-Ion Batteries, *J. Phys. Chem.* 2011; 115: 8923–8927.
- [39] Mykhailiv O, Zubyk H, Plonska-brzezinska ME, *Inorganica Chimica Acta* Carbon nano-onions : Unique carbon nanostructures with fascinating properties and their potential applications, *Inorganica Chim. Acta* 2017; 468: 49–66.
- [40] Amora MD, Camisasca A, Lettieri S, Giordani S, Toxicity assessment of carbon nanomaterials in zebrafish during development, *Nanomaterials* 2017; 7: 414.
- [41] Qiao Z, Li J, Zhao N, Shi C, Nash P, Graphitization and microstructure transformation of nanodiamond to onion-like carbon, *Scr. Mater* 2006; 54: 225–229.

- [42] Plonska-brzezinska ME, Lapinski A, Wilczewska AZ, Dubis AT, The synthesis and characterization of carbon nano-onions produced by solution ozonolysis, *Carbon* 2011; 9: 5079-5089.
- [43] Gu W, Peters N, Yushin G, Functionalized carbon onions, detonation nanodiamond and mesoporous carbon as cathodes in Li-ion electrochemical energy storage devices, *Carbon N. Y.* 2012; 53: 292–301.
- [44] Li ZQ, Lu CJ, Xia ZP, Zhou Y, Luo Z, X-ray diffraction patterns of graphite and turbostratic carbon, *Carbon* 2007; 45: 1686–1695.
- [45] Kargar H, Torabi V, Akbari A, Behjatmanesh-Ardakani R, Sahraei A, Tahir MN, Pd(II) and Ni(II) complexes containing an asymmetric Schiff base ligand: Synthesis, x-ray crystal structure, spectroscopic investigations and computational studies, *J. Mol. Struct.* 2020; 1205: 127642.
- [46] Xu B, Yang X, Wang X, Guo J, Liu X, Short communication A novel catalyst support for DMFC : Onion-like fullerenes, *J. Power Sources* 2006; 162: 160–164.
- [47] Wang B, Chen Y, Chang T, Jiang Z, Huang Z, Wang S, Chang C, Chen Y, Wei J, Yang S, Fang T, Environmental Facet-dependent catalytic activities of Pd / rGO : Exploring dehydrogenation mechanism of dodecahydro-N-ethylcarbazole, *Appl. Catal. B Environ.* 2020; 266: 118658.
- [48] Bach Delpeuch A, Jacquot M, Chatenet M, Cremers C, The influence of mass-transport conditions on the ethanol oxidation reaction (EOR) mechanism of Pt/C electrocatalysts, *Phys. Chem. Chem. Phys.* 2016; 18: 25169–25175.
- [49] Lesiak B, Jiricek P, Bieloshapka I, Chemical and structural properties of Pd nanoparticle-decorated graphene electron spectroscopic methods and quases, *Appl. Surf. Sci* 2017; 404: 300–309.
- [50] Fujimoto A, Yamada Y, Koinuma M, Sato S, Origins of sp³C peaks in C1s X-ray Photoelectron Spectra of Carbon Materials, *Anal. Chem.* 2016; 88: 6110–6114.

- [51] Domashevskaya EP, Chuvenkova OA, Ryabtsev SV, Yurakov YA, Kashkarov VM, Shchukarev AV, Turishchev SY, Electronic structure of undoped and doped SnO_x nanolayers, *Thin Solid Films* 2013; 537: 137–144.
- [52] Tsyruľnikov PG, Afonassenko TN, Koshcheev SV, Boronin AI, State of palladium in palladium-aluminosilicate catalysts as studied by XPS and the catalytic activity of the catalysts in the deep oxidation of methane, *Kinet. Catal.* 2007; 48: 728–734.
- [53] Sikeyi LL, Adekunle AS, Maxakato NW, Electro-catalytic Activity of Carbon Nanofibers Supported Palladium Nanoparticles for Direct Alcohol Fuel Cells in Alkaline Medium, *Electrocatalysis* 2019; 10: 420–428.
- [54] Du J, Liu L, Yu Y, Zhang Y, Lv H, Chen A, *Journal of Materials Science & Technology* N-doped ordered mesoporous carbon spheres derived by confined pyrolysis for high supercapacitor performance, *J. Mater. Sci. Technol.* 2019; 35: 2178–2186.
- [55] Villarroel-rocha J, Barrera D, Sapag K, Microporous and Mesoporous Materials Introducing a self-consistent test and the corresponding modification in the Barrett, Joyner and Halenda method for pore-size determination, *Microporous Mesoporous Mater* 2014; 200: 68–78.
- [56] Jeong JH, Lee YH, Kim B, Relationship between microstructure and electrochemical properties of 2lignin-derived carbon nanofibers prepared by thermal treatment, *Synth. Met.* 2020; 260: 116287.
- [57] Walsh FC, Low CTJ, *Surface & Coatings Technology* A review of developments in the electrodeposition of tin, *Surf. Coat. Technol.* 2016; 288: 79–94.
- [58] Miah R, Ohsaka T, Observation of ‘inverted peak’ during molecular oxygen reduction at Au electrode in alkaline media, *Electrochim. Acta* 2007; 52: 6378–6385.

- [59] Fu S, Zhu C, Zhou Y, Yang G, Jeon J, Lemmon J, Du D, Nune SK, Lin Y, *Electrochimica Acta* Metal-organic framework derived hierarchically porous nitrogen-doped carbon nanostructures as novel electrocatalyst for oxygen reduction reaction, *Electrochim. Acta* 2015; 178: 287–293.
- [60] Wan Y, Xu J, Lv R, Heterogeneous electrocatalysts design for nitrogen reduction reaction under ambient conditions, *Mater. Today* 2019; 27: 69–90.
- [61] Granzier-Nakajima T, Fujisawa K, Anil V, Terrones M, Yeh YT, Controlling nitrogen doping in graphene with atomic precision: Synthesis and characterization, *Nanomaterials* 2019; 9: 1–18.
- [62] Tan Z, Ni K, Chen G, Zeng W, Tao Z, Ikram M, Zhang Q, Wang H, Sun L, Zhu X, Wu X, Ji H, Ruoff RS, Zhu Y, Incorporating Pyrrolic and Pyridinic Nitrogen into a Porous Carbon made from C60 Molecules to Obtain Superior Energy Storage, *Adv. Mater* 2017; 29: 1–8.
- [63] Iii SEG, Tengco JMM, Yang Y, Regalbuto JR, Castano CE, *Applied Catalysis A, General Electrostatic adsorption-microwave synthesis of palladium nanoparticles on graphene for improved cross-coupling activity*, *Appl. Catal.* 2018; 550: 168–175.
- [64] An H, Pan L, Cui H, Zhou D, Wang B, Zhai J, Li Q, Pan Y, Electrocatalytic performance of Pd nanoparticles supported on TiO₂-MWCNTs for methanol, ethanol, and isopropanol in alkaline media, *J. Electroanal. Chem.* 2015; 741: 56–63.
- [65] Chem JM, Hu G, Nitze F, Sharifi T, Barzegar HR, Thomas W, enhanced electrocatalysts for electro-oxidation of small molecules, *J. Mater. Chem.* 2012; 22: 8541–8548.
- [66] Kakaei K, Dorraji M, *Electrochimica Acta* One-pot synthesis of Palladium Silver nanoparticles decorated reduced graphene oxide and their application for ethanol oxidation in alkaline media, *Electrochim. Acta* 2014; 143: 207–215.

- [67] Yu O, Lisitsyn AS, Kibis LS, Andrei I, Boronin AI, Slavinskaya EM, Stonkus OA, Yashnik SA, Ismagilov ZR, Influence of the nitrogen-doped carbon nanofibers on the catalytic properties of supported metal and oxide nanoparticles, *Catal. Today* 2018; 341: 125–133.
- [68] Hiep T, Mohapatra D, Mahato N, Parida S, *Journal of Industrial and Engineering Chemistry* Effect of nitrogen doping on the catalytic activity of carbon nano-onions for the oxygen reduction reaction in microbial fuel cells, *J. Ind. Eng. Chem.* 2020; 81: 269–277.
- [69] Antolini E, Carbon supports for low-temperature fuel cell catalysts, *Appl. Catal. B Environ.* 2009; 88: 1–24.
- [70] Wang Q, He H, Luan J, Tang Y, Huang D, Peng Z, Wang H, *Electrochimica Acta* Synergistic effect of N-doping and rich oxygen vacancies induced by nitrogen plasma endows TiO₂ superior sodium storage performance, *Electrochim. Acta* 2019; 309: 242–252.
- [71] Hassan KM, Hathoot AA, Maher R, Abdel Azzem M, *Electrocatalytic oxidation of ethanol at Pd, Pt, Pd/Pt and Pt/Pd nano particles supported on poly 1,8-diaminonaphthalene film in alkaline medium*, *RSC Adv.* 2018; 8: 15417–15426.
- [72] Neghmouche NS, Lanez T, *Calculation of Diffusion Coefficients and Layer Thickness for Oxidation the Ferrocene using Voltammetry Technique*, *Int. J. Chem. Stud.* 2013; 1: 2321–4902.
- [73] Niu W, Wang Y, He J, Liu W, Liu M, *Nano Energy* Highly stable nitrogen-doped carbon nanotubes derived from carbon dots and metal-organic frameworks toward excellent efficient electrocatalyst for oxygen reduction reaction, *Nano Energy* 2019; 63: 103788.
- [74] Nahil MA, Williams PT, *Surface chemistry and porosity of nitrogen-containing activated carbons produced from acrylic textile waste*, *Chem. Eng. J.* 2012; 184: 228–237.

[75] Moraes LPR, Matos BR, Radtke C, Santiago EI, Fonseca FC, Amico SC, Malfatti CF, Direct Synthesis and performance of palladium-based electrocatalysts in alkaline direct ethanol fuel cell, *Int. J. Hydrogen Energy* 2016; 41: 6457–6468.

[76] Maciej A, Simka W, Electrocatalytic properties of Co decorated graphene and graphene oxide for small organic molecules oxidation, *Int. J. Hydrogen Energy* 2019; 5: 1769-1783.

[77] Bera B, Kar T, Chakraborty A, Neergat M, Influence of nitrogen-doping in carbon on equivalent distributed resistance and capacitance – Implications to Electrocatalysis of oxygen reduction reaction Influence of nitrogen-doping in carbon on equivalent distributed resistance and capacitance – Imp, *J. Electroanal. Chem.* 2017; 805: 184–192.

CHAPTER 4

Platinum Nanoparticles Loaded on Pristine and Boron Oxide Modified Carbon Nano-Onions for Enhanced Ammonia Electrooxidation in Alkaline Direct Ammonia Fuel Cells

L.L. Sikeyi, T.D. Ntuli, T.H. Mongwe, N.W. Maxakato, N.J. Coville, M.S. Maubane-Nkadimeng, Platinum Nanoparticles Loaded on Pristine and Boron Oxide Modified Carbon Nano-Onions for Enhanced Ammonia Electrooxidation in Alkaline Direct Ammonia Fuel Cells, *J. Electroanal. Chem.* 917 (2022) 116411. <https://doi.org/10.2139/ssrn.3982297>. Impact factor: 4.598.

1. Sikeyi - Synthesis and Characterization, Writing-Original Draft, Validation
2. Ntuli – Data Curation
3. Mongwe - Flame pyrolysis method
4. Maxakato - Resources, Supervision
5. Coville - Reviewing and Editing, Resources, Supervision
6. Maubane-Nkadimeng- Conceptualization, Resources, Supervision

Ludwe L Sikeyi^a, Themba D Ntuli^{a,d}, Thomas H Mongwe^{a,d}, Nobanathi W Maxakato^b, Neil J Coville^{a,c} and Manoko S Maubane-Nkadimeng^{a,c,d *}

^a Molecular Sciences Institute, School of Chemistry, University of Witwatersrand, Braamfontein, 2050, South Africa, ^b Department of Chemical Sciences, University of Johannesburg, Doornfontein, 2021, South Africa. ^c DSI-NRF Centre of Excellence in Strong Materials, University of Witwatersrand, Braamfontein, 2050, South Africa. ^d Microscopy and Microanalysis Unit, University of Witwatersrand, Braamfontein, 2050, South Africa

Abstract

Well dispersed ultrafine platinum nanoparticles (Pt NPs) loaded on pristine (p-CNOs) and boron oxide modified carbon nano-onions (B-CNOs) were successfully synthesized by the ethylene glycol reduction method. The obtained materials showed the presence of the face centered cubic structure of Pt with an average particle size of 4.6 ± 0.9 nm (p-CNOs) and 4.4 ± 0.5 nm (B-CNOs) under the alcohol reduction conditions. Energy dispersive X-ray spectroscopy and X-ray photoelectron spectroscopy confirmed the presence of C, O, B, and Pt on the surface of CNOs. Transmission electron microscopy images showed that the addition of B and Pt onto the surface of CNOs did not alter their morphology. The electrochemical catalytic performance of Pt/p-CNO, unwashed (uw) Pt/B-CNO, washed (w) Pt/B-CNO and commercial Pt/C nanocatalysts were evaluated towards ammonia oxidation in alkaline electrolyte. The Pt/B-CNO_{uw} hybrid nanocatalysts showed enhanced catalytic activity, better stability, and fast charge transfer for ammonia oxidation reactions as compared to Pt/B-CNO_w, Pt/p-CNO and the commercial Pt/C hybrids. The improved electrocatalytic activity of the Pt/B-CNO_{uw} hybrid is ascribed to an increase of the electronic conductivity of the carbon nano onions by boron oxide and the enhancement of the interaction with water due to the boron on the support, which could contribute to the oxidation of intermediate products from the ammonia electro-oxidation.

Keywords: Carbon nano onions; Cyclic voltammetry; Boron oxide; Direct ammonia fuel cell; Nanocatalysts.

4. Introduction

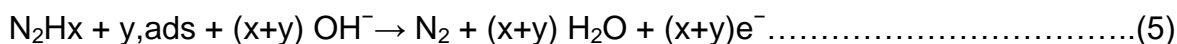
Environmental problems and the growing global demand for energy have both motivated intensive research activities to identify new sources of clean and sustainable energy sources to replace fossil fuels such as oil and coal [1]. Currently, non-renewable resources such as fossil fuels (oil, coal, and natural gas) are still the main sources of energy [2]. As the use of energy keeps growing, practical fossil fuel stores will decline. To satisfy growing energy demands,

exploitation of fossil fuels in delicate geographical zones has occurred, bringing about an expansion in financial related and environmental costs in their investigation and extraction activities [3]. Development of energy devices such as fuel cells, that will reduce atmospheric air pollution is thus required [4]. Fuel cells are environmentally friendly energy devices that use chemicals as fuel sources that generally produce clean energy. There are six distinct types of fuel cells and these are classified according to the electrolyte they utilize and their working temperature (either high or low temperature) [5].

Much current research on the alkaline fuel cell (AFC) uses alcohols as fuel. The AFC is one of the fuel cell systems used by the National Aeronautics and Space Administration (NASA) to power the Apollo series spacecraft [6]. AFC's were first studied in the 1960s and today mainly use an aqueous solution of potassium hydroxide (KOH) in water as the electrolyte; the cell works at low temperatures (90 °C to 100 °C) [7]. Another type of AFC is the alkaline direct ammonia fuel cell (DAFC) which has been considered for vehicle applications, because of their fast start-up advantage compared to the direct alcohol fuel cell [8].

The interest in the DAFC arises since NH₃ is easy to handle and transport as a liquid fuel [9]. Ammonia also has many advantages over alternative fuels such as methanol, formic acid, and hydrogen due to its economic and environmental characteristics/benefits, its higher power density, lower toxicity, and lower source-to-tank energy cost for a vehicle [10]. Moreover, the ammonia oxidation reaction (AOR) in alkaline media allows for the use of platinum group metals (PGMs) such as iridium, ruthenium, rhodium, osmium, and palladium [11]. AOR studies have revealed a slow reaction at low temperatures and that highly active nanocatalysts are needed to change ammonia to nitrogen at useful process rates [12]. The well-accepted mechanism for the oxidation of ammonia in alkaline conditions on a Pt anode was first presented by Gerischer and Mauerer [13]. This mechanism includes dehydrogenation of adsorbed ammonia species and evolution of nitrogen gas:





where x, y = 1 or 2.

The ammonia oxidation reaction on a Pt anode in an alkaline electrolyte has affirmed the high surface sensitivity of this reaction, where ammonia is preferentially oxidized on monocrystalline Pt (100), and is rather sluggish on Pt (111) and Pt (110) planes [14]. This is because of the higher absorption energies of NH_3 and NH_2 intermediates (0.7 eV) higher for Pt(100) than for Pt(111)) and lower adsorption rate of N_{ad} on Pt(100) than those of the other facets [15]. Studies in oriented crystal electrodes, mainly Pt (100) and Pt(111), also showed the ammonia electrooxidation as a surface confined process [16–18]. Rosca and Koper studied the structure sensitivity of ammonia electro-oxidation on Pt (111) and Pt (100) surfaces using cyclic voltammetry and chronoamperometry. On Pt (111) they found low activity, with NH and N being the dominant surface intermediates. The activity was higher on Pt (100), where adsorbed NH_2 was the dominant surface intermediate [19]. The AOR on Pt (and other PGMs) follows the mechanism shown in reactions (1) to (6) above. Here, the dehydrogenated adsorbed ammonia species, NH_2ads and NHads , are dynamic species and Nads is an inert surface adsorbed nitrogen [20]. Several research studies have been focused on the advancement of other metal nanocatalysts for ammonia oxidation in alkaline conditions, but until now Pt remains the best electrocatalyst for this process [21]. In the past few years, studies on Pt catalysts (mono-metallic, bimetallic and multi-metallic) and variation of catalyst supports for the DAFC systems have continued [22–26]. Most supports used in DAFCs are made of

carbon. The carbon support material can have a range of morphologies and these can be modified by chemical reactions and heteroatom doping and this can impact on the Pt dispersion and particle size [27,28]. The support materials thus strongly affect the performance, stability, and effectiveness of the electrocatalyst used in a DAFC [29].

Cunci et al. reported on Pt/erGO (erGO = reduced graphene oxide), synthesized using a rotating disk slurry electrodeposition (RoDSE) technique, without the use of a reducing agent, for the ammonia oxidation reaction. The Pt/erGO electrocatalyst showed higher current density when compared to a Pt/C electrocatalyst in the electrochemical experiments [30]. Pt nanoparticles supported on boron doped diamond (BDD) were studied by chronoamperometry and cyclic voltammetry electrodeposition methods. The Pt-BDD nanocatalysts electrodeposited by chronoamperometry showed a significant improvement in catalytic activity when compared to the catalyst electrodeposited by cyclic voltammetry [31]. Carbon nano-onions (CNOs), with good electrical and thermal conductivity, and surface area, have shown a high stability in a fuel cell environment [32]. Santiago et al. reported Pt decoration of pristine CNOs obtained by a RoDSE technique that was used in the methanol oxidation reaction [33].

Enhancement of the activity of Pt/carbon electrodes by surface modification e.g. attachment of functional groups to the sidewalls or ends of the carbon nanomaterials through covalent bonds has been reported [34]. The common element added to a carbon surface is O and this addition has generally led to enhanced electrochemical activity of the carbon surface.

There are also reports of the use of B to modify a carbon electrode surface, either by creating defects, or by functionalization to give B containing carbons. The surface modification of anode and cathode nanomaterials with boron oxide in Li-ion batteries has been an approach to accomplish improvement in the electrochemical activity, and reduction in unfavourable electrolyte side reactions. The B has thus prevented transition metal dissolution and stabilized the surface structure of nanomaterials [35–38].

Recently, it has been demonstrated that the modification of $\text{LiNi}_{1/3}\text{Co}_{1/3}\text{Mn}_{1/3}\text{O}_2$ (NCM111) with boron oxide (B_2O_3) led to an increase in the structural stability, density and conductivity of the NCM111[39]. B_2O_3 @NCM111 had a higher Li^+ chemical diffusion coefficient as compared to pristine NCM111. This enhancement was related to the expansion of the interlayer carbon distances due to the B_2O_3 , prompting a much easier lithium-ion intercalation /de-intercalation. Tsierkezos et al. reported carbon nanotubes modified with boron oxide nanoparticles towards a ferrocyanide redox system in potassium chloride solution [40]. Electrochemistry results showed that the boron oxide modified multiwalled carbon nanotubes (B-MWCNTs) gave faster electrochemical reactions and that is was more sensitive than unmodified acid-treated MWCNTs in the redox reaction due to boron oxide modification.

The above data suggest that B_2O_3 could also be used to enhance the activity of Pt/CNO electrodes in the DAFC. Boron trioxide (B_2O_3) has a large band-gap and high chemical stability in acidic media due to strong B-O bonding [41]. B_2O_3 in B-CNO and Pt/B-CNO nanocatalysts, can produce a three-dimensional B-O network, where the 3D-coordinated $[\text{BO}_3]$ with a non-bridging oxygen is the key to accomplish high catalytic performance, fast electron transfer and the long term stability. Furthermore, the strong covalent B-O bonding can improve the structural and thermal stability of B-CNO and Pt/B-CNO electrocatalysts. In this study, we report on the use of pristine CNOs (p-CNO) and boron oxide modified CNOs (B-CNO) as support materials for use in DAFCs. A flame pyrolysis method was used to synthesize the CNOs [42]; the Pt was attached to the surface of the p-CNO and B-CNO support materials using an ethylene glycol reduction method [43]. To the best of our knowledge, a detailed study of the synthesis of Pt/B-CNOs for use in direct ammonia fuel cells has not previously been reported. The unwashed Pt/B-CNO electrocatalyst exhibited a higher electrocatalytic activity for the ammonia oxidation reaction when compared to the washed Pt/B-CNO, Pt/p-CNO and a standard Pt/C-based electrocatalyst.

4.1. Experimental

4.1.1. Materials and methods

The following materials, without purification, were used to prepare the electrocatalysts and electrolyte solutions used in this study: ethylene glycol > 99.9% (Sigma-Aldrich), Nafion solution > 5 wt.%, (Sigma-Aldrich), H_2PtCl_6 > 98.0% (Sigma-Aldrich), Pt/C commercial standard > 10% loading (Sigma-Aldrich), boric acid > 50% (Sigma-Aldrich), sodium hydroxide pellets (Sigma-Aldrich) and ammonium hydroxide > 30% (v/v) (Sigma-Aldrich).

4.1.2. Synthesis of carbon nano-onions (CNOs)

CNOs with onion-like morphology were synthesized using a flame pyrolysis method as described in previous work [42]. Coconut oil was used as the carbon source for the growth of p-CNOs. Coconut oil is hydrocarbon-rich complex with a chain-length of 14 to 18 carbon atoms. The coconut oil was obtained by melting coconut butter into a 400 mL beaker inside an oven at 60°C. The glass container wick was filled with this liquid oil (50 mL) using a syringe and placed under the brass collecting plate (BCP). The wick immersed in oil in a glass container was ignited to create a flame. A deep-black powder was produced by the flame due to incomplete burning of the oil in the center zone of the glowing flame (temperature ca. 800–1000 °C). After 1 h the carbogenic black powder was collected from the BCP and a yield of 2.98 % was obtained, based on the oil used. The coconut oil-derived CNOs were purified by refluxing in 2M nitric acid for 3 h to give pristine carbon nano-onions (p-CNOs). The p-CNOs were filtered and dried in an oven at 100 °C for overnight.

4.1.3. Boron oxide modification of the pristine carbon nano-onions (p-CNO)

Boron oxide modified carbon nano-onions (B-CNOs) were synthesized by a chemical vapor deposition method using boric acid as boron source and argon as

a carrier gas [44]. Two reactions were performed with different B₂O₃:p-CNO ratios (1:5 and 2:5). About 100 mg of p-CNOs and boric acid (20 mg or 40 mg) were manually mixed together using a pestle and mortar for 1 h. The sample was transferred into a ceramic boat which was placed inside an electric tube furnace. The furnace was heated from 50 °C to 100 °C at 1.0 K min⁻¹ and then kept at 100 °C for 1 h. The carbon was then heated at 10 K min⁻¹ to 1000 °C in the electric furnace under a stream of argon gas. The product was heated at 1000 °C for 2 h, and then cooled slowly to room temperature. The final products (referred to as unwashed (uw) B-CNO1 and unwashed (uw) B-CNO2) that formed in the two reactions were allowed to cool to room temperature and a yield of ca. 92 % was obtained. The two samples were refluxed in deionized water to eliminate residual boron oxide (3 h at 110 °C), centrifuged at 18000 rpm for 30 min, rinsed several times with distilled water and then dried in an oven for 24 h at 100 °C. These samples were called washed (w) B-CNO3 and (w) washed B-CNO4.

4.1.4. Synthesis of Pt/p-CNO, unwashed (uw) Pt/B-CNO, and washed (w) Pt/B-CNO electrocatalysts.

The platinum-based electrocatalysts were synthesized using the alcohol reduction method [43]. In this procedure, p-CNO, unwashed B-CNO (B-CNO_{uw}), and washed B-CNO (B-CNO_w) were separately dispersed in ethylene glycol and a calculated amount of H₂PtCl₆ was added to produce, under stirring for 30 min, 10% wt Pt loaded supports. The resulting mixtures were sonicated in an ultrasound bath for a further 30 min. The three solutions (containing either Pt/p-CNO or Pt/B-CNO_{uw} and Pt/B-CNO_w nanocatalysts) were then refluxed for 6 h. The resulting suspensions were centrifuged at 18000 rpm for 30 min and washed with deionized water to remove residual chloride. The nanocomposites were dried at 100 °C overnight to give the Pt-based electrocatalysts. Fig. 1 shows a schematic representation of the synthesis of p-CNO, unwashed B-CNO and the electrocatalysts.

4.1.5. Physicochemical characterization

The surface morphology and microstructure of all the CNOs and Pt/CNO nanomaterials were examined using a JEOL JEM-2100F transmission electron microscope at 200 kV. Scanning electron microscopy elemental analysis was conducted on a Carl Zeiss Sigma field emission scanning electron microscope (FESEM) equipped with an Oxford X-act detector for energy dispersive X-ray (EDS) measurements. Raman spectra were obtained using a Horiba Jobin Yvon Raman spectrometer with a laser wavelength of ($\lambda = 514$ nm). Thermal properties of the CNOs and Pt/CNO nanomaterials were studied using a Perkin Elmer 6000 thermogravimetric analyzer. The surface area and the pore size of the materials were calculated using a Micromeritics Tristar 3000 surface area and porosity analyser using the Brunauer-Emmett-Teller method (BET). X-ray powder diffraction (XRD) patterns were acquired using Bruker D2 Phaser with the radiation source of Cu K α and wavelength of 1.5406 Å generated at 30 kV and 10 mA. X-ray photoelectron spectroscopy (XPS) data of the materials were obtained from a Thermo Scientific ESCALAB 250Xi spectrometer with a monochromatic Al K α (1486.7 eV) source operating with an X-ray power of 300 W and high-resolution pass energy of 20 eV.

4.1.6. Electrochemical characterization

The electrochemical experiments were carried out in an Ivium Compactstat potentiostat, using a conventional three-electrode pyrex glass cell compartment. The electrode configuration system consisted of a working electrode (glassy carbon electrode), a reference electrode (Ag/AgCl in 3M KCl), and a counter electrode (platinum wire). Electrocatalytic activity of the Pt based nanocatalysts were studied in 0.5 M NaOH + 1 M NH₄OH solution by performing cyclic voltammetry (CV), chronoamperometry (CA) and electrochemical impedance spectroscopy (EIS) measurements. Before conducting the electrochemical measurements, a homogeneous ink of the electrocatalysts were prepared by adding 10 mg of the sample in a solution of 1 ml ethanol and 2 drops of 5 wt.% Nafion followed by sonication for 30 min. The above prepared black

electrocatalysts ink (10 μL) was drop cast, using a micropipette, onto the surface of a clean glassy carbon electrode and then dried at room temperature for 1 h. The electrolyte was de-aerated by purging with argon gas for 20 min before the electrochemical measurements were performed to eliminate any oxygen interference. The electroactive surface area (ECSA) of the Pt based nanocatalysts was measured from the CV curves recorded at 50 mV s^{-1} in 0.5 M NaOH and its value was normalized by the geometric area (0.196 cm^2) of the working electrode. Current values acquired in CV and CA experiments in 0.5 M NaOH + 1 M NH_4OH solution were normalized per ECSA of the electrocatalysts. All test outcomes were compared with a commercial 10 % wt Pt/C nanocatalyst under similar reaction conditions.

4.2. Results and discussion

4.2.1. Structural and morphological analysis

The CNOs and Pt/CNOs were prepared as described in the literature. This is shown schematically in Fig 4.1.

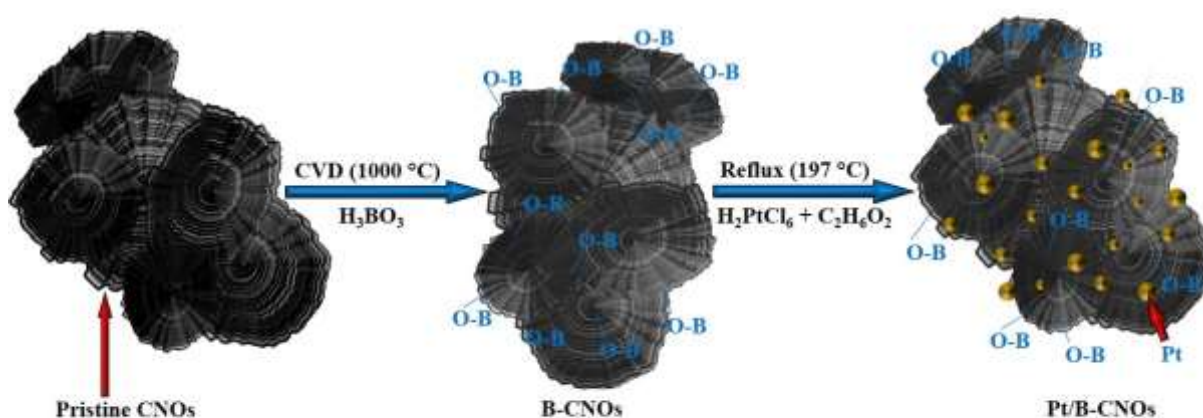


Figure 4.1: Schematic representation of the preparation of the B-CNO and Pt/B-CNO nanocatalysts using the chemical vapor deposition and alcohol reduction methods (O-B = BO bond on CNO surface).

4.2.2. Transmission electron microscopy (TEM)

Fig. 4.2 shows TEM images of the p-CNO, unwashed B-CNO, Pt/p-CNO, and unwashed Pt/B-CNO nanomaterials. The TEM micrographs depicted in Fig. 4.2(a) and (b) shows that the pristine and boron oxide modified CNO exhibit a quasi-spherical morphology with particle sizes ranging from 30 to 70 nm (Supplementary section, and (Fig. S1(a and b))). Furthermore, the TEM micrographs of the p-CNO and B-CNO showed carbon onion like structure with multi concentric graphite shells (see Fig. 4.2(c) and (d)). As presented in Fig. 4.2(e), the Pt NPs are uniformly dispersed on the surface of the CNO support material. Fig. 4.2(f) and the B-CNO surface. From the TEM images, the mean Pt particle size of Pt/p-CNO and Pt/B-CNO was found to be 4.6 ± 0.9 nm and 4.4 ± 0.5 nm using image J software respectively (Fig. S1(c) and Fig. S1(d)). Surprisingly, the mean particles sizes obtained by TEM micrographs are similar for all materials suggesting that the different supports increase the platinum nanoparticles accessible area. The mean Pt particle size of the prepared platinum-based electrocatalysts was similar to the ones that were reported by Mashindi et al. [45] and Gwebu et al. for oxygen reduction and alcohol oxidation reactions, respectively[46].

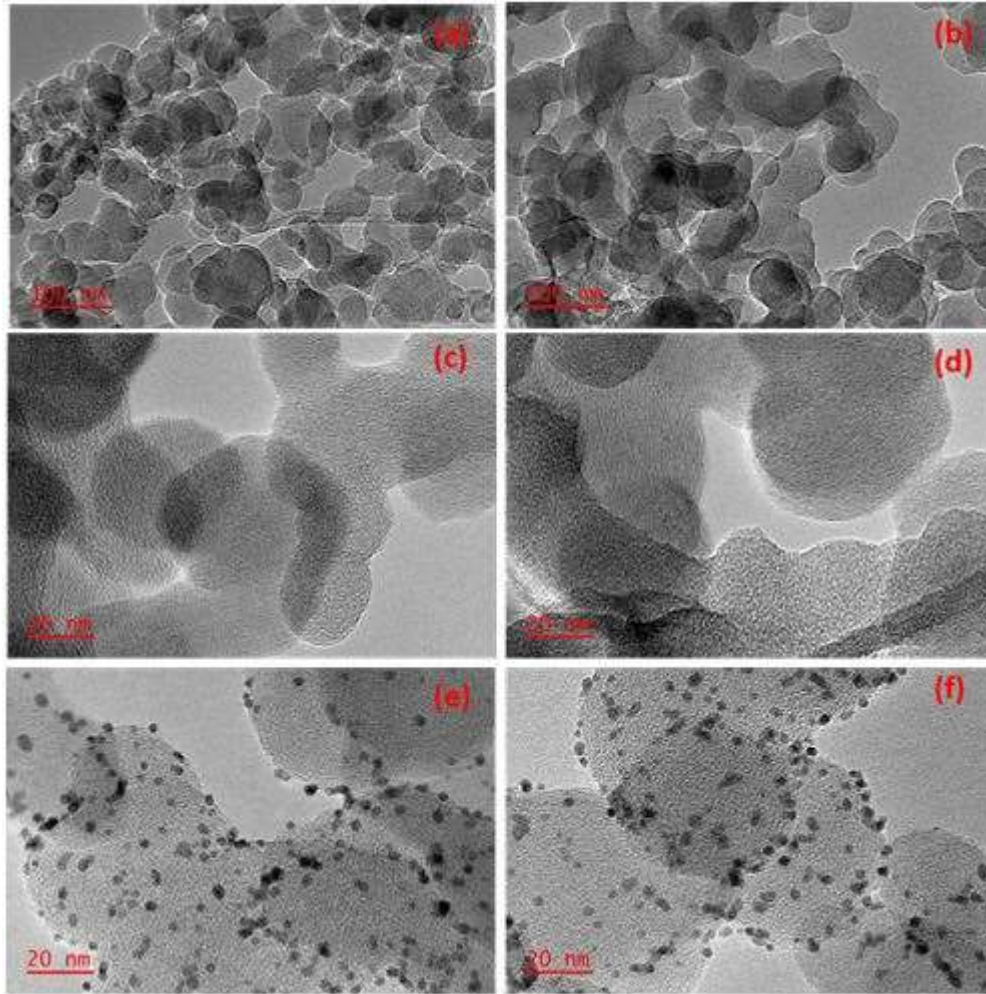


Figure 4.2: TEM micrographs of (a and c) p-CNO, (b and d) B-CNO (e) Pt/p-CNO and (f) Pt/B-CNO nanomaterials.

4.2.3. Scanning electron microscopy (SEM)

Fig. 4.3 displays the typical morphology of the unwashed B-CNO and unwashed Pt/B-CNO nanomaterials obtained from SEM measurements. SEM images also show CNO agglomerates or conglomerates with the CNOs ranging between 30 to 70 nm diameter for both materials (see Fig. 4.3 (a) and (b)). The CNO shape/morphology observed from the SEM images was similar to that of CNOs made from olive oil [42]. The EDS spectra in Fig. 4.3 (c) and (d), reveals the presence of C, O, B, and Pt elements in the nanomaterials.

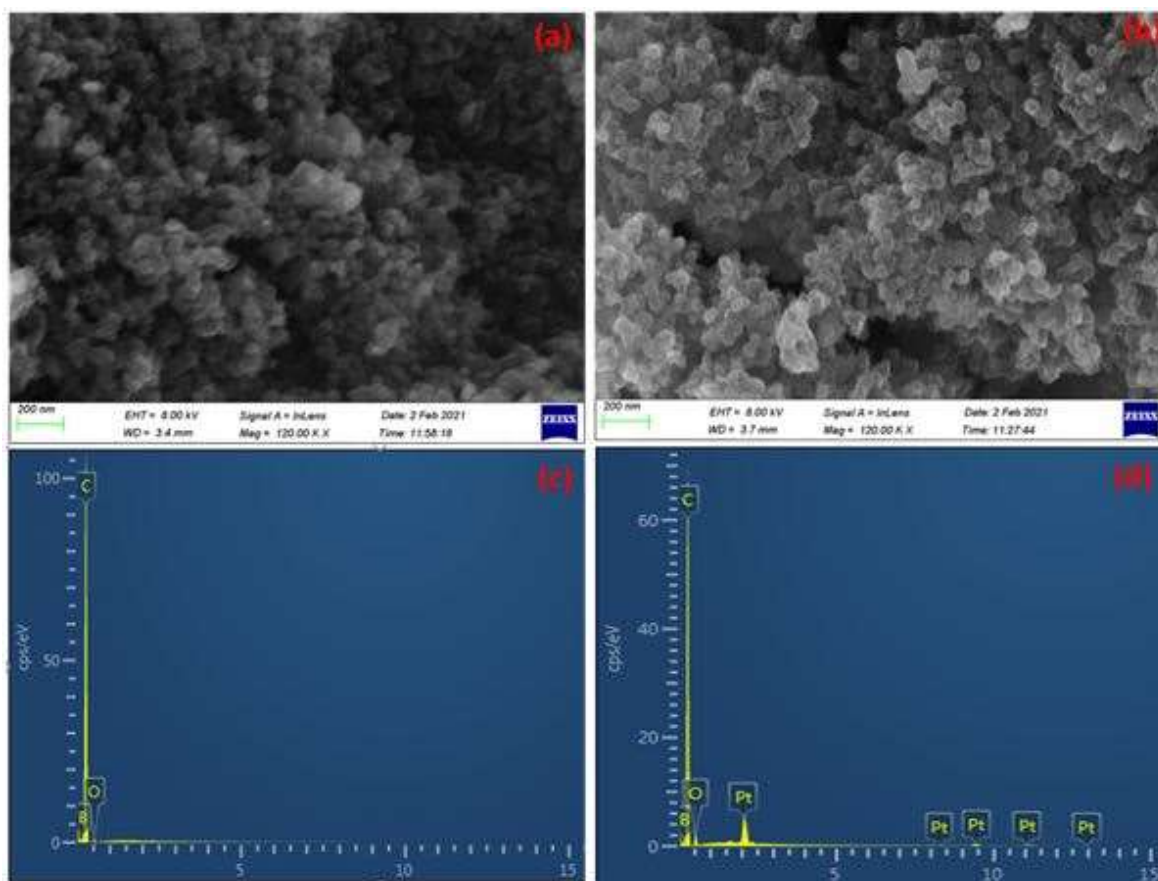


Figure 4.3: Typical SEM micrographs of (a) B-CNO (b) Pt/B-CNO and EDX profile of (c) B-CNO (d) Pt/B-CNO nanomaterials.

4.2.4. Raman spectroscopy

The chemical bonding and structural defects in the p-CNO and unwashed B-CNO nanomaterials were ascertained using Raman spectroscopy. As shown in Fig. 4.4, the two peaks, at $\sim 1352\text{ cm}^{-1}$ and $\sim 1584\text{ cm}^{-1}$ correspond to the D-band (sp^3 hybridized C atoms) and G-band (sp^2 hybridized C atoms), respectively [47]. The D peak is related to structural defects and disordered carbon atoms while the G peak is due to the graphitic carbon onion rings originating from the sp^2 hybridized carbon atoms [48]. The D-peak reveals a moderately wide shape because of the large bond length variation in the carbon onion structure [49]. Annealing of the B-CNO at higher temperature resulted in sharper D- and G-bands and larger secondary carbon peaks [50]. The ratios of the D- and G-modes were calculated from their peak areas to determine the structural defects and disorder degree in

the carbon nanomaterials. The results are summarized in Table 4.1. The I_D/I_G ratio of the B-CNOs was found to be higher than that of the p-CNOs, indicating the formation of defects due to boron oxide modification [51]. It has been reported that the defect-rich nature existing in the CNOs can lead to a systematic enhancement in electrocatalytic performances [50].

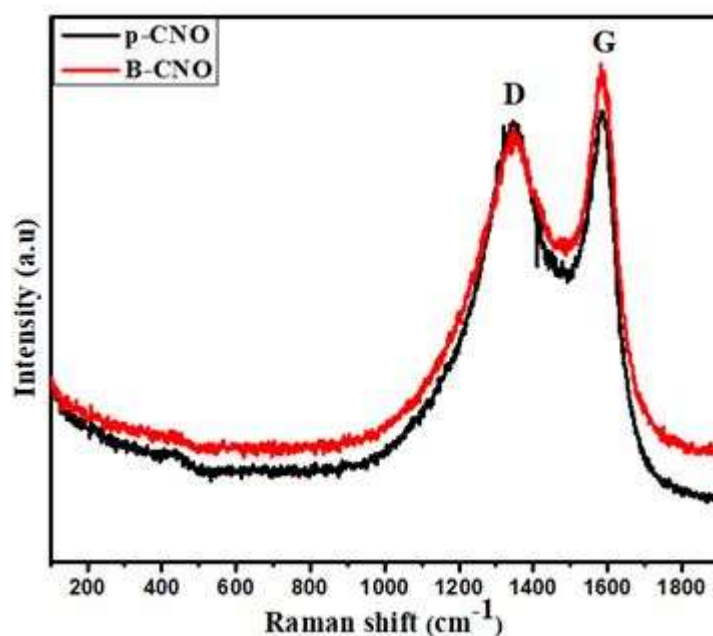


Figure 4.4: Raman spectra for p-CNO and B-CNO nanomaterials.

Table 4.1: Raman data showing peak positions, intensities, and intensity ratios for p-CNO and unwashed B-CNO

Sample	D band		G band		Area ratio (I_D/I_G)
	Position (cm^{-1})	Area	Position/ (cm^{-1})	Area	
p-CNO	1352	273047	1584	92473	2.95
B-CNO	1352	292146	1584	90756	3.21

4.2.5. Thermogravimetric analysis (TGA)

TGA analysis was used to evaluate the thermal stability of the new CNOs (Fig. S2). The p-CNO decomposed completely (0% residual weight) on oxidation, however, the unwashed B-CNO showed a large peak at 102 °C, and a residue was left behind ($T > 600$ °C). The peak at 102 °C can be ascribed to the dehydration of HBO_2 into B_2O_3 [52] and the residue was confirmed to be B_2O_3 by removal with washing in deionized water for 3 h at 110 °C.

The samples were washed in water for 3 h at 110 °C and this removed the B_2O_3 species as shown by the TGA data in Fig.S2. Thus, the amount of B_2O_3 in the unwashed B-CNO (ca 15-20%) was removed by the washing process (< 3% residue) [52].

Differential-thermogravimetric (TGA-DTG) plots of the Pt/p-CNO and unwashed Pt/B-CNO nanomaterials are shown in Fig 4.5. Fig. 4.5 (b) shows a two stage TGA weight loss for the Pt/p-CNO (243 °C and 462 °C) and a three stage weight loss for Pt/B-CNO (165 °C, 251 °C and 432 °C). The extra peak seen for Pt/B-CNO at 165 °C is assigned to the transformation of B_2O_3 to H_3BO_3 [53]. This was confirmed by performing TGA experiments on washed Pt/B-CNO (Fig S3) where this peak is seen to have disappeared after washing.

The two major peaks (ca. 250 °C and 450 °C) found in both Pt/p-CNO and unwashed Pt/B-CNO are due to carbon oxidation of the CNOs. The position of the high temperature peak for both Pt/p-CNO and Pt/B-CNO, due to the aromatic carbon oxidation, was observed to decrease relative to the CNOs without Pt [54] (from about 650 °C to ca 450 °C). This is not unexpected and is associated with a Pt catalysed reaction due to the Pt [55]. The peak at 243 °C and 250 °C were due to direct interaction of the Pt with part of the carbon surface [56].

The TGA measurements were also utilized to calculate the weight proportion of Pt in the synthesized Pt/p-CNO and unwashed Pt/B-CNO electrocatalysts. The residual weight of the Pt/p-CNO (7.2%) and unwashed Pt/B-CNO (7%) are lower than the 10% nominal Pt loading due to some carbon loss during the synthesis.

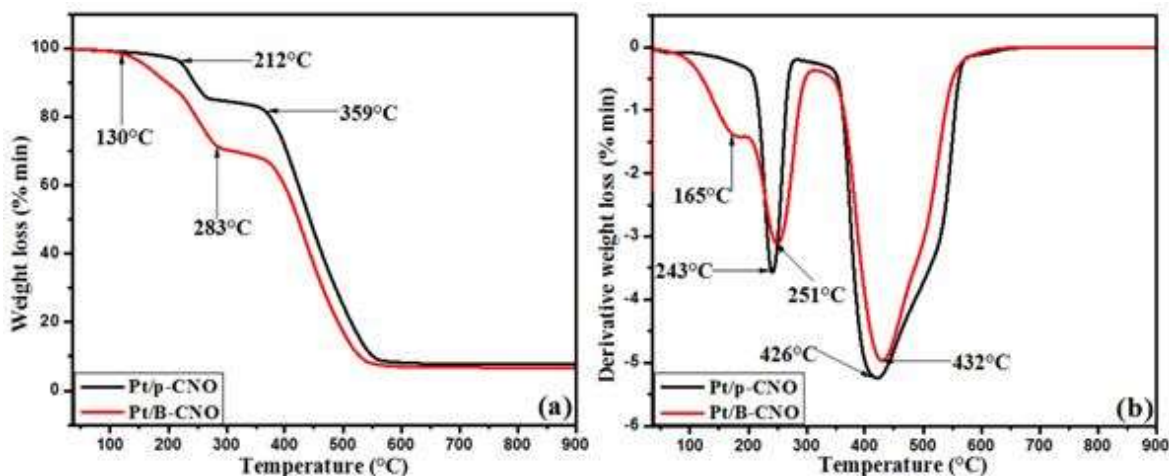


Figure 4.5: (a) TGA profile and (b) TGA derivatives of Pt/p-CNO and unwashed Pt/B-CNO (1:5) nanomaterials.

4.2.6. X-ray diffraction spectroscopy (XRD)

Fig. 4.6 shows the XRD patterns of the p-CNO, unwashed B-CNO, Pt/p-CNO, and unwashed Pt/B-CNO samples. The broad XRD peak appearing at $2\theta = 24.98^\circ$ of the B-CNO, Pt/p-CNO, and Pt/B-CNO is attributed to the (002) plane of the hexagonal structure of carbon suggesting that the synthesized carbon material was amorphous [57]. The XRD pattern for the Pt/p-CNO and Pt/B-CNO samples display the four characteristic diffraction peaks at 39.85° , 46.48° , 67.95° , and 81.80° corresponding to the face-centered cubic (fcc) structure of the Pt (111), (200), (220) and (311) facets, respectively [58]. The diffraction peaks for the Pt/p-CNO and Pt/B-CNO are in full agreement with the standard diffraction data for bulk platinum (JCPDF# 04 8027) [26]. No peaks were observed corresponding to impurity phases demonstrating the high purity of the nanomaterials. These results indicate that the Pt NPs were successfully incorporated inside the structure of p-CNO and unwashed B-CNO support materials. The mean crystallite size of the Pd/p-CNO and Pt/B-CNO were calculated to be 4.91 nm and 4.88 nm from the Pt (111) peak using the Debye–Scherer equation (see equation S1). The Pt particle size measured from the XRD data are in good agreement with the data measured using TEM images. The Pt (111) facet has been related to the activity in the ammonia oxidation reaction in alkaline electrolyte [22]. Therefore, the prepared

Pt/p-CNO and Pt/B-CNO have the appropriate shapes to be used as an anode in fuel cells.

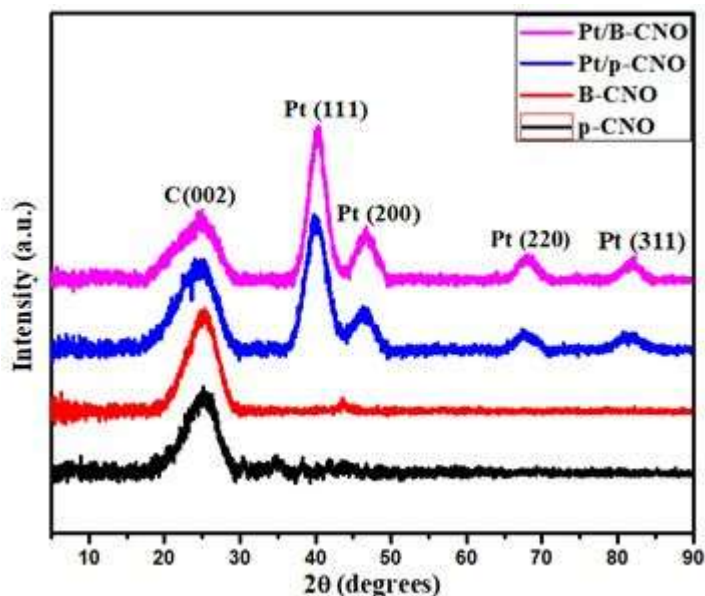


Figure 4.6: X-ray diffractograms of p-CNO, B-CNO, Pt/p-CNO and Pt/B-CNO, nanomaterials.

4.2.7. X-ray photoelectron spectroscopy (XPS)

Fig. S4 (a) demonstrates the full XPS survey spectra of the unwashed B-CNO and unwashed Pt/B-CNO and confirms the existence of C 1s at 284.1 eV, O 1s at 532.0 eV, B 1s at 193 eV, and Pt 4f at 72.7 eV elements in the nanocomposite materials. The elemental composition of B-CNO and unwashed Pt/B-CNO nanomaterials are shown in Table 4.2. In Fig. 4.7 (a), the fitted curves from the high-resolution C1s spectra of B-CNO and Pt/B-CNO nanomaterials at 284.1 eV, 285.0 eV, 286.0 eV, 288.0 eV, and 289.5 eV are assigned to the sp^2 C-C, sp^3 C-C, C-O, C=O, and O-C=O in aromatic rings, respectively [59]. The high-resolution O1s XPS spectra in Fig. 4.7 (b), show deconvoluted peaks at 529.5 eV, 531.7 eV, and 533.1 eV which are attributed to metal oxide, C-O, and C=O, groups respectively [33]. The B 1s XPS spectrum can be deconvoluted into two peaks. (see Fig. 4.7 (c)) [60]. The XPS peak at 193 eV is associated with a B-O bond and its presence is due to

residual B-O bonds (B_2O_3) [50]. A small peak (ca. 3%) at ca 190.5 corresponds to the presence of a B-C bond. This indicates that some B doping of the CNO has occurred in the reaction. As shown in Fig. 4.7 (d) the XPS Pt 4f spectra for the Pt/B-CNO nanomaterial consist of two signals which are ascribed to Pt 4f7/2 and Pt 4f5/2 with the spin-orbit energy splitting of 1.2 eV [61]. These two signals Pt 4f7/2 and Pt 4f5/2 are comprised of two sub-districts, from 69.2 eV to 73.1 eV and 73.3 eV to 79.1 eV BE regions, respectively. The deconvoluted two peaks of the BE Pt 4f7/2 sub-region at 70.6 eV and 72.5 eV correspond to platinum metallic ions (Pt^{0+}) and Pt ions (Pd^{3+}) in a platinum oxide, respectively [62]. Finally, the BE Pt 4f5/2 sub-region is deconvoluted into doublets peaks at 75.4 eV and 76.8 eV which are attributed to Pt ions (Pt^{0+}) and (Pd^{2+}) in Pt oxide [63].

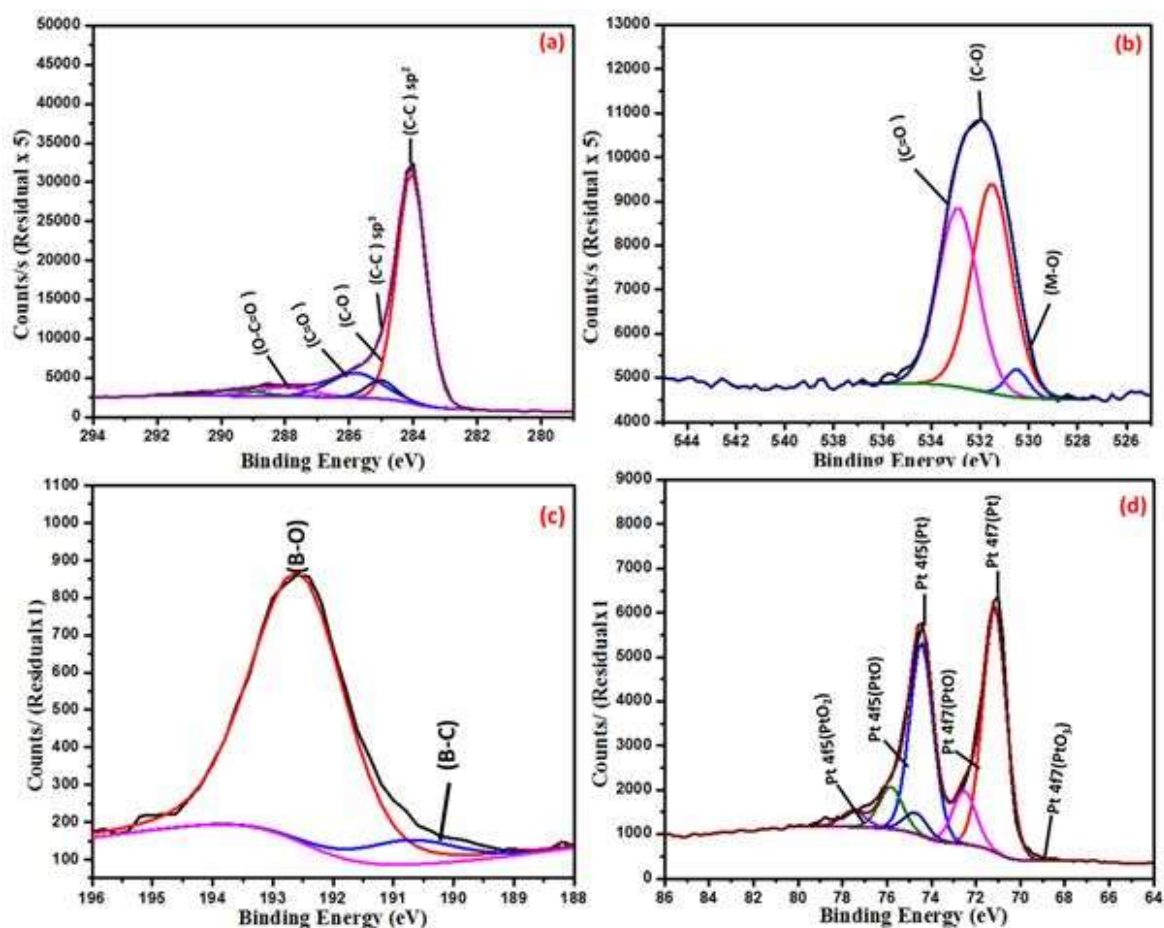


Figure 4.7: XPS spectra (a) C 1s of Pt/B-CNO (b), O 1s of Pt/B-CNO (c) B 1s of Pt/B-CNO and (d) Pt 4f of Pt/B-CNO.

Table 4.2: Elemental composition of B-CNO and Pt/B-CNO obtained from XPS data

Sample	Carbon	Oxygen	Boron	Platinum
B-CNO	82.1	15.4	2.5	0
Pt/B-CNO	78.7	12.8	1.2	6.9

4.2.8. Brunauer-Emmett-Teller Nitrogen adsorption (BET)

Fig. S4 shows the nitrogen adsorption-desorption isotherms and pore size distribution of the synthesized unwashed B-CNO and unwashed Pt/B-CNO nanomaterials and Table 4.3 summarizes the surface areas and pore volumes of the unwashed B-CNO and Pt/B-CNO electrocatalysts. As presented in the table, Pt/B-CNO reveals a higher surface area of 94 m²/g as compared to the B-CNO (72 m²/g) which is due to the presence of platinum nanoparticles dispersed on the B-CNO catalyst support surface. Both B-CNO and Pt/B-CNO materials have micropores and voids (ca. 40 nm).

Table 4.3: BET surface area of unwashed B-CNO and Pt/B-CNO nanomaterial

Sample	Surface area (m ² g ⁻¹)	Pore volume (cm ³ g ⁻¹)
B-CNO	72	0.43
Pt/B-CNO	94	0.78

4.2.9. Summary of findings

The data reveal that the reaction involving B₂O₃ and the CNOs gave CNOs that were modified by the boron. This procedure has been used previously to dope

carbon materials [44]. In this study the procedure led to a mixture of reacted CNOs and B₂O₃. The residual B₂O₃ could readily be removed by hot water washing. This led to a product that was clearly impacted by the reaction of the boron as seen from the Raman, TEM and TGA data. Two possibilities exist – the B only modified the CNO surface and/or the CNO reacted with the B to give a CNO doped or functionalized with boron. It appears that some of the CNO could have reacted with the boron as seen by the small amount of residue left in the TGA experiment after the washing process (< 3% B₂O₃; ca 0.5% B), as confirmed by XPS data. However the amount of B doped is small with most of the B in the form of B₂O₃. For this reason the products are referred to as boron modified CNOs. The Pt was added to the boron modified CNOs and gave the expected Pt/B-CNO materials. The commercial Pt/C, Pt/p-CNO, unwashed (uw) Pt/B-CNO, and washed (w) Pt/B-CNO electrocatalysts were tested in 0.5 NaOH and 0.5 M NaOH + 1M NH₄OH solutions.

4.2.10. Electrocatalytic behaviour of the nanocatalysts

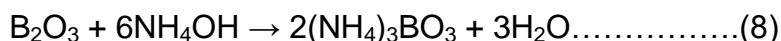
Reactions of B₂O₃ with carbons have been described and the data suggested that the primary role of the B was to generate defected carbon surface. Interactions to give C-O-B or CB bonds at the surface are possible but the literature data suggested unlikely. This is also true from the data generated from the B₂O₃ reaction with the CNOs. XPS and TGA imply little to no reaction of B with the CNOs while the Raman data suggest the formation of a more defective carbon after the reaction (1000 °C for 2 h).

The TGA and Raman data suggest that some B₂O₃ has remained in the B-CNO structure (prior to washing). This suggests that the B₂O₃ which is slightly soluble in cold water could modify the electrochemical reactions performed in water. Reactions were thus carried in B₂O₃ contained in 0.5 M NaOH/1 M NH₄OH to establish the effect of the B₂O₃ on the reaction.

Boron trioxide reacts with sodium hydroxide to produce sodium tetraborate and water. Sodium hydroxide - diluted solution. Crystallization of the product confirms Na₂B₄O₇ is produced.



Boron trioxide reacts with 1 M ammonium hydroxide to produce ammonium borate and water.



4.2.11. Electrochemical surface area (ECSA)

Cyclic voltammetry (CV) curves were used to measure the electrochemical active surface area (ECSA) of Pt/C, Pt/p-CNO, Pt/B-CNOuw, and Pt/B-CNOw electrocatalysts in 0.5 M NaOH at a scan rate of 50 mVs⁻¹ in the potential range -0.8 to 0.4 E/ V vs Ag/AgCl (Fig. 4.8 (a)). The voltammograms are very similar and correspond to the typical voltammogram of Pt nanoparticles in alkaline medium [64]. All the CV curves reveal distinctive potential regions. These are the hydrogen adsorption/desorption region (Q_H) (-0.8 to -0.5 V), the double-layer potential region (-0.5 to -0.1 V), the Pt oxidation region (-0.06 to 0.4 V), PtO reduction region (-0.16 to -0.43 V) and the hydrogen evolution region (-0.8 V) [65]. The proton adsorption/desorption peaks observed between -0.8 to -0.5 V are typically ascribed to the sorption hydrogen species bonded to polycrystalline Pt [66] as confirmed by TEM, EDS, XRD, and XPS studies. The current density is the current set per unit geometric area of the electrode. The ECSA of the prepared electrocatalysts was calculated from the potentiodynamic curve by integrating the coulombic charge response in the hydrogen adsorption/desorption region (-0.8 to -0.5 V) and was used to normalize the currents for the ammonia oxidation reaction (AOR) in alkaline electrolyte. The ECSA of Pt-based electrocatalysts was calculated from the CV curves by employing equation 9:

$$ECSA\ OF\ Pt[m^2\ g^{-1}] = \frac{Q_H[mC]}{Q_{density}[mC\ cm^{-2}] \times L_{metal}[mg]} \quad (9)$$

where Q_H is the charge for the hydrogen adsorption/desorption, Q_{density} is the specific charge for a hydrogen monolayer on Pt (0.21 mC cm⁻²), L_{metal} is the metal loading (mg) [67] estimated from TGA.

The ECSA of Pt/B-CNOuw electrocatalyst was determined to be 44.35 m² g⁻¹ which is higher than that for Pt/B-CNOw (39.16 m² g⁻¹), Pt/p-CNO (32.93 m² g⁻¹)

and the Pt/C electrocatalysts ($28.01 \text{ m}^2 \text{ g}^{-1}$). The higher ECSA value for the Pt/B-CNOuw indicates that the Pt nanocatalyst is a better catalyst than Pt/B-CNOw, Pt/p-CNO and Pt/C. are shown in Table 4.4.

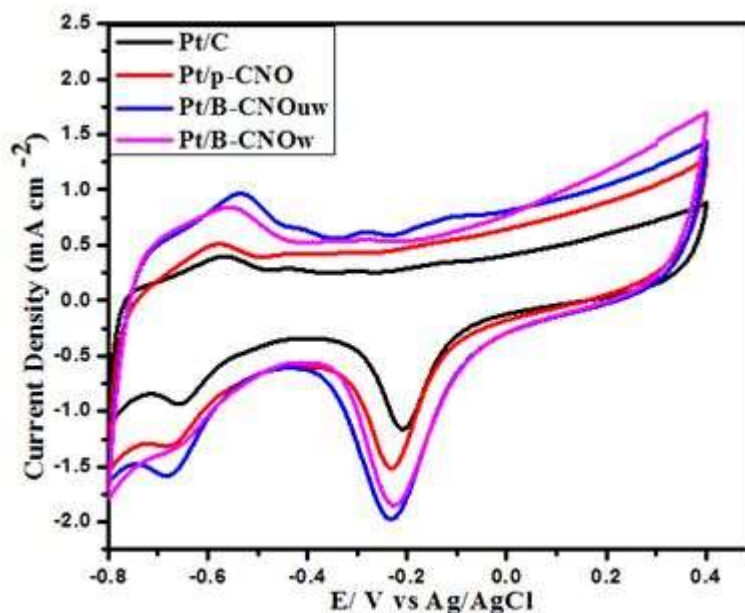


Figure 4.8: (a) CV curves of Pt/C, Pt/p-CNO, Pt/B-CNOuw and Pt/B-CNOw modified electrodes in 0.5 M NaOH solution at scan rate 50 mV s^{-1} .

Table 4.4: Charge for the hydrogen adsorption, platinum loading and the electrochemical active surface area

Nanocatalysts	Charge [mC]	Pt loading [g]	ECSA [m^2g^{-1}]
Pt/B-CNOuw	0.652	0.070	44.35
Pt/B-CNOw	0.574	0.071	39.16
Pt/p-CNO	0.498	0.072	32.93
Pt/C	0.453	0.077	28.01

Fig. 4.9 shows the CV curves for the Pt/C, Pt/p-CNO, Pt/B-CNOuw, and Pt/B-CNOw electrocatalysts in 0.5 M NaOH + 1 M NH_4OH solution at a scan rate of 50

mV s⁻¹. There is a comparative resemblance seen for all CV curves, i.e., an anodic current peak observed at -0.32 V to -0.04 V (Ag/AgCl), which is accredited to the electro-oxidation of ammonia to nitrogen [68]. The shape of the CV curves in the ammonia oxidation reaction (AOR) is similar to the ones reported for PtAu/C nanocatalysts synthesized using the borohydride reduction method [24]. The currents of the Pt GC modified electrodes were normalized by ECSA. It will be noticed that the current densities consider the ECSA determined to form the hydrogen adsorption-desorption region which tests the existence of platinum [69]. The onset potential of the Pt/B-CNO_{uw} (-0.384 V vs Ag| AgCl) electrocatalysts for AOR is lower as compared to the Pt/B-CNO_w (-0.365 V vs Ag| AgCl), Pt/p-CNO (-0.369 V vs Ag|AgCl) and commercial Pt/C (-0.358 V vs Ag|AgCl) electrocatalysts, showing that the boron oxide inhibits the electro-oxidation of ammonia at lower potentials [70]. As can be seen from the CV curves in Fig. 4.9, the current densities follow the order Pt/B-CNO_{uw} GC (0.20 mA cm⁻²) > Pt/B-CNO_w GC (0.17 mA cm⁻²) > Pt/p-CNO (0.13 mA cm⁻²) > Pt/C GC (0.11 mA cm⁻²). The superior electrocatalytic performance of the B-CNO_{uw} decorated Pt NPs is mainly attributed to an increase of the electronic conductivity of the carbon nano onions by boron oxide, the high electrochemical accessible area and the enhancement of the interaction with water due to the boron on the support, which could contribute to the oxidation of intermediate products from the ammonia electro-oxidation reaction[15]. Also, this improvement was due to a higher number of edge-plane sites and oxygen-contained functional groups introduced on the surface of the B-CNO_{uw} support material [71]. Moreover, the porous nature, degree of graphitization and the high specific surface area of the B-CNOs enhances the dispersion and platinum particle size [44,72]. Comparative electrocatalytic activity of our synthesized electrocatalysts with other similar Pt-based electrocatalysts for ammonia oxidation reactions in alkaline conditions are shown in Table 4.5. It is evident that the B-CNO electrocatalyst exhibits lower catalytic performance towards AOR when compared to the other electrocatalysts listed.

Table 4.5: Comparison of the current density for unwashed Pt/B-CNO, washed Pt/B-CNO and Pt/p-CNO against other Pt/C nanocatalysts for ammonia oxidation reactions

Nanocatalysts	Fuel (M)	Electrolyte (M)	CD (mA cm^{-2})	Ref.
Pt/B-CNOuw	1 NH_4OH	0.5 NaOH	0.20	This work
Pt/B-CNOw	1 NH_4OH	0.5 NaOH	0.17	This work
Pt/p-CNO	1 NH_4OH	0.5 NaOH	0.13	This work
Pt-BDD	0.1 NH_3	0.2 NaOH	0.22	[31]
Pt/MPC	1 NH_4OH	0.5 H_2SO_4	0.19	[73]
Pt/C nanocubes	0.1 NH_3	0.1 M KOH	0.25	[74]
Pt/RGO	1 NH_4OH	0.5 H_2SO_4	0.27	[75]

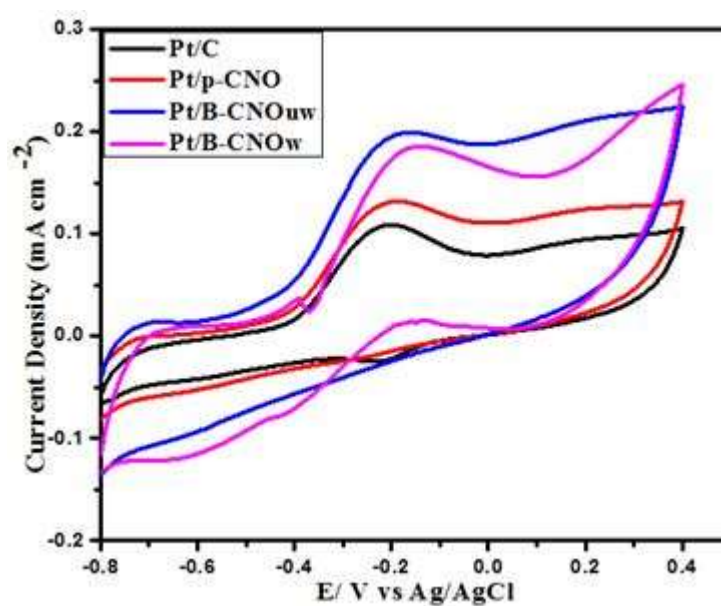


Figure 4.9: (a) CV curves for Pt/C, Pt/p-CNO, Pt/B-CNOuw and Pt/B-CNOw modified electrodes in 0.5 M NaOH + 1M NH_4OH at a scan rate of 50 mV s^{-1} .

4.2.12. Chronoamperometry (CA)

The stability study of the Pt/C, Pt/p-CNO, and Pt/B-CNOuw, Pt/B-CNOw nanocatalysts was performed using CA after 2000 s. Fig. 4.10 reveals current-time responses for the three-platinum based electrocatalysts in 0.5 M NaOH + 1M NH₄OH solution for an applied potential of -0.30 V. The current density values of the Pt/C, Pt/p-CNO and Pt/B-CNOuw, Pt/B-CNOw nanocatalysts are 0.07 mA cm⁻², 0.09 mA cm⁻², 0.11 mA cm⁻², and 0.14 mA cm⁻² respectively. The introduction of boron oxide nanoparticles onto the surface of the CNO supported Pt NPs in alkaline ammonia oxidation reactions improved the electrocatalytic stability and poison tolerance [76]. These results confirm that the boron oxide modification produced boron-containing species that bonded strongly with the poisoning nitrogenous intermediates, and thus that the Pt/B-CNOuw was not deactivated by the N_{ads} species as compared to the Pt/B-CNOw, Pt/C and Pt/p-CNO electrocatalysts [77].

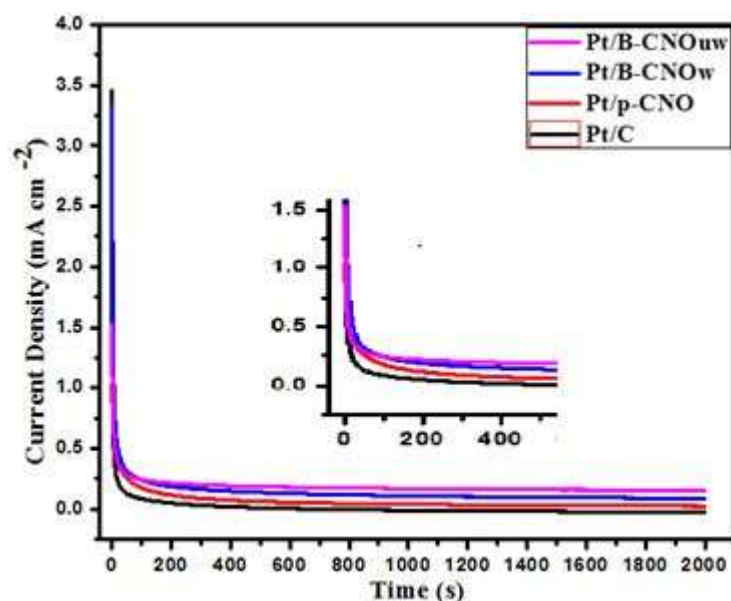


Figure 4.10: (a) chronoamperometric curves for Pt/C, Pt/p-CNO, Pt/B-CNOuw and Pt/B-CNOw modified electrodes in 0.5 M NaOH + 1M NH₄OH for an applied potential of -0.30 V.

4.2.13. Electrochemical impedance spectroscopy (EIS)

EIS was used to evaluate the electron-transfer kinetics and intrinsic behavior of the Pt-based electrocatalysts in the ammonia oxidation reaction in alkaline conditions. The Nyquist plots of the Pt/C, Pt/p-CNO, Pt/B-CNO_w, and Pt/B-CNO_w nanocatalysts in 0.5 M NaOH + 1M NH₄OH solution at the constant potential of -0.2 V are presented in Fig. 4.11. The Nyquist plots contained an impedance arc in the frequency range from 0.005 Hz to 1000 kHz. The equivalent circuit which was fitted using Zview software to the EIS data are shown in Fig. 4.11(b) in which the CPE represents the constant phase element, R_{ct} represents the charge-transfer resistance, R_s represents the solution resistance and Z_w represents the Warburg impedance for the electrocatalytic oxidation of ammonia in alkaline media [78]. A smaller impedance arc diameter indicates a smaller charge transport resistance and better electrocatalytic performance [79]. The electrocatalyst with small Pt NPs had the smallest R_{ct} value at 0.2 V, which agrees with the higher electrocatalytic performance seen in both the chronoamperometry and cyclic voltammetry studies. The EIS equivalent circuit parameters are summarized in Table 4.6. As is shown in Fig. 4.11 (a), the R_{ct} value for Pt/B-CNO_w is relatively smaller than that of Pt/B-CNO_w, Pt/p-CNO and Pt/C indicating the fastest reaction kinetic towards electro-oxidation of ammonia in alkaline electrolyte. These results distinctly show that boron oxide modification enhances the electrical conductivity and charge transfer reactions [80,81].

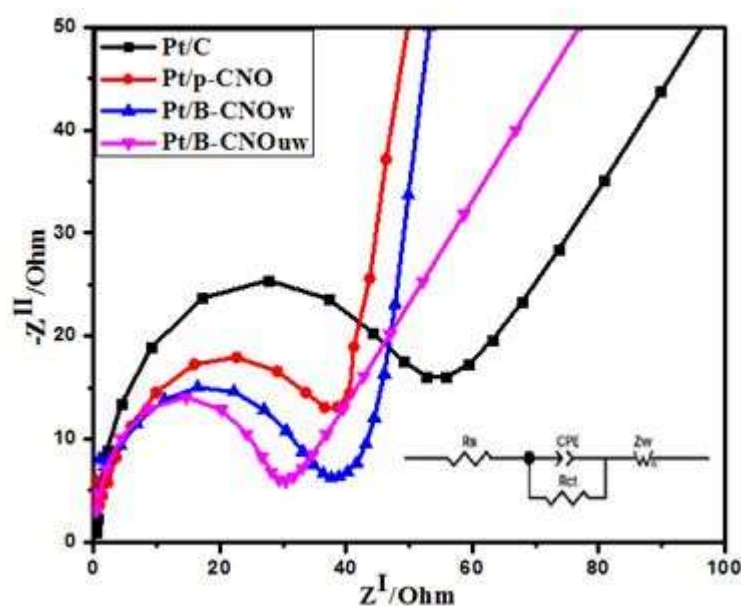


Figure 4.11: Nyquist plots of Pt/C, Pt/p-CNO, Pt/B-CNOuw and Pt/B-CNOw modified GC electrode in (a) in 0.5 M NaOH + 1M NH₄OH and the equivalent circuit diagram.

Table 4.6: The EIS circuit parameters of Pt/C, Pt/p-CNO, Pt/B-CNOuw and Pt/B-CNOw nanocatalysts

0.5 M NaOH + 1 M NH ₄ OH				
Nanocatalysts	R_s (<i>Ohm</i>)	R_{ct} (<i>Ohm</i>)	CPE (μF)	Z_w ($\Omega s^{-1/2}$)
Pt/C	25.4± 0.28	54.5± 0.98	110.5± 4.22	7.0E-06
Pt/p-CNO	21.6± 0.25	38.1± 1.06	136.7± 3.13	4.0E-06
Pt/B-CNOuw	14.3± 0.22	29.7± 1.47	152.4± 2.96	2.0E-06
Pt/B-CNOw	19.4±0.26	38.5±1.21	143.2± 4.07	5.0E-06

Conclusions

In summary, boron oxide modified carbon nano onions have been synthesized via the CVD method using boric acid. Highly dispersed Pt nanoparticles decorated on pristine, and boron oxide modified CNOs were successfully prepared using the ethylene glycol reduction method. The as-obtained Pt/p-CNO, Pt/B-CNOuw, and Pt/B-CNOw nanocatalysts revealed network structure, extraordinary distribution, and smaller Pt NPs size to provide the abundance of active sites to show electrocatalytic performances. The Pt/B-CNOuw electrocatalysts showed higher ECSA when compared to the Pt/B-CNOw, Pt/p-CNO and Pt/C, due to the existence of boron atoms on the p-CNO structure, improving the number of active sites for attachment and nucleation of Pt nanoparticles. Regardless of the greater

ECSA of Pt/B-CNO_{uw}, its electrocatalytic activity, stability and charge electron transfer toward ammonia oxidation was excellent as compared to the Pt/B-CNO_w, Pt/p-CNO and Pt/C nanocatalysts. The comparable AOR performance of Pt/B-CNO_{uw} nanocatalysts with Pt/B-CNO_w, Pt/p-CNO and commercial Pt/C suggests that it could replace the expensive 10% Pt/C nanocatalysts in fuel cells in the future.

Acknowledgments

This work is based on the research supported in part by the National Research Foundation (NRF) of South Africa (Grant Numbers: 118137, 118148), the University of the Witwatersrand (Postgraduate Merit Award, University Research Council) and a NRF-DAAD grant (Grant number: 117841). The authors also acknowledge the efforts and support provided by the University of Johannesburg (Faculty of Science, University Research Council, and Centre for Nanomaterials Science Research). We also wish to acknowledge Mr. Siyasanga Mpelane at the University of Johannesburg (Auckland Park) for the high magnification TEM data and Dr Boitumelo Matsoso for data discussions.

References

- [1] A. Brouzgou, S.Q. Song, P. Tsiakaras, Low and non-platinum electrocatalysts for PEMFCs: Current status, challenges and prospects, *Appl. Catal. B Environ.* 127 (2012) 371–388. <https://doi.org/10.1016/j.apcatb.2012.08.031>.
- [2] S. Eris, Z. Daşdelen, F. Sen, Enhanced electrocatalytic activity and stability of monodisperse Pt nanocomposites for direct methanol fuel cells, *J. Colloid Interface Sci.* 513 (2018) 767–773. <https://doi.org/10.1016/j.jcis.2017.11.085>.
- [3] A. Zadick, L. Dubau, K. Artyushkova, A. Serov, P. Atanassov, M. Chatenet, Nickel-based electrocatalysts for ammonia borane oxidation: enabling materials for

carbon-free-fuel direct liquid alkaline fuel cell technology, *Nano Energy*. 37 (2017) 248–259. <https://doi.org/10.1016/j.nanoen.2017.05.035>.

[4] A.O. Neto, R.R. Dias, M.M. Tusi, M. Linardi, E. V. Spinacé, Electro-oxidation of methanol and ethanol using PtRu/C, PtSn/C and PtSnRu/C electrocatalysts prepared by an alcohol-reduction process, *J. Power Sources*. 166 (2007) 87–91. <https://doi.org/10.1016/j.jpowsour.2006.12.088>.

[5] D. Akinyele, E. Olabode, A. Amole, Review of fuel cell technologies and applications for sustainable microgrid systems, *Inventions*. 5 (2020) 1–35. <https://doi.org/10.3390/inventions5030042>.

[6] G. Merle, M. Wessling, K. Nijmeijer, Anion exchange membranes for alkaline fuel cells: A review, *J. Memb. Sci.* 377 (2011) 1–35. <https://doi.org/10.1016/j.memsci.2011.04.043>.

[7] H. Zhang, G. Lin, J. Chen, The performance analysis and multi-objective optimization of a typical alkaline fuel cell, *Energy*. 36 (2011) 4327–4332. <https://doi.org/10.1016/j.energy.2011.04.009>.

[8] Y. Zhao, B.P. Setzler, J. Wang, J. Nash, T. Wang, B. Xu, Y. Yan, An Efficient Direct Ammonia Fuel Cell for Affordable Carbon-Neutral Transportation, *Joule*. 3 (2019) 2472–2484. <https://doi.org/10.1016/j.joule.2019.07.005>.

[9] K. Ryu, G.E. Zacharakis-Jutz, S.C. Kong, Performance enhancement of ammonia-fueled engine by using dissociation catalyst for hydrogen generation, *Int. J. Hydrogen Energy*. 39 (2014) 2390–2398. <https://doi.org/10.1016/j.ijhydene.2013.11.098>.

[10] R. Lan, S. Tao, Ammonia as a suitable fuel for fuel cells, *Front. Energy Res.* 2 (2014). <https://doi.org/10.3389/fenrg.2014.00035>.

[11] F.J. Vidal-Iglesias, J. Solla-Gullón, V. Montiel, J.M. Feliu, A. Aldaz, Screening of electrocatalysts for direct ammonia fuel cell: Ammonia oxidation on PtMe (Me: Ir, Rh, Pd, Ru) and preferentially oriented Pt(1 0 0) nanoparticles, *J.*

Power Sources. 171 (2007) 448–456.
<https://doi.org/10.1016/j.jpowsour.2007.06.015>.

[12] J.N. Renner, L.F. Greenlee, A.M. Herring, K.E. Ayers, Electrochemical synthesis of ammonia: A low pressure, low temperature approach, *Electrochem. Soc. Interface*. 24 (2015) 51–57. <https://doi.org/10.1149/2.F04152if>.

[13] R. Acevedo, C.M. Poventud-Estrada, C. Morales-Navas, R.A. Martínez-Rodríguez, E. Ortiz-Quiles, F.J. Vidal-Iglesias, J. Sollá-Gullón, E. Nicolau, J.M. Feliu, L. Echegoyen, C.R. Cabrera, Chronoamperometric Study of Ammonia Oxidation in a Direct Ammonia Alkaline Fuel Cell under the Influence of Microgravity, *Microgravity Sci. Technol.* 29 (2017) 253–261. <https://doi.org/10.1007/s12217-017-9543-z>.

[14] A. Allagui, M. Oudah, X. Tuae, S. Ntais, F. Almomani, E.A. Baranova, Ammonia electro-oxidation on alloyed PtIr nanoparticles of well-defined size, *Int. J. Hydrogen Energy*. 38 (2013) 2455–2463. <https://doi.org/10.1016/j.ijhydene.2012.11.079>.

[15] V.A. Ribeiro, I.C. de Freitas, A.O. Neto, E. V. Spinacé, J.C.M. Silva, Platinum nanoparticles supported on nitrogen-doped carbon for ammonia electro-oxidation, *Mater. Chem. Phys.* 200 (2017) 354–360. <https://doi.org/10.1016/j.matchemphys.2017.07.088>.

[16] V. Rosca, M.T.M. Koper, Electrocatalytic oxidation of ammonia on Pt(111) and Pt(100) surfaces, *Phys. Chem. Chem. Phys.* 8 (2006) 2513–2524. <https://doi.org/10.1039/b601306f>.

[17] H.S. Pillai, H. Xin, New Insights into Electrochemical Ammonia Oxidation on Pt(100) from First Principles, *Ind. Eng. Chem. Res.* 14 (2019). <https://doi.org/10.1021/acs.iecr.9b01471>.

[18] D. Skachkov, C. Venkateswara Rao, Y. Ishikawa, Combined first-principles molecular dynamics/density functional theory study of ammonia electrooxidation

on Pt(100) electrode, *J. Phys. Chem. C.* 117 (2013) 25451–25466. <https://doi.org/10.1021/jp4048874>.

[19] V. Rosca, M. Duca, M.T. DeGroot, M.T.M. Koper, Nitrogen Cycle Electrocatalysis, *Chem. Rev.* 109 (2009) 2209–2244. <https://doi.org/10.1021/cr8003696>.

[20] H. Gerischer, A. Mauerer, Untersuchungen Zur anodischen Oxidation von Ammoniak an Platin-Elektroden, *J. Electroanal. Chem.* 25 (1970) 421–433. [https://doi.org/10.1016/S0022-0728\(70\)80103-6](https://doi.org/10.1016/S0022-0728(70)80103-6).

[21] J. Yang, H. Muroyama, T. Matsui, K. Eguchi, Development of a direct ammonia-fueled molten hydroxide fuel cell, *J. Power Sources.* 245 (2014) 277–282. <https://doi.org/10.1016/j.jpowsour.2013.06.143>.

[22] T.L. Lomocso, E.A. Baranova, Electrochemical oxidation of ammonia on carbon-supported bi-metallic PtM (M = Ir, Pd, SnOx) nanoparticles, *Electrochim. Acta.* 56 (2011) 8551–8558. <https://doi.org/10.1016/j.electacta.2011.07.041>.

[23] C.M. Hung, Electrochemical properties of PtPdRh alloy catalysts for ammonia electrocatalytic oxidation, *Int. J. Hydrogen Energy.* 37 (2012) 13815–13821. <https://doi.org/10.1016/j.ijhydene.2012.03.147>.

[24] J.C.M. Silva, S.G. Da Silva, R.F.B. De Souza, G.S. Buzzo, E. V. Spinacé, A.O. Neto, M.H.M.T. Assumpção, PtAu/C electrocatalysts as anodes for direct ammonia fuel cell, *Appl. Catal. A Gen.* 490 (2015) 133–138. <https://doi.org/10.1016/j.apcata.2014.11.015>.

[25] R. Lan, J.T.S. Irvine, S. Tao, Ammonia and related chemicals as potential indirect hydrogen storage materials, *Int. J. Hydrogen Energy.* 37 (2012) 1482–1494. <https://doi.org/10.1016/j.ijhydene.2011.10.004>.

[26] M.H.M.T. Assumpção, R.M. Piasentin, P. Hammer, R.F.B. De Souza, G.S. Buzzo, M.C. Santos, E. V. Spinacé, A.O. Neto, J.C.M. Silva, Oxidation of ammonia using PtRh/C electrocatalysts: Fuel cell and electrochemical evaluation, *Appl.*

Catal. B Environ. 174–175 (2015) 136–144.
<https://doi.org/10.1016/j.apcatb.2015.02.021>.

[27] Y. Lu, S. Du, R. Steinberger-Wilckens, One-dimensional nanostructured electrocatalysts for polymer electrolyte membrane fuel cells—A review, *Appl. Catal. B Environ.* 199 (2016) 292–314.
<https://doi.org/10.1016/j.apcatb.2016.06.022>.

[28] Z. Liang, W. Guo, R. Zhao, T. Qiu, H. Tabassum, R. Zou, Engineering atomically dispersed metal sites for electrocatalytic energy conversion, *Nano Energy*. 64 (2019) 103917. <https://doi.org/10.1016/j.nanoen.2019.103917>.

[29] P.Y. You, S.K. Kamarudin, Recent progress of carbonaceous materials in fuel cell applications: An overview, *Chem. Eng. J.* 309 (2017) 489–502.
<https://doi.org/10.1016/j.cej.2016.10.051>.

[30] L. Cunci, C.A. Velez, I. Perez, A. Suleiman, E. Larios, M. José-Yacamán, J.J. Watkins, C.R. Cabrera, Platinum electrodeposition at unsupported electrochemically reduced nanographene oxide for enhanced ammonia oxidation, *ACS Appl. Mater. Interfaces*. 6 (2014) 2137–2145.
<https://doi.org/10.1021/am4052552>.

[31] Y. Hernández-Lebrón, L. Cunci, C.R. Cabrera, Ammonia oxidation at electrochemically platinum-modified microcrystalline and polycrystalline boron-doped diamond electrodes, *Electrocatalysis*. 7 (2016) 184–192.
<https://doi.org/10.1007/s12678-015-0295-5>.

[32] K. Chatterjee, M. Ashokkumar, H. Gullapalli, Y. Gong, Nitrogen-rich carbon nano-onions for oxygen reduction reaction, *Carbon N. Y.* 130 (2018) 645–651.
<https://doi.org/10.1016/j.carbon.2018.01.052>.

[33] D. Santiago, G.G. Rodríguez-Calero, A. Palkar, D. Barraza-Jimenez, D.H. Galvan, G. Casillas, A. Mayoral, M. Jose-Yacamán, L. Echegoyen, C.R. Cabrera, Platinum electrodeposition on unsupported carbon nano-onions, *Langmuir*. 28 (2012) 17202–17210. <https://doi.org/10.1021/la3031396>.

- [34] V.N. Khabashesku, M.X. Pulikkathara, Chemical modification of carbon nanotubes, *Mendeleev Commun.* 16 (2006) 61–66. <https://doi.org/10.1070/MC2006v016n02ABEH002316>.
- [35] M. Vijayakumar, G. Hirankumar, M.S. Bhuvaneshwari, S. Selvasekarapandian, Influence of B₂O₃ doping on conductivity of LiTiO₂ electrode material, *J. Power Sources.* 117 (2003) 143–147. [https://doi.org/10.1016/S0378-7753\(03\)00110-1](https://doi.org/10.1016/S0378-7753(03)00110-1).
- [36] S.-H. Han, J.H. Song, T. Yim, Y.-J. Kim, J.-S. Yu, S. Yoon, Communication—Improvement of Structural Stability during High-Voltage Cycling in High-Nickel Cathode Materials with B₂O₃ Addition, *J. Electrochem. Soc.* 163 (2016) A748–A750. <https://doi.org/10.1149/2.1011605jes>.
- [37] X. Liu, H. Luo, Y. Lei, A. Lu, Effect of B₂O₃ Addition on Structure and Properties of SiO₂–R₂O–BaO–ZnO Glasses, *Mater. Focus.* 2 (2013) 125–130. <https://doi.org/10.1166/mat.2013.1063>.
- [38] A. Zhou, W. Wang, Q. Liu, Y. Wang, X. Yao, F. Qing, E. Li, T. Yang, L. Zhang, J. Li, Stable, fast and high-energy-density LiCoO₂ cathode at high operation voltage enabled by glassy B₂O₃ modification, *J. Power Sources.* 362 (2017) 131–139. <https://doi.org/10.1016/j.jpowsour.2017.06.050>.
- [39] J. Li, Z. Liu, Y. Wang, R. Wang, Investigation of facial B₂O₃ surface modification effect on the cycling stability and high-rate capacity of LiNi_{1/3}Co_{1/3}Mn_{1/3}O₂ cathode, *J. Alloys Compd.* 834 (2020) 155150. <https://doi.org/10.1016/j.jallcom.2020.155150>.
- [40] N.G. Tsierkezos, U. Ritter, Y.N. Thaha, C. Downing, Application of multi-walled carbon nanotubes modified with boron oxide nanoparticles in electrochemistry, *Ionics (Kiel).* 21 (2015) 3087–3095. <https://doi.org/10.1007/s11581-015-1496-x>.
- [41] N.S. Saetova, A.A. Raskovalov, B.D. Antonov, T. V. Yaroslavtseva, O.G. Reznitskikh, N.I. Kadyrova, The influence of lithium oxide concentration on the

transport properties of glasses in the Li₂O-B₂O₃-SiO₂ system, *J. Non. Cryst. Solids.* 443 (2016) 75–81. <https://doi.org/10.1016/j.jnoncrysol.2016.04.025>.

[42] L.L. Sikeyi, T.D. Ntuli, T.H. Mongwe, N.W. Maxakato, E. Carleschi, B.P. Doyle, N.J. Coville, M.S. Maubane-Nkadimeng, Microwave assisted synthesis of nitrogen doped and oxygen functionalized carbon nano onions supported palladium nanoparticles as hybrid anodic electrocatalysts for direct alkaline ethanol fuel cells, *Int. J. Hydrogen Energy.* 46 (2021) 10862–10875. <https://doi.org/10.1016/j.ijhydene.2020.12.154>.

[43] L.L. Sikeyi, T. Matthews, A.S. Adekunle, N.W. Maxakato, Electro-oxidation of Ethanol and Methanol on Pd/C, Pd/CNFs and Pd–Ru/CNFs Nanocatalysts in Alkaline Direct Alcohol Fuel Cell, *Electroanalysis.* 32 (2020) 2681–2692. <https://doi.org/10.1002/elan.202060260>.

[44] Y. Lin, Y. Zhu, B. Zhang, Y.A. Kim, M. Endo, D.S. Su, substitutional boron : the relationship between electronic properties and catalytic performance, *J. Mater. Chem. A.* 3 (2015) 21805–21814. <https://doi.org/10.1039/c5ta03141a>.

[45] V. Mashindi, P. Mente, N. Mpofo, T.N. Phaahlamohlaka, O. Makgae, A.I. Kirkland, R. Forbes, K.I. Ozoemena, P.B. Levecque, N.J. Coville, Platinum supported on pristine and nitrogen-doped bowl-like broken hollow carbon spheres as oxygen reduction reaction catalysts, *J. Appl. Electrochem.* 51 (2021) 991–1008. <https://doi.org/10.1007/s10800-021-01554-0>.

[46] S.S. Gwebu, P.N. Nomngongo, P.N. Mashazi, T. Nyokong, N.W. Maxakato, Platinum nanoparticles supported on Carbon nanodots as anode catalysts for direct alcohol fuel cells, *Int. J. Electrochem. Sci.* 12 (2017) 6365–6378. <https://doi.org/10.20964/2017.07.09>.

[47] D. Mohapatra, S. Badrayyana, S. Parida, Facile wick-and-oil flame synthesis of high-quality hydrophilic onion-like carbon nanoparticles, *Mater. Chem. Phys.* 174 (2016) 112–119. <https://doi.org/10.1016/j.matchemphys.2016.02.057>.

[48] T.H. Han, D. Mohapatra, N. Mahato, S. Parida, J.H. Shim, A.T.N. Nguyen, V.Q. Nguyen, M.H. Cho, J.J. Shim, Effect of nitrogen doping on the catalytic

activity of carbon nano-onions for the oxygen reduction reaction in microbial fuel cells, *J. Ind. Eng. Chem.* 81 (2020) 269–277. <https://doi.org/10.1016/j.jiec.2019.09.014>.

[49] A. Camisasca, A. Sacco, R. Brescia, S. Giordani, Boron/Nitrogen-Codoped Carbon Nano-Onion Electrocatalysts for the Oxygen Reduction Reaction, *ACS Appl. Nano Mater.* 1 (2018) 5763–5773. <https://doi.org/10.1021/acsanm.8b01430>.

[50] O. Mykhailiv, K. Brzezinski, B. Sulikowski, Z. Olejniczak, M. Gras, G. Lota, A. Molina-Ontoria, M. Jakubczyk, L. Echegoyen, M.E. Plonska-Brzezinska, Boron-Doped Polygonal Carbon Nano-Onions: Synthesis and Applications in Electrochemical Energy Storage, *Chem. - A Eur. J.* 23 (2017) 7132–7141. <https://doi.org/10.1002/chem.201700914>.

[51] Y. Lin, Y. Zhu, B. Zhang, Y.A. Kim, M. Endo, D.S. Su, Boron-doped onion-like carbon with enriched substitutional boron: The relationship between electronic properties and catalytic performance, *J. Mater. Chem. A.* 3 (2015) 21805–21814. <https://doi.org/10.1039/c5ta03141a>.

[52] Z.N. Tetana, S.D. Mhlanga, N.J. Coville, Chemical vapour deposition syntheses and characterization of boron-doped hollow carbon spheres, *Diam. Relat. Mater.* 74 (2017) 70–80. <https://doi.org/10.1016/j.diamond.2017.02.005>.

[53] F. Sevim, F. Demir, M. Bilen, H. Okur, Kinetic analysis of thermal decomposition of boric acid from thermogravimetric data, *Korean J. Chem. Eng.* 23 (2006) 736–740. <https://doi.org/10.1007/BF02705920>.

[54] A. Harley-Trochimczyk, T. Pham, J. Chang, E. Chen, M.A. Worsley, A. Zettl, W. Mickelson, R. Maboudian, Platinum Nanoparticle Loading of Boron Nitride Aerogel and Its Use as a Novel Material for Low-Power Catalytic Gas Sensing, *Adv. Funct. Mater.* 26 (2016) 433–439. <https://doi.org/10.1002/adfm.201503605>.

[55] Y. Ma, C. Ricciuti, T. Miller, J. Kadlowec, H. Pearlman, Enhanced catalytic combustion using sub-micrometer and nano-size platinum particles, *Energy and Fuels.* 22 (2008) 3695–3700. <https://doi.org/10.1021/ef800327m>.

- [56] O.A. Baturina, S.R. Aubuchon, K.J. Wynne, Thermal stability in air of Pt/C catalysts and PEM fuel cell catalyst layers, *Chem. Mater.* 18 (2006) 1498–1504. <https://doi.org/10.1021/cm052660e>.
- [57] V. Dhand, J.S. Prasad, M.V. Rao, S. Bharadwaj, Flame synthesis of carbon nano onions using liquefied petroleum gas without catalyst, *Mater. Sci. Eng. C* 33 (2013). <https://doi.org/10.1016/j.msec.2012.10.029>.
- [58] V.K. Puthiyapura, W.F. Lin, A.E. Russell, D.J.L. Brett, C. Hardacre, Effect of Mass Transport on the Electrochemical Oxidation of Alcohols Over Electrodeposited Film and Carbon-Supported Pt Electrodes, *Top. Catal.* 61 (2018) 240–253. <https://doi.org/10.1007/s11244-018-0893-6>.
- [59] D. Mohapatra, O. Muhammad, M.S. Sayed, S. Parida, J.-J. Shim, In situ nitrogen-doped carbon nano-onions for ultrahigh-rate asymmetric supercapacitor, *Electrochim. Acta.* 331 (2020) 135363. <https://doi.org/10.1016/j.electacta.2019.135363>.
- [60] T.J. Li, M.H. Yeh, W.H. Chiang, Y.S. Li, G.L. Chen, Y.A. Leu, T.C. Tien, S.C. Lo, L.Y. Lin, J.J. Lin, K.C. Ho, Boron-doped carbon nanotubes with uniform boron doping and tunable dopant functionalities as an efficient electrocatalyst for dopamine oxidation reaction, *Sensors Actuators, B Chem.* 248 (2017) 288–297. <https://doi.org/10.1016/j.snb.2017.03.118>.
- [61] J. Yang, S.H. Kim, S.K. Kwak, H.K. Song, Curvature-Induced Metal-Support Interaction of an Islands-by-Islands Composite of Platinum Catalyst and Carbon Nano-onion for Durable Oxygen Reduction, *ACS Appl. Mater. Interfaces.* 9 (2017) 23302–23308. <https://doi.org/10.1021/acsami.7b04410>.
- [62] F.E. López-Suárez, C.T. Carvalho-Filho, A. Bueno-López, J. Arboleda, A. Echavarría, K.I.B. Eguiluz, G.R. Salazar-Banda, Platinum-tin/carbon catalysts for ethanol oxidation: Influence of Sn content on the electroactivity and structural characteristics, *Int. J. Hydrogen Energy.* 40 (2015) 12674–12686. <https://doi.org/10.1016/j.ijhydene.2015.07.135>.

- [63] C. Jackson, G.T. Smith, D.W. Inwood, A.S. Leach, P.S. Whalley, M. Callisti, T. Polcar, A.E. Russell, P. Levecque, D. Kramer, Electronic metal-support interaction enhanced oxygen reduction activity and stability of boron carbide supported platinum, *Nat. Commun.* 8 (2017) 1–11. <https://doi.org/10.1038/ncomms15802>.
- [64] J.R. Barbosa, M.N. Leon, C.M. Fernandes, R.M. Antoniassi, O.C. Alves, E.A. Ponzio, J.C.M. Silva, PtSnO₂/C and Pt/C with preferential (100) orientation: High active electrocatalysts for ammonia electro-oxidation reaction, *Appl. Catal. B Environ.* 264 (2020) 118458. <https://doi.org/10.1016/j.apcatb.2019.118458>.
- [65] F. Chekin, S. Bagheri, S.B. Abd Hamid, Synthesis of Pt doped TiO₂ nanoparticles: Characterization and application for electrocatalytic oxidation of L-methionine, *Sensors Actuators, B Chem.* 177 (2013) 898–903. <https://doi.org/10.1016/j.snb.2012.12.002>.
- [66] S. Grigoriev, E. Lyutikova, S. Martemianov, V. Fateev, C. Lebouin, P. Millet, Palladium-based electrocatalysts for PEM applications, 16th World Hydrog. Energy Conf. 2006, WHEC 2006. 1 (2006) 344–352.
- [67] J. Clavilier, D. Armand, B.L. Wu, Electrochemical study of the initial surface condition of platinum surfaces with (100) and (111) orientations, *J. Electroanal. Chem.* 135 (1982) 159–166. [https://doi.org/10.1016/0022-0728\(82\)90013-4](https://doi.org/10.1016/0022-0728(82)90013-4).
- [68] C. Zhong, W.B. Hu, Y.F. Cheng, On the essential role of current density in electrocatalytic activity of the electrodeposited platinum for oxidation of ammonia, *J. Power Sources.* 196 (2011) 8064–8072. <https://doi.org/10.1016/j.jpowsour.2011.05.058>.
- [69] J. Liu, W. Hu, C. Zhong, Y.F. Cheng, Surfactant-free electrochemical synthesis of hierarchical platinum particle electrocatalysts for oxidation of ammonia, *J. Power Sources.* 223 (2013) 165–174. <https://doi.org/10.1016/j.jpowsour.2012.09.074>.

- [70] S. Xiao, F. Luo, H. Hu, Z. Yang, Boron and nitrogen dual-doped carbon nanospheres for efficient electrochemical reduction of N₂ to NH₃, *Chem. Commun.* 56 (2020) 446–449. <https://doi.org/10.1039/c9cc07708a>.
- [71] A. Shaikh, S. Parida, Facile sonochemical synthesis of highly dispersed ultrafine Pd nanoparticle decorated carbon nano-onions with high metal loading and enhanced electrocatalytic activity, *RSC Adv.* 6 (2016) 83711–83719. <https://doi.org/10.1039/c6ra18190b>.
- [72] Y. Holade, C. Morais, K. Servat, T.W. Napporn, K.B. Kokoh, Enhancing the available specific surface area of carbon supports to boost the electroactivity of nanostructured Pt catalysts, *Phys. Chem. Chem. Phys.* 16 (2014) 25609–25620. <https://doi.org/10.1039/c4cp03851g>.
- [73] C.M. Poventud-Estrada, R. Acevedo, C. Morales, L. Betancourt, D.C. Diaz, M.A. Rodriguez, E. Larios, M. José-Yacaman, E. Nicolau, M. Flynn, C.R. Cabrera, Microgravity Effects on Chronoamperometric Ammonia Oxidation Reaction at Platinum Nanoparticles on Modified Mesoporous Carbon Supports, *Microgravity Sci. Technol.* 29 (2017) 381–389. <https://doi.org/10.1007/s12217-017-9558-5>.
- [74] Y.T. Chan, K. Siddharth, M. Shao, Investigation of cubic Pt alloys for ammonia oxidation reaction, *Nano Res.* 13 (2020) 1920–1927. <https://doi.org/10.1007/s12274-020-2712-1>.
- [75] L. Cunci, C.V. Rao, C. Velez, Y. Ishikawa, C.R. Cabrera, Graphene-Supported Pt, Ir, and Pt-Ir Nanoparticles as Electrocatalysts for the Oxidation of Ammonia, *Electrocatalysis.* 4 (2013) 61–69. <https://doi.org/10.1007/s12678-012-0120-3>.
- [76] I. González-González, Y. Hernández-Lebrón, E. Nicolau, C.R. Cabrera, Ammonia Oxidation Enhancement at Square-Wave Treated Platinum Particle Modified Boron-Doped Diamond Electrodes, *ECS Trans.* 33 (2019) 201–209. <https://doi.org/10.1149/1.3484517>.

- [77] N.J. Bunce, D. Bejan, Mechanism of electrochemical oxidation of ammonia, *Electrochim. Acta.* 56 (2011) 8085–8093. <https://doi.org/10.1016/j.electacta.2011.07.078>.
- [78] E. Hernández-Balaguera, H. Vara, J.L. Polo, An electrochemical impedance study of anomalous diffusion in PEDOT-coated carbon microfiber electrodes for neural applications, *J. Electroanal. Chem.* 775 (2016) 251–257. <https://doi.org/10.1016/j.jelechem.2016.06.007>.
- [79] Y. Yang, S. Yu, L. Gao, X. Wang, S. Yan, The properties of PdRu /C with respect to the electro-oxidation of methanol and ethanol, *Int. J. Electrochem. Sci.* 14 (2019) 1270–1282. <https://doi.org/10.20964/2019.02.50>.
- [80] M. Ullah, E. Ahmed, F. Hussain, A.M. Rana, R. Raza, Electrical conductivity enhancement by boron-doping in diamond using first principle calculations, *Appl. Surf. Sci.* 334 (2015) 40–44. <https://doi.org/10.1016/j.apsusc.2014.07.157>.
- [81] D. Becker, K. Jüttner, The impedance of fast charge transfer reactions on boron doped diamond electrodes, *Electrochim. Acta.* 49 (2003) 29–39. <https://doi.org/10.1016/j.electacta.2003.04.003>.

CHAPTER 5

Efficient electrooxidation of ammonia using platinum supported on titania/sulfur-doped onion like carbon nanoparticles in direct ammonia fuel cells

L.L. Sikeyi, L.R. Bila, T.D. Ntuli, C.T. Selepe, N.W. Maxakato, N.J. Coville, M.S. Maubane-Nkadimeng, Efficient electrooxidation of ammonia using platinum supported on titania / sulfur-doped onion like carbon nanoparticles in direct ammonia fuel cells, *Diam. Relat. Mater.* 132 (2023) 109612. <https://doi.org/10.1016/j.diamond.2022.109612>. Impact factor: 3.804.

1. Sikeyi - Synthesis and characterization, Writing-Original Draft, Validation
2. Bila - Method
3. Ntuli – Data Curation
4. Selepe - Software
5. Maxakato - Resources, Supervision
6. Coville - Reviewing and Editing, Resources, Supervision
7. Maubane-Nkadimeng- Conceptualization, Resources, Supervision

Ludwe L Sikeyi^a, Laercia R Bila^a, Themba D Ntuli^a, Cyril T Selepe^b, Nobanathi W Maxakato^b, Neil J Coville^{a,c} and Manoko S Maubane-Nkadimeng^{a,c,d*}

^a Molecular Sciences Institute, School of Chemistry, University of the Witwatersrand, Braamfontein,2050, South Africa, ^b Department of Chemical Sciences, University of Johannesburg, Doornfontein,2021, South Africa. ^c DSI-NRF Centre of Excellence in Strong Materials, University of the Witwatersrand, Braamfontein,2050, South Africa. ^d Microscopy and Microanalysis Unit, University of Witwatersrand, Braamfontein,2050, South Africa

Abstract

This study reports on the synthesis of platinum supported on titania oxide nanoparticles decorated on sulfur doped onion-like carbon nanoparticles (S-OLCNs) as electrocatalysts for ammonia oxidation reactions in alkaline media. S-OLCNs (S = 1.6 %) were synthesized in a one-step flame pyrolysis method using thiophene as the starting material and titania nanoparticles were prepared using a microwave-assisted hydrolysis technique (5-10% titania decoration). Pt/S-OLCN, Pt/TiO₂ and Pt/TiO₂/S-OLCN electrocatalysts (10 % Pt loading) were synthesized by the ethylene glycol assisted reduction method. Transmission electron microscopy studies confirmed the presence of well dispersed spherically shaped Pt NPs on the surface of the S-OLCN, TiO₂ and TiO₂/S-OLCN support materials (d = 1.93 ± 0.38, 1.98 ± 0.79 nm, 2.13 ± 0.52 nm, respectively). XRD patterns confirmed the anatase phase for the titania. The Pt/S-OLCN, Pt/TiO₂ and Pt/TiO₂/S-OLCN and Pt/C electrocatalysts were investigated in the ammonia oxidation reaction (AOR). The existence of the well-dispersed TiO₂ (and Pt) on the S-OLCNs gave rise to enhanced AOR catalytic performance when compared to Pt/S-OLCN, Pt/TiO₂ and commercial 10 wt% Pt/C catalysts. Furthermore, the Pt/TiO₂/S-OLCN electrocatalyst exhibited better long term stability and a faster charge transfer resistance than Pt/S-OLCN, Pt/TiO₂ and commercial 10 wt% Pt/C electrocatalysts. These results indicate that the incorporation of TiO₂ nanoparticles into Pt/S-OLCN is an effective strategy to improve the AOR activity of Pt by facilitating the electron transfer process during the catalytic reactions.

Keywords: Ammonia oxidation reactions; Cyclic voltammetry; Nano-catalysts; Onion-like carbon nanoparticles; Sulfur doping

5. Introduction

The electrochemical oxidation of ammonia has attracted much attention in recent years because of the effective use of ammonia as a fuel for electric energy generation in direct ammonia fuel cells (DAFCs) [1]. Ammonia as a liquid fuel is an excellent and appropriate chemical energy carrier since it is easy to handle under

low pressure, has a high hydrogen density and can be easily oxidized into hydrogen and nitrogen at elevated temperatures [2]. Also, ammonia is easy to transport, produce, and store. The development of the alkaline direct ammonia fuel cell (DAFC) has been used to convert ammonia into hydrogen (and nitrogen) under mild conditions, with ammonium hydroxide and potassium hydroxide used as a fuel and electrolyte respectively [3].

DAFCs have many advantages over alternative fuel cells such as the direct methanol fuel cell (DMFC). This is seen in terms of cost/type of the anode and the cathode kinetics [4]. The DAFC generates only nitrogen and water whereas the DMFC generates carbon dioxide (and hydrogen). The DAFC has a clear economic advantage as well, in that it is much faster, more efficient and is more cost effective when compared to the DMFC. The DAFCs do, however have some disadvantages such as: the ammonia electrocatalytic oxidation reaction is sluggish/slow require a high loading of the metal in the electrocatalyst to achieve acceptable reaction rates.

Pt is an example of the commonly used catalyst in a DAFC, because it provides a high electrocatalytic performance, good current density, long-term stability and excellent work functions [5]. However, its use has some limitations limited fuel cells, as Pt is expensive and there are limited Pt resources in the world and its applications have been limited by two problems. These are: (i) the catalyst has a high overpotential (> 0.5 V) and, (ii) it shows accelerated deactivation. Therefore, it is crucial to design new high performance nanocatalysts for the electrocatalytic oxidation of ammonia in fuel cells and at the same time to reduce the Pt loading in the electrocatalyst [6]. One way to achieve this is through the use of new catalyst support materials.

Both carbon-based materials and metal oxides possess the required properties for their use as catalyst support materials [7]. These properties include: (i) high surface areas that are required for the dispersion of catalyst particles, (ii) the ability to conduct electricity, and (iii) the ability to maintain stability in reactions under ammonia electrocatalytic oxidation conditions.

Carbon materials such as conductive carbon, carbon nanotubes (CNTs), carbon black (CB), carbon nanofibers (CNFs), graphene (GR), carbon nano-onions (CNOs) etc., are the commonly used support materials for FC electrocatalyst [8].

Recently, CNOs has attracted attention as a support material for metal nanoparticles in energy storage and conversions. Carbon nano-onions (CNOs) and heteroatom doped CNOs as well as their related onion-like carbon counterparts (OLCNs) are examples of support materials that have used as catalyst supports in fuel cells [9]. CNOs and OLCNs are part of the multi-fullerene family; the OLCNs (sometimes referred to as CNOs) are made up of quasi-sphere-shaped and polyhedral shaped nano-graphitic layers of carbon atoms [10].

Doping with non-metal heteroatoms like sulfur, phosphorus, nitrogen and boron has been shown to increase the performance of carbon-based catalysts. This is due to the enhancement of the active sites in the graphitic framework together with interdependent coupling effects between heteroatoms [11]. Most studies on carbon doping have focused on the use of N, O and B dopants. Sulfur, like N and O act as electron donors, and doping with sulfur has been shown to affect the electron density of states differently when compared to nitrogen doping [12].

Studies on the use of S doped carbons in electrochemical reactions are well documented in literature. For example, Yang et al. reported the synthesis of S-doped graphene (S-G) using benzyl disulfide (BDS) as sulfur precursor and graphene oxide (GO) as carbon source. The electrochemical analysis of the S-doped graphene in alkaline electrolyte demonstrated an enhanced catalytic performance for oxygen reduction reaction (ORR) when compared to the standard Pt/C nanocatalyst [13]. In another study, Fan et al. reported on Pt nanoparticles loaded on sulfur doped carbon nanotubes that were prepared using an assisted autoclave method. The synthesized Pt/S-MWCNT electrocatalyst showed higher catalytic performance, CO-tolerance and improved long-term durability for the methanol oxidation reaction when compared to undoped Pt/MWCNT or a Pt/C commercial nanocatalyst (MOR) [14].

The performance of Pt-based electrocatalysts for ammonia oxidation reactions can be enhanced by modification of the carbon support materials by using carbons mixed with inorganic supports [15]. Inorganic metal oxides such MoO₃, SnO₂, CeO₂, WO₃, Al₂O₃, and TiO₂ have all been used as catalyst supports due to their higher stability in fuel cells [16–18]. In particular, TiO₂ (anatase phase) is regularly used as a support material because of its good specific surface area and strong interconnection with metal nanoparticles [19]. The addition of metal oxides, like

TiO₂, to a standard Pt/C to generate Pt/TiO_x/C nanocomposites have been shown to modify the electronic and structural properties of platinum [20]. A carbon-TiO₂ support has shown a high resistance to the electrochemical corrosion of carbon [20]. The TiO₂ modified the synergy between the carbon in the C-TiO₂ and the catalyst nanoparticles [21].

Interestingly, a recent study by Liu et al. revealed a preparation of Pt/TiO₂ nanotubes by the galvanostatic electrodeposition method [22]. On the other hand, while studying the ammonia oxidation reaction (AOR) on indium tin oxide (ITO) decorated with Pt nanoparticles, Li et al. revealed a high mass specific electrocatalytic activity of the Pt/ITO electrode towards AOR which was better than the commercial Pt/C electrode. This was ascribed to the effect of Pt nanoparticles (NPs) on the indium tin oxide substrate [23].

In this study, we present the use of S doped onion-like carbon nanoparticles (S-OLCNs) as a carbon support and TiO₂/S-OLCN as a composite support material for use in an alkaline direct ammonia fuel cell. The S-OLCNs were synthesized from thiophene using the flame pyrolysis method, using methodology as reported in our previous work [24]. Platinum NPs were added to the surface of the S-OLCNs and TiO₂/S-OLCN support materials using the ethylene glycol reduction method. The sulfur functional groups are expected to facilitate the attachment of titania and platinum nanoparticles to the surface of the S-OLCNs. The synthesis of a TiO₂/S-OLCN structure could improve the anti-corrosion and anti-poisoning properties of the electrocatalyst. To the best of our knowledge, a detailed study on the TiO₂/S-OLCN support for platinum nanoparticles as electrocatalysts for direct ammonia fuel cells has not been previously reported. As discussed, the composite-modified (Pt/TiO₂/S-OLCN) electrode exhibited high catalytic performance for the oxidation of ammonia in alkaline electrolyte when compared to the Pt/S-OLCN, Pt/TiO₂ and a standard Pt modified electrode. The reasons for this finding are described.

5.1 Experimental

5.1.1. Materials

All chemicals were used as received to prepare the nanomaterials for the study: thiophene (99% ; Sigma-Aldrich), titanium butoxide (99.7%; Sigma-Aldrich), ethanol (99.9%; Sigma-Aldrich), acetylacetone (99.9% ; Sigma-Aldrich), sodium hydroxide (Sigma-Aldrich), ammonium sulphate (99%; Sigma-Aldrich), dihydrogen hexachloroplatinate (98.0% ; Sigma-Aldrich), Nafion solution (> 5 wt.%; Sigma-Aldrich), ethylene glycol (> 99.9% ; Sigma-Aldrich), ammonium hydroxide (>30% ; Sigma-Aldrich), potassium hydroxide (> 30% ; Sigma-Aldrich), 10% Pt/C commercial standard (Sigma-Aldrich).

5.1.2. Synthesis of sulfur doped onion-like carbon nanoparticles (S-OLCNs)

S-OLCNs were synthesized using a simplified flame pyrolysis method as described by Mohapatra et al. [24]. From a typical laboratory-made design, 60 mL of thiophene (organic precursor) was placed into a 100 ml beaker and after ignition in air (in a fume hood) gave the S-OLCNs. Here, the thiophene acted as the sulfur source as well as the carbon source to produce the desired S-OLCNs. It was shown from a previous report that a flame could produce an appropriate high-temperature environment (800 – 1000 °C) that was effective for the preparation of pristine OLCNs. In this study, ignited thiophene (C₄H₄S) readily decomposed in air. Using a brass plate collector, the S-OLCNs were formed in the upper part of the flame. The product in the form of black carbon nanoparticles (S-OLCNs) was collected and a yield of 3.15% was obtained. The S-OLCNs nanomaterial was used without additional post-processing or purification.

5.1.3. Synthesis of titanium dioxide (TiO₂) anatase

Titanium butoxide (2.0139g) was dissolved into 20 mL of 99.9% ethanol and 70 mL of deionized water. The solution was stirred for 30 minutes at 50 °C and a white suspension was obtained. Acetylacetone (10 mL) was added slowly into the

resulting white suspension and the flask contents stirred for 30 minutes to complete the hydrolysis reaction. The white suspension was then transferred into a 100 ml Teflon reaction vessel and the vessel placed into an Anton Paar microwave reactor (750W). The titanium suspension was then heated for 30 minutes at 180 °C. The resulting product from the microwave irradiation reaction was filtered and washed numerous times with double distilled water. The white solid that was obtained was dried in an oven at 100 °C overnight. The TiO₂ sample was calcined in a muffle furnace at 500 °C for 24 hours to obtain TiO₂ anatase.

5.1.4. Synthesis of TiO₂/S-OLCN composite support material

S-OLCNs (400 mg) and TiO₂ anatase powder (26.7 mg) were dispersed in 60 mL of NaOH aqueous solution (10 M) and 10 mL of ammonium sulfate (1 M (NH₄)₂SO₄) solution using ultrasonication at 40 °C for 70 minutes (to produce a 10% wt. TiO₂ loading on the S-OLCNs). The suspension was transferred into a Teflon-lined stainless-steel autoclave and kept at 200 °C for 24 hours in a muffle furnace. The precipitate was cooled down naturally and collected using the 1000 mL Millipore filter system through a 0.22 µm polytetrafluoroethylene (PTFE) filter. The precipitate was washed thoroughly with deionized water a considerable number of times to remove any excess NH₄⁺ ions, and then it was dried at 100 °C overnight. A light brown powder was obtained. The product was placed into a quartz boat that was calcined at 450 °C under argon for 2.5 hours to obtain the TiO₂/S-OLCN composite support material.

5.1.5. Synthesis of Pt/S-OLCN, Pt/TiO₂, and Pt/TiO₂/S-OLCN electrocatalysts

The platinum-based nanocatalysts were prepared by the ethylene assisted reduction method [25]. In this procedure, 200 mg of each support (S-OLCN, TiO₂, and TiO₂/S-OLCN) was dispersed in 20 mL of ethylene glycol and 42.0 mg of H₂PtCl₆ (to produce a 10% wt. Pt loading) was then added and the mixture stirred for 30 minutes. The obtained mixtures were sonicated in an ultrasound bath for another 30 minutes. The Pt/S-OLCN, Pt/TiO₂, and Pt/TiO₂/S-OLCN nanocatalysts solutions were then placed into three round bottom flasks and the solutions were

then refluxed at 200 °C for 6 hours. The resulting mixtures were centrifuged at 18 000 rpm for 25 minutes and washed a considerable number of times with distilled water to eliminate residual chloride ions. The nanomaterials were dried at 100 °C for 24 h to obtain the Pt-based nanocatalysts.

5.1.6. Material characterization

The structure and morphology of the samples were recorded using a JEOL transmission electron microscope (TEM) model JEM-2100F operated at 200 kV. Surface micrographs and Energy dispersive X-rays (EDX) were obtained using a ZEISS Sigma 300 VP Oxford Field Emission Scanning Electron Microscope (SEM) instrument. The Fourier transform infrared (FTIR) spectra were obtained on a PerkinElmer Spectrum 100 instrument. Raman spectra of the OLCNs were acquired using a Raman spectrometer model Horiba Jobin Yvon with a laser wavelength of $\lambda = 514$ nm. The thermal stability of the samples was investigated using a Perkin Elmer 6000 thermogravimetric (TGA) analyzer. The specific surface areas and porosity characterization of the samples were analyzed using the Brunauer-Emmett-Teller method (BET) on a Micromeritics Tristar 3000 surface area analyzer. Powder X-ray diffraction (PXRD) patterns for the samples were obtained on a Bruker D2 Phaser diffractometer using a Cu K α radiation source ($\lambda=0.15405$ nm) generated at 30 kV and 10 mA. To determine the chemical states of the samples, X-ray photoelectron spectroscopy (XPS, Thermo Scientific ESCALAB 250Xi instrument) was performed with a high-resolution pass energy of 20 eV , monochromatic Al K α (1486.7 eV) source.

5.1.7. Electrochemical measurements

Electrochemical measurements were investigated out using a Dropsens potentiostat. A glassy carbon (GC) electrode with a geometrical surface area of 0.196 cm² was utilized as a working electrode for the cyclic voltammetry (CV), chronoamperometry (CA), and electrochemical impedance spectroscopy (EIS) measurements. A platinum (Pt) wire was used as the counter electrode and a saturated silver/silver chloride electrode (Ag/AgCl) with a bridge tube as a

reference electrode. The Ag/AgCl reference electrode cannot be used in ammonia buffer as Ag/AgCl forms a soluble complex with NH_3 . The Ag/AgCl reference electrode was putted inside the bridge tube that had a ceramic glass frit to prevent the filling electrolyte (3.4 molar KCl) doesn't leak into the sample; this also prevents contamination of the Pt counter electrode with ions such as chloride or potassium. Additionally, Pt is also susceptible to sulfur compounds, nitrogen compounds, and CO, leading to Pt poisoning due to strong chemisorption. Therefore, electrolyte purification to remove the poisonous impurities is necessary if Pt is chosen as the counter electrode. The working electrodes were prepared using an ink made of the electrocatalyst. This was done by dispersing 10 mg of nanocatalysts in 1 mL of isopropyl alcohol with 5 μL Nafion solution (5 wt.%) and mixing for 15 min in an ultrasonic bath. After that, 15 μL aliquot of the electrocatalyst inks was pipetted onto the surface of the glassy carbon electrode and dried at ambient temperature. The loading of Pt in the electrocatalysts on the glassy carbon electrode is ca. 0.045 mg cm^{-2} . Prior to any electrochemical studies, the electrolyte solution was purged with argon for 20 min to remove any oxygen interference. CV, CA and EIS measurements were performed in solutions containing 1 M KOH and 1 M NH_4OH saturated with argon gas. For all Pt based electrocatalysts, the electroactive surface area (ECSA) values were normalized by the geometric surface area of the working (GC) electrode. Currents obtained in the CV and CA curves were normalized by the ECSA of the platinum based electrocatalysts.

5.2 Results and Discussion

5.2.0. Physical characterization

5.2.1. Transmission electron microscopy (TEM)

A typical TEM micrograph of the TiO_2 -anatase nanoparticles is given in Fig. S1 (a) which shows the classical shape and agglomerated structure of anatase titania nanoparticles with an average diameter of $93.8 \pm 11.5 \text{ nm}$ (see Fig. S2 (a)). The TEM micrograph depicted in Fig. 5.1(a) shows the as-synthesized S-OLCNs with

an almost spherical morphology and the inset of Selected Area Electron Diffraction (SAED) that confirms the presence of amorphous and fullerene like structure established on the basis of high magnification TEM. The onion-like concentric shell structure of the S-OLCNs was preserved even though the OLCNs were doped, which verified that the doping step did not alter the onion-like structure. The S-OLCNs contained disordered concentric graphitic multi-shells with an average diameter of 51.4 ± 8.27 nm as indicated in Fig. S2(b) [26]. A TEM image of the TiO_2 /S-OLCN mixture is shown in Fig. 5.1(c) (and sup Fig. S1(c)). The data clearly shows that the material is comprised of a mixture of the two supports. It is not possible to determine the degree of interaction of the two components. TEM images of the carbon supports that contain Pt are also shown in Fig. 5.1(b) and (d) (Pt/S-OLCN and Pt/ TiO_2 /S-OLCN). Fig. 5.1 (e) demonstrates the high resolution TEM image of Pt/ TiO_2 /S-OLCN nanomaterial. In Pt/ TiO_2 /S-OLCN, Pt nanoparticles showed the better crystallinity and *d*-spacing value of 0.23 nm (111), whereas TiO_2 anatase exhibits the fringe distance of 0.352 nm (Fig. S1 (e)). Fig. 5.1 (f–g) represents the energy dispersive X-ray spectroscopy (TEM-EDX) spectra of Pt/ TiO_2 /S-OLCN captured on the selected area of sample. It clearly shows that Pt and TiO_2 nanoparticles are uniformly dispersed on S-OLCN surface. A TEM image of Pt supported on TiO_2 is shown in Sup Fig. S1 (d). As seen in all images the Pt nanoparticles are well dispersed. A comparison of the data indicates that in the composite the Pt preferentially binds to the carbon (S-OLCNs), even though the composite contains 10% TiO_2 . The platinum nanoparticles appear to be marginally larger (2.13 ± 0.52 nm) when incorporated into the TiO_2 /S-OLCN composite support, as compared to the S-OLCN support (1.93 ± 0.38 nm). A TEM micrograph of the Pt/ TiO_2 nanomaterial is presented in Fig. S1 (d) and also shows small platinum particles (1.98 ± 0.79 nm) well distributed on the titanium dioxide surface.

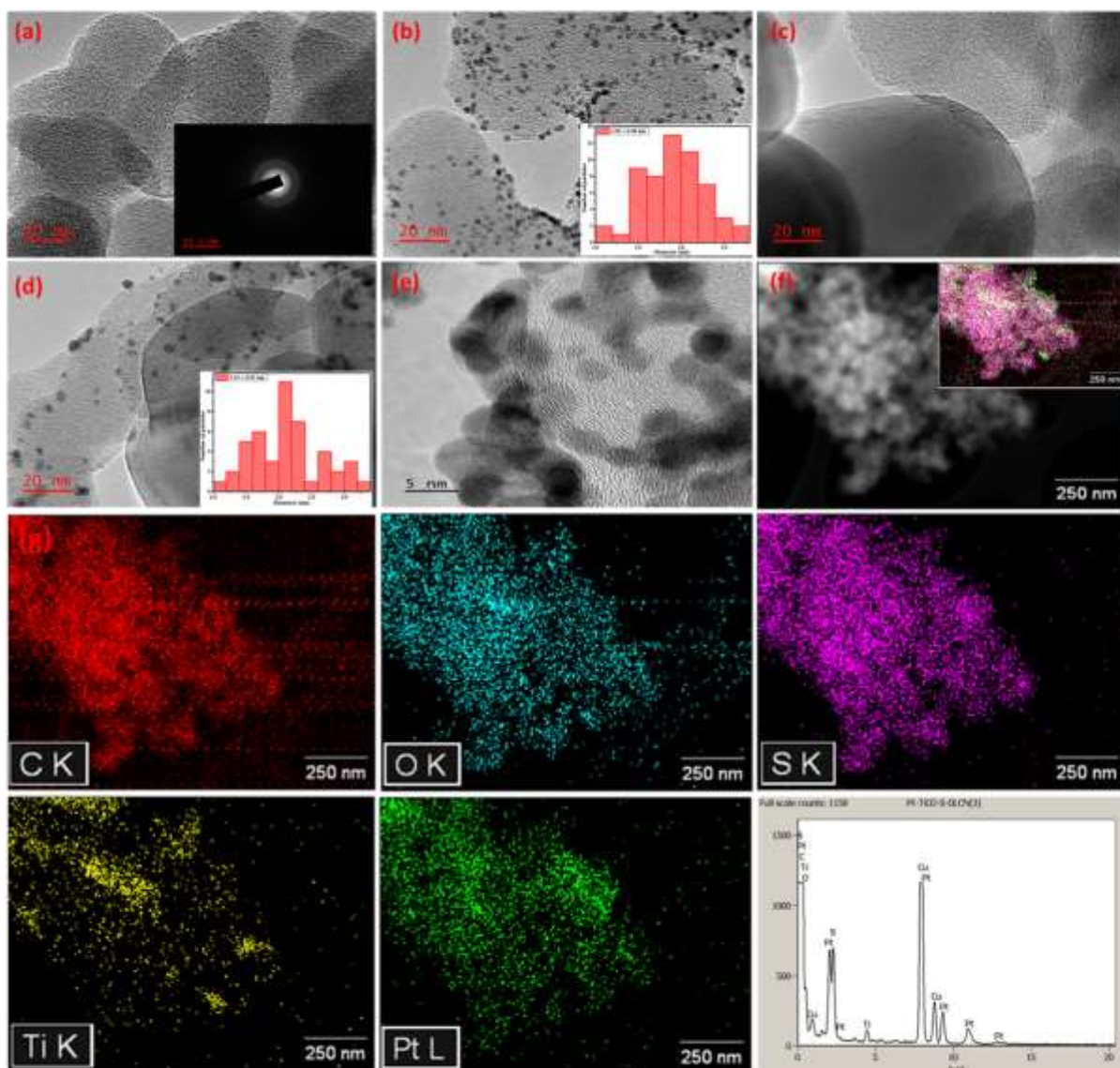


Figure 5.1: High Magnification TEM micrographs of (a) S-OLCN, (b) Pt/S-OLCN and inset image of histogram representing Pt nanoparticle size is $(1.93 \pm 0.38 \text{ nm})$, (c) $\text{TiO}_2/\text{S-OLCN}$, (d) $\text{Pt/TiO}_2/\text{S-OLCN}$ and inset image of histogram representing Pt nanoparticle size is $(2.13 \pm 0.52 \text{ nm})$, (e) high resolution TEM micrographs of $\text{Pt/TiO}_2/\text{S-OLCN}$, (f) HR-TEM image of selected area of $\text{Pt/TiO}_2/\text{S-OLCN}$ and inset is corresponding EDX mapping represents the combination of elements in $\text{Pt/TiO}_2/\text{S-OLCN}$, (g) TEM-EDX elemental color mapping of the C, O, S, Ti, Pt elements.

5.2.2. Scanning electron microscopy (SEM)

The SEM micrographs of the S-OLCNs, TiO₂/S-OLCN, Pt/OLCNs and Pt/TiO₂/S-OLCN nanomaterials are shown in Fig. 5.2. These images display agglomerates of quasi-spherical morphology for the S-OLCNs [27] and the TiO₂ nanoparticles (Fig. 2 (a) and (b) respectively). The SEM image in Fig. 5.2 (b) also shows that the addition of the TiO₂ nanoparticles did not alter the morphology of the S-OLCNs

Fig. 5.2 (c) and (d) shows the SEM images of Pt/S-OLCN and Pt/TiO₂/S-OLCN nanomaterials and indicated no significant changes in the sizes/shapes of the support particles. The TiO₂ anatase and Pt/TiO₂ images in Fig. S3 (a) and (b) consists of non-uniform shaped particles, which are conglomerates of large grains of the TiO₂. It can be observed that TiO₂ images show large particle sizes in the range between 60 nm and 140 nm diameter. The mixture of the two supports, with different sizes, is shown by the circles in the Fig 5.2 (d). The image is dominated by the carbon, in agreement with the use of 10% TiO₂. The Pt NPs were, as expected, not seen in the SEM images at the image resolution used.

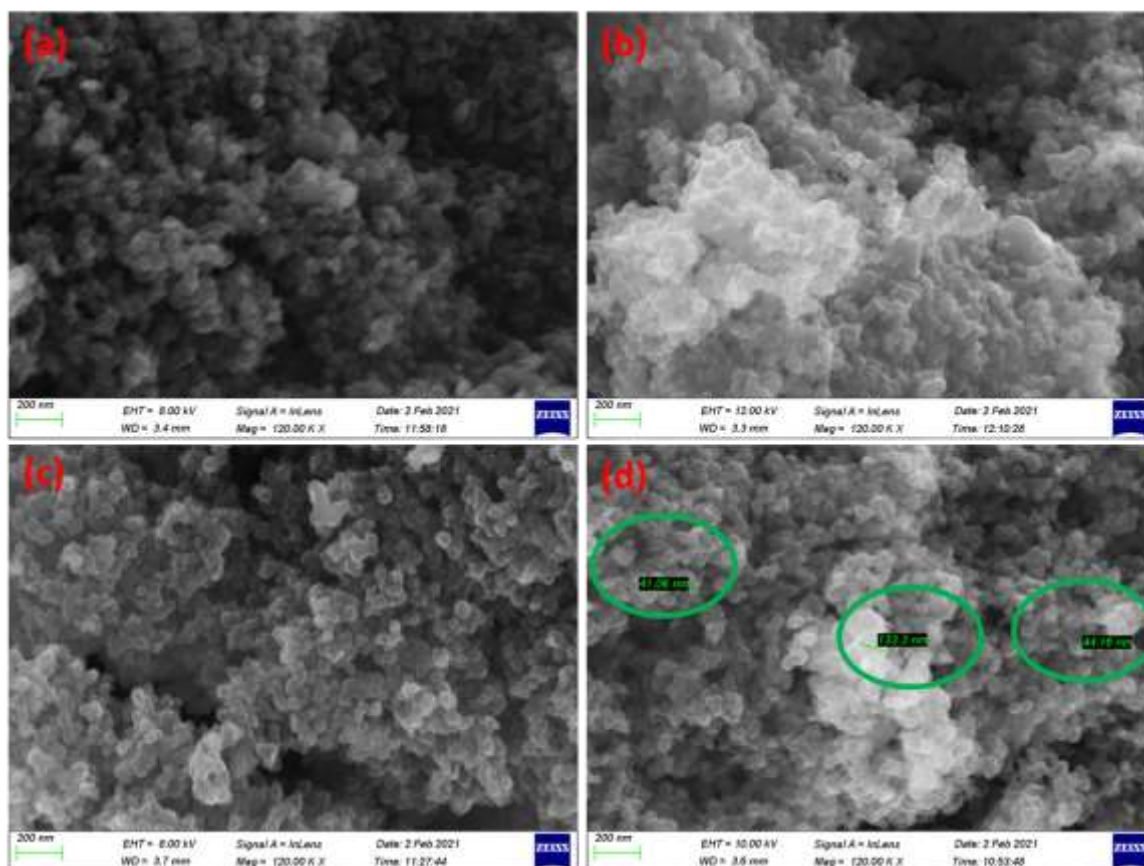


Figure 5.2: Typical SEM micrographs of (a) S-OLCN (b) TiO₂/S-OLCN, (c) Pt/S-OLCN (d) Pt/TiO₂/S-OLCN nanomaterials.

5.2.3. Energy dispersive X-ray spectroscopy (EDS)

Elemental analyses of the S-OLCN, TiO₂/S-OLCN, Pt/S-OLCN and Pt/TiO₂/S-OLCN nanocomposite materials were studied using EDS. The EDS spectra shown in Fig. S4 (a and b), confirmed the presence of carbon, oxygen, sulphur, and titanium in the S-OLCN and TiO₂/S-OLCN support materials. Also, the EDS also confirmed the presence platinum in the Pt/S-OLCN (Fig. S4 (c)) and in Pt/TiO₂/S-OLCN (Fig. S4 (d)).

5.2.4. Fourier transform infrared and Raman spectroscopy

The FTIR spectrum of the S-OLCN is shown in Fig. 5.3. (a). The peak at 3416 cm⁻¹ is due to a OH stretch mode [28]. The peak at 1624 cm⁻¹ is assigned to a C=C stretch in aryl rings [27]. The peak at 1404 cm⁻¹ is attributed to the C-O-H stretch due to the existence of carboxylic functional groups [26] and the signal at 1109 cm⁻¹ is assigned to a S=O/C-O stretching modes. This peak at 1109 cm⁻¹ also consists of contributions from the S=O stretch (sulfoxide) and a C-O stretch (alcohol group) [29]. The large peaks of interest at 744 cm⁻¹ and 611 cm⁻¹ are assigned to a C-S and S-O stretching modes [30]. The FTIR data thus suggest that the S-OLCNs contain a carbon backbone structure and that the S-doping process did not damage the carbon framework.

Raman spectroscopy was used to ascertain the extent of structural imperfections in the graphitic carbon nanomaterial [24]. Fig. 5.3. (b), indicates the Raman spectra of the S-OLCN support material which showed two primary peaks. These were the D-band was found at 1346 cm⁻¹ and the G-band at 1633 cm⁻¹. The D-band is associated with defects that are caused by doping, whilst the G-band is the result of the in-plane vibrational stretch of ordered sp²-bonded carbon atoms. [31]. Thomas et al. reported that for their S-OLCN material, that the D-band (1335

cm^{-1}) and the G-band (1570 cm^{-1}) shifted downwards when compared to planar graphite. For example, the G-band got graphite typically occurs at 1582 cm^{-1} [32]. Interestingly, an upshift of the G-band was reported for p-CNO (ca. 1588 cm^{-1}) [26]. The reason for this upshift is suggested to be related to the tensile stress caused within the graphene planes by bending after doping [24]. The upshift confirmed the modifications of the carbon. The areas of the D and G bands were used to determine the I_D/I_G ratio, found to be 1.16. This I_D/I_G ratio was larger when compared to that reported by Mohapatra et al. (0.72) for a similar S-CNO material [24].

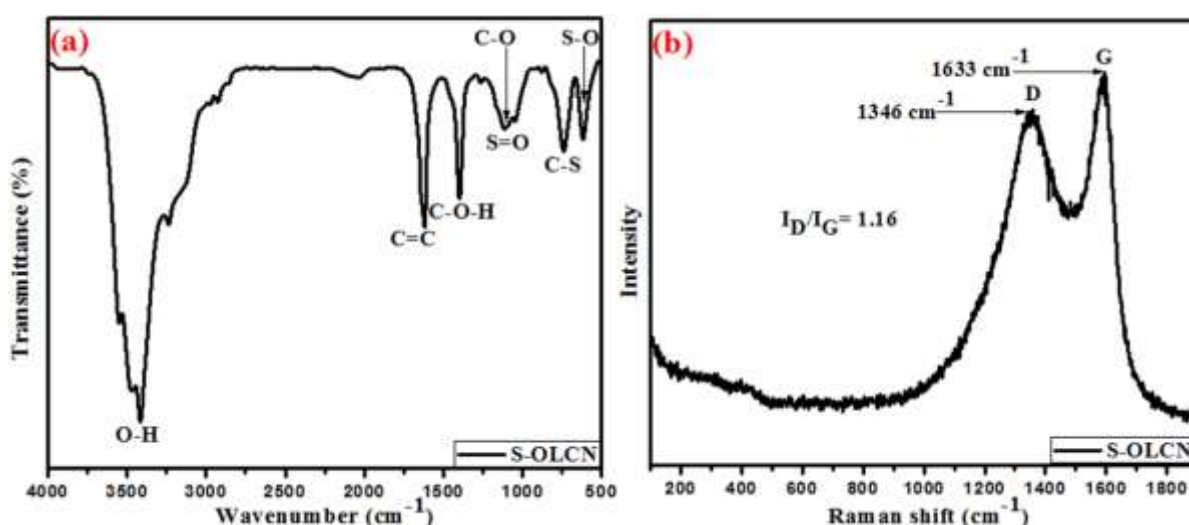


Figure 5.3: (a) FTIR spectrum and (b) Raman spectrum of the S-OLCN nanomaterials.

5.2.5. Thermogravimetric analysis (TGA)

The TGA and TGA derivative data were used to compare the stability of S-OLCN and $\text{TiO}_2/\text{S-OLCN}$, Pt/S-OLCN and $\text{Pt/TiO}_2/\text{S-OLCN}$ nanomaterials under air in the temperature range of 35°C – 900°C . As shown in Fig. S5 (b), the TGA derivative curve showed maximum decomposition temperatures of 643°C and 577°C for S-OLCNs and $\text{TiO}_2/\text{S-OLCN}$ respectively, which is ascribed to carbon thermal oxidation of the carbon [33]. The introduction of TiO_2 facilitated the thermal oxidation of the carbon. The residual weight of the $\text{TiO}_2/\text{S-OLCN}$ was found to be 9.9% and is due to the presence of TiO_2 nanoparticles.

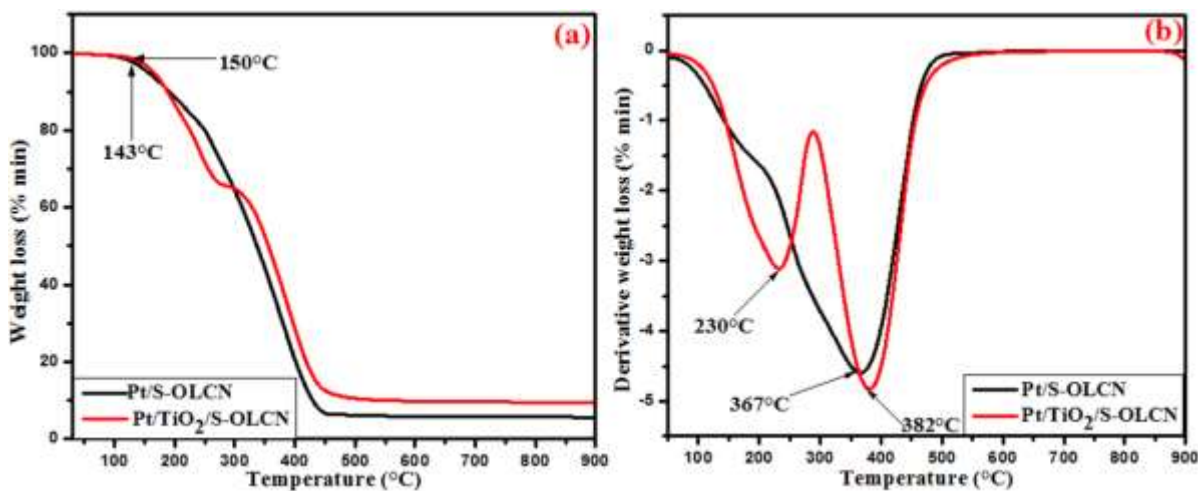


Figure 5.4: (a) thermogravimetric analysis profiles and (b) differential thermogravimetric analysis curves of Pt/S-OLCN and Pt/TiO₂/S-OLCN nanomaterials.

The TGA and TGA derivative profiles of Pt/S-OLCN and Pt/TiO₂/S-OLCN indicated in Fig. 5.4. (367 °C and 382 °C for Pt/S-OLCN and Pt/TiO₂/S-OLCN (Fig. 5.4 (b)) are due to carbon oxidation. The introduction of Pt NPs increased the combustion of the carbon and hence lowered the thermal stability of the nanomaterials when compared to the non-Pt supports [34].

The residual weight of the Pt/TiO₂/S-OLCN was found to be 9.5 % and includes contributions from both TiO₂ and Pt. The residual weight of Pt/S-OLCN, due to the PtO₂ was found to be 5.8 %, suggesting that the TiO₂ content was ca 5%. The residual weight obtained in both materials was less than the 10% Pt theoretical loading.

5.2.6. X-ray diffraction spectroscopy (XRD)

Fig. 5.5 shows the X-ray diffraction patterns for the S-OLCN, TiO₂ anatase, Pt/S-OLCN, and Pt/TiO₂/S-OLCN nanomaterials. The XRD peak at $2\theta = 24.98^\circ$ in the S-OLCN, Pt/S-OLCN, and Pt/TiO₂/S-OLCN spectra is attributed to the carbon (002) hexagonal structure while the intense diffraction peaks at $2\theta = 39^\circ, 47^\circ, 68^\circ$ and 82° correlate to platinum (111), (200), (220), and (311) planes (JCPDS card.

No 01-087-0646) [25]. The XRD pattern of TiO₂ indicates sharp peaks at 2 θ = 25.6°, 38.4°, 48.7°, 54.5°, 55.8°, 63.3°, 69.2°, 70.9°, 75.6°, 83.2° attributed to the TiO₂ anatase structure (JCPDS card. No 01-075-2544). The introduction of TiO₂ NPs to the carbon has negligible influence on the Pt crystal size of Pt/TiO₂/S-OLCN nanomaterial. The average crystallite size of the Pt/S-OLCN, and Pt/TiO₂/S-OLCN were estimated to be 2.2 nm, and 2.4 nm from the Pt (111) peak, using the Debye–Scherrer equation. Also, the average crystallite size of the TiO₂ anatase in Pt/S-OLCN-TiO₂ was found to be 94.5 nm from the TiO₂ (101) peak. These are similar to the data obtained from the TEM measurements. The mean crystallite size of the Pt nanoparticles of the platinum-based nanomaterials are also similar to those were reported by Ahmed et al. [35] and Wang et al. [40] that were used for methanol oxidation and oxygen reduction reactions, respectively.

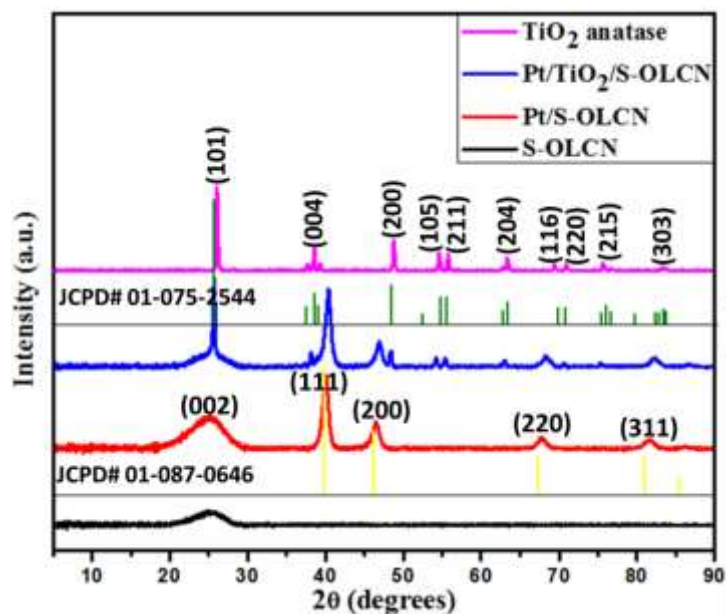


Figure 5.5: X-ray diffractograms of S-OLCN, Pt/S-OLCN, Pt/TiO₂/S-OLCN, and TiO₂ anatase nanomaterials.

5.2.7. X-ray photoelectron spectroscopy (XPS)

Fig. 5.6 (a) shows the XPS survey spectra of the Pt/TiO₂/S-OLCN and confirmed the existence of C 1s at 284.4eV, O 1s at 532.6 eV, S 2p at 163.9 eV, Ti 2p at

458.7 eV and Pt 4f at 72.8 eV elements in the ternary composite nanomaterial. The elemental composition of the Pt/TiO₂/S-OLCN sample is shown in Table 5.1.

Table 5.1: Elemental composition of Pt/TiO₂/S-OLCN sample obtained from XPS data

Sample	Carbon	Oxygen	Sulfur	Titanium	Platinum
Pt/TiO ₂ /S-OLCN	75.1	14.3	1.6	2.1	4.9

In Fig. 5.6 (b) the high-resolution XPS C1s spectrum of Pt/TiO₂/S-OLCN nanomaterial revealed six peaks. The two peaks that appeared at binding energies 284.1 and 284.9 eV correspond to sp² and sp³ hybridized carbon atoms, respectively [36]. The peak at a binding energy of 285.6 eV is assigned to a C–S bond suggesting the binding of S to an sp³ carbon atom [24]. The three peaks that appeared at binding energies 286.3, 287.5 eV and 288.8 eV are attributed to the C–O, C=O and O–C=O functional groups indicating the existence of carbonyl groups, respectively. The XPS spectrum of the oxygen O1s orbital shown in Fig. 5.6 (c), was deconvoluted into three peaks at 530.2 eV, 531.7 eV, and 532.9 eV which are ascribed to the Ti–O bond in anatase, and the C–O, and C=O carbonyl groups, respectively [37]. The high-resolution S2p spectrum showed peaks at ca 163 and 165 eV due to the presence of the expected S2p_{1/2} and S2p_{3/2} doublet in the correct ratio of ca. 1 to 2 (see Fig. 5.6 (d)). The location of the S2p_{3/2} is consistent with RSH, C=S and C–S bonds, confirming the sulfur doping of the OLCN structure [24]. As can be seen in Fig. 5.6 (e), the Ti 2p XPS spectrum, exhibited spin-orbit coupling (1.0 eV) for Ti 2p³ at 459.2 eV suggesting the presence of a titanium (IV) species [38]. The XPS Pt 4f spectrum showed two distinct peaks for Pt4f_{5/2} and 4f_{7/2} located at 71.2 eV and 74.5 eV, respectively, which can be deconvoluted into two peaks. The peaks located at 71.2 eV and 74.5 eV were attributed to metallic platinum (Pt⁰) and Pt^{II} in Fig. 5.7 (f) [39]. The existence of the strong peaks for platinum Pt^{II} in the Pt4f spectra indicates the presence of oxidized Pt and a possible Pt–O–Ti interaction [40].

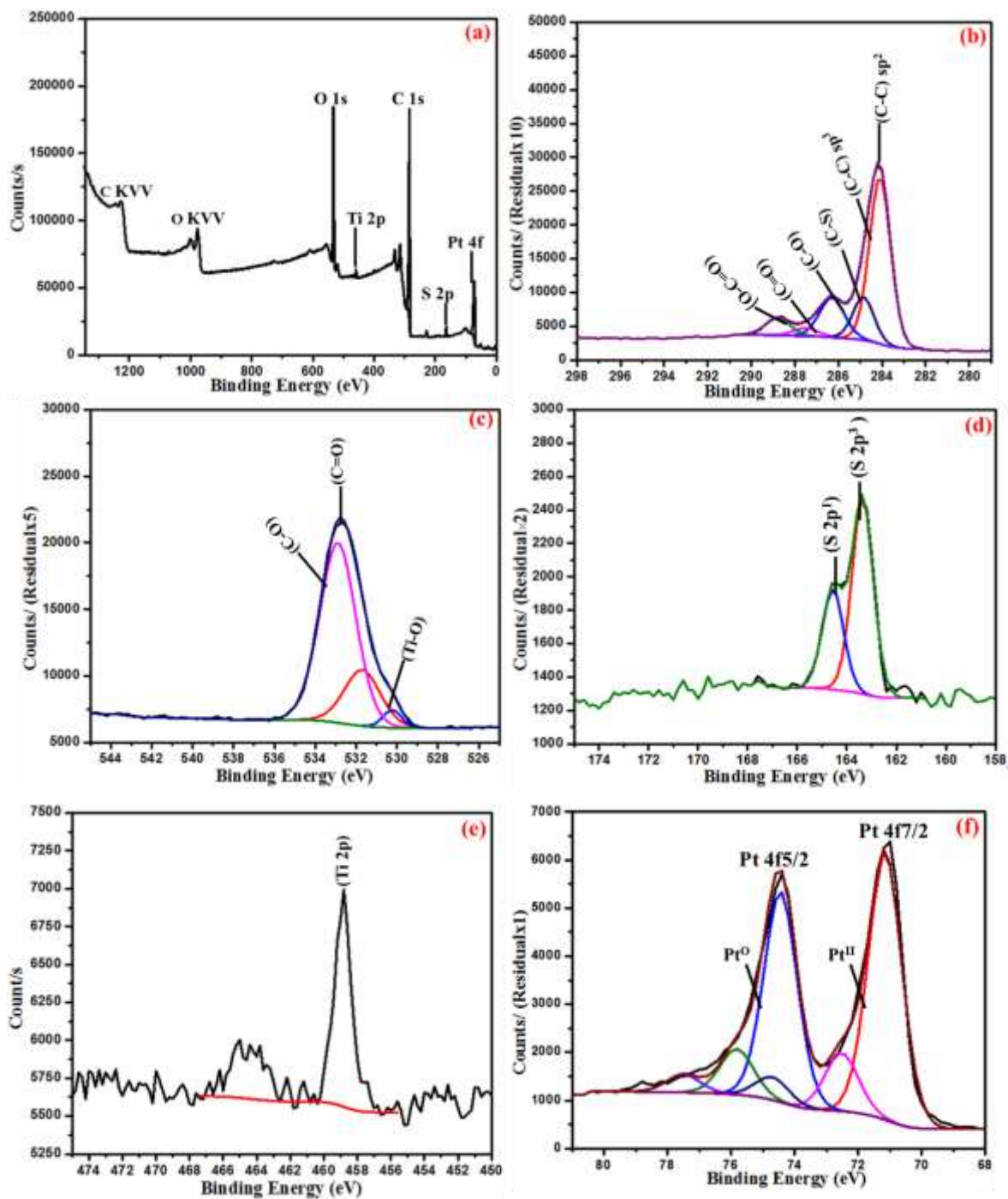


Figure 5.6: XPS (a) survey spectra of Pt/TiO₂/S-OLCN (b), C 1s of Pt/TiO₂/S-OLCN (c) O 1s of Pt/TiO₂/S-OLCN (d) S 2p of Pt/TiO₂/S-OLCN (e) Ti 2p of Pt/TiO₂/S-OLCN and (f) Pt 4f of Pt/TiO₂/S-OLCN.

5.2.8. Brunauer-Emmett-Teller nitrogen adsorption (BET) data

The BET technique was used to measure the specific surface area of the nanomaterials. Nitrogen adsorption-desorption isotherms and the pore size distribution data (derived from the desorption branch for Pt/S-OLCN and Pt/TiO₂/S-OLCN materials) are shown in Fig. S6. Table 5.2 lists the BET surface area data obtained for the electrocatalyst support materials. The BET surface area of S-OLCN was determined to be 55 m² g⁻¹, which is higher than the TiO₂/S-OLCN (27 m² g⁻¹), Pt/TiO₂ (34 m² g⁻¹), Pt/S-OLCN (46 m² g⁻¹) and Pt/TiO₂/S-OLCN (52 m² g⁻¹) electrocatalysts. Presumably this is due to the Pt and TiO₂ nanoparticles which have been well dispersed and block the pores of the S-OLCN catalyst support surface [41].

Table 5.2: BET surface area of the platinum supported on sulfur-doped onion like carbon nanoparticles-titania nanomaterials

Sample	Surface area (m ² g ⁻¹)	Pore volume (cm ³ g ⁻¹)
S-OLCN	55	0.19
S-OLCN-TiO ₂	27	0.28
Pt/S-OLCN	46	0.31
Pt/TiO ₂ /S-OLCN	52	0.34
Pt/TiO ₂	34	0.10

5.3. Electrocatalytic behaviour of the Pt based electrocatalysts

5.3.1. Electrochemical surface area (ECSA)

The electrochemically active surface area (ECSA) of the Pt/C, Pt/TiO₂, Pt/S-OLCN and Pt/TiO₂/S-OLCN nanocatalysts was determined using cyclic voltammetry (CV) recorded at a scan rate of 50 mVs⁻¹ in 1 M KOH solution (Fig. 5.7). The electrocatalyst currents were normalized using the geometric area of the

working electrode. ECSA of the Pt-based nanocatalysts was estimated from equation 1 [33].

$$ECSA_{Pt,cat} = \frac{Q_H[mC]}{Q_{density}[mCcm^{-2}] \times L_{metal}[mg]} \quad (1)$$

The CV curves of the four electrocatalysts are very similar to that of polycrystalline Pt, which displayed distinctive potential regions including the H-adsorption/desorption peaks, the double layer peak and the Pt oxide formation/reduction peaks. All the Pt-based nanocatalysts exhibited hydrogen adsorption/desorption peaks between -0.8 and -0.5 V (vs Ag/AgCl), which are ascribed to the adsorption/desorption of both weakly and strongly bonded hydrogen species.

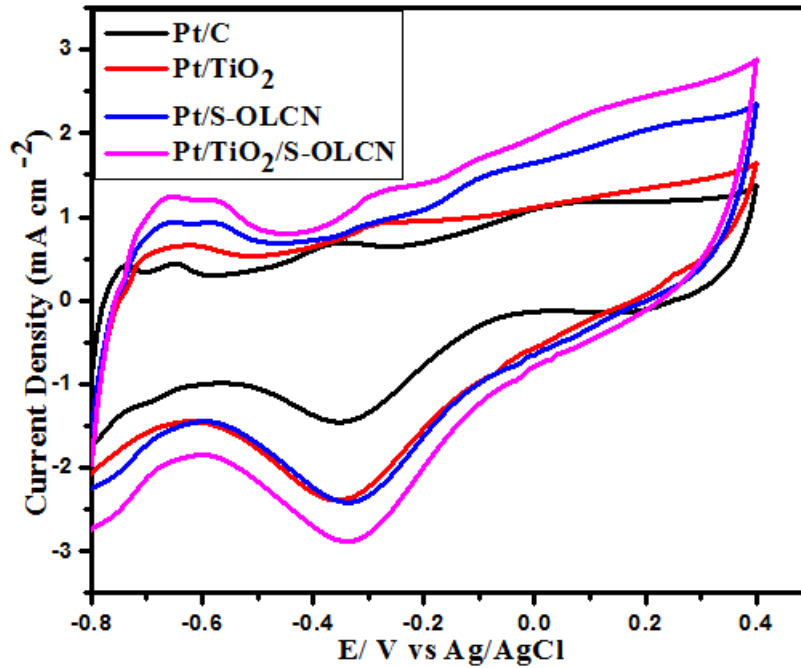


Figure 5.7: (a) CV curves for the Pt/C, Pt/TiO₂, Pt/S-OLCN and Pt/TiO₂/S-OLCN nanocatalysts in 1 M KOH at a scan rate of 50 mV s⁻¹.

The ECSA data followed the order: Pt/TiO₂/S-OLCN (49.89 m² g⁻¹) > Pt/S-OLCN (45.13 m² g⁻¹) > Pt/TiO₂ (41.37 m² g⁻¹) > Pt/C (36.52 m² g⁻¹). The enhanced ECSA of the Pt/TiO₂/S-OLCN can be ascribed to the generation of new active sites at the interface between Pt and TiO₂ NPs, enhanced by the S-OLCNs [42,43].

5.3.2. Cyclic voltammetry (CV)

CVs were measured in ammonia-containing solution at a scan rate 50 mV s^{-1} and the data are shown in Fig. 5.8 for the Pt/C, Pt/TiO₂, Pt/S-CNO and Pt/TiO₂/S-OLCN modified electrodes. The reported currents were normalized using the ECSA data. The cyclic voltammograms (in 1 M KOH + 1M NH₄OH solution) displayed voltammetric profiles that are very similar to the one obtained for the Pt-NCs prepared by the polyol method [44]. The ammonia oxidation peaks are clearly seen for the four electrocatalysts at around -0.51 to -0.16 E/ V vs Ag/AgCl. It is observed that the onset potential for ammonia oxidation reaction on commercial Pt/C catalyst (-0.492 V vs Ag| AgCl) has higher values than the ones obtained using Pt/TiO₂/S-OLCN, Pt/S- OLCN and Pt/TiO₂ catalysts. Surprisingly, the Pt/S-OLCN and Pt/TiO₂ (-0.514 V vs Ag|AgCl) nanocatalysts has the same lower values of onset potential as compared to Pt/TiO₂/S-OLCN (-0.501 V vs Ag|AgCl) nanocatalysts for ammonia oxidation in alkaline electrolyte. These lower onset potentials confirm that the Pt nanoparticles had been successfully dispersed on the surface of the TiO₂/S-OLCN. It is suggested that the different interactions with these support materials modified the electronic structure of Pt, causing the easier catalysis and dissociation of ammonia [37].

The CV curves showed the following order: Pt/TiO₂/S-OLCN (0.52 mA cm^{-2}) Pt/S-OLCN (0.41 mA cm^{-2}) > Pt/TiO₂ (0.38 mA cm^{-2}) > Pt/C (0.33 mA cm^{-2}). These results demonstrate the enhanced catalytic performance of the sulfur doped carbon in Pt/TiO₂/S-OLCN electrocatalyst. The larger ECSA of Pt/TiO₂/S-OLCN could supply more active sites for the AOR and improve the electrocatalytic efficiency. In addition, the Pt/TiO₂/S-OLCN electrocatalysts shows higher catalytic activity as compared to our previous study of the synthesized undoped Pt/p-OLCN (0.13 mA cm^{-2}) electrocatalyst [33]. This is attributed to the surface wettability and hydrophilicity of S-OLCNs support, which improve interactions between the electrolyte ions, the analyte and the surface of the electrode [45]. The dissociative adsorption of water molecules on the titanium dioxide support material generated Ti-OH surface groups. These Ti-OH groups near the Pt nanoparticles may

promote the removal of nitrogenous groups bonded on the Pt atoms (Pt-N_{ads} poisoning interaction) which was modified by the TiO₂ support [22]. According to Liu et al. Pt/titanium dioxide nanotube showed enhanced electrocatalytic performance towards AOR process in the ammonia activation and adsorption under UV-light illumination [22]. A comparative analysis of catalytic performance of the nanocatalysts reported in this study with other similar Pt/C catalysts for the electrochemical ammonia oxidation reactions is revealed in Table 5.3. It is evident that the synthesized nanocatalysts in general shows better catalytic activity towards AOR than the other nanocatalysts listed.

Table 5.3: Comparison of Pt/TiO₂, Pt/S-OLCN and Pt/TiO₂/S-OLCN to other Pt/C catalysts reported for ammonia oxidation reactions

Electrocatalysts	Fuel (M)	Electrolyte (M)	CD (mA cm ⁻²)	Ref.
Pt/TiO ₂ /S-OLCN	1 NH ₄ OH	1 KOH	0.52	This work
Pt/S-OLCN	1 NH ₄ OH	1 KOH	0.41	This work
Pt/TiO ₂	1 NH ₄ OH	1 KOH	0.38	This work
Pt/TiO ₂ nanotubes	0.1 NH ₃	1 KOH	0.36	[22]
Pt/MnO ₂	0.2 NH ₄ OH	1KOH	0.51	[46]
Pt/SnO ₂ /C	0.5 NH ₄ OH	1 KOH	0.71	[1]

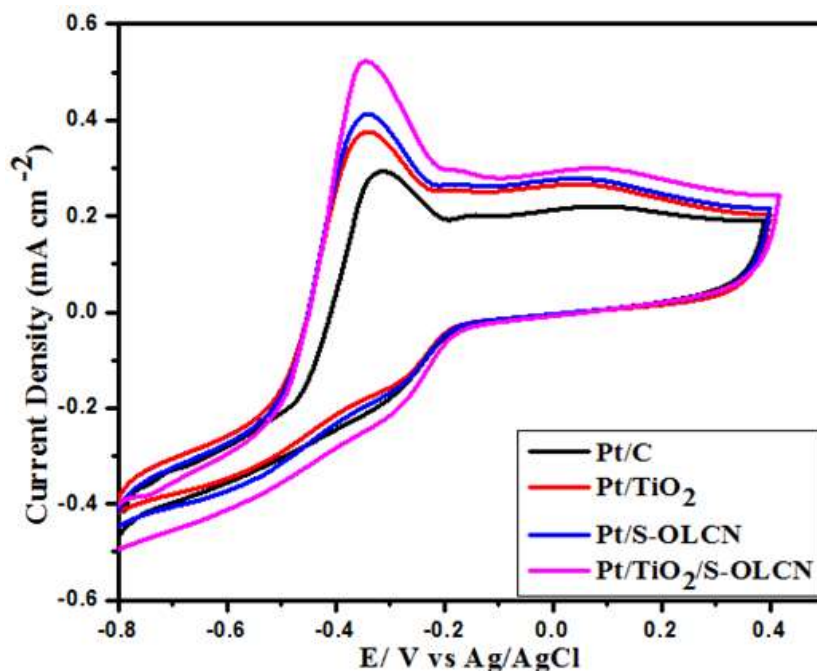


Figure 5.8: CV curves of the Pt/C, Pt/TiO₂, Pt/S-OLCN and Pt/TiO₂/S-OLCN modified electrodes in 1 M KOH + 1M NH₄OH at a scan rate of 50 mV s⁻¹.

5.3.3. Chronoamperometry (CA)

The CA measurements of the Pt/C, Pt/TiO₂, Pt/S-OLCN and Pt/TiO₂/S-OLCN modified electrodes, were also carried out in the solution of 1 M KOH containing 1M NH₄OH at a constant potential of - 0.3 V. As shown in Fig. 5.9, the current density for the ammonia oxidation reactions on all four electrocatalysts gradually decreased and then became stable with the increasing time. The current density after 2000 s of measurement followed the order: Pt/TiO₂/S-OLCN (0.28 mA cm⁻²) > Pt/S-OLCN (0.17 mA cm⁻²) > Pt/TiO₂ (0.11 mA cm⁻²) > Pt/C (0.09 mA cm⁻²). The improved catalytic activity of Pt/TiO₂/S-OLCN electrocatalyst is ascribed to the strong metal-support interaction between platinum nanoparticles and S-OLCN-TiO₂ composite support material [47]. Also, this could be due to the “spill over” effect whereby adsorbed intermediates on the Pt sites move to neighboring Ti-OH species to assist in accelerated oxidation [48]. Titanium dioxide assists the platinum catalyst in avoiding deactivation form nitrogen intermediates (Pt-N_{ads}) that poisoning the Pt formed during the ammonia oxidation reaction process [22]. Additionally, the strong electron transfer interconnection from the Pt NPs to the S

groups in onion structure will change the electronic state of the Pt catalyst surface[49] and thus improve the catalytic activity of Pt/TiO₂/S-OLCN toward the AOR.

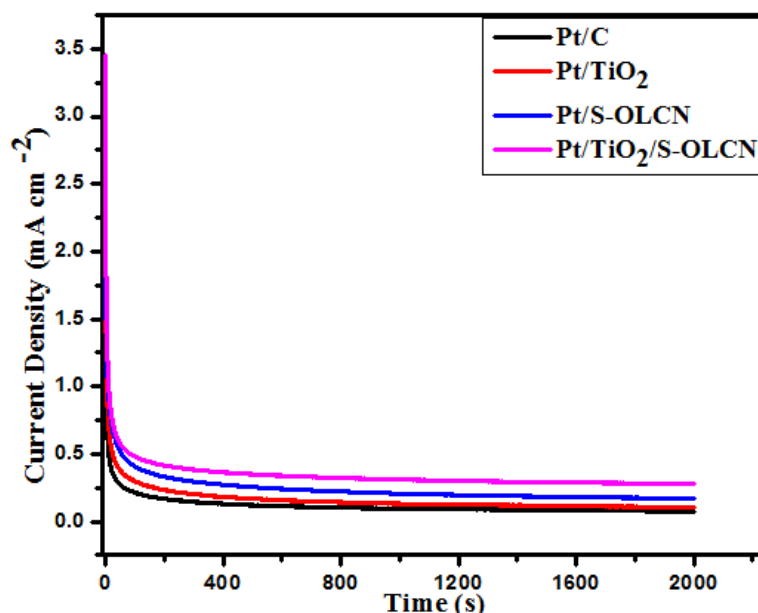


Figure 5.9: CA curves for Pt/C, Pt/TiO₂, Pt/S-OLCN and Pt/TiO₂/S-OLCN electrocatalysts in 1 M KOH + 1M NH₄OH at the potential peak of the ammonia oxidation.

5.2.4. Electrochemical impedance spectroscopy (EIS)

EIS measurements were carried out to investigate the electrode/electrolyte interface resistance and the reaction kinetics of the Pt-based nanocatalysts towards the ammonia oxidation in alkaline electrolyte. Nyquist plots at the constant potential of -0.2 V of the Pt/C, Pt/TiO₂, Pt/S-OLCN and Pt/TiO₂/S-OLCN modified electrodes in Ar saturated of 1 M KOH containing 1M NH₄OH solution are shown in Fig. 5.10. Nyquist impedance plots of the Pt-based electrocatalysts from 1000 kHz to 0.005 Hz were recorded. The relevant parameters (solution resistance (R_s), charge transfer resistance (R_{CT}) and Warburg impedance (Z_w)) are summarized in Table 5.4 [50]. The Nyquist impedance arc is shown in Fig. 5.10, the data show that the Pt/TiO₂/S-OLCN electrocatalyst exhibits the faster charge transmission

and highest conductivity. These results are consistent with the catalytic activity obtained from the CV and CA data.

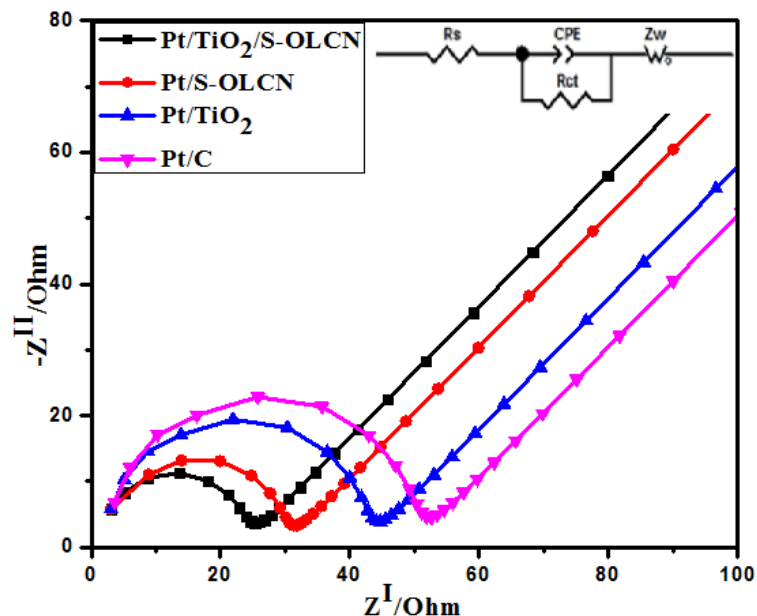


Figure 5.10: Nyquist plots of Pt/C, Pt/TiO₂, Pt/S-OLCN and Pt/TiO₂/S-OLCN electrocatalysts in 1 M KOH + 1M NH₄OH and along with the equivalent circuit (inset).

Table 5.4: Electrochemical impedimetric data of Pt/C, Pt/TiO₂, Pt/S-OLCN and Pt/TiO₂/S-OLCN electrocatalysts

1M KOH + 1 M NH ₄ OH				
Electrocatalysts	R _s (Ohm)	R _{ct} (Ohm)	CPE (μF)	Z _w (Ω s ^{-1/2})
Pt/C	21.5± 0.45	51.2± 3.32	164.9± 8.61	6.0E-06
Pt/TiO ₂	19.9± 0.41	43.1± 2.95	158± 9.24	8.0E-06
Pt/S-OLCN	13.8± 0.47	30.9± 3.75	172± 5.34	5.0E-06
Pt/TiO ₂ /S-OLCN	11.1±0.42	24.7±3.63	167.6± 7.48	7.0E-06

Conclusions

In this study, sulfur doped onion-like carbon nanoparticles (S-OLCNs) were successfully synthesized in a one-step flame pyrolysis method using thiophene as both the carbon and sulfur source. The $\text{TiO}_2/\text{S-OLCN}$ composite support material was designed to have well dispersed titania nanoparticles on a carbon nano onion surface using a hydrothermal reaction process. The ultrafine Pt nanoparticles were successfully deposited on the S-OLCN, TiO_2 and $\text{TiO}_2/\text{S-OLCN}$ surfaces by the alcohol assisted reduction method. The TEM, XRD and XPS results confirmed the formation of highly decorated ultrafine Pt NPs with an average diameter of 2.0 nm that were strongly bonded to the S-OLCN, TiO_2 and $\text{TiO}_2/\text{S-OLCN}$ framework. The ternary composite-modified ($\text{Pt}/\text{TiO}_2/\text{S-OLCN}$) electrode demonstrated higher catalytic performance, better long-term stability and smaller charge transfer resistance for the ammonia oxidation reaction in alkaline medium as compared to Pt/S-OLCN, Pt/ TiO_2 , and Pt/C modified electrodes. It was suggested that the superior electrocatalytic performance resulted from a strong Pt-support interaction and the better accessibility of ultrafine Pt nanoparticles to the reactants on the $\text{TiO}_2/\text{S-OLCN}$ composite support material. A protecting effect of $\text{TiO}_2/\text{S-OLCN}$ towards Pt that evades the adsorption of ammonia and nitrogenous intermediates on the platinum surface was observed. Therefore, the $\text{Pt}/\text{TiO}_2/\text{S-OLCN}$ electrocatalyst is a good anode electrocatalyst for ammonia tolerant-oxidation reaction in direct alkaline fuel cells. Further studies to explore this electrocatalyst type are underway.

Acknowledgments

This work is based on the research supported in part by the National Research Foundation (NRF) of South Africa (Grant Numbers: 118137, 118148), the University of the Witwatersrand (Postgraduate Merit Award, University Research Council) and a NRF-DAAD grant (Grant number: 117841). The authors also acknowledge the efforts and support provided by the University of Johannesburg (Faculty of Science, University Research Council, and Centre for Nanomaterials

Science Research). We also wish to acknowledge Mr. Siyasanga Mpelane at the University of Johannesburg (Auckland Park) for the high magnification TEM data.

References

- [1] J.R. Barbosa, M.N. Leon, C.M. Fernandes, R.M. Antoniassi, O.C. Alves, E.A. Ponzio, J.C.M. Silva, PtSnO₂/C and Pt/C with preferential (100) orientation: High active electrocatalysts for ammonia electro-oxidation reaction, *Appl. Catal. B Environ.* 264 (2020) 118458. <https://doi.org/10.1016/j.apcatb.2019.118458>.
- [2] L.A. Diaz, G.G. Botte, Mathematical modeling of ammonia electrooxidation kinetics in a Polycrystalline Pt rotating disk electrode, *Electrochim. Acta.* 179 (2015) 519–528. <https://doi.org/10.1016/j.electacta.2014.12.162>.
- [3] K. Endo, Y. Katayama, T. Miura, Pt–Ir and Pt–Cu binary alloys as the electrocatalyst for ammonia oxidation, *Electrochim. Acta.* 49 (2004) 1635–1638. <https://doi.org/10.1016/j.electacta.2003.11.024>.
- [4] Y. Zhao, B.P. Setzler, J. Wang, J. Nash, T. Wang, B. Xu, Y. Yan, An Efficient Direct Ammonia Fuel Cell for Affordable Carbon-Neutral Transportation, *Joule.* 3 (2019) 2472–2484. <https://doi.org/10.1016/j.joule.2019.07.005>.
- [5] J.C.M. Silva, S.G. Da Silva, R.F.B. De Souza, G.S. Buzzo, E. V. Spinacé, A.O. Neto, M.H.M.T. Assumpção, PtAu/C electrocatalysts as anodes for direct ammonia fuel cell, *Appl. Catal. A Gen.* 490 (2015) 133–138. <https://doi.org/10.1016/j.apcata.2014.11.015>.
- [6] C. Zhong, W.B. Hu, Y.F. Cheng, Recent advances in electrocatalysts for electro-oxidation of ammonia, *J. Mater. Chem. A.* 1 (2013) 3216–3238. <https://doi.org/10.1039/c2ta00607c>.
- [7] M.J. Lázaro, S. Ascaso, S. Pérez-Rodríguez, J.C. Calderón, M.E. Gálvez, M.J. Nieto, R. Moliner, A. Boyano, D. Sebastián, C. Alegre, L. Calvillo, V. Celorrio, Carbon-based catalysts: Synthesis and applications, *Comptes Rendus Chim.* 18 (2015) 1229–1241. <https://doi.org/10.1016/j.crci.2015.06.006>.

- [8] X. Chen, F. He, Y. Shen, Y. Yang, H. Mei, S. Liu, T. Mori, Y. Zhang, Effect of Carbon Supports on Enhancing Mass Kinetic Current Density of Fe-N/C Electrocatalysts, *Chem. - A Eur. J.* 23 (2017) 14597–14603. <https://doi.org/10.1002/chem.201703020>.
- [9] A. Shaikh, B.K. Singh, D. Mohapatra, S. Parida, Nitrogen-Doped Carbon Nano-Onions as a Metal-Free Electrocatalyst, *Electrocatalysis*. 10 (2019) 222–231.
- [10] V. Dhand, M. Yadav, S.H. Kim, K.Y. Rhee, A comprehensive review on the prospects of multi-functional carbon nano onions as an effective, high-performance energy storage material, *Carbon N. Y.* 175 (2021) 534–575. <https://doi.org/10.1016/j.carbon.2020.12.083>.
- [11] A. Camisasca, A. Sacco, R. Brescia, S. Giordani, Boron/Nitrogen-Codoped Carbon Nano-Onion Electrocatalysts for the Oxygen Reduction Reaction, *ACS Appl. Nano Mater.* 1 (2018) 5763–5773. <https://doi.org/10.1021/acsanm.8b01430>.
- [12] A. Priyadarsini, B.S. Mallik, Effects of Doped N, B, P, and S Atoms on Graphene toward Oxygen Evolution Reactions, *ACS Omega*. 6 (2021) 5368–5378. <https://doi.org/10.1021/acsomega.0c05538>.
- [13] Z. Yang, Z. Yao, G. Li, G. Fang, H. Nie, Z. Liu, X. Zhou, X. Chen, S. Huang, Sulfur-Doped Graphene as an Efficient Metal-free Cathode Catalyst for Oxygen Reduction, *ACS Nano*. 6 (2012) 205–211. <https://doi.org/10.1021/nn203393d>.
- [14] J.J. Fan, Y.J. Fan, R.X. Wang, S. Xiang, H.G. Tang, S.G. Sun, A novel strategy for the synthesis of sulfur-doped carbon nanotubes as a highly efficient Pt catalyst support toward the methanol oxidation reaction, *J. Mater. Chem. A*. 5 (2017) 19467–19475. <https://doi.org/10.1039/c7ta05102f>.
- [15] T.L. Lomocso, E.A. Baranova, Electrochemical oxidation of ammonia on carbon-supported bi-metallic PtM (M = Ir, Pd, SnOx) nanoparticles, *Electrochim. Acta*. 56 (2011) 8551–8558. <https://doi.org/10.1016/j.electacta.2011.07.041>.

- [16] P. Munnik, P.E. De Jongh, K.P. De Jong, Recent Developments in the Synthesis of Supported Catalysts, *Chem. Rev.* 115 (2015) 6687–6718. <https://doi.org/10.1021/cr500486u>.
- [17] F. Chekin, S. Bagheri, S.B. Abd Hamid, Synthesis of Pt doped TiO₂ nanoparticles: Characterization and application for electrocatalytic oxidation of L-methionine, *Sensors Actuators, B Chem.* 177 (2013) 898–903. <https://doi.org/10.1016/j.snb.2012.12.002>.
- [18] C. Martín, G. Solana, P. Malet, V. Rives, Nb₂O₅-supported WO₃: A comparative study with WO₃/Al₂O₃, *Catal. Today.* 78 (2003) 365–376. [https://doi.org/10.1016/S0920-5861\(02\)00301-2](https://doi.org/10.1016/S0920-5861(02)00301-2).
- [19] S. Bagheri, N. Muhd Julkapli, S. Bee Abd Hamid, Titanium dioxide as a catalyst support in heterogeneous catalysis, *Sci. World J.* 2014 (2014) 14925–14931. <https://doi.org/10.1155/2014/727496>.
- [20] B. Ruiz-Camacho, O. Martínez-Álvarez, H.H. Rodríguez-Santoyo, V. Granados-Alejo, Pt/C and Pt/TiO₂-C electrocatalysts prepared by chemical vapor deposition with high tolerance to alcohols in oxygen reduction reaction, *J. Electroanal. Chem.* 725 (2014) 19–24. <https://doi.org/10.1016/j.jelechem.2014.04.019>.
- [21] S.S. Gwebu, T. Matthews, W.N. Maxakato, Pt Nanoparticles on Carbon Nanodots-Titania Composite for Enhanced Electro Oxidation of Alcohol Fuels, *J. Electrochem. Energy Convers. Storage.* 19 (2022) 1–8. <https://doi.org/10.1115/1.4050000>.
- [22] J. Liu, B. Liu, Z. Ni, Y. Deng, C. Zhong, W. Hu, Improved catalytic performance of Pt/TiO₂ nanotubes electrode for ammonia oxidation under UV-light illumination, *Electrochim. Acta.* 150 (2014) 146–150. <https://doi.org/10.1016/j.electacta.2014.10.119>.
- [23] S. Li, H. Chen, J. Liu, Y. Deng, X. Han, W. Hu, C. Zhong, Size- and Density-Controllable Fabrication of the Platinum Nanoparticle/ITO Electrode by

Pulse Potential Electrodeposition for Ammonia Oxidation, *ACS Appl. Mater. Interfaces*. 9 (2017) 27765–27772. <https://doi.org/10.1021/acsami.7b08604>.

[24] D. Mohapatra, G. Dhakal, M.S. Sayed, B. Subramanya, J.J. Shim, S. Parida, Sulfur Doping: Unique Strategy To Improve the Supercapacitive Performance of Carbon Nano-onions, *ACS Appl. Mater. Interfaces*. 11 (2019) 8040–8050. <https://doi.org/10.1021/acsami.8b21534>.

[25] S. Meenakshi, K.G. Nishanth, P. Sridhar, S. Pitchumani, Spillover effect induced Pt-TiO₂/C as ethanol tolerant oxygen reduction reaction catalyst for direct ethanol fuel cells, *Electrochim. Acta*. 135 (2014) 52–59. <https://doi.org/10.1016/j.electacta.2014.04.142>.

[26] L.L. Sikeyi, T.D. Ntuli, T.H. Mongwe, N.W. Maxakato, E. Carleschi, B.P. Doyle, N.J. Coville, M.S. Maubane-Nkadimeng, Microwave assisted synthesis of nitrogen doped and oxygen functionalized carbon nano onions supported palladium nanoparticles as hybrid anodic electrocatalysts for direct alkaline ethanol fuel cells, *Int. J. Hydrogen Energy*. 46 (2021) 10862–10875. <https://doi.org/10.1016/j.ijhydene.2020.12.154>.

[27] T.D. Ntuli, T.H. Mongwe, L.L. Sikeyi, O. Mkhari, N.J. Coville, E.N. Nxumalo, M.S. Maubane-Nkadimeng, Removal of hexavalent chromium via an adsorption coupled reduction mechanism using olive oil derived carbon nano-onions, *Environ. Nanotechnology, Monit. Manag.* 16 (2021) 100477. <https://doi.org/10.1016/j.enmm.2021.100477>.

[28] O. Butsyk, P. Olejnik, E. Romero, M.E. Plonska-Brzezinska, Postsynthetic treatment of carbon nano-onions: Surface modification by heteroatoms to enhance their capacitive and electrocatalytic properties, *Carbon N. Y.* 147 (2019) 90–104. <https://doi.org/10.1016/j.carbon.2019.02.063>.

[29] H. Sun, G. Li, A. Xu, Z. Xu, S. Wu, Sulfur-doped hollow soft-balled mesoporous carbon particles as ultra-fast, durable hosts for potassium storage, *J. Alloys Compd.* 906 (2022) 164311. <https://doi.org/10.1016/j.jallcom.2022.164311>.

- [30] S.R. Kamali, C.N. Chen, D.C. Agrawal, T.H. Wei, Sulfur-doped carbon dots synthesis under microwave irradiation as turn-off fluorescent sensor for Cr(III), *J. Anal. Sci. Technol.* 12 (2021). <https://doi.org/10.1186/s40543-021-00298-y>.
- [31] Y. Qiu, J. Huo, F. Jia, B.H. Shanks, W. Li, N- and S-doped mesoporous carbon as metal-free cathode catalysts for direct biorenewable alcohol fuel cells, *J. Mater. Chem. A.* 4 (2015) 83–95. <https://doi.org/10.1039/c5ta06039g>.
- [32] K. Bogdanov, A. Fedorov, V. Osipov, T. Enoki, K. Takai, T. Hayashi, V. Ermakov, S. Moshkalev, A. Baranov, Annealing-induced structural changes of carbon onions: High-resolution transmission electron microscopy and Raman studies, *Carbon* N. Y. 73 (2014) 78–86. <https://doi.org/10.1016/j.carbon.2014.02.041>.
- [33] L.L. Sikeyi, T.D. Ntuli, T.H. Mongwe, N.W. Maxakato, N.J. Coville, M.S. Maubane-Nkadimeng, Platinum Nanoparticles Loaded on Pristine and Boron Oxide Modified Carbon Nano-Onions for Enhanced Ammonia Electrooxidation in Alkaline Direct Ammonia Fuel Cells, *J. Electroanal. Chem.* 917 (2022) 116411. <https://doi.org/10.2139/ssrn.3982297>.
- [34] V. Mashindi, P. Mente, N. Mpofo, T.N. Phaahlamohlaka, O. Makgae, A.I. Kirkland, R. Forbes, K.I. Ozoemena, P.B. Levecque, N.J. Coville, Platinum supported on pristine and nitrogen-doped bowl-like broken hollow carbon spheres as oxygen reduction reaction catalysts, *J. Appl. Electrochem.* 51 (2021) 991–1008. <https://doi.org/10.1007/s10800-021-01554-0>.
- [35] L.M. Ahmed, I. Ivanova, F.H. Hussein, D.W. Bahnemann, Role of platinum deposited on TiO₂ in photocatalytic methanol oxidation and dehydrogenation reactions, *Int. J. Photoenergy.* 2014 (2014) 5564–5568. <https://doi.org/10.1155/2014/503516>.
- [36] Q. Zhang, W. Huang, J. ming Hong, B.Y. Chen, Deciphering acetaminophen electrical catalytic degradation using single-form S doped graphene/Pt/TiO₂, *Chem. Eng. J.* 343 (2018) 662–675. <https://doi.org/10.1016/j.cej.2018.02.089>.

- [37] J. Wang, M. Xu, J. Zhao, H. Fang, Q. Huang, W. Xiao, T. Li, D. Wang, Anchoring ultrafine Pt electrocatalysts on TiO₂-C via photochemical strategy to enhance the stability and efficiency for oxygen reduction reaction, *Appl. Catal. B Environ.* 237 (2018) 228–236. <https://doi.org/10.1016/j.apcatb.2018.05.085>.
- [38] K. Zhang, J. Qiu, J. Wu, Y. Deng, Y. Wu, L. Yan, Morphological tuning engineering of Pt@TiO₂/graphene catalysts with optimal active surfaces of support for boosting catalytic performance for methanol oxidation, *J. Mater. Chem. A.* 10 (2022) 4254–4265. <https://doi.org/10.1039/d1ta09359b>.
- [39] R. Cui, S. Liu, X. Guo, H. Huang, J. Wang, B. Liu, Y. Li, D. Zhao, J. Dong, B. Sun, N-Doping Holey Graphene TiO₂-Pt Composite as Efficient Electrocatalyst for Methanol Oxidation, *ACS Appl. Energy Mater.* 3 (2020) 2665–2673. <https://doi.org/10.1021/acsaem.9b02364>.
- [40] Y. Guo, L. Tang, Y. Zhang, H. Wei, X. Shu, J. Cui, Y. Wang, J. Liu, Q. Li, X. Sun, Y. Wu, Construction of three-dimensional hierarchical Pt/TiO₂@C nanowires with enhanced methanol oxidation properties, *Int. J. Hydrogen Energy.* 45 (2020) 33440–33447. <https://doi.org/10.1016/j.ijhydene.2020.09.052>.
- [41] Y. Pei, Y. Niu, W. Zhang, Y. Zhang, J. Ma, Z. Li, Ionic liquid microemulsion mediated synthesis of Pt/TiO₂ nanocomposites for ammonia borane hydrolysis, *Int. J. Hydrogen Energy.* 47 (2022) 2819–2831. <https://doi.org/10.1016/j.ijhydene.2021.10.215>.
- [42] L. Xiong, A. Manthiram, Synthesis and characterization of methanol tolerant Pt/TiO_x/C nanocomposites for oxygen reduction in direct methanol fuel Cells, *Electrochim. Acta.* 49 (2004) 4163–4170. <https://doi.org/10.1016/j.electacta.2004.04.011>.
- [43] H.J. Kim, D.Y. Kim, H. Han, Y.G. Shul, PtRu/C-Au/TiO₂ electrocatalyst for a direct methanol fuel cell, *J. Power Sources.* 159 (2006) 484–490. <https://doi.org/10.1016/j.jpowsour.2005.10.101>.

- [44] H.Y. Sun, G.R. Xu, F.M. Li, Q.L. Hong, P.J. Jin, P. Chen, Y. Chen, Hydrogen generation from ammonia electrolysis on bifunctional platinum nanocubes electrocatalysts, *J. Energy Chem.* 47 (2020) 234–240. <https://doi.org/10.1016/j.jechem.2020.01.035>.
- [45] D. Mohapatra, G. Dhakal, M.S. Sayed, B. Subramanya, J. Shim, S. Parida, Sulfur Doping: Unique Strategy To Improve the Supercapacitive Performance of Carbon Nano-onions, *ACS Appl. Mater. Interfaces.* 11 (2019) 8040–8050. <https://doi.org/10.1021/acsami.8b21534>.
- [46] S. Ntais, A. Serov, N.I. Andersen, A.J. Roy, E. Cossar, A. Allagui, Z. Lu, X. Cui, E.A. Baranova, P. Atanassov, Promotion of Ammonia Electrooxidation on Pt nanoparticles by Nickel Oxide Support, *Electrochim. Acta.* 222 (2016) 1455–1463. <https://doi.org/10.1016/j.electacta.2016.11.124>.
- [47] O. Dulub, W. Hebenstreit, U. Diebold, Imaging cluster surfaces with atomic resolution: The strong metal-support interaction state of pt supported on TiO₂(110), *Phys. Rev. Lett.* 84 (2000) 3646–3649. <https://doi.org/10.1103/PhysRevLett.84.3646>.
- [48] S.S. Gwebu, P.N. Nomngongo, N.W. Maxakato, Pt/CNDs-TiO₂ electrocatalyst for direct alcohol fuel cells, *Mater. Today Proc.* 5 (2018) 10460–10469. <https://doi.org/10.1016/j.matpr.2017.12.377>.
- [49] Q. Zhang, W. Huang, J. ming Hong, B.Y. Chen, Deciphering acetaminophen electrical catalytic degradation using single-form S doped graphene/Pt/TiO₂, *Chem. Eng. J.* 343 (2018) 662–675. <https://doi.org/10.1016/j.cej.2018.02.089>.
- [50] E. Hernández-Balaguera, H. Vara, J.L. Polo, An electrochemical impedance study of anomalous diffusion in PEDOT-coated carbon microfiber electrodes for neural applications, *J. Electroanal. Chem.* 775 (2016) 251–257. <https://doi.org/10.1016/j.jelechem.2016.06.007>.

CHAPTER 6

Ag and Zn promoted Pd-based electrocatalyst for enhanced methanol oxidation in alkaline direct methanol fuel cells

This chapter will be submitted in the journal.

1. Sikeyi - Synthesis and characterization, Writing-Original Draft, Validation
2. Bila - Software
3. Ntuli – Data Curation
4. Maxakato - Resources, Supervision
5. Coville - Reviewing and Editing, Resources, Supervision
6. Maubane-Nkadimeng- Conceptualization, Resources, Supervision

Ludwe L Sikeyi^a, Themba D Ntuli^{a,d}, Laercia Bila^a, Nobanathi W Maxakato^b, Neil J Coville^{a,c} and Manoko S Maubane-Nkadimeng^{a,c,d} *

^a Molecular Sciences Institute, School of Chemistry, University of Witwatersrand, Braamfontein, 2050, South Africa, ^b Department of Chemical Science, University of Johannesburg, Doornfontein, 2021, South Africa. ^c DSI-NRF Centre of Excellence in Strong Materials, University of Witwatersrand, Braamfontein, 2050, South Africa. ^d Microscopy and Microanalysis Unit, University of Witwatersrand, Braamfontein, 2050, South Africa

Abstract

Bimetallic (Pd/Ag and Pd/Zn) electrocatalysts supported on nitrogen-doped onion-like carbon nanoparticles (N-OLCNs) were prepared in a one pot synthesis method using sodium borohydride as a reducing agent. The N-OLCNs with rich defective sites were synthesized using a flame pyrolysis method, using acetonitrile as both carbon source and the doping agent. X-ray diffraction data showed the formation of Pd/Ag and Pd/Zn alloys supported on the surface of the N-OLCNs. Transmission electron microscopy analysis confirmed the existence of well

dispersed, spherically shaped Pd/Ag (16.9 ± 4.8 nm) and Pd/Zn (10.4 ± 1 nm) on the surface of the N-OLCNs. The Pd/N-OLCN, Pd/Ag/N-OLCN, Pd/Zn/N-OLCN and Pd/C electrocatalysts were studied in the methanol oxidation reaction (MOR). The incorporation of Ag and Zn improved the Pd/N-OLCN physiochemical properties and catalytic performance towards MOR in alkaline electrolyte. The bimetallic (Pd/Ag/N-OLCN and Pd/Zn/N-OLCN) electrocatalysts exhibited superior anti-poisoning tolerance, better electrocatalytic stability and fast charge transfer resistance as compared to monometallic (Pd/N-OLCN and Pd/C) electrocatalysts in the methanol electrooxidation in alkaline media. The electron transfer from the Ag^+ and Zn^{2+} species to the Pd, modified the active sites of Pd by increasing the electron density at Pd and hence promoted the desorption of methanol. Furthermore, the improved catalytic performance could be related to the strong metal–support interaction.

Keywords: Cyclic voltammetry; Electrocatalysts; Direct methanol fuel cell; Nitrogen doping; Onion like carbon nanoparticles.

6. Introduction

In the past few decades, the development of direct alcohol fuel cells (DAFCs) as powerful energy sources has attracted tremendous interest, due to their reasonable power density and high electromotive force for portable electronic devices and electric vehicles [1]. DAFCs are devices in which chemical energy is stored in small alcohol molecules that are directly converted into electrical energy via electrochemical reactions [2]. Liquid alcohol fuels, such as ethanol and methanol, are the most popular type of fuels used in DAFCs due to their high energy density, low cost, facile handling, and easy storage. However, the slow kinetics for the ethanol oxidation reaction (EOR) is a major barrier at the anode that limits the development of direct ethanol fuel cells (DEFCs) [3]. The cleavage of the C-C bond in the ethanol molecule is a difficult step as compared to C-H bond cleavage [4]. Furthermore, the removal of water and residues from ethanol oxidation reactions are critical for obtaining a high electrooxidation activity.

Therefore, significant research efforts have been devoted to the development of metal-carbon based electrocatalysts for the direct methanol fuel cells (DMFCs) [5].

The oxidation kinetics of methanol is faster in alkaline electrolytes such as potassium hydroxide or sodium hydroxide as compared to acid electrolytes such as sulphuric acid [6]. Use of basic media allows for utilizing cost effective metal based electrocatalysts that can facilitate the development of the DMFC. Thus, Pd-based nanostructured electrocatalysts have been shown to be excellent catalysts in methanol oxidation reactions in alkaline conditions [7].

The use of palladium in the commercialization of DMFCs is, however, limited due to its expense. Alloying Pd catalysts with cheaper metals like Zn, Fe, Ag, Co, and Ni has become an approach to form less expensive bimetallic catalysts for the methanol electro-oxidation reaction in alkaline media [8,9]. Furthermore, alloying Pd with a metal of smaller lattice constant is expected to result in a Pd lattice contraction, which will moderate the oxygen species chemisorptive bond strength [10]. Thus, bimetallic nanocatalysts have shown enhanced catalytic activity when compared to their monometallic counterparts [11]. For example, Yang et al. reported on bimetallic Pd-Ag/C nanocatalysts with different particle sizes (synthesized using a one-pot solvothermal co-reduction method) for formic acid oxidation reactions. The Pd-Ag-S/C (S-smaller size) electrocatalyst exhibited higher catalytic activity as compared to Pd-Ag-L/C (L-larger size) and the commercial Pd/C. This was suggested to be due to generation of a higher electrochemical surface area (ECSA) due to the smaller metal particle sizes [12]. Bampos et al. prepared bimetallic Pd-Zn/C electrocatalysts with different mass ratios (3:1 to 1:3) using a wet impregnation method for the oxygen reduction reaction (ORR) in 0.1 M HClO₄ electrolyte. The Pd-Zn(3:1)/C bimetallic electrocatalyst with a higher mass ratio of Pd showed better ORR activity than a Pd-Zn(1:3)/C catalyst, and a Pd/C electrocatalyst, in 0.1 M HClO₄ electrolyte [13]. Thus, studies have shown that combining Pd with Zn and Ag not only changes the properties of Pd, but also enhances its activity and resistance, and also reduces the cost of the electrodes for use of Pd electrocatalysts in DMFCs.

Carbon support materials play a major role in enhancing the catalytic activity of the electrocatalysts in direct alcohol fuel cells. Amongst the carbon nano materials, spherically shaped carbons have been used in a wide range of applications such as in supercapacitors, electrochemical catalysis, energy storage, sensors and water treatment [14–16]. For these applications, the carbons are required to possess a large external surface area, nanoscopic size, high electrical conductivity, large-scale synthesis and excellent tribological behavior [17]. The quasi-spherical nanostructure, the concentric graphene shells and graphitic defects, of carbon can enhance the chemical reactivity of spherical carbons [18]. The spherically shaped carbon family includes both carbon nano onions (CNOs) and their related onion-like nano-carbon counterparts (OLCNs); OLCNs are often referred to as CNOs even though in many cases they do not have a true onion like structure. These CNOs/OLCNs have been employed as catalyst supports in fuel cells [19]. The electronic transport and structure of CNOs/OLCNs can be tailored by heteroatom doping. In particular, the existence of nitrogen heteroatoms in the spherical structure can strongly improve the electrocatalytic activity of the carbon through Faradaic redox reactions created by graphitic-N, pyrrolic N (N–H), pyridinic-N and pyridinic N+–O- [20] bonds. Furthermore, nitrogen doping increases the charge carrier density, specific surface area, and electron transport of carbons [21]. The nitrogen doping into the sp²-hybridized carbon structure can modify their surface chemical activities, electronic structures and provide an alternative strategy to improve the catalytic activity of the electrocatalyst [22].

This study has focused on improving the direct methanol alkaline fuel cell (DMAFC) performance by using highly active ternary Pd/Ag/N-OLCN and Pd/Zn/N-OLCN electrocatalysts in a basic (sodium hydroxide) electrolyte. N-OLCNs were prepared by a flame pyrolysis method in one step using acetonitrile as a carbon source and a nitrogen precursor [18]. The bimetallic Pd-Ag, Pd-Zn and monometallic Pd nanoparticles, supported over the N-OLCNs, were synthesized using a one pot synthesis method. The ternary Pd/Zn/N-OLCN electrocatalyst exhibited superior catalytic activity, better long-term stability and fast electron transfer for methanol oxidation reactions in alkaline media when

compared to Pd/Ag/N-OLCN, Pd/N-OLCN and commercial Pd/C electrocatalysts. A proposal for this observation is reported.

6.1 Experimental

6.1.1. Materials and methods

The following materials, without purification, were used to prepare the electrocatalysts and electrolyte solutions used in this study: sodium borohydride > 99.5% (Sigma-Aldrich), Nafion solution > 5 wt.%, (Sigma-Aldrich), palladium chloride > 98.0% (Sigma-Aldrich), silver chloride > 98.0% (Sigma-Aldrich), zinc chloride > 98.0% (Sigma-Aldrich), Pd/C commercial standard > 10% loading (Sigma-Aldrich), acetonitrile > 99.5% (Sigma-Aldrich), sodium hydroxide pellets (Sigma-Aldrich) and methanol > 99.9% (Sigma-Aldrich).

6.1.2. Synthesis of nitrogen doped onion-like carbon nanoparticles (N-OLCNs)

N-OLCN nanoparticles were prepared using the flame pyrolysis method as previously reported [18]. In summary, the required quantity of acetonitrile was placed in a 100 mL glass beaker and ignited in air in a fume hood conditions to prevent the emission of any dangerous gases. The set-up was made to collect the carbon particles as they were produced, which were placed over a conical flask filled with water for cooling. No post-processing or purification was undertaken (yield 3.5%).

6.1.3. Synthesis of Ag/N-OLCN, Zn/N-OLCN, Pd/N-OLCN, Pd/Ag/N-OLCN and Pd/Zn/N-OLCN electrocatalysts

The palladium-based electrocatalysts were synthesized using a one pot synthesis method [23]. Typically, 200 mg of N-OLCNs were mixed with a 20 mL solution of sodium borohydride under continuous stirring for 30 min. In the one-step synthesis of the monometallic and bimetallic nanoparticles, 13.3 mg of AgCl₂, 20.8 mg ZnCl₂ and 16.9 PdCl₂ were simultaneously dispersed into different mixtures of N-OLCNs, followed by reflux at 100 °C for 6 h. Firstly, in this method Ag/N-OLCN and Zn/N-

OLCN electrocatalysts were prepared by mixing 5% Ag and 5% Zn with different mixtures of N-OLCN support materials using borohydride reduction method. Secondly, in this procedure the two reactions were performed with 6% Pd: 4% Ag and 6% Pd: 4% Zn to give a 10% overall loading. The reaction mixture became dark grey within several minutes under reflux. The obtained slurries were centrifuged at 6000 rpm for 25 min and rinsed with double distilled water to remove residual chloride. The obtained monometallic and bimetallic (Ag/N-OLCN, Zn/N-OLCN, Pd/N-OLCN, Pd/Ag/N-OLCN and Pd/Zn/N-OLCN) electrocatalysts were dried in an oven at 100 °C for 24 h.

6.1.4. Physicochemical characterization

The structure and morphology of the samples were recorded using a JEOL transmission electron microscope (TEM) model JEM-2100F operated at 200 kV. Surface micrographs and energy dispersive X-ray (EDX) images of the samples were obtained using a ZEISS Sigma 300 VP Oxford Field Emission Scanning Electron Microscope (SEM) instrument. The thermal stability of the samples was investigated using a Perkin Elmer 6000 thermogravimetric (TGA) analyzer. The specific surface areas and porosity characterization of the samples were analyzed using the Brunauer-Emmett-Teller method (BET) with a Micromeritics Tristar 3000 surface area analyzer. Powder X-ray diffraction (PXRD) patterns of the samples were obtained on a Bruker D2 Phaser diffractometer using a Cu K α radiation source ($\lambda = 0.15405$ nm) generated at 30 kV and 10 mA. X-ray photoelectron spectroscopy (XPS) data of the samples were acquired on a Thermo Scientific ESCALAB 250Xi spectrometer with a monochromatic Al K α (1486.7 eV) source operating with an X-ray power of 300 W and high-resolution pass energy of 20 eV.

6.1.5. Electrochemical characterization

Electrochemical measurements were carried out using a Dropsens potentiostat. A glassy carbon (GC) electrode with a geometrical surface area of 0.196 cm² was utilized as a working electrode for cyclic voltammetry (CV), chronoamperometry (CA) and electrochemical impedance spectroscopy (EIS) measurements. A

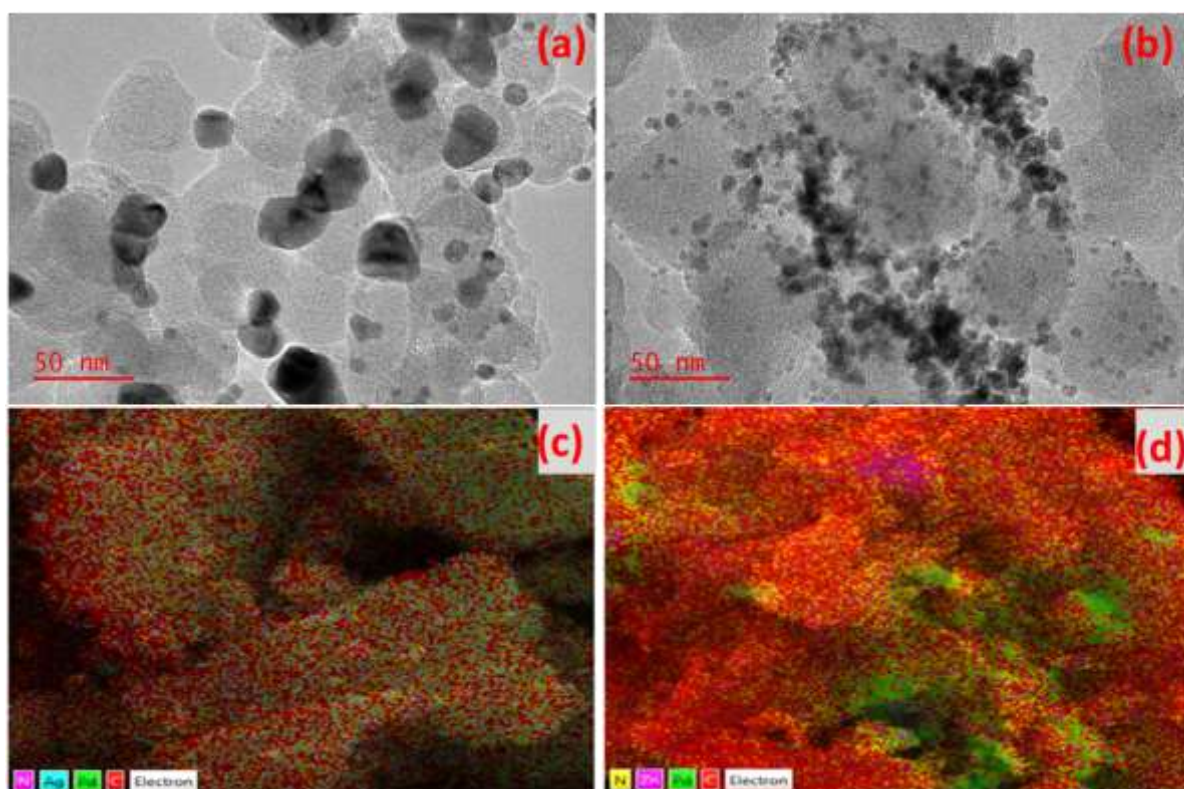
saturated silver silver chloride electrode (Ag/AgCl) and platinum wire were used as reference and counter electrodes, respectively. The working electrode was prepared using an ink made by dispersing 10 mg of nanocatalysts in 1 mL of isopropyl alcohol with 5 μ L Nafion solution (5 wt.%) and mixing for 15 min in an ultrasonic bath. After that, 15 μ L aliquot of the electrocatalyst inks was pipetted onto the surface of the glassy carbon electrode and dried at room temperature. The loading of Pt on the electrocatalysts on the glassy carbon electrode was around 0.052 mg cm⁻². Prior to any electrochemical studies, the electrolyte solution was purged with argon for 20 min to remove any oxygen from the solution. CV, CA and EIS measurements were performed in solutions containing aq. 1 M NaOH + 1 M CH₃OH saturated with argon gas. The electroactive surface area (ECSA) values of the Pt based electrocatalysts were normalized by the geometric surface area of the working electrode. Currents obtained in CV, CA and EIS experiments were normalized per ECSA of the platinum based electrocatalysts.

6.2. Results and discussion

6.2.1. Transmission electron microscopy (TEM) and Energy dispersive X-ray spectroscopy (EDS) mapping

Fig. S1 displays the TEM micrographs of the N-OLCN (inset the SAED image), Pd/N-OLCN Ag/N-OLCN and Zn/N-OLCN. Fig. S1 (a) reveals concentric turbostratic shells for the N-OLCN with disordered concentric multiple layers with an interplanar spacing of ca. 0.33 nm [24] and the SAED image confirms that the material is amorphous. As shown in Fig. S1 (b) the palladium nanoparticles were well dispersed onto the surface of N-OLCN [24]. From TEM images, the mean Pd particle size of Pd/N-OLCN was found to be 4.7 nm. Silver nanoparticles were dispersed on the N-OLCN with particle size ranging from 15-20 nm. Zinc nanoparticles were agglomerated onto the surface of N-OLCN support material. The data indicate that the Ag and the Zn do not disperse well on the N-OLCN surface.

Fig. 6.1 shows the typical TEM images, EDS mapping and particle size distribution of the as prepared bimetallic Pd/Ag/N-OLCN and Pd/Zn/N-OLCN catalysts. As shown in Fig. 1(a) Pd/Ag nanoparticles are better dispersed on the surface of the N-OLCN support material with a wide range of particle sizes and an average size of 16.9 ± 4.8 nm (Fig. 6.1(e)). Fig. 6.1(b) shows well distributed Pd/Zn nanoparticles on the N-OLCN support surface with some agglomeration of the metal crystallites. The average Pd/Zn nanoparticle size was found to be 10.4 ± 1.8 nm. The EDS mapping shown in Fig. 6.1(c and d), confirmed the existence of carbon, nitrogen, silver, zinc and palladium in the bimetallic Pd/Ag/N-OLCN and Pd/Zn/N-OLCN nanomaterials. This suggests that the Pd affects the Zn and Ag interaction with the carbon surface.



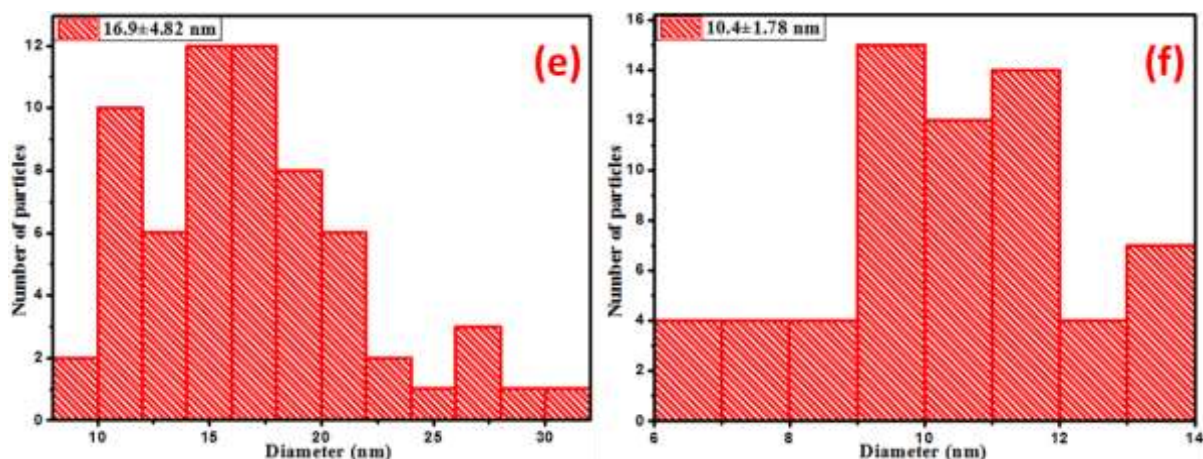


Figure 6.1: TEM micrographs, EDX mapping and average particle size of (a, c and e) Pd/Ag/N-OLCN, (b, d and f) Pd/Zn/N-OLCN nanomaterials.

6.2.2. Thermogravimetric analysis (TGA)

The TGA data for the N-OLCN, Zn/N-OLCN, Ag/N-OLCN, Pd/Zn/N-OLCN and Pd/Ag-N-OLCN nanocatalysts are presented in Fig. 6.2. The TGA profile of the mono and bimetallic nanomaterials shown in Fig. 6.2 (a).

A comparison of the TGA data of the N-OLCN with the metal loaded materials indicates that the Zn and Ag do not catalyze the carbon oxidation reaction. The derivative peaks all occur at ca. 640 °C with the exception being the Pd/Zn/N-OLCN catalyst. Here two peaks can be seen (deconvoluted) with first peak occurring at 562 °C. Also, the derivative peak of the Pd/N-OLCN occurs at ca 680 °C as shown in Fig. S2. Indeed closer inspection of the Pd/Ag/N-OLCN also reveals a shoulder at the low temperature side of the main peak. This would suggest that in both these samples two types of metal particles are formed with different carbon oxidation rates. The reason for this observation, is not clear at this stage, but may relate to particles with different Pd and Zn (or Ag) concentrations. The residual weight of both Zn/N-OLCN and Ag/N-OLCN is 6.2 % and for both Pd/Zn/N-OLCN and Pd/Ag/N-OLCN is 12.1% respectively. In addition, the residual weight of the Pd/N-OLCN is 9.8 % which is closer to the nominal 10% Pd loading (see Fig. S 2) [24].

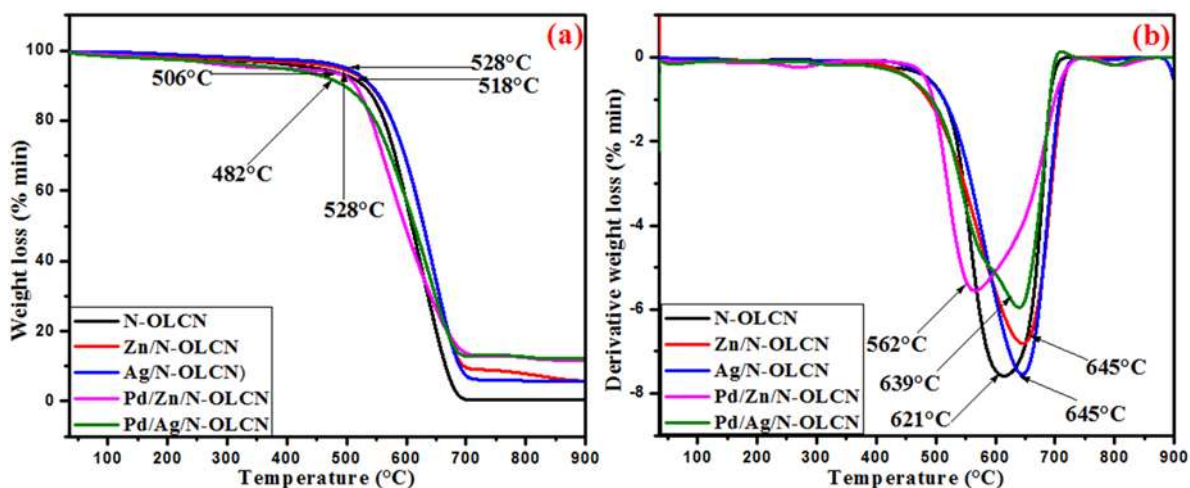


Figure 6.2: (a) TGA profile and (b) TGA derivatives of N-OLCN, Zn/N-OLCN, Ag/N-OLCN, Pd/Zn/N-OLCN and Pd/Ag/N-OLCN nanomaterials.

6.2.3. X-ray diffraction spectroscopy (XRD)

The XRD pattern for Pd/N-OLCN at 40.08° , 46.7° , 68.4° , and 82.0° are assigned to (111), (200), (220) and (222) planes of palladium facets (see Fig. S2) [25]. Fig. 6.3 shows the powder XRD patterns for the synthesized Zn/N-OLCN, Ag/N-OLCN, Pd/Zn/N-OLCN and Pd/Ag/N-OLCN nanomaterials. The XRD peak at 2θ value at ca. 25° for the mono and bimetallic nanomaterials is ascribed to the hexagonal system of C (002) graphite plane [26].

The XRD patterns for the Zn/N-OLCN and Pd/Zn/N-OLCN nanomaterials show the presence of Zn and Pd, respectively. The measured peak positions, 2θ , of the Pd/Zn/N-OLCN, Pd/Ag/N-OLCN, and Pd/N-OLCN crystalline planes from (111) to (222) are shown in Table S1. The four diffraction peaks at $2\theta = 31.2^\circ$, 33.7° , 35.9° , 46.9° and 67.6° were attributed to the wurtzite structure of ZnO while the peaks at 40.4° , 46.9° , 68.6° , and 82.3° corresponds to nanocrystalline Pd metal [9]. When comparing the XRD patterns for Pd in Pd/Zn/N-OLCN a greater positive shift of the Pd-Zn peaks to higher angle values is observed. This shift is an indication that Zn is alloyed to the palladium [9]. As shown in Fig. 6.3, the XRD peaks for Ag/N-OLCN at 38.1° and 46.1° correspond to Ag with fcc structure. The peaks for Pd/Ag/N-OLCN at 39.8° , 46.1° , 67.7° and 81.6° correspond to the Pd crystallographic (111), (200), (220), and (222) planes with the shifts suggesting the

formation of an fcc PdAg alloy. For Pd/Ag/N-OLCN the Pd peaks shift to a smaller 2θ angle due to the existence of Ag, indicating that the Pd is alloyed to Ag metal [27]. The average crystallite size of the Pd/Ag/N-OLCN and Pd/Zn/N-OLCN were estimated to be 15.5 nm, and 9.8 nm from the Pd (111) peak, using the Debye–Scherrer equation. XRD data are in good agreement with the data measured using TEM images. No characteristic peaks from other phases were detected.

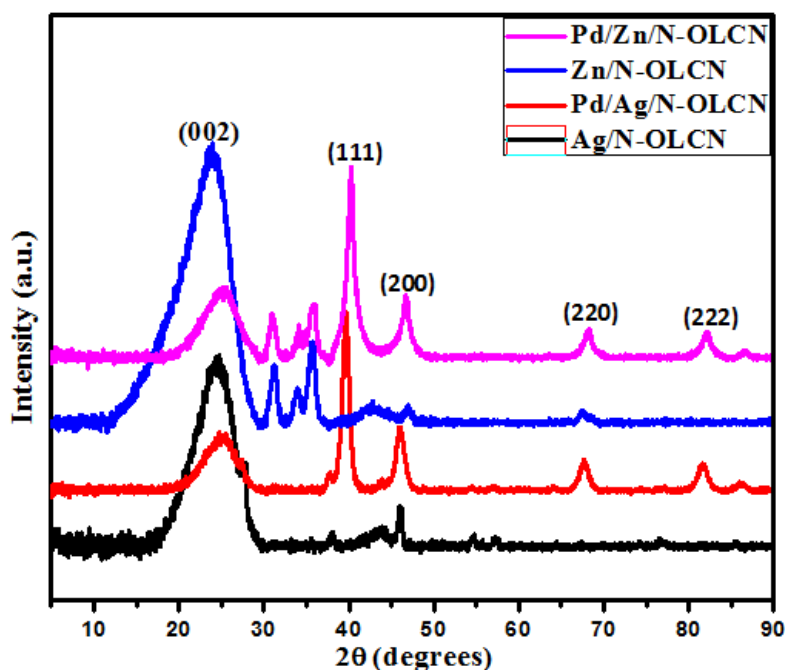


Figure 6.3: X-ray diffractograms of Ag/N-OLCN, Pd/Ag/N-OLCN, Zn/N-OLCN and Pd/Zn/N-OLCN nanomaterials.

6.2.4. X-ray photoelectron spectroscopy (XPS)

XPS measurements were carried out on Pd/Zn/N-OLCN and Pd/Ag/N-OLCN to determine the oxidation state and surface composition of the palladium bimetallic nanomaterials (Fig. 6.4). The XPS survey spectra confirmed the presence of C, O, N, Zn, and Ag and Pd elements in the two samples (Fig. S 4 (a)). The elemental composition of the Pd/Zn/N-OLCN and Pd/Ag/N-OLCN samples is shown in Table 6.1. The surface data are similar to that expected from the synthesis procedure used to make the 10% catalysts (6 % Pd).

Table 6.1: Elemental composition data obtained from Pd/Ag/N-OLCN and Pd/Zn/N-OLCN XPS data.

Sample	Carbon	Oxygen	Nitrogen	Zinc	Silver	Palladium
Pd/Zn/N-OLCN	81.8	4.3	3.5	4.4	-----	6.1
Pd/Ag/N-OLCN	82.1	4.5	3.3	-----	4.2	5.9

Deconvolution of the C 1s spectra of Pd/Zn/N-OLCN (Fig 6.4 (a)) and Pd/Ag/N-OLCN (see Fig. S 4 (b)) was performed and peaks were assigned to (C-C) sp² (284.2 eV), (C-C) sp³ (284.7 eV), (C-O) (285.7 eV), (C=O) (287.1 eV), (O-C=O) (288.7 eV) and (C-C) sp² (284.2 eV), (C-C) sp³ (284.7 eV), (C-O) (285.7 eV), (C=O) (287.1 eV) and (O-C=O) (288.5 eV), respectively [14]. Chemical identification and quantification of the constituents of the Pd/Zn/N-OLCN and Pd/Ag/N-OLCN nanomaterials are shown in Table S2. Fig. 6.4 (b) shows the deconvoluted peaks of the O 1s XPS spectra of Pd/Zn/N-OLCN and Pd/Ag/N-OLCN (see Fig. S 4 (b)) which were allocated to organic C-O (532.0 eV), organic C=O (533.4 eV), metal oxide (530.5 eV) and C-O (531.9 eV), organic C=O (533.3 eV), metal oxide (530.5 eV), respectively. The high-resolution N 1s XPS peak of Pd/Zn/N-OLCN is shown Fig. 6.4 (c) and Pd/Ag/N-OLCN(see Fig. S 4 (b)), were deconvoluted into four peaks that correspond to pyridine-type nitrogen (N-1) (397.5 eV), pyrrole type nitrogen (N-2) (400.3 eV), graphitic type nitrogen (N-3) (402.1 eV), oxidized type nitrogen (N-4) (404.2 eV) and pyridine-type nitrogen (N-1) (398.5 eV), pyrrole type nitrogen (N-2) (400.4 eV), graphitic type nitrogen (N-3) (402.1 eV), and oxidized type nitrogen (N-4) (404.3 eV), respectively [18]. The existence of these nitrogen species in the carbon structure provides abundant electrochemical active catalytic sites for an improved interaction and fuel cell behavior [25]. Fig. 6.4(d) shows the XPS Zn2p core level spectra of the Pd/Zn/N-OLCN nanomaterial, which was deconvoluted into two peaks at 1022.5 and 1045.5 eV. These corresponds to zinc oxide (Zn 2p^{3/2}) and metallic zinc (Zn 2p^{1/2}) respectively [28,29]. The high resolution XPS spectra of Ag 3d in Pd/Ag/N-OLCN nanomaterial was deconvoluted into two peaks at 367.4 eV and 373.1eV, which are ascribed to the metallic Ag⁰ and to Ag⁺ of Ag₂O, respectively (Fig. 6.4e) [30]. The incorporation of Ag and Zn modified the electronic structure of Pd, which was

confirmed by the downward shift of the Pd metal. In Fig. 6.4 (f) the high resolution XPS Pd 3d spectra for Pd/Zn/N-OLCN sample are fitted to two pairs of doublets, between 335.2 eV (3.8%) and 340.4 eV (2.3%), and Pd/Ag/N-OLCN(see Fig. S 4 (b)) sample are fitted to two pairs of doublets, between 335.1 eV (3.6%) and 340.5 eV (2.5%), confirming that the metallic Pd surface contains the Pd⁰ and Pd²⁺ species [31].

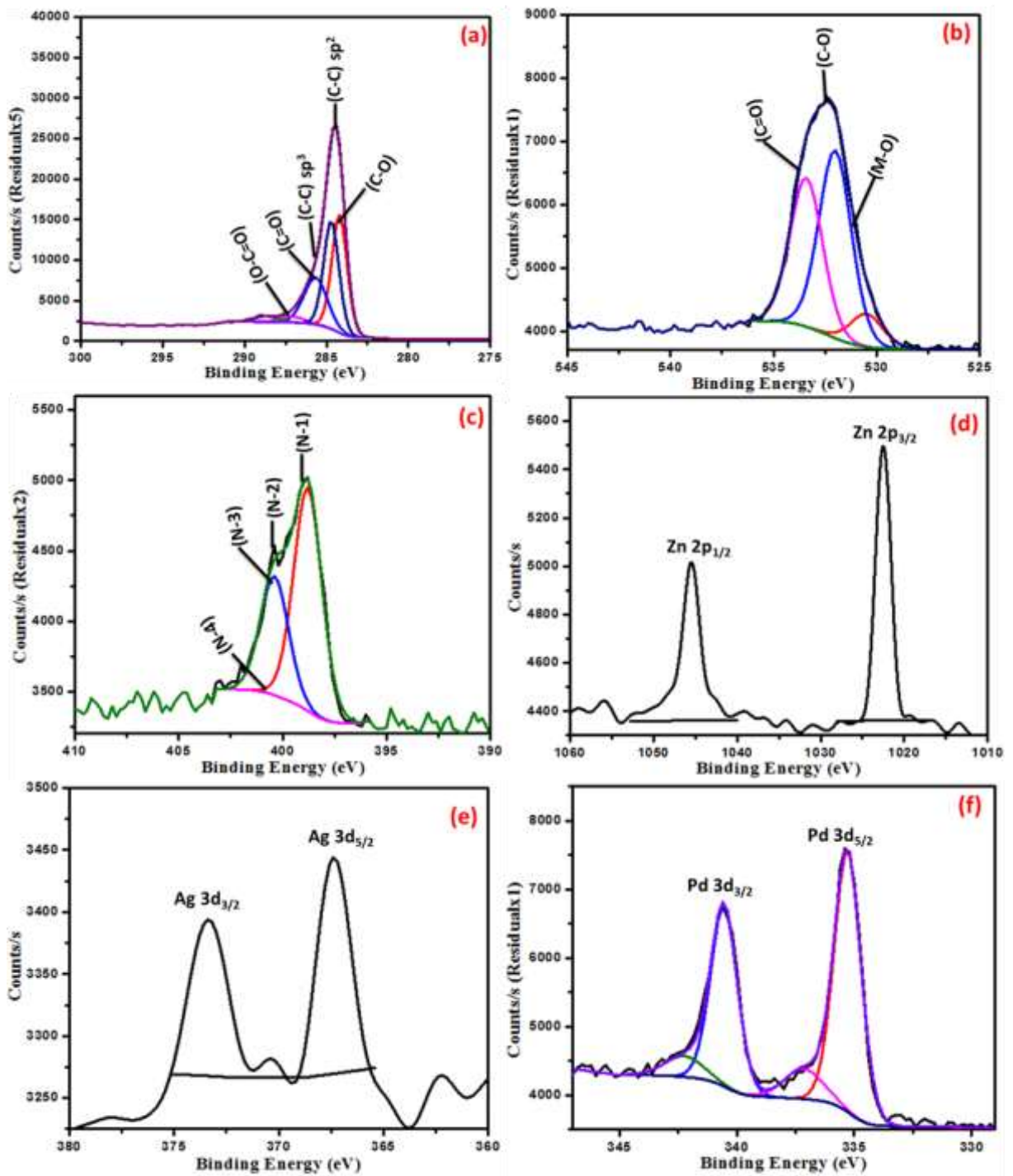


Figure 6.4: XPS spectra of Pd/N-CNO-Zn and Pd/N-CNO-Ag for (a) C 1s (b), O 1s (c) N 1s, (d) Zn 2p, (e) Ag 3d for Pd/Ag/N-OLCN and (f) Pd 3d.

6.2.5. Brunauer-Emmett-Teller Nitrogen adsorption (BET)

As displayed in Table 6.2, the BET surface areas of the bimetallic and monometallic electrocatalysts were comparable to the BET surface areas of the carbon support material. Nitrogen (N₂) physisorption analysis and the Barrett, Joyner, and Halenda (BJH) technique were used to ascertain the specific surface area (SSA), pore volume and pore size distribution (PSD) of the N-OLCN, Pd/N-OLCN, Pd/Ag/N-OLCN and Pd/Zn/N-OLCN nanomaterials. The BET surface areas of N-OLCN, Pd/N-OLCN, Pd/Ag/N-OLCN and Pd/Zn/N-OLCN were obtained as 73.2, 52.6, 62.2 and 68.3 m²g⁻¹ respectively, indicating that palladium based electrocatalysts exhibit lower SSA and higher pore volumes as compared to the support material. The decrease in the BET surface area of the palladium based electrocatalysts is due to the Pd, Zn and Ag nanoparticles which have been well dispersed and block the porous space inside the N-OLCN support material. The existence of mesoporous and microporous structure on the surface of the electrocatalyst may improve thermal and chemical stability and enhance the overall electrocatalytic activity [32].

Table 6.2: BET surface area of N-OLCN, Pd/N-OLCN, Pd/Ag/N-OLCN and Pd/Zn/N-OLCN nanomaterial

Sample	Surface area (m ² g ⁻¹)	Pore volume (cm ³ g ⁻¹)
N-OLCN	73.20	0.11
Pd/N-OLCN	52.56	0.19
Pd/Ag/N-OLCN	62.24	0.14
Pd/Zn/N-OLCN	68.30	0.12

6.3. Electrocatalytic behaviour of the nanocatalysts

6.3.1. Electrochemical surface area (ECSA)

Fig 6.5. shows the cyclic voltammograms (CV) for the Pd/C, Pd/N-OLCN, Pd/Ag/N-OLCN- and Pd/ Zn/N-OLCN nanocatalysts in a Ag-saturated electrolyte of 1 M NaOH at a scan rate 50 mV s⁻¹. As depicted in Fig. 6.5, the CV curves of Pd/C, Pd/N-OLCN, Pd/Ag/N-OLCN and Pd/Zn/N-OLCN demonstrate the typical characteristics of palladium containing nanocatalysts in alkaline conditions. The voltammetric curves show four distinctive potential regions in the anodic scan. Potential region one (QH) (-0.7 V) is attributed to the hydrogen-adsorption peak area, potential region two (-0.6 to -0.3 V) is accredited to the formation of palladium hydroxides Pd(OH), while potential region three and four (-0.3 to 0.4 V) are associated with the oxidation of palladium, silver and zinc, respectively. The palladium oxide reduction peaks for Pd/Ag/N-OLCN and Pd/ Zn/N-OLCN are more prominent as compared to Pd/N-OLCN and Pd/C, suggesting that the nanocatalysts are composed of bimetallic nanoparticles. The current values for the Pd electrocatalysts have been normalized by the electrode geometric surface area to give the current density. The electrochemical active surface areas (ECSAs) of the four nanocatalysts were calculated by integrating the palladium oxide reduction peak from the CV curves and using equation 5 [33].

$$ECSA_{Pd,cat} = \frac{Q_o[mC]}{Q_{density}[mCcm^{-2}] \times L_{metal}[mg]} \quad (5)$$

where QO is the electro-oxidation charge resulting from the integration of the PdO reduction peaks, Qdensity is the electric reduction charge for an oxygen monolayer on Pd (0.405 mC cm⁻²) and Lmetal is the total mass of Pd loaded on the glassy carbon electrode in mg. The ECSA data followed the order: Pd/ Zn/N-OLCN (79.89 m² g⁻¹) > Pd/Ag/N-OLCN (75.13 m² g⁻¹) > Pd/N-OLCN (58.37 m² g⁻¹) > Pd/C (53.52 m² g⁻¹). The enhanced ECSA of the Pd/Zn/N-OLCN and Pd/Ag/N-OLCN can be ascribed to the generation of new active sites at the interface between Pd and the metal (Zn and Ag) NPs, improved

by the N-OLCNs.

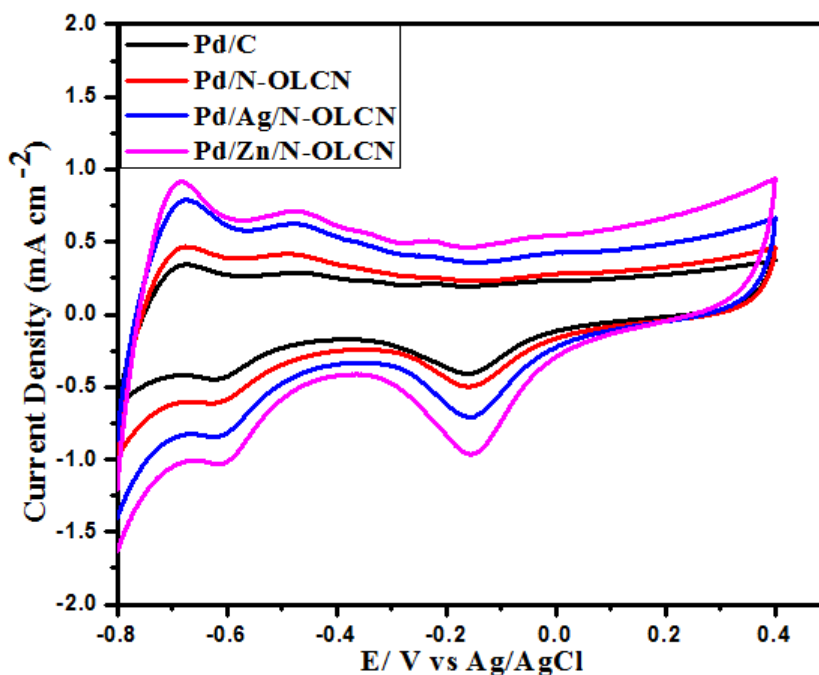
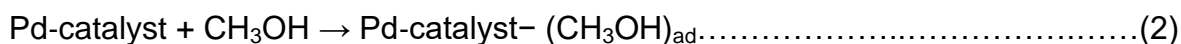
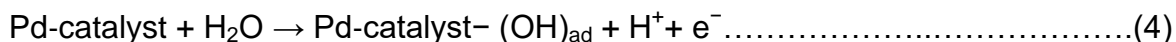
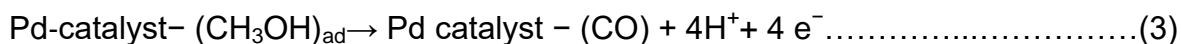


Figure 6.5: (a) CV curves of Pd/C, Pd/N-OLCN, Pd/Ag/N-OLCN- and Pd/ Zn/N-OLCN modified electrodes in 1 M NaOH solution at scan rate 50 mV s^{-1} .

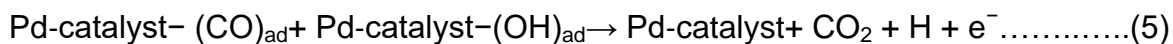
Fig. 6.6 compares the cyclic voltammetric curves for the Pd/C, Pd/N-OLCN, Pd/Ag/N-OLCN and Pd/ Zn/N-OLCN electrocatalysts in 1 M NaOH + 1 M CH₃OH solution at a scan rate of 50 mV s^{-1} . All CV curves of the electrocatalysts revealed two typical characteristic peak currents for the methanol oxidation reaction (MOR). A clear anodic current peak in the forward sweep (i_f) and a cathodic current peak in the reverse sweep (i_b) can be detected for all the palladium based electrocatalysts. In a MOR, the anodic peak current density at the forward sweep (i_f) indicates the dehydrogenation of adsorbed methanol to generate Pd-adsorbed chemisorbed species such as carbon monoxide (CO). This Pd-adsorbed CO can function as an electrocatalyst poison, while the peak current density at the reverse sweep (i_b) is mainly attributed with the oxidation of adsorbed chemisorbed species [34]. The MOR can be demonstrated by the subsequent reactions:

In forward scan:





In reverse scan:



The catalytic activity shown by the cyclic voltammograms of the synthesized electrocatalysts towards the methanol oxidation reactions (MOR) can be discussed in terms of three parameters: (1) the forward anodic peak current, (2) the onset oxidation potential and (3) CO tolerance [35]. As shown in Fig. 6.6, the Pd/Zn/N-OLCN (19.7 mA cm⁻²) displayed a higher peak current density and hence the best activity as compared to the Pd/Ag/N-OLCN (17.6 mA cm⁻²), Pd/N-OLCN (12.8 mA cm⁻²), and a commercial Pd/C (10.5 mA cm⁻²) electrocatalyst for MOR, in alkaline media. The addition of Zn and Ag to the Pd/N-OLCN significantly enhanced the catalytic activity towards MOR in an alkaline electrolyte. This might be ascribed to the nitrogen doped onion like carbon nanoparticles which produce a strong interlinkage between Pd and (Zn and Ag) nanoparticles resulting in a high electronic conduction and metal nanoparticle dispersion. Interestingly, the smaller sized particle of the Pd/Zn/N-OLCN electrocatalyst observed by TEM, suggest that the increased catalytic activity of this electrocatalyst is related to its larger BET specific surface area and electrochemical active surface area as compared to the Pd/Ag/N-OLCN electrocatalyst [12]. The onset potential for Pd/Zn/N-OLCN (-0.32 V) showed the most negative value (compare with Pd/Ag/N-OLCN (-0.29 V), Pd/N-OLCN (-0.27 V), and Pd/C (-0.26 V)). This is proposed to be due to the bifunctional complex. Zn is an oxophilic element which has an oxygen adsorbing character which releases the carbonaceous intermediate species and assists the methanol electrooxidation leading to the more negatively onset oxidation potential and improved catalytic performance [36]. Also, the existence of Ag metal can promote the electrooxidation of reaction chemisorbed species, especially carbon monoxide adsorption. As a result, alloying Pd with Ag hinders the poisoning of the active Pd sites, such as CO intermediates and enhances the electrocatalytic activity [37]. The ratio of the forward current oxidation peak (I_f) to the reversed current oxidation peak (I_b) is used measure the poison tolerance resulted by

carbonaceous species accumulation on Pd based electrocatalysts towards MOR [38]. The I_f/I_b ratio of the forward and backward currents is 1.3 on Pd/Zn/N-OLCN, 1.1 on Pd/Ag/N-OLCN, 1.0 on Pd/N-OLCN and 0.9 on Pd/C. A high I_f/I_b ratio demonstrates efficient methanol oxidation during the forward sweep and small accumulation of carbonaceous intermediates. A comparative analysis of current density of the electrocatalysts reported in this study with other similar Pd/C catalysts for the methanol oxidation reactions is revealed in Table 6.3. It is evident that our prepared electrocatalysts in general reveals higher catalytic activity towards methanol oxidation reactions (MOR) than the other catalysts listed.

Table 6.3: Comparison of Pd/N-OLCN, Pd/Ag/N-OLCN and Pd/Zn/N-OLCN to other Pd/C catalysts reported for MOR

Electrocatalysts	Fuel (M)	Electrolyte (M)	CD (mA cm ⁻²)	Ref.
Pd/Zn/N-OLCN	1 CH ₃ OH	1 NaOH	19.7	This work
Pd/Ag/N-OLCN	1 CH ₃ OH	1 NaOH	17.6	This work
Pd/N-OLCN	1 CH ₃ OH	1 NaOH	12.9	This work
Pd/Zn/N-C	1 C ₂ H ₅ OH	1 KOH	18.1	[41]
Pd/Ag/C	0.5 CH ₃ OH	1KOH	15.8	[42]
Pd/Fe/GCN	0.5 C ₂ H ₅ OH	0.5 KOH	17.4	[43]
Pd/CO/N-G	1 CH ₃ OH	1 KOH	21.3	[44]

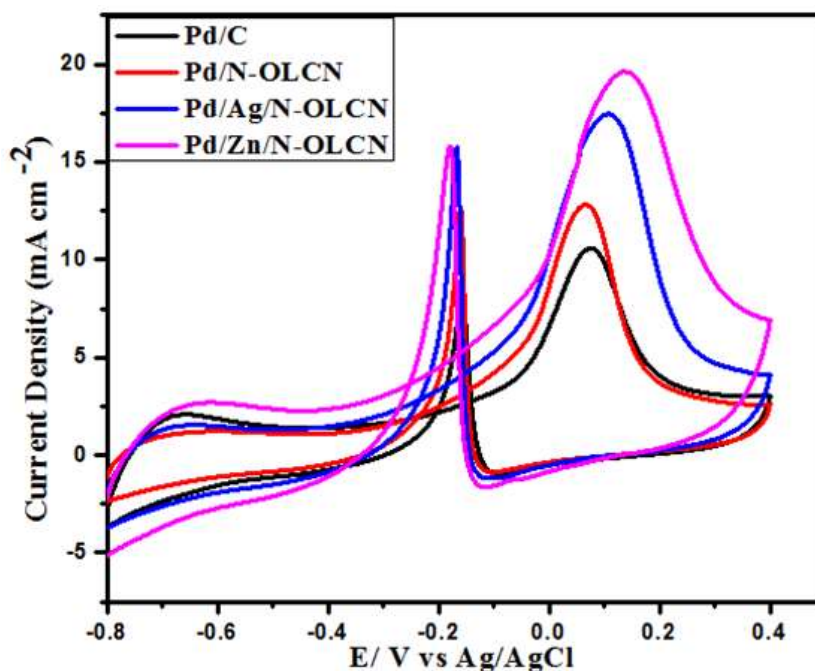


Figure 6.6: CV curves for the Pd/C, Pd/N-OLCN, Pd/Ag/N-OLCN and Pd/Zn/N-OLCN electrocatalysts in 1 M NaOH + 1 M CH₃OH solution at a scan rate of 50 mV s⁻¹.

6.3.2. The effect of scan rate on the current density

Since Pd/Ag/N-OLCN and Pd/Zn/N-OLCN electrocatalysts had a better low onset oxidation potential, poison tolerance towards carbonaceous intermediates and higher peak current densities, than the Pd/N-OLCN and Pd/C electrocatalysts, further examinations were accomplished utilizing these electrocatalysts. Fig. 6.7, indicates distinctive CVs for the Pd/Ag/N-OLCN and Pd/Zn/N-OLCN in the presence of 1 M NaOH + 1 M CH₃OH solution. As displayed in Fig. 6.7 (a) and (c), the catalytic activity for both bimetallic electrocatalysts increased with the positive shift of the anodic oxidation peak current as the scan rate increased from 10 mV s⁻¹ to 100 mV s⁻¹. A plot of the anodic current density and the square root of the sweep rate investigated are shown in Fig. 6.7 (b) and (d). The anodic peak current density is seen to be linearly associated to the square root of the scan rates, demonstrating a typical diffusion controlled reaction kinetics [43].

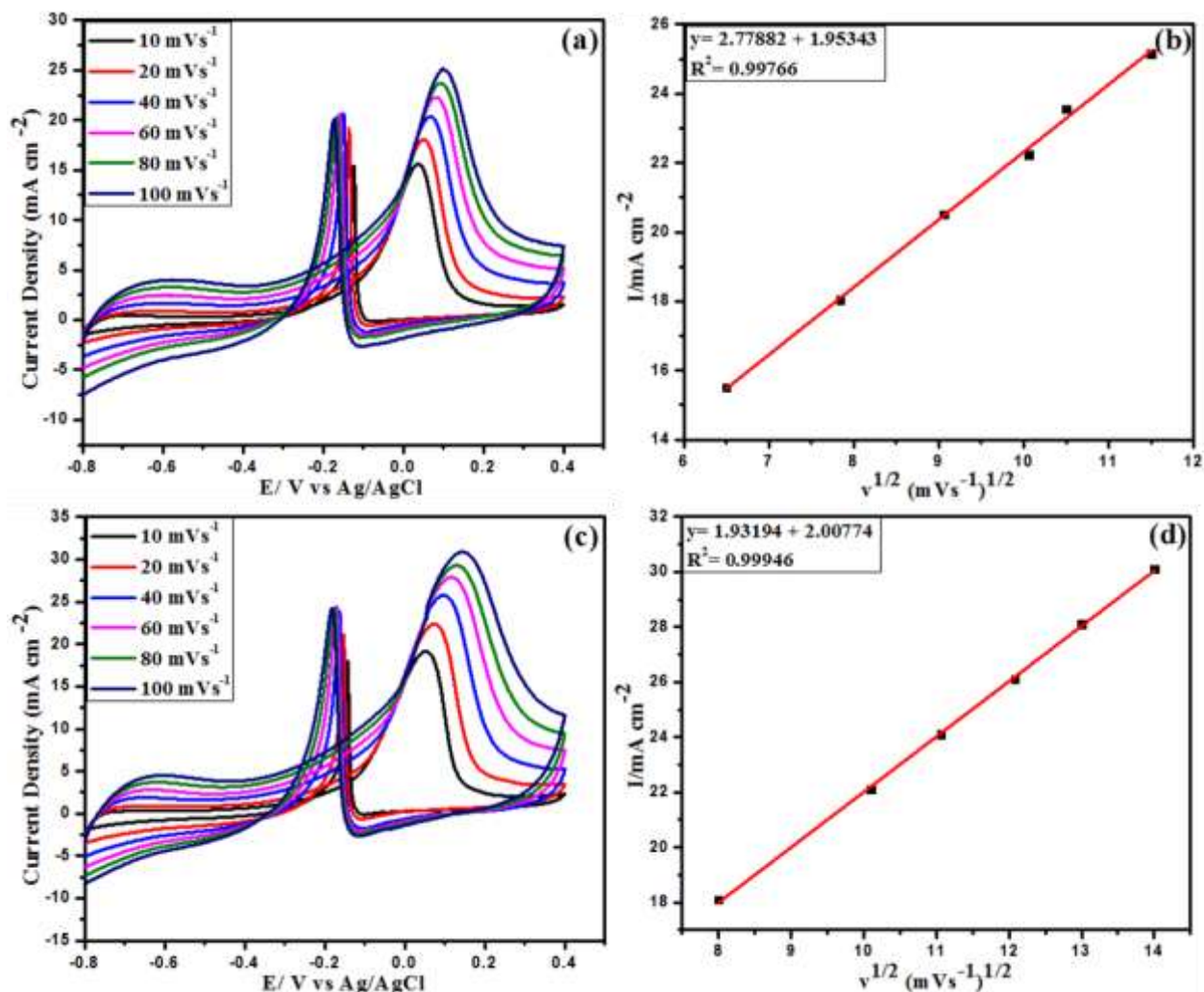


Figure 6.7: CV curves for the Pd/Ag/N-OLCN and Pd/Zn/N-OLCN electrocatalysts in 1 M NaOH + 1 M CH₃OH at different scan rates (a and c) and the plots of peak current density vs. square root of scan rates (b and d).

6.3.3. Chronoamperometry (CA)

CA tests were done to study the electrocatalytic stability of the Pd/C, Pd/N-OLCN, Pd/Ag/N-OLCN and Pd/Zn/N-OLCN electrocatalysts in methanol oxidation reaction in alkaline conditions at applied potential of -0.30 V. Fig. 6.8 displays the behavior of the peak current density as a function of time. Stability studies were carried out for all the Pd based electrocatalysts in 1 M NaOH + 1 M CH₃OH solution for a period of 2000 s. As shown in Fig. 6.8 the current densities for the Pd/C, Pd/N-OLCN, Pd/Ag/N-OLCN and Pd/Zn/N-OLCN electrocatalysts decayed rapidly

initially, mainly because of the formation of poisoning chemisorbed species like CO_{ad} on the Pd active sites, and then slowly stabilized. It can be observed that the Pd/Zn/N-OLCN (4.1 mA cm⁻²) electrocatalyst produced a higher potentiostatic current density followed by Pd/Ag/N-OLCN (3.6 mA cm⁻²), Pd/N-OLCN (3.0 mA cm⁻²) and Pd/C (2.5 mA cm⁻²), indicating that this electrocatalyst was the most stable towards MOR in alkaline media. Chronoamperometry measurements confirmed that the bimetallic electrocatalysts had better steady state catalytic performance as compared to the monometallic electrocatalysts. This enhancement in electrocatalytic stability was associated with the stronger interaction between Pd and (Zn and Ag) nanoparticles on the N-OLCN surface as observed by XRD and CV studies [31,39].

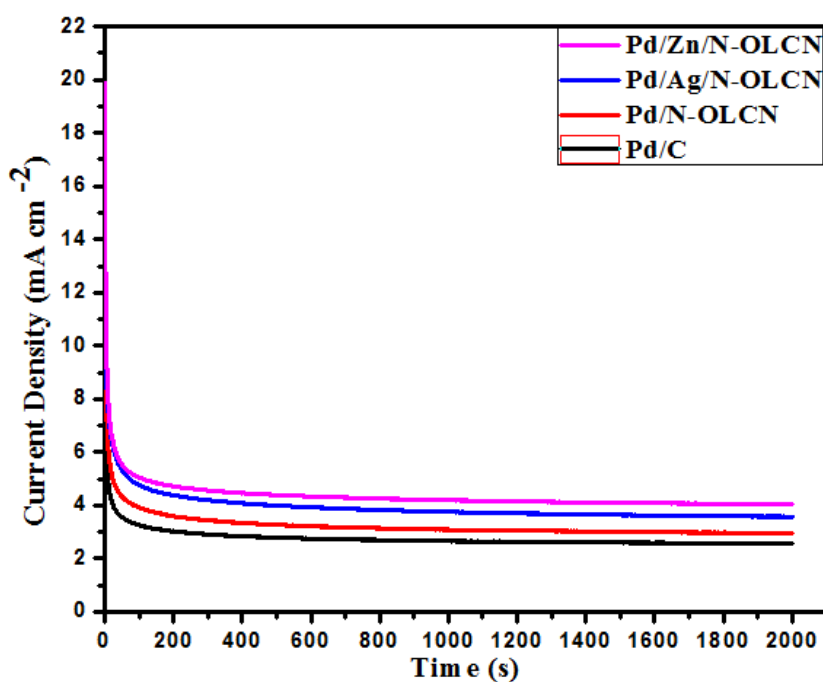


Figure 6.8: chronoamperometric curves for Pd/C, Pd/N-OLCN, Pd/Ag/N-OLCN and Pd/ Zn/N-OLCN modified electrodes in 1 M NaOH + 1M CH₃OH for an applied potential of -0.30 V.

6.3.4. Electrochemical impedance spectroscopy (EIS)

The EIS investigations were utilized to compare the reaction process of methanol oxidation on the Pd/C, Pd/N-OLCN, Pd/Ag/N-OLCN and Pd/Zn/N-OLCN modified

electrodes. The Nyquist impedance for all electrocatalysts in the electrolyte 1 M NaOH containing 1M CH₃OH solution in the frequency range from 1000 kHz to 0.005 Hz are presented in Fig. 6.9. The EIS experimental data were fitted using the electrical equivalent circuit inserted in Figure 6.9. The R_s-solution resistance, R_{ct}- charge transfer resistance and the CPE- constant phase element are associated with the double layer capacitor of the electrode [44]. The radius of the semicircle was used to estimate the charge transfer resistance of the electrocatalysts at the interface between the electrode and the electrolyte. The relevant parameters (solution resistance (R_s), charge transfer resistance (R_{CT}) and constant phase element (CPE) are summarized in Table 6.4. The smaller impedance arc diameter demonstrated the smaller charge transfer resistance and the higher electrocatalytic activity for the methanol oxidation reactions [45]. Obviously, the corresponding R_{ct} of Pd/Zn/N-OLCN is smaller as compared to Pd/Ag/N-OLCN, Pd/N-OLCN and Pd/C, indicating that Pd/Zn/N-OLCN catalysts displayed the smallest electron transfer resistance relative to the other catalysts. The faster charge transfer resistance at the interface between electrode and electrolyte suggest that the electrocatalysts acquire better electrode dynamics [46]. These results are corresponding to the excellent catalytic activity obtained from the CV and CA studies.

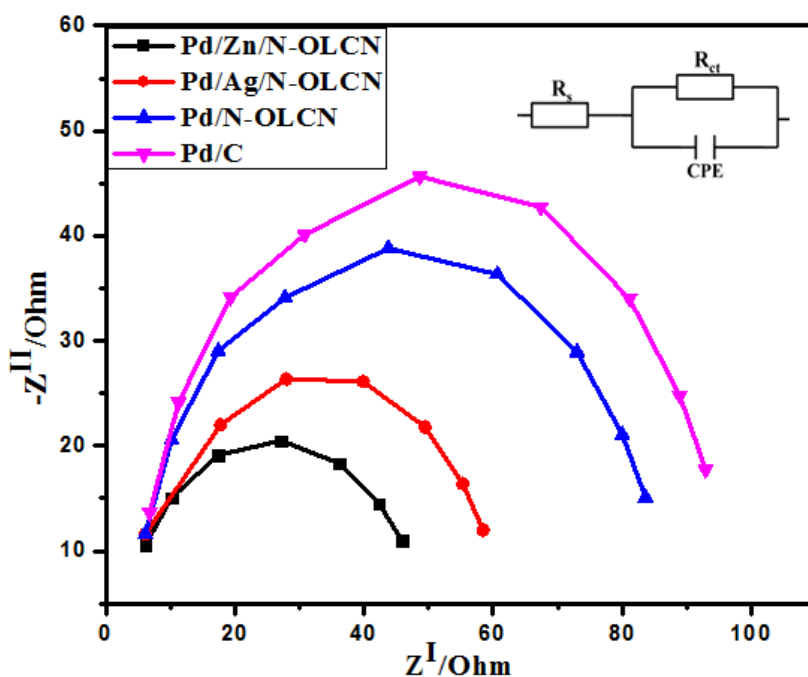


Figure 6.9: Nyquist plots of Pd/C, Pd/N-OLCN, Pd/Ag/N-OLCN and Pd/ Zn/N-OLCN modified electrodes in 1 M NaOH + 1M CH₃OH and the equivalent circuit diagram (insert).

Table 6.4: The EIS circuit parameters of Pd/C, Pd/N-OLCN, Pd/Ag/N-OLCN and Pd/Zn/N-OLCN nanocatalysts

Electrocatalysts	R_s (Ohm)	R_{ct} (Ohm)	CPE (μF)
Pd/C	45.6	92.8	194.1
Pd/N-OLCN	38.7	83.3	140.9
Pd/Ag/N-OLCN	26.2	58.5	189.7
Pd/Zn/N-OLCN	20.6	45.8	179.2

Conclusions

In summary, nitrogen-doped onion like carbon nanoparticles (N-OLCNs) has been synthesized via a flame pyrolysis method using acetonitrile as a starting material. The dispersed Pd/Ag and Pd/Zn nanoparticles supported on the N-OLCNs were successfully synthesized using the sodium borohydride reduction method. The TEM results confirmed the smaller particle size and better dispersion of the Pd/Zn particles as compared to the larger Pd/Ag nanoparticles on the N-OLCN surface. The most significant difference in XRD observation between the Pd/Zn/N-OLCN and Pd/Ag/N-OLCN catalysts is the degree of peak shifting, Pd-Zn peaks shift to higher angle values. In contrast, Pd-Ag peaks shift to a smaller 2θ angle because both Zn and Ag are highly alloyed to the Pd structure. The incorporation of Ag and Zn modified the electronic structure of Pd, which was affirmed by the downward shift of the Pd using XPS analysis. Among the four nanocatalysts, Pd/Zn/N-OLCN and Pd/Ag/N-OLCN revealed the highest peak current densities, more negatively onset potentials and excellent CO-tolerance than the other nanocatalysts in methanol oxidation reaction in alkaline media. Furthermore, the stability studies carried out using chronoamperometry revealed that Pd/Zn/N-OLCN and Pd/Ag/N-OLCN nanocatalysts were more stable in MOR as compared to Pd/N-OLCN and

commercial Pd/C nanocatalysts. Moreover, Pd/Zn/N-OLCN and Pd/Ag/N-OLCN has a very fast charge transfer rate than the other nanocatalysts in MOR as shown in EIS test. The encouraging catalytic performance demonstrates that the Pd/Zn/N-OLCN and Pd/Ag/N-OLCN can be a promising electrocatalysts for methanol oxidation in fuel cells.

Acknowledgments

This work is based on the research supported in part by the National Research Foundation (NRF) of South Africa (Grant Numbers: 118137, 118148), the University of the Witwatersrand (Postgraduate Merit Award, University Research Council) and a NRF-DAAD grant (Grant number: 117841). The authors also acknowledge the efforts and support provided by the University of Johannesburg (Faculty of Science, University Research Council, and Centre for Nanomaterials Science Research). We also wish to acknowledge Mr. Siyasanga Mpelane at the University of Johannesburg (Auckland Park) for the high magnification TEM data and Dr Boitumelo Matsoso for data discussions.

References

- [1] Z. Yin, Y. Zhang, K. Chen, J. Li, W. Li, P. Tang, H. Zhao, Q. Zhu, X. Bao, D. Ma, Monodispersed bimetallic PdAg nanoparticles with twinned structures: Formation and enhancement for the methanol oxidation, *Sci. Rep.* 4 (2014). <https://doi.org/10.1038/srep04288>.
- [2] M.H. de Sá, A.M.F.R. Pinto, V.B. Oliveira, Passive Small Direct Alcohol Fuel Cells for Low-Power Portable Applications: Assessment Based on Innovative Increments since 2018, *Energies.* 15 (2022) 3787. <https://doi.org/10.3390/en15103787>.
- [3] R. Carrera-Cerritos, C. Salazar-Hernandez, I.R. Galindo-Esquivel, R. Fuentes-Ramirez, Effect of the Reduction Temperature of PdAg Nanoparticles during the Polyol Process in the Ethanol Electrooxidation Reaction, *J. Nanomater.* 2018 (2018). <https://doi.org/10.1155/2018/9451421>.

- [4] Y. Wang, S. Zou, W. Bin Cai, Recent advances on electro-oxidation of ethanol on Pt- and Pd-based catalysts: From reaction mechanisms to catalytic materials, *Catalysts*. 5 (2015) 1507–1534. <https://doi.org/10.3390/catal5031507>.
- [5] E. Antolini, E.R. Gonzalez, Alkaline direct alcohol fuel cells, *J. Power Sources*. 195 (2010) 3431–3450. <https://doi.org/10.1016/j.jpowsour.2009.11.145>.
- [6] W.A. Auriyani, D. Bustan, S. Haryati, The Electrolyte-Fuel Concentrations Effects on Direct Methanol Alkaline Fuel Cell (DMAFC) Through Non-Noble Metal Catalysts, *J. Sci. Appl. Technol.* 5 (2021) 25. <https://doi.org/10.35472/jsat.v5i1.388>.
- [7] Y. Yang, S. Yu, L. Gao, X. Wang, S. Yan, The properties of PdRu /C with respect to the electro-oxidation of methanol and ethanol, *Int. J. Electrochem. Sci.* 14 (2019) 1270–1282. <https://doi.org/10.20964/2019.02.50>.
- [8] V.F. Ruiz-Ruiz, R. González-Olvera, R. Díaz-Pardo, I. Betancourt, I. Zumeta-Dubé, D. Díaz, N. Farfán, M.J. Arellano-Jiménez, Mechanochemically obtained Pd–Ag nanoalloys. Structural considerations and catalytic activity, *Materialia*. 4 (2018) 166–174. <https://doi.org/10.1016/j.mtla.2018.09.031>.
- [9] X.L. Liang, X. Dong, G.D. Lin, H. Bin Zhang, Carbon nanotube-supported Pd-ZnO catalyst for hydrogenation of CO₂ to methanol, *Appl. Catal. B Environ.* 88 (2009) 315–322. <https://doi.org/10.1016/j.apcatb.2008.11.018>.
- [10] L. Zhang, Q. Chang, H. Chen, M. Shao, Recent advances in palladium-based electrocatalysts for fuel cell reactions and hydrogen evolution reaction, *Nano Energy*. 29 (2016) 198–219. <https://doi.org/10.1016/j.nanoen.2016.02.044>.
- [11] H. You, S. Yang, B. Ding, H. Yang, Synthesis of colloidal metal and metal alloy nanoparticles for electrochemical energy applications, *Chem. Soc. Rev.* 42 (2013) 2880–2904. <https://doi.org/10.1039/c2cs35319a>.
- [12] L. Yang, Y. Wang, H. Feng, H. Zeng, C. Tan, J. Yao, J. Zhang, L. Jiang, Y. Sun, PdAg Nanoparticles with Different Sizes: Facile One-Step Synthesis and

High Electrocatalytic Activity for Formic Acid Oxidation, Chem. - An Asian J. 16 (2021) 34–38. <https://doi.org/10.1002/asia.202001253>.

[13] G. Bampos, D.I. Kondarides, S. Bebelis, Pd–Zn/C bimetallic electrocatalysts for oxygen reduction reaction, J. Appl. Electrochem. 48 (2018) 675–689. <https://doi.org/10.1007/s10800-018-1199-x>.

[14] Y. Zhang, A. Reed, D.Y. Kim, Nitrogen doped carbon nano-onions as efficient and robust electrocatalysts for oxygen reduction reactions, Curr. Appl. Phys. 18 (2018) 417–423. <https://doi.org/10.1016/j.cap.2018.02.001>.

[15] A. Zhang, Z. Zheng, F. Cheng, Z. Tao, J. Chen, Preparation of Li₄Ti₅O₁₂ submicrospheres and their application as anode materials of rechargeable lithium-ion batteries, Sci. China Chem. 54 (2011) 936–940. <https://doi.org/10.1007/s11426-011-4296-9>.

[16] D. Mohapatra, G. Dhakal, M.S. Sayed, B. Subramanya, J. Shim, S. Parida, Sulfur Doping : Unique Strategy To Improve the Supercapacitive Performance of Carbon Nano-onions, ACS Appl. Mater. Interfaces. 11 (2019) 8040–8050. <https://doi.org/10.1021/acsami.8b21534>.

[17] M. Zeiger, N. Jäckel, V.N. Mochalin, V. Presser, Review: Carbon onions for electrochemical energy storage, J. Mater. Chem. A. 4 (2016) 3172–3196. <https://doi.org/10.1039/c5ta08295a>.

[18] D. Mohapatra, N.S.K. Gowthaman, M.S. Sayed, J.J. Shim, Simultaneous ultrasensitive determination of dihydroxybenzene isomers using GC electrodes modified with nitrogen-doped carbon nano-onions, Sensors Actuators, B Chem. 304 (2020) 127325. <https://doi.org/10.1016/j.snb.2019.127325>.

[19] T.H. Mongwe, N.J. Coville, M.S. Maubane-Nkadimeng, Synthesis of onion-like carbon nanoparticles by flame pyrolysis, Nanoscience. 8 (2022) 198–220. <https://doi.org/10.1039/9781839167218-00198>.

[20] O. Ornelas, J.M. Sieben, R. Ruiz-Rosas, E. Morallón, D. Cazorla-Amorós, J. Geng, N. Soin, E. Siores, B.F.G. Johnson, On the origin of the high capacitance

of nitrogen-containing carbon nanotubes in acidic and alkaline electrolytes, *Chem. Commun.* 50 (2014) 11343–11346. <https://doi.org/10.1039/c4cc04876h>.

[21] G. Wu, A. Santandreu, W. Kellogg, S. Gupta, O. Ogoke, H. Zhang, H.L. Wang, L. Dai, Carbon nanocomposite catalysts for oxygen reduction and evolution reactions: From nitrogen doping to transition-metal addition, *Nano Energy*. 29 (2016) 83–110. <https://doi.org/10.1016/j.nanoen.2015.12.032>.

[22] K. Chatterjee, M. Ashokkumar, H. Gullapalli, Y. Gong, Nitrogen-rich carbon nano-onions for oxygen reduction reaction, *Carbon N. Y.* 130 (2018) 645–651. <https://doi.org/10.1016/j.carbon.2018.01.052>.

[23] L.L. Sikeyi, T. Matthews, A.S. Adekunle, N.W. Maxakato, Electro-oxidation of Ethanol and Methanol on Pd/C, Pd/CNFs and Pd–Ru/CNFs Nanocatalysts in Alkaline Direct Alcohol Fuel Cell, *Electroanalysis*. 32 (2020) 2681–2692. <https://doi.org/10.1002/elan.202060260>.

[24] L.L. Sikeyi, T.D. Ntuli, T.H. Mongwe, N.W. Maxakato, E. Carleschi, B.P. Doyle, N.J. Coville, M.S. Maubane-Nkadimeng, Microwave assisted synthesis of nitrogen doped and oxygen functionalized carbon nano onions supported palladium nanoparticles as hybrid anodic electrocatalysts for direct alkaline ethanol fuel cells, *Int. J. Hydrogen Energy*. 46 (2021) 10862–10875. <https://doi.org/10.1016/j.ijhydene.2020.12.154>.

[25] V. Dhand, J.S. Prasad, M.V. Rao, S. Bharadwaj, Flame synthesis of carbon nano onions using liquefied petroleum gas without catalyst Flame synthesis of carbon nano onions using liquefied petroleum gas without catalyst, (2013). <https://doi.org/10.1016/j.msec.2012.10.029>.

[26] S. Fu, C. Zhu, D. Du, Y. Lin, Facile One-Step Synthesis of Three-Dimensional Pd-Ag Bimetallic Alloy Networks and Their Electrocatalytic Activity toward Ethanol Oxidation, *ACS Appl. Mater. Interfaces*. 7 (2015) 13842–13848. <https://doi.org/10.1021/acsami.5b01963>.

- [27] L.L. Sikeyi, T.D. Ntuli, T.H. Mongwe, N.W. Maxakato, E. Carleschi, B.P. Doyle, N.J. Coville, M.S. Maubane-Nkadimeng, Microwave assisted synthesis of nitrogen doped and oxygen functionalized carbon nano onions supported palladium nanoparticles as hybrid anodic electrocatalysts for direct alkaline ethanol fuel cells, *Int. J. Hydrogen Energy*. 46 (2021) 10862–10875. <https://doi.org/10.1016/j.ijhydene.2020.12.154>.
- [28] D. Zhang, C. Du, J. Chen, Q. Shi, Q. Wang, S. Li, W. Wang, X. Yan, Q. Fan, Improvement of structural and optical properties of ZnAl₂O₄:Cr³⁺ ceramics with surface modification by using various concentrations of zinc acetate, *J. Sol-Gel Sci. Technol.* 88 (2018) 422–429. <https://doi.org/10.1007/s10971-018-4820-x>.
- [29] D. V. Glyzdova, E. V. Khramov, N.S. Smirnova, I.P. Prosvirin, A. V. Bukhtiyarov, M. V. Trenikhin, T.I. Gulyaeva, A.A. Vedyagin, D.A. Shlyapin, A. V. Lavrenov, Study on the active phase formation of Pd-Zn/Sibunit catalysts during the thermal treatment in hydrogen, *Appl. Surf. Sci.* 483 (2019) 730–741. <https://doi.org/10.1016/j.apsusc.2019.03.215>.
- [30] L.X. Chen, J.N. Zheng, A.J. Wang, L.J. Wu, J.R. Chen, J.J. Feng, Facile synthesis of porous bimetallic alloyed PdAg nanoflowers supported on reduced graphene oxide for simultaneous detection of ascorbic acid, dopamine, and uric acid, *Analyst*. 140 (2015) 3183–3192. <https://doi.org/10.1039/c4an02200a>.
- [31] J. Shi, J. Wang, Y. Chen, Y. Sun, B. Liu, Y. Fan, Ag-Pd core-shell electrocatalysts for ethanol oxidation and oxygen reduction reactions in alkaline medium, *JPhys Mater.* 4 (2021). <https://doi.org/10.1088/2515-7639/abc733>.
- [32] O.A. Ojelade, S.F. Zaman, Co₂ hydrogenation to methanol over PdZn/CeO₂ catalyst, *Comptes Rendus L'Academie Bulg. Des Sci.* 72 (2019) 732–739. <https://doi.org/10.7546/CRABS.2019.06.05>.
- [33] A. Elsheikh, J. McGregor, Synthesis and characterization of pdagni/c trimetallic nanoparticles for ethanol electrooxidation, *Nanomaterials*. 11 (2021). <https://doi.org/10.3390/nano11092244>.

- [34] S. Roy, S. Payra, S. Challagulla, R. Arora, S. Roy, C. Chakraborty, Enhanced Photoinduced Electrocatalytic Oxidation of Methanol Using Pt Nanoparticle-Decorated TiO₂-Polyaniline Ternary Nanofibers, ACS Omega. 3 (2018) 17778–17788. <https://doi.org/10.1021/acsomega.8b02610>.
- [35] S. Ali, R. Ahmed, M.S. Ansari, Evaluation of Stability and Catalytic Activity Of direct Methanol Fuel Cell nano-catalysts by Cyclic Voltammetry, NUST J. Eng. Sci. 6 (2013) 21–26. <https://doi.org/10.24949%2Fnjcs.v6i1.42>.
- [36] M.A. Matin, A. Kumar, R.R. Bhosale, M.A.H. Saleh Saad, F.A. Almomani, M.J. Al-Marri, PdZn nanoparticle electrocatalysts synthesized by solution combustion for methanol oxidation reaction in an alkaline medium, RSC Adv. 7 (2017) 42709–42717. <https://doi.org/10.1039/c7ra07013f>.
- [37] Y. Wang, Z.M. Sheng, H. Yang, S.P. Jiang, C.M. Li, Electrocatalysis of carbon black- or activated carbon nanotubes-supported Pd-Ag towards methanol oxidation in alkaline media, Int. J. Hydrogen Energy. 35 (2010) 10087–10093. <https://doi.org/10.1016/j.ijhydene.2010.07.172>.
- [38] C. Te Hsieh, J.Y. Lin, S.Y. Yang, Carbon nanotubes embedded with PtRu nanoparticles as methanol fuel cell electrocatalysts, Phys. E Low-Dimensional Syst. Nanostructures. 41 (2009) 373–378. <https://doi.org/10.1016/j.physe.2008.08.060>.
- [39] Y. Qiu, J. Zhang, J. Jin, J. Sun, H. Tang, Q. Chen, Z. Zhang, W. Sun, G. Meng, Q. Xu, Y. Zhu, A. Han, L. Gu, D. Wang, Y. Li, Construction of Pd-Zn dual sites to enhance the performance for ethanol electro-oxidation reaction, (n.d.). <https://doi.org/10.1038/s41467-021-25600-9>.
- [40] I. Petriev, P. Pushankina, I. Lutsenko, N. Shostak, M. Baryshev, Synthesis, electrocatalytic and gas transport characteristics of pentagonally structured star-shaped nanocrystallites of pd-ag, Nanomaterials. 10 (2020) 1–19. <https://doi.org/10.3390/nano10102081>.

- [41] S. Ghosh, S. Bysakh, R.N. Basu, Bimetallic Pd₉₆Fe₄ nanodendrites embedded in graphitic carbon nanosheets as highly efficient anode electrocatalysts, *Nanoscale Adv.* 1 (2019) 3929–3940. <https://doi.org/10.1039/c9na00317g>.
- [42] R. Kiyani, S. Rowshanzamir, M.J. Parnian, Nitrogen doped graphene supported palladium-cobalt as a promising catalyst for methanol oxidation reaction: Synthesis, characterization and electrocatalytic performance, *Energy*. 113 (2016) 1162–1173. <https://doi.org/10.1016/j.energy.2016.07.143>.
- [43] K.M. Hassan, A.A. Hathoot, R. Maher, M. Abdel Azzem, Electrocatalytic oxidation of ethanol at Pd, Pt, Pd/Pt and Pt/Pd nano particles supported on poly 1,8-diaminonaphthalene film in alkaline medium, *RSC Adv.* 8 (2018) 15417–15426. <https://doi.org/10.1039/c7ra13694c>.
- [44] D. Morales-Acosta, D. López de la Fuente, L.G. Arriaga, G. Vargas Gutiérrez, F.J. Rodríguez Varela, Electrochemical investigation of Pt-Co/MWCNT as an alcohol-tolerant ORR catalyst for direct oxidation fuel cells, *Int. J. Electrochem. Sci.* 6 (2011) 1835–1854.
- [45] A.K. Ipadeola, R. Barik, S.C. Ray, K.I. Ozoemena, Bimetallic Pd/SnO₂ Nanoparticles on Metal Organic Framework (MOF)-Derived Carbon as Electrocatalysts for Ethanol Oxidation, *Electrocatalysis*. 10 (2019) 366–380. <https://doi.org/10.1007/s12678-019-00518-5>.
- [46] R.M. Abdel Hameed, Enhanced ethanol electro-oxidation reaction on carbon supported Pd-metal oxide electrocatalysts, *J. Colloid Interface Sci.* 505 (2017) 230–240. <https://doi.org/10.1016/j.jcis.2017.05.095>.
- [47] F. Seland, R. Tunold, D.A. Harrington, Impedance study of methanol oxidation on platinum electrodes, *Electrochim. Acta.* 51 (2006) 3827–3840. <https://doi.org/10.1016/j.electacta.2005.10.050>.

CHAPTER 7

CONCLUSIONS AND RECOMMENDATIONS

7.1. Conclusion

In **Chapter 3**, an overview of synthesis methods and electrochemical applications of the metal-free catalysts and metal carbon-based catalysts used in this study were described. The onion like carbon nanomaterials, CNOs (OLCNs), were successfully synthesized utilizing flame pyrolysis. The pristine carbons were then purified and modified by chemical oxidation and nitrogen doping methods. Furthermore, the Pd/CNO electrocatalysts were prepared using a microwave synthesis method. Spectroscopic and microscopic examination of the new materials confirmed the successful modification of the CNOs indicating the presence of oxygen and nitrogen functional groups on the CNOs and the attachment of Pd NPs to the onion like structure. The N-CNOs revealed lower thermal stability than the ox-CNOs and the p-CNOs. The materials were all tested for electrochemical activity and the synthesized N-CNOs (and Pd/N-CNOs) nanocatalysts exhibited a significantly improved electrocatalytic performance and superior long-term stability when compared to the ox-CNOs (and Pd/ox-CNOs) as well as the p-CNOs (and Pd/p-CNOs) towards ethanol oxidation reaction in an alkaline electrolyte. The results indicate how modification of CNOs with oxygen and nitrogen functional groups, as well as the synthesis of the equivalent Pd catalysts on the different CNOs, can provide a means for the facile synthesis of either Pd-free or Pd carbon-based catalysts by reasonable design and that will lead to catalysts with enhanced activity. The data are consistent with other reports in the literature and thus indicated a facile process for making electrocatalysts from CNOs.

In **Chapter 4**, boron oxide modified carbon nano-onions were synthesized via a CVD method using boric acid. Highly dispersed Pt nanoparticles decorated on pristine, and boron oxide modified CNOs were successfully prepared using the ethylene glycol reduction method. The as-obtained Pt/p-CNO, Pt/B-CNO_{uw}, and

Pt/B-CNOw nanocatalysts revealed a network structure, and a distribution of small Pt NPs to provide an abundance of active sites that showed excellent electrocatalytic performance. The Pt/B-CNOw electrocatalysts showed higher ECSA when compared to the Pt/B-CNOw, Pt/p-CNO and Pt/C catalysts, due to the existence of boron atoms in the p-CNO structure. This improved the number of active sites for attachment and nucleation of Pt nanoparticles. Regardless of the greater ECSA of Pt/B-CNOw, its electrocatalytic activity, stability and charge electron transfer toward ammonia oxidation was excellent as compared to the Pt/B-CNOw, Pt/p-CNO and Pt/C nanocatalysts. The comparable AOR performance of Pt/B-CNOw nanocatalysts when compared to Pt/B-CNOw, Pt/p-CNO and commercial Pt/C suggests that, with further work, that it could possibly replace the expensive 10% Pt/C nanocatalysts in fuel cells.

In **Chapter 5**, sulfur doped onion-like carbon nanoparticles (S-OLCNs) were successfully synthesized in a one-step flame pyrolysis method using thiophene as both the carbon and sulfur source. A $\text{TiO}_2/\text{S-OLCN}$ composite support material was designed to have well dispersed titania nanoparticles on a carbon nano-onion surface using a hydrothermal reaction process. The ultrafine Pt nanoparticles were successfully deposited on the S-OLCN, TiO_2 and $\text{TiO}_2/\text{S-OLCN}$ surfaces by the alcohol assisted reduction method. The TEM, XRD and XPS results confirmed the formation of highly decorated ultrafine Pt NPs with an average diameter of 2.0 nm that were strongly bonded to the S-OLCN, TiO_2 and $\text{TiO}_2/\text{S-OLCN}$ supports. The ternary composite modified ($\text{Pt}/\text{TiO}_2/\text{S-OLCN}$) electrode demonstrated higher catalytic performance, better long-term stability and smaller charge transfer resistance for the ammonia oxidation reaction in alkaline medium as compared to Pt/S-OLCN, Pt/ TiO_2 , and Pt/C modified electrodes. It was suggested that the superior electrocatalytic performance resulted from a strong Pt-support interaction and the better accessibility of ultrafine Pt nanoparticles to the reactants on the $\text{TiO}_2/\text{S-OLCN}$ composite support material. A protecting effect of $\text{TiO}_2/\text{S-OLCN}$ towards Pt that evades the adsorption of ammonia and nitrogenous intermediates on the platinum surface was observed. Therefore, the $\text{Pt}/\text{TiO}_2/\text{S-OLCN}$ electrocatalyst is a good anode electrocatalyst for ammonia tolerant-oxidation

reaction in direct alkaline fuel cells. Further studies to explore this electrocatalyst type are underway in our laboratory.

In **Chapter 6**, nitrogen-doped onion like carbon nanoparticles (N-OLCNs) has been synthesized via a flame pyrolysis method using acetonitrile as a starting material. The well dispersed ultrafine Pd/Ag and Pd/Zn nanoparticles supported on nitrogen doped OLCNs were successfully synthesized using the sodium borohydride reduction method. The TEM results confirmed the smaller particle size and uniform dispersion of Pd/Zn as compared to the larger Pd/Ag nanoparticles on the N-OLCN surface. The incorporation of Ag and Zn to modify the electronic structure of Pd, was affirmed by the down shift of the d-band center on Pd using XPS analysis. Among the four nanocatalysts, Pd/Zn/N-OLCN and Pd/Ag/N-OLCN revealed the highest peak current densities, more negative onset potentials and better CO-tolerance than observed for the other nanocatalysts in the methanol oxidation reaction in alkaline media. Furthermore, the stability studies carried out using chronoamperometry revealed that the Pd/Zn/N-OLCN and Pd/Ag/N-OLCN nanocatalysts were more stable in MOR as compared to Pd/N-OLCN and the commercial Pd/C nanocatalysts. Moreover, Pd/Zn/N-OLCN and Pd/Ag/N-OLCN showed a very fast charge transfer rate when compared to the other nanocatalysts in MOR as shown by EIS data. The encouraging catalytic performance demonstrates that the Pd/Zn/N-OLCN and Pd/Ag/N-OLCN can be a promising electrocatalysts for methanol oxidation in fuel cells.

7.2. Recommendations for further work

Despite the fact that this study might be regarded as reasonably successful, it still leaves a number of issues that can be further investigated and addressed. The objective of the work was to enhance the method for designing catalysts for ethanol, methanol and ammonia oxidation reactions. This goal was achieved through investigating different carbon sources to make the onion-like carbon nanoparticles which were modified by heteroatom dopants, and the addition of mono and bimetallic catalysts. As a result, the following proposals can be made for future investigations:

- ❖ The synthesis and use of new support materials such as graphitic carbon nitride and hollow carbon spheres due to their shape/surface functional groups/ surface areas.
- ❖ Heteroatom doping of these new support materials with nitrogen, boron, sulphur and phosphorus for enhancement of their physical and chemical properties.
- ❖ Use of inorganic metal oxides such as NiO, MnO₂ and SnO₂ together with carbon as a catalyst. Development of new supported catalysts that includes Pt and Pd based bimetallic and trimetallic (Au, Rh, Ir, Ru and Zr) catalysts for alcohol and ammonia oxidation reactions in fuel cells.
- ❖ To design innovative liquid electrolytes to improve electrochemical efficiency of the catalysts fuel cells.

Appendix A: Supplementary Information

CHAPTER 3

1. Transmission electron microscopy

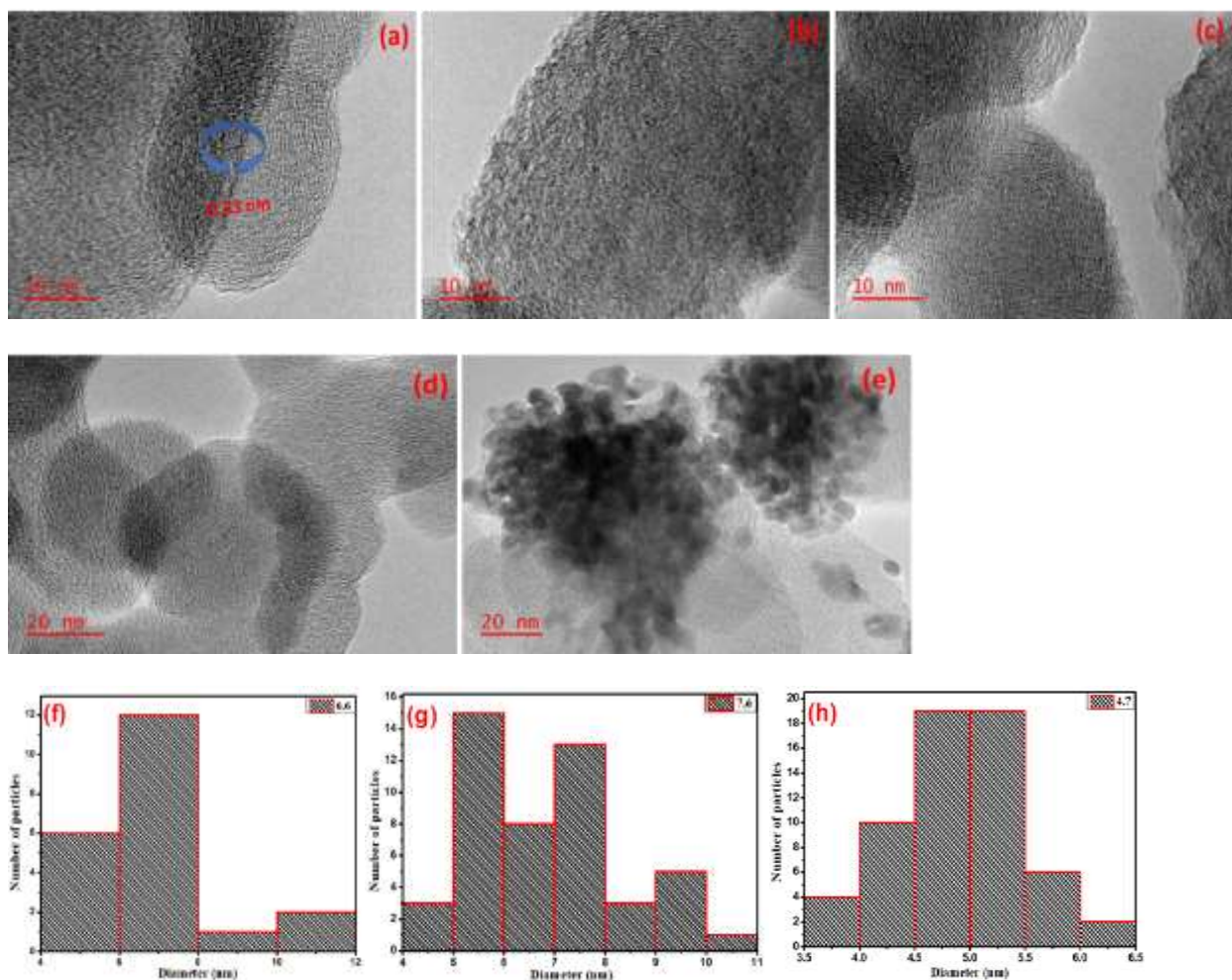


Figure S1. TEM micrographs of; (a) p-CNO, (b) Ox-CNO, (c) N-CNO, (d) p-CNO (different magnification), (e) Pd/p-CNO and the average Pd particle sizes of (f) Pd/p-CNO, (g) Pd/Ox-CNO and (h) Pd/N-CNO nanomaterials.

2. Scanning electron microscopy

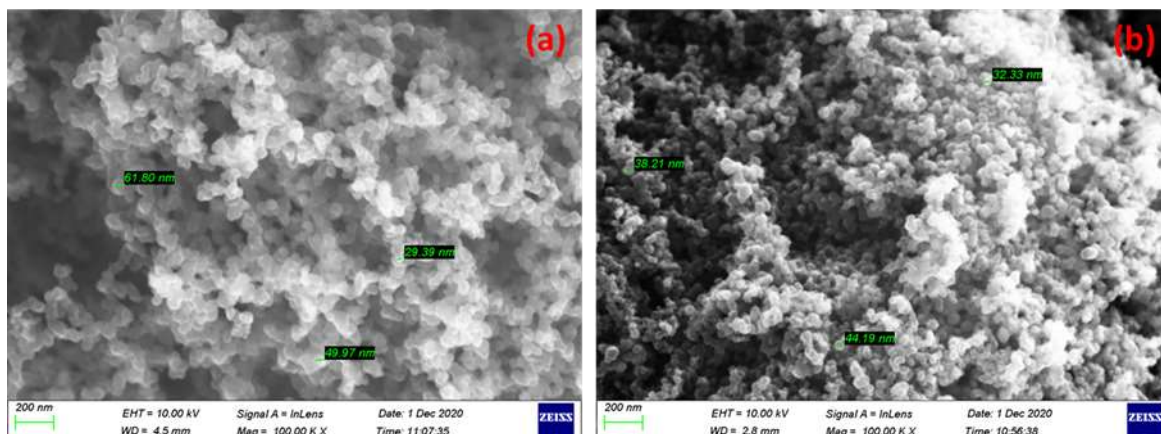


Figure S2. SEM images of (a) ox-CNO and (b) N-CNO nanomaterials

3. Atomic force microscopy

Fig. S3 gives the topography of the synthesized CNO and the corresponding Pd/CNO electrocatalysts. The image surface areas were calculated to be $1.523 \mu\text{m}^2$ (p-CNO), $1.968 \mu\text{m}^2$ (ox-CNO), $1.857 \mu\text{m}^2$ (N-CNO), $1.457 \mu\text{m}^2$ (Pd/p-CNO), $1.724 \mu\text{m}^2$ (Pd/ox-CNO) and $1.625 \mu\text{m}^2$ (Pd/N-CNO) for the synthesized CNOs and the corresponding electrocatalysts respectively.

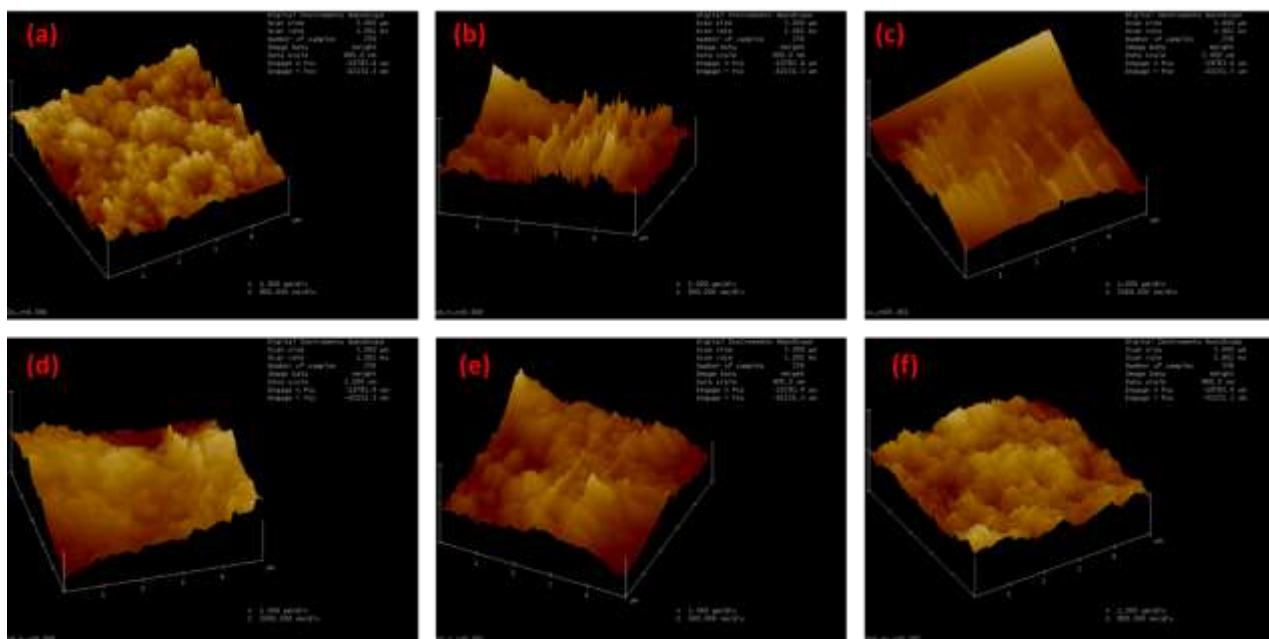


Fig. S3. AFM images of the (a) p-CNO, (b) ox-CNO, (c) N-CNO, (d) Pd/p-CNO, (e) Pd/N-CNO, and (f) Pd/ox-CNO nanomaterials.

4. Thermogravimetric analysis

The DTG plots show the temperatures of maximum weight loss due to carbon oxidation at about 690 °C for the three Pd/CNO samples. It is clear that the Pd does not aid in the carbon oxidation as the peaks do not change substantially relative to data. The first-order derivative curves showed that the Pd/N-CNO nanomaterial has a high decomposition temperature and more stable compared to Pd/p-CNO and Pd/ox-CNO nanomaterial in Fig. S4 (a). The high decomposition temperature for Pd/N-CNO is due to the successful introduction between the nitrogen atoms of the CNO and Pd nanoparticles. The Pd/p-CNO and Pd/ox-CNO nanomaterial also showed weight losses between 220°C and 270 °C which can be ascribed to the conversion of palladium oxide (PdO) to metallic palladium nanoparticles (PdNPs) and oxygen functional groups on the surface of the carbon nano onions unlikely as seen without Pd in Fig. S4 (b) [36]. The broader peak for Pd/ox-CNO indicated that the decomposition of this nanomaterial occurs from two different sites. This may relate to Pd attaching to the surface via two different types of 'O' groups.

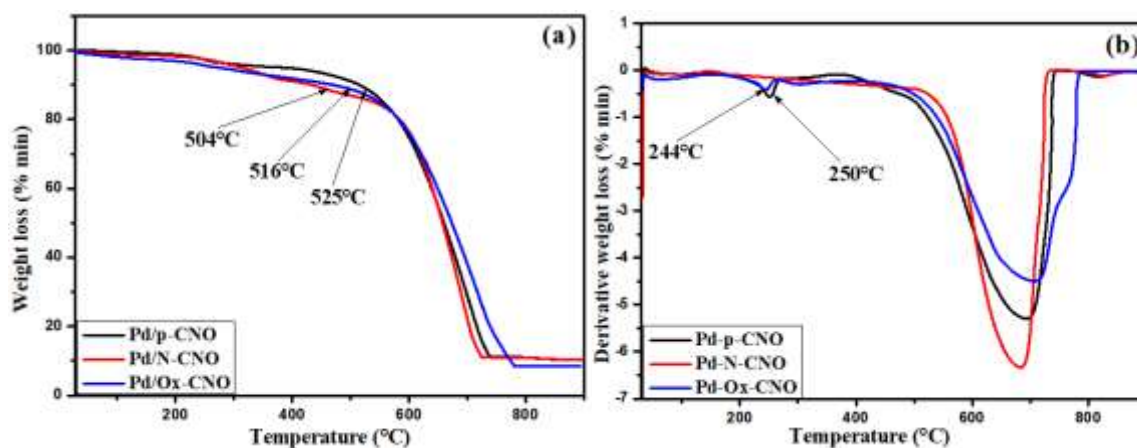
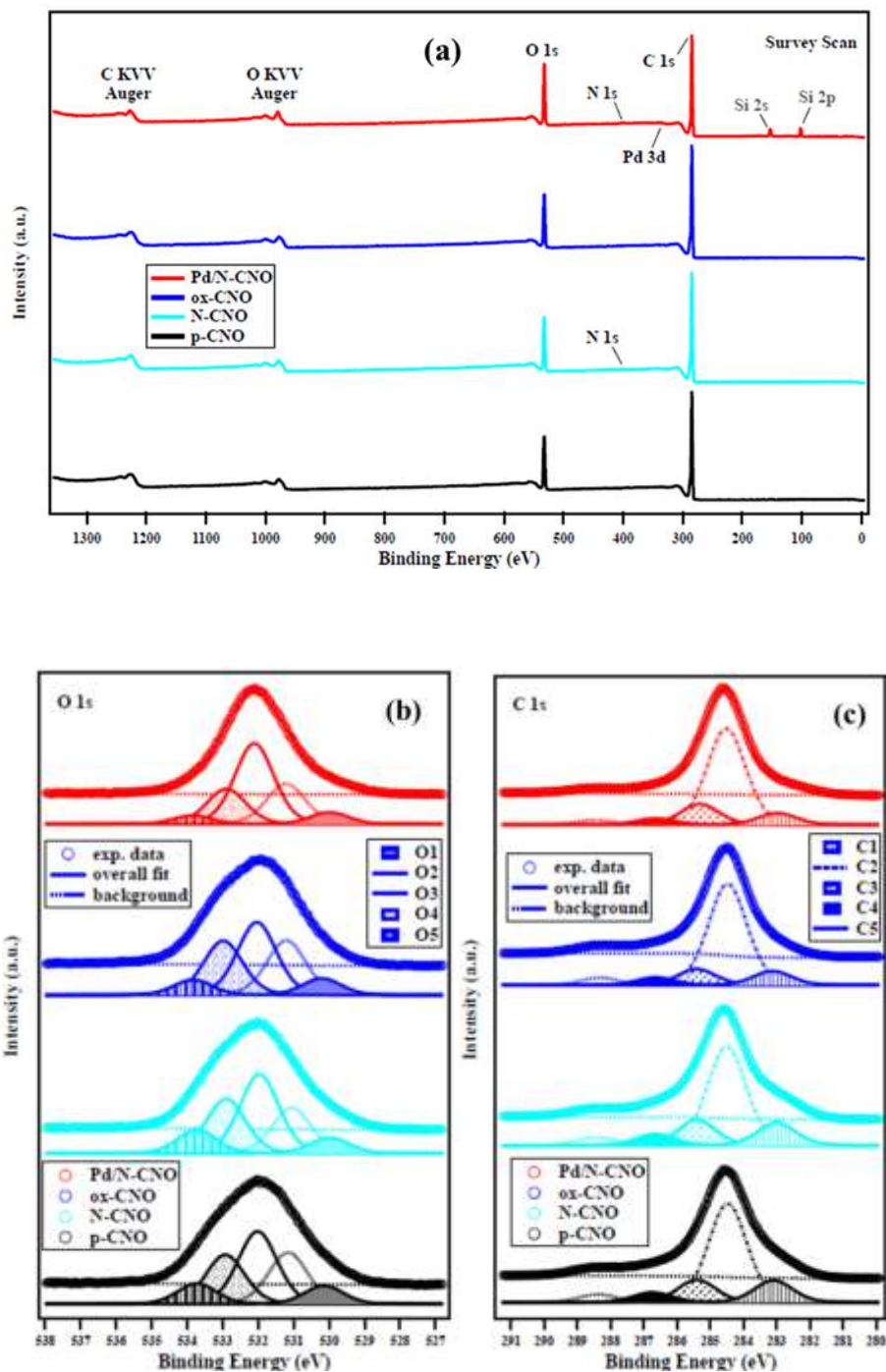


Figure S4: Shows the; (a) TGA profile and (b) TGA derivatives of Pd/p-CNO, Pd/N-CNO, and Pd/ox-CNO nanomaterials.

5. X-ray photoelectron spectroscopy



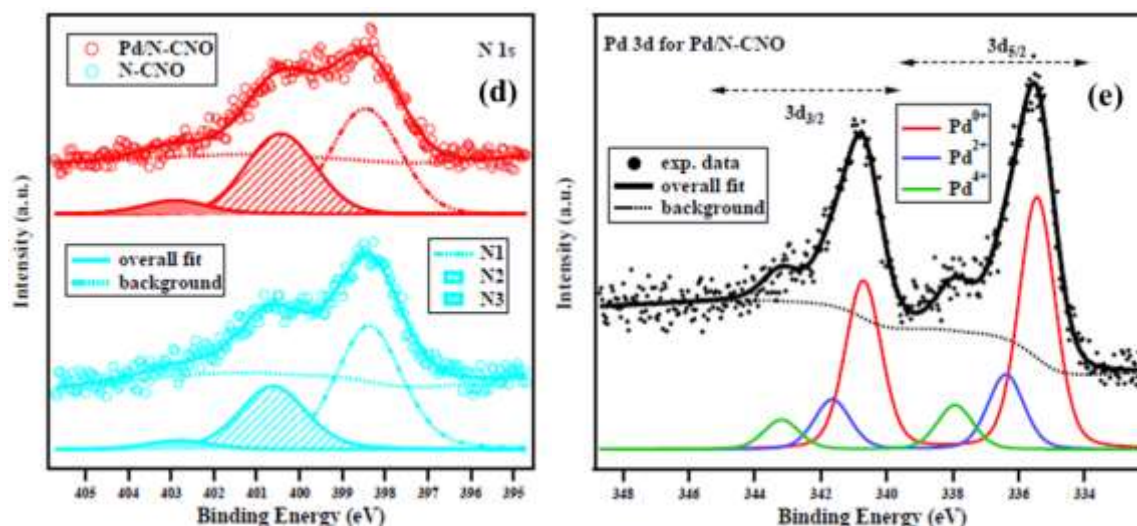


Figure S5: (a) XPS wide survey scans of p-CNO, N-CNO, ox-CNO, and Pd/N-CNO. XPS spectra (b), O 1s of p-CNO, N-CNO, ox-CNO and Pd/N-CNO (c) C 1s of p-CNO, N-CNO, ox-CNO and Pd/N-CNO (d) N 1s of N-CNO and Pd/N-CNO (e) Pd 3d of Pd/N-CNO nanomaterials.

Table S1. BEs (in eV) and relative percentage areas (in %) of the five components of the O 1s core level for the CNO samples

Sample	O1 BE (eV)	O2 BE (eV)	O3 BE (eV)	O4 BE (eV)	O5 BE (eV)	O1 area (%)	O2 area (%)	O3 area (%)	O4 area (%)	O5 area (%)
Pd/N-CNO	529.98	531.22	532.11	532.9	533.85	6.7	22.9	45.7	19.9	4.8
ox-CNO	530.21	531.21	532.04	532.99	533.84	7.8	25.6	34.1	25.4	7.1
N-CNO	529.98	531.06	531.97	532.91	533.73	7.2	20.9	36.2	24.9	10.8
p-CNO	530.15	531.16	532.02	532.93	533.73	8.6	24.3	34.2	23.2	9,7

Table S2. BEs (in eV) and relative percentage areas (in %) of the five components of the C 1s core level for the CNO samples

Sample	C1 BE (eV)	C2 BE (eV)	C3 BE (eV)	C4 BE (eV)	C5 BE (eV)	C1 area (%)	C2 area (%)	C3 area (%)	C4 area (%)	C5 area (%)
Pd/N-CNO	282.98	284.51	285.31	286.64	288.46	8.3	68.8	14.8	4.6	3.5
ox-CNO	283.12	284.47	285.4	286.64	288.32	9.6	68.9	11.0	5.4	5.1
N-CNO	283.01	284.5	285.4	286.65	288.42	13.6	59.2	15.3	6.8	5.1
p-CNO	283.09	284.47	285.42	286.74	288.38	13.6	61.3	14.0	6.2	4.9

Table S3. BEs (in eV) and relative percentage areas (in %) of the three components of the N 1s core level for Pd/N-CNO and N-CNO

Sample	N1 BE (eV)	N2 BE (eV)	N3 BE (eV)	N1 area (%)	N2 area (%)	N3 area (%)
Pd/N-CNO	398.46	400.44	402.9	53.1	40.3	6.6
N-CNO	398.38	400.62	402.81	63.1	32.4	4.5

CHAPTER 4

The Pt (111) crystalline plane was utilized to compute the average crystallite size of platinum nanoparticles according to the Debye-Scherrer equation:

$$D = k \times \lambda / \text{FWHM} \times \cos \theta \dots\dots\dots \text{S1}$$

In this equation, D is the particle size (nm), $k = 0.89$ for spherical particles, FWHM is the full width of the peak at half maximum, $\lambda = 0.154$ is the wavelength of the X-ray and $\theta = (111)$ is the angle of reflection at the maximum diffraction.

4. Transmission electron microscopy

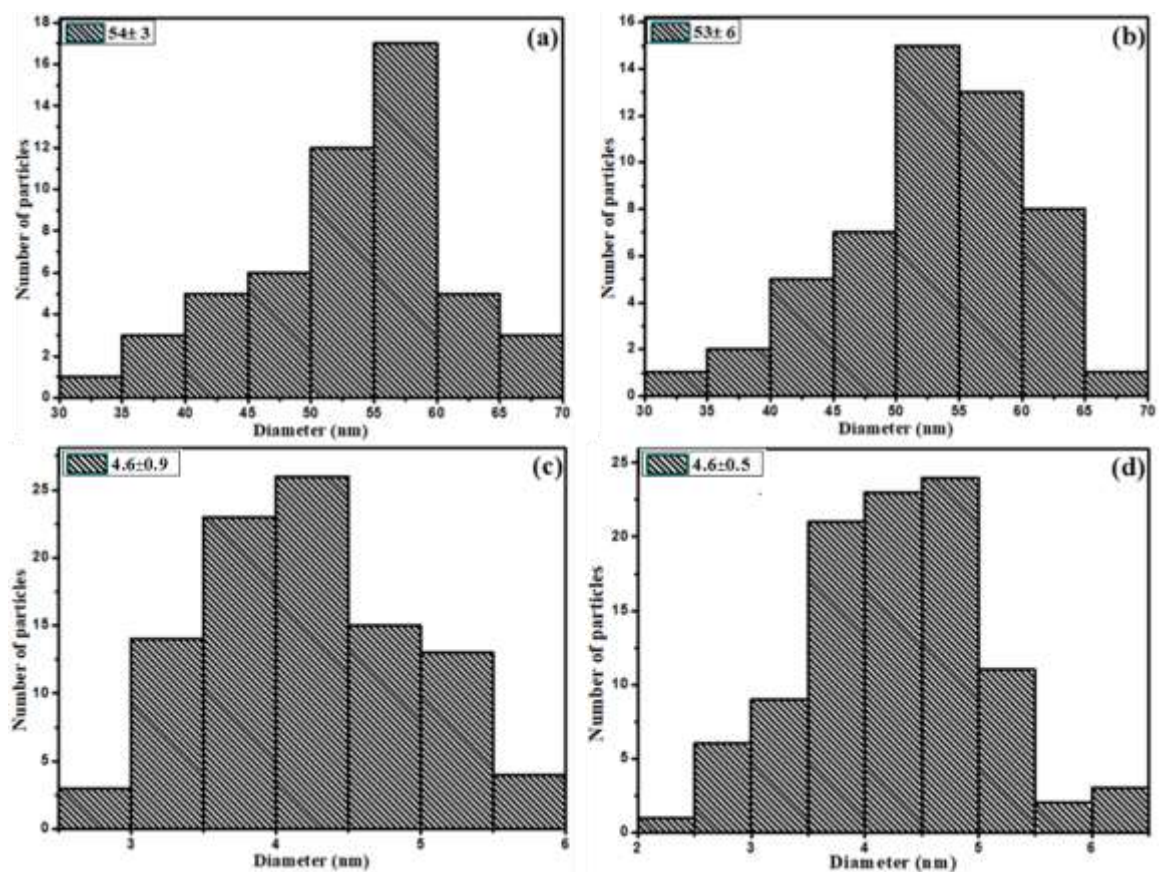


Figure S1: Average TEM Pt particle sizes of (a) p-CNO, (b) B-CNO (c) Pt/p-CNO, (d) Pt/B-CNO nanomaterials.

2. Thermogravimetric analysis (TGA)

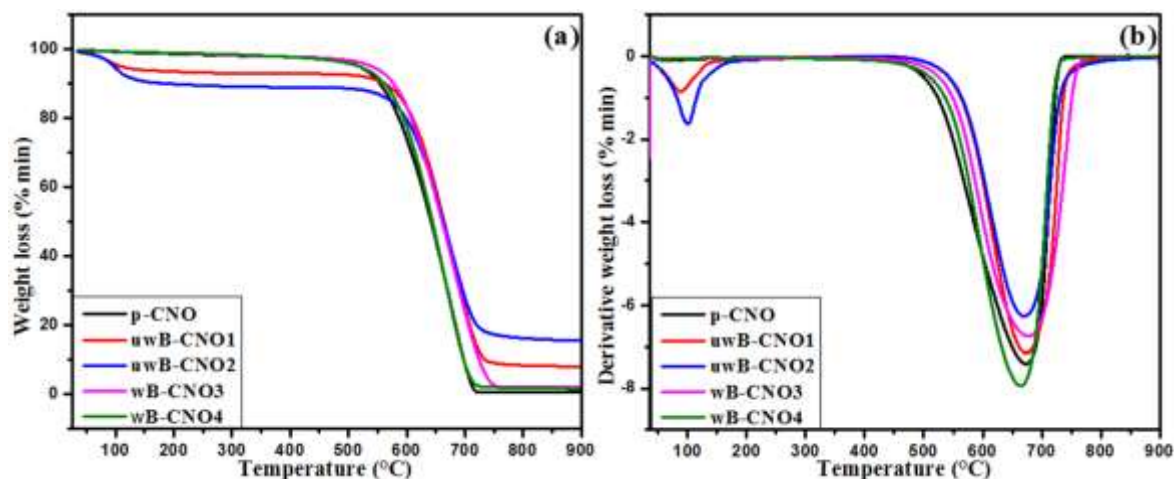


Figure S2: TGA profile and TGA derivatives of (a and b) p-CNO, washed B-CNO, unwashed B-CNO nanomaterials.

p-CNO=pristine

uwB-CNO1= unwashed B_2O_3 : p-CNO ratios (1:5)

uwB-CNO2= unwashed B_2O_3 : p-CNO ratios (2:5)

wB-CNO= washed B_2O_3 : p-CNO ratios (1:5)

wB-CNO= washed B_2O_3 : p-CNO ratios (2:5)

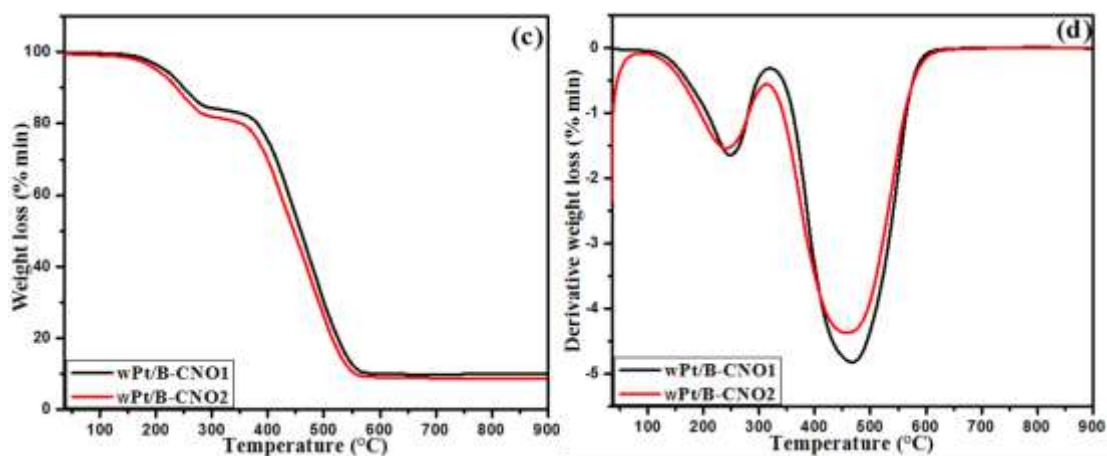


Figure S3: TGA profile and TGA derivatives of washed Pt/B-CNO nanomaterials.

wPt/B-CNO1= Pt on washed B-CNO1

wPt/B-CNO1= Pt on washed B-CNO2

5. X-ray photoelectron spectroscopy (XPS)

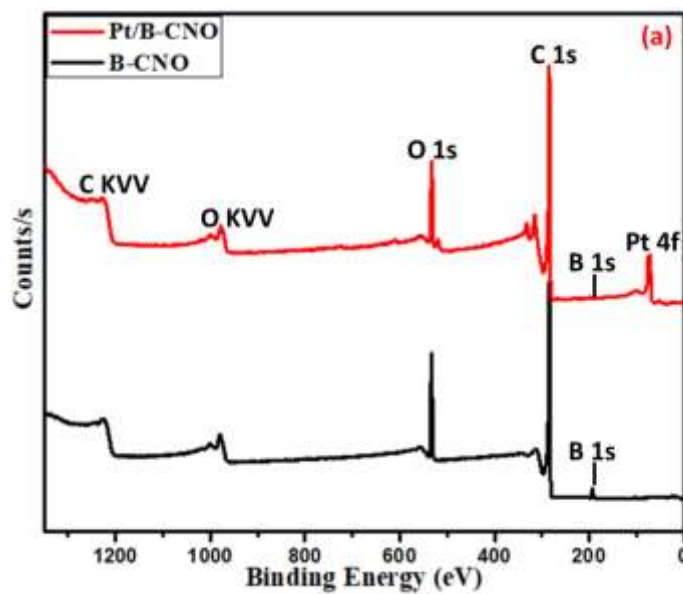


Figure S4: (a) XPS wide survey scans and elemental composition of unwashed B-CNO and Pt/B-CNO nanomaterials.

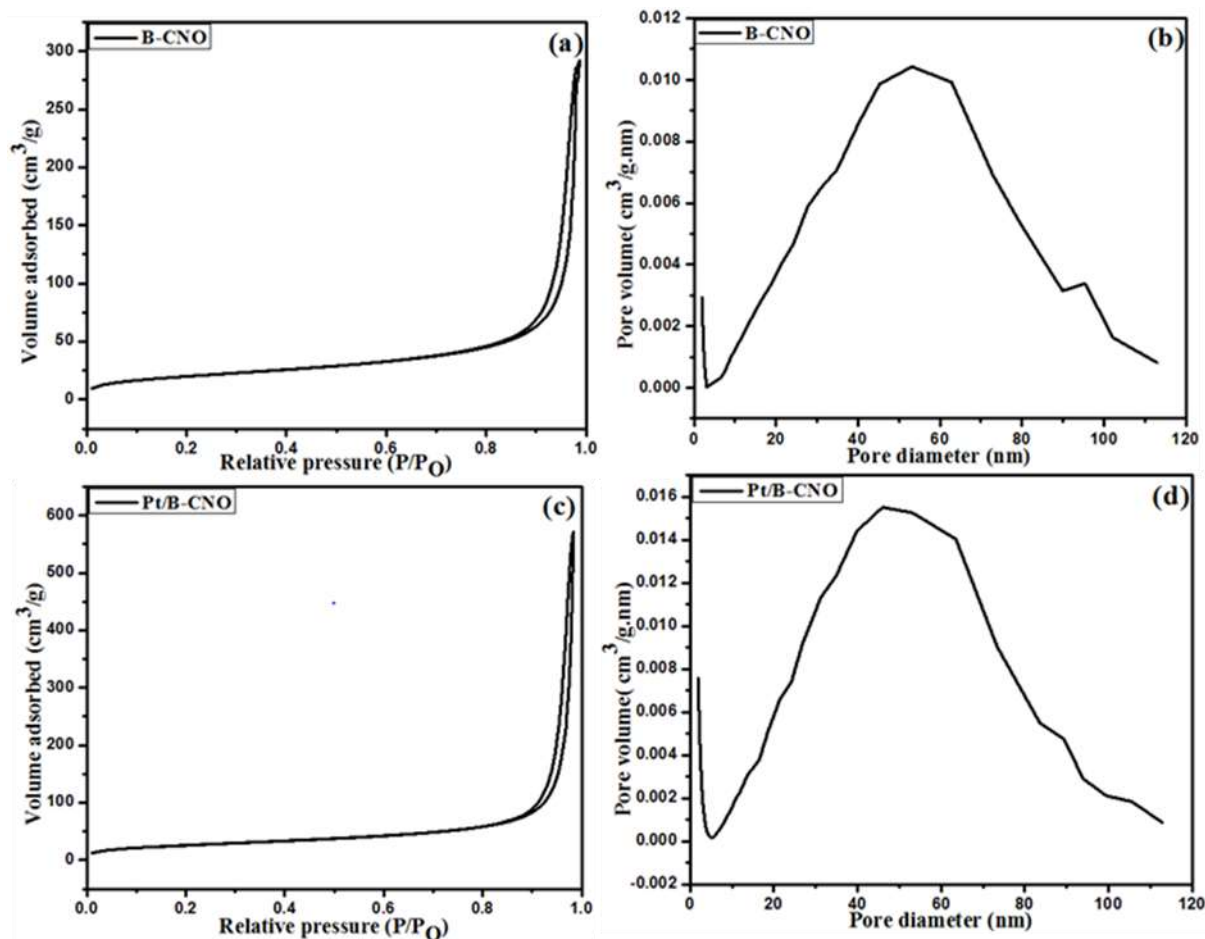


Figure S5. N₂ adsorption/desorption isotherms of (a and c) unwashed B-CNO and Pt/B-CNO and Pore size distribution curve of (b and d) B-CNO and Pt/B-CNO nanomaterials.

6. Electrocatalytic behaviour of the metal-free catalysts

3.1 Cyclic voltammetry

The voltammetry results performed at 0.5 M NaOH and on 0.5 M NaOH + 1M NH₄OH at a scan rate of 50 mVs⁻¹ are displayed on Fig S6 (a) and (b), respectively. As shown in Fig S (a), the B-CNO_{uw} electrocatalyst exhibit higher anodic current peak as compared to B-CNO_w and p-CNO catalysts in 0.5 M NaOH solution. The B-CNO_{uw} electrocatalyst has also shown a higher catalytic activity than B-CNO_w and p-CNO catalysts towards ammonia electro-oxidation in alkaline media. The enhanced electrocatalytic activity might be related to the high accessible area of B-CNO_{uw} material and the enhancement of the interaction with

water due to the boron oxide onto the carbon nano onins, which could contribute to the oxidation of intermediate products from ammonia electro-oxidation.

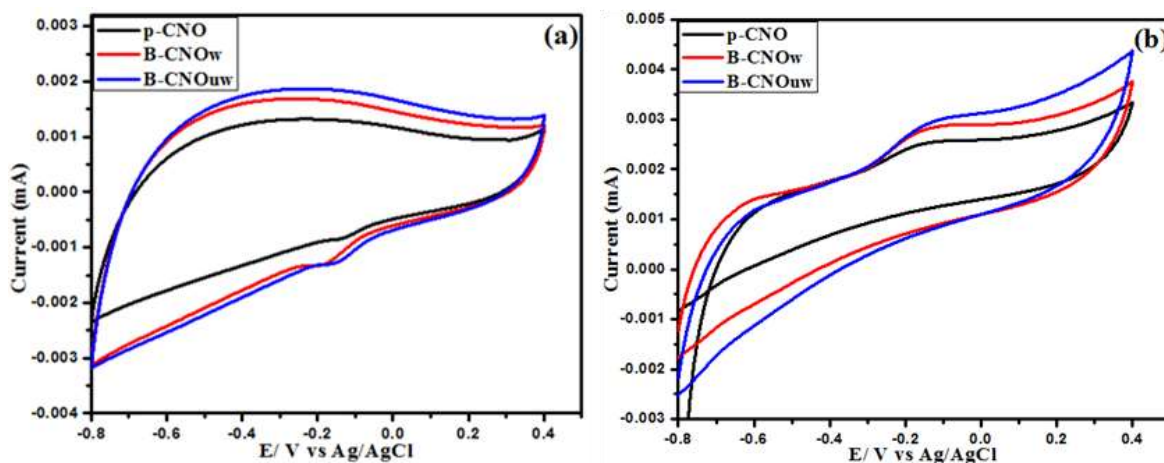


Figure S6. CV curves of p-CNO, B-CNOw and B-CNOuw modified electrodes in (a) 0.5 M NaOH and (b) 0.5 M NaOH + 1M NH₄OH at a scan rate of 50 mV s⁻¹.

3.2 Chronoamperometry

The unwashed (uw) B-CNO electrocatalyst was tested in ammonia oxidation reaction in alkaline media by chronoamperometric responses in comparison to the washed (w) B-CNO and p-CNO catalysts (**Fig S7**). The results in Fig S7 indicate that the B-CNOuw catalyst exhibits a much better stability than the B-CNOw and p-CNO catalysts in 0.5 M NaOH + 1M NH₄OH solution for an applied of -0.30 V. This behavior of B-CNOuw catalyst appears to indicate that boron oxide on the carbon nano onins is effective in weakening the poisoning by Nad species.

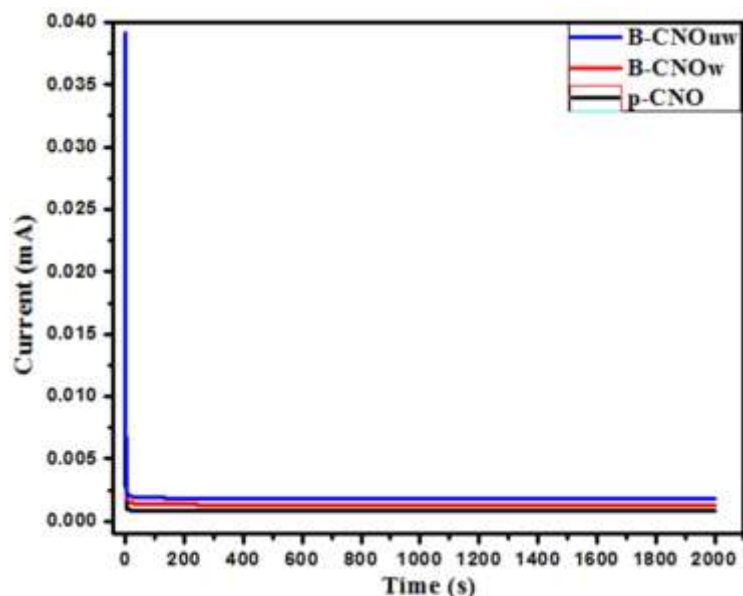


Figure S7. (a) chronoamperometric curves for p-CNO, B-CNOw and B-CNOuw modified electrodes in 0.5 M NaOH + 1M NH₄OH for an applied potential of -0.30 V.

4.1. Electrocatalytic behaviour of the metal based catalysts

The electrochemical properties of washed Pt/B-CNO electrocatalysts was evaluated by CV technique in 0.5 M NaOH solution (Fig S8 (a)). By accumulating H-adsorption charge the electrochemically active surface area (ECSA) of Pt/B-CNO electrocatalysts is measured to be 39.84 m² g⁻¹. The catalytic activity of Pt/B-CNO electrocatalysts was investigated by CV in 0.5 M NaOH + 1M NH₄OH solution (Fig S8 (b)). The AOR peak current of Pt/B-CNO electrocatalysts is 0.18 mA cm⁻². The durability of Pt/B-CNO electrocatalysts for AOR was assessed by chronoamperometry tests (Fig S8 (c)). Within 2000 s, Pt/B-CNO reveals a higher current (0.12 mA cm⁻²) suggesting better activity and stability. EIS at Pt/B-CNO electrocatalysts was carried out to analyze the charge transfer capability of AOR (Fig S8 (c)). The charge transfer resistance of HER at Pt-NCs is measured to be 35.9±1.63 Ω.

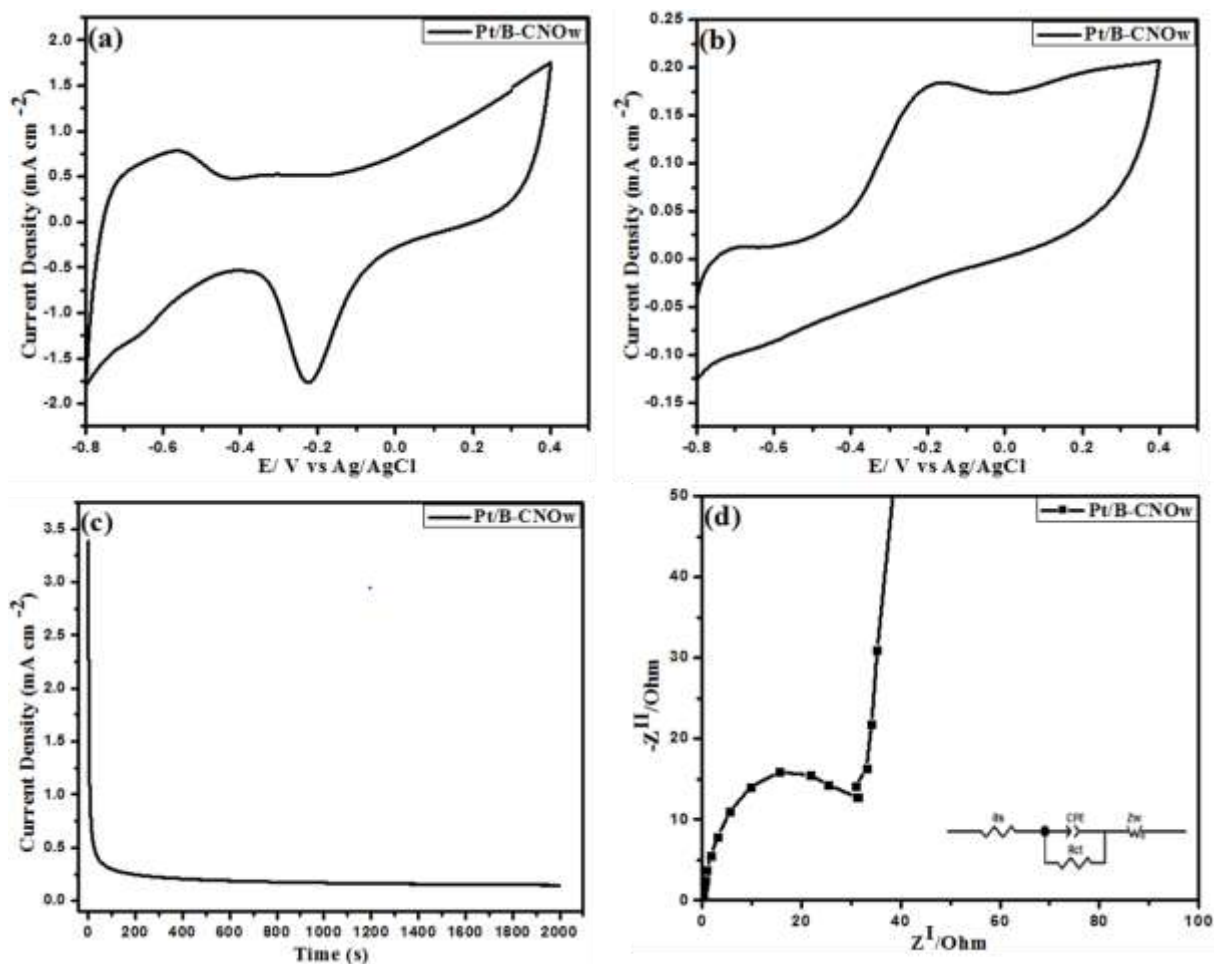
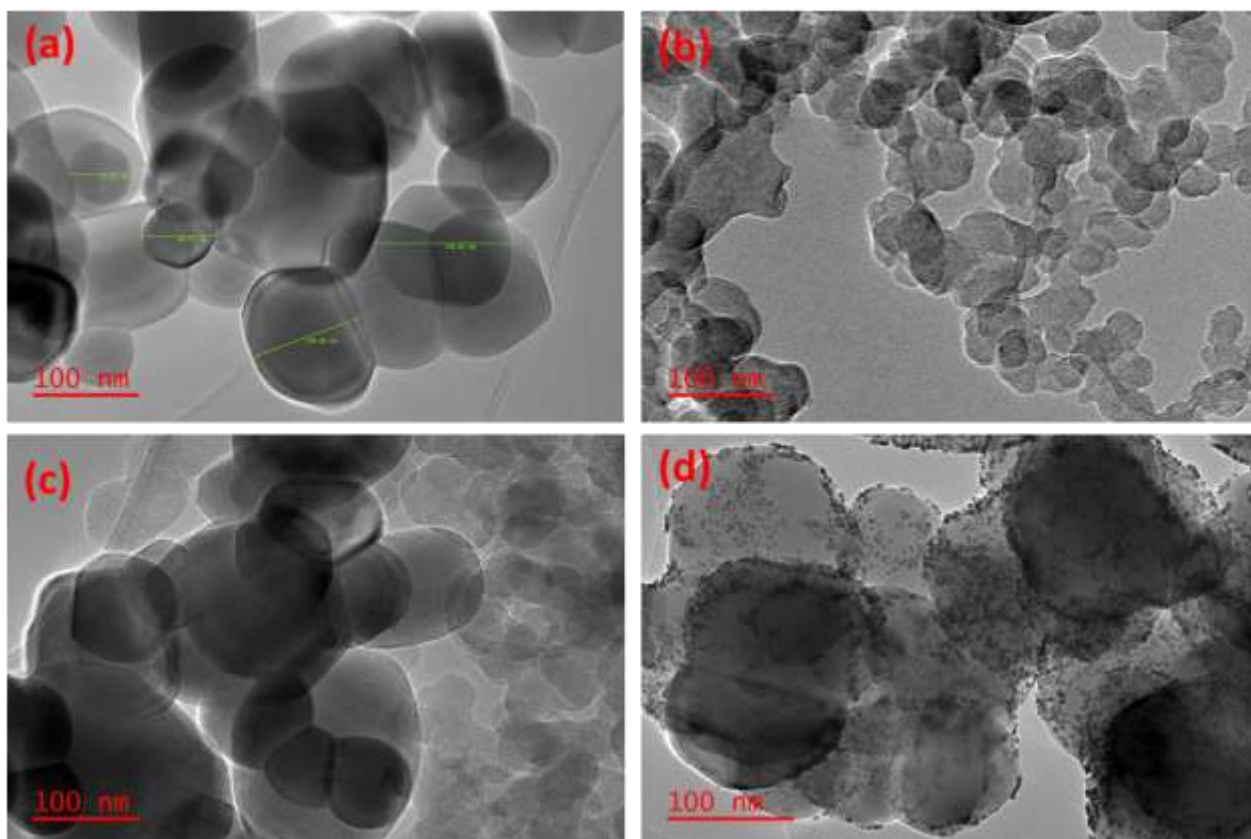


Figure S8. CV curves of Pt/B-CNOw (2:5) modified electrode in (a) 0.5 M NaOH, (b) 0.5 M NaOH + 1M NH₄OH, (c) chronoamperometric curves for Pt/B-CNOw and (d) Nyquist plots of Pt/B-CNOw in 0.5 M NaOH + 1M NH₄OH and the equivalent circuit diagram.

CHAPTER 5

1. Transmission electron microscopy



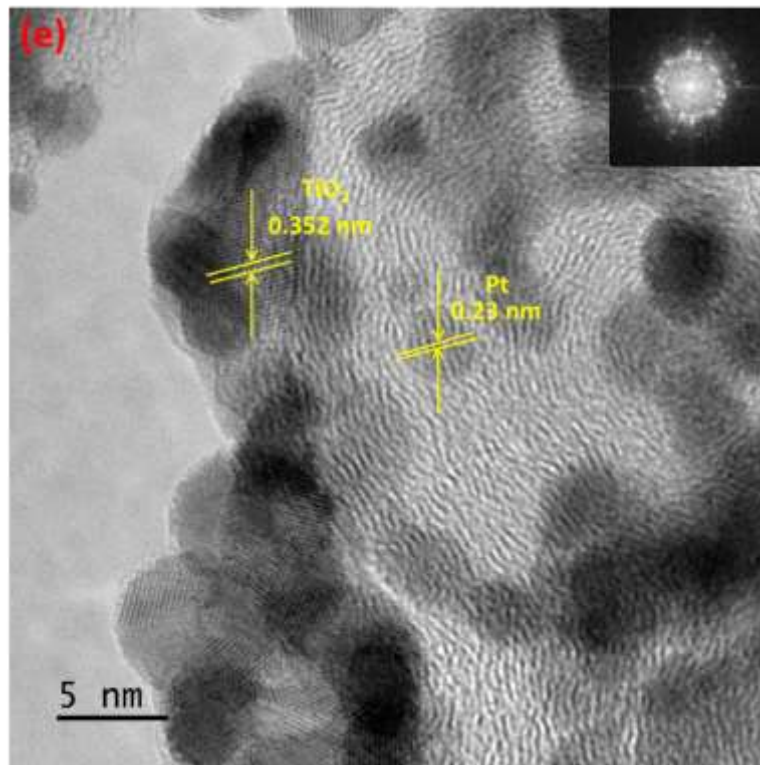


Fig. S1. High magnification TEM micrographs of (a) TiO_2 , (b) S-OLCN, (c) TiO_2 /S-OLCN, (d) Pt/ TiO_2 and high resolution TEM (e) Pt/ TiO_2 /S-OLCN nanomaterials.

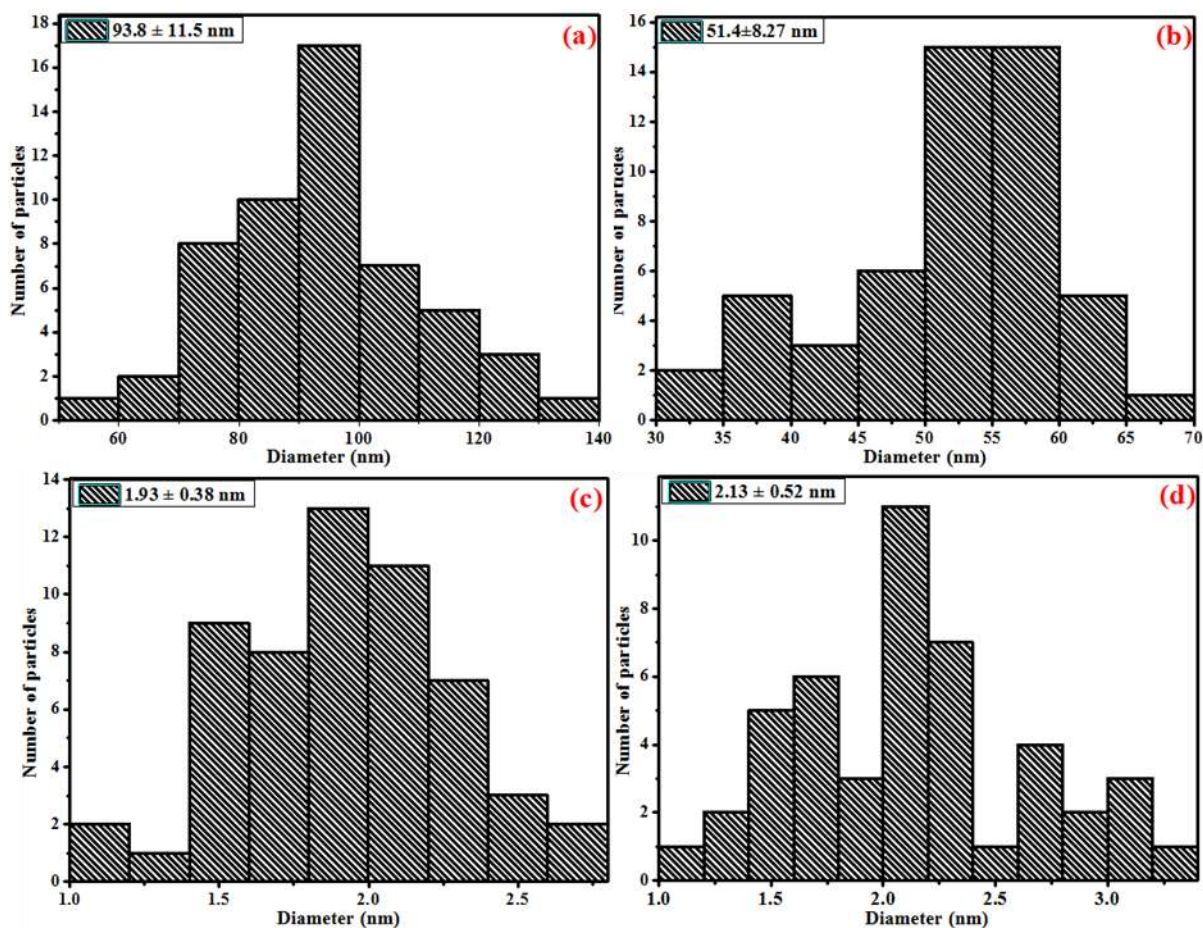


Fig S2. Average particle size of (a) TiO_2 , (b) S-OLCN, (c) Pt/S-OLCN, and (d) Pt/ TiO_2 /S-OLCN nanomaterials.

1. Scanning electron microscopy (SEM)

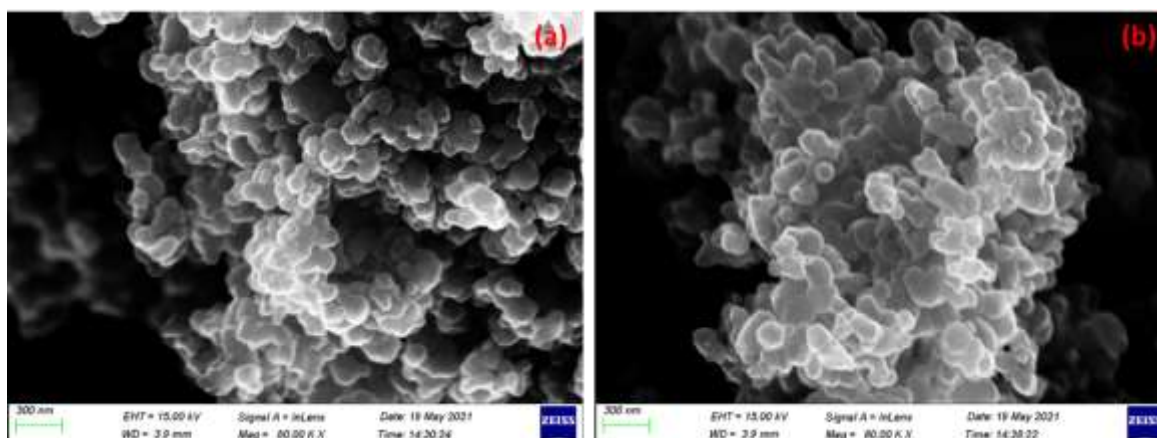


Fig S3. Typical SEM micrographs of (a) TiO_2 and (b) Pt/ TiO_2 nanomaterials.

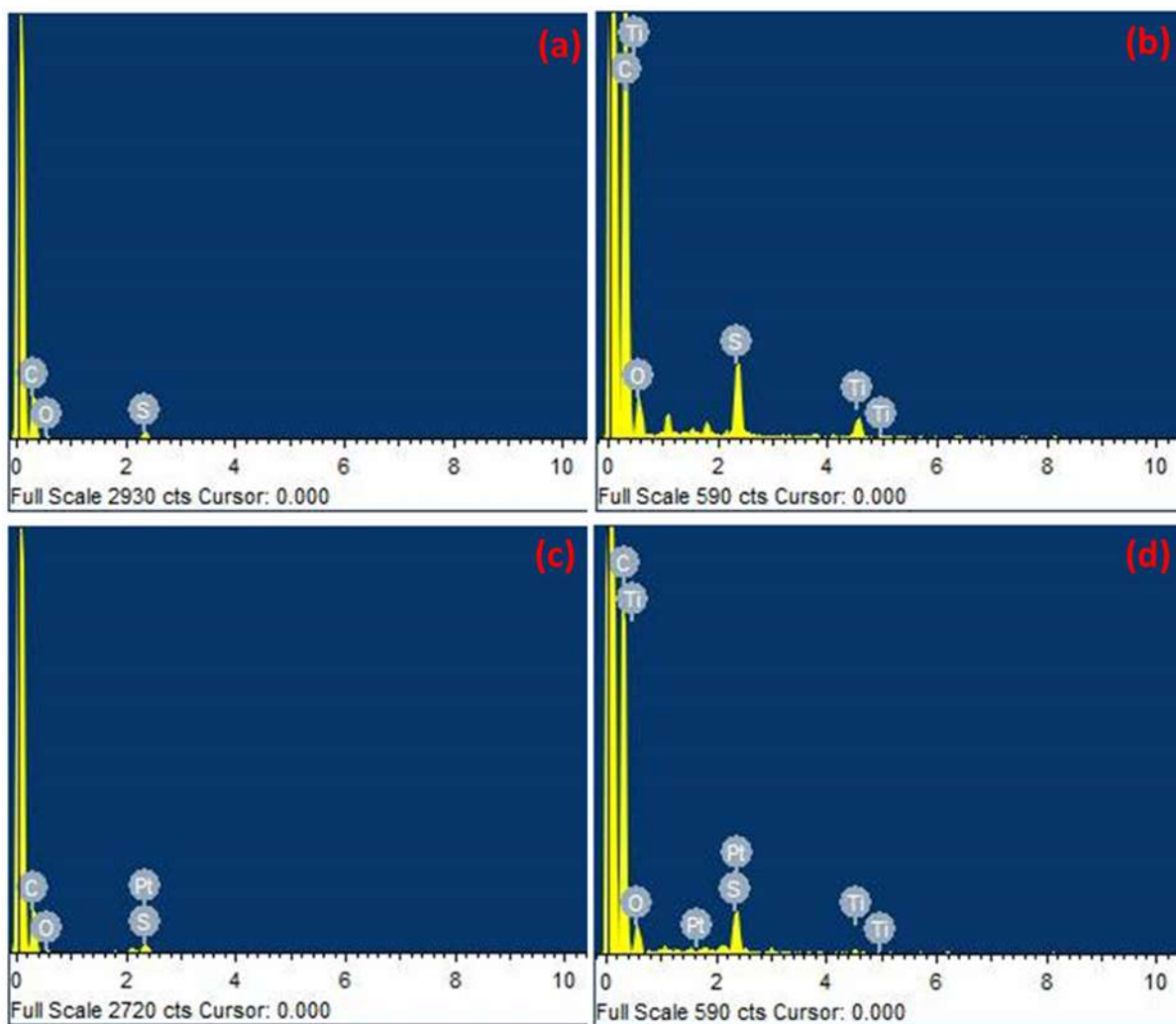


Fig.S4. EDX profile of (a) S-OLCN (b) TiO₂/S-OLCN, (c) Pt/S-OLCN (d) Pt/TiO₂/S-OLCN nanomaterials.

3. Thermogravimetric analysis (TGA)

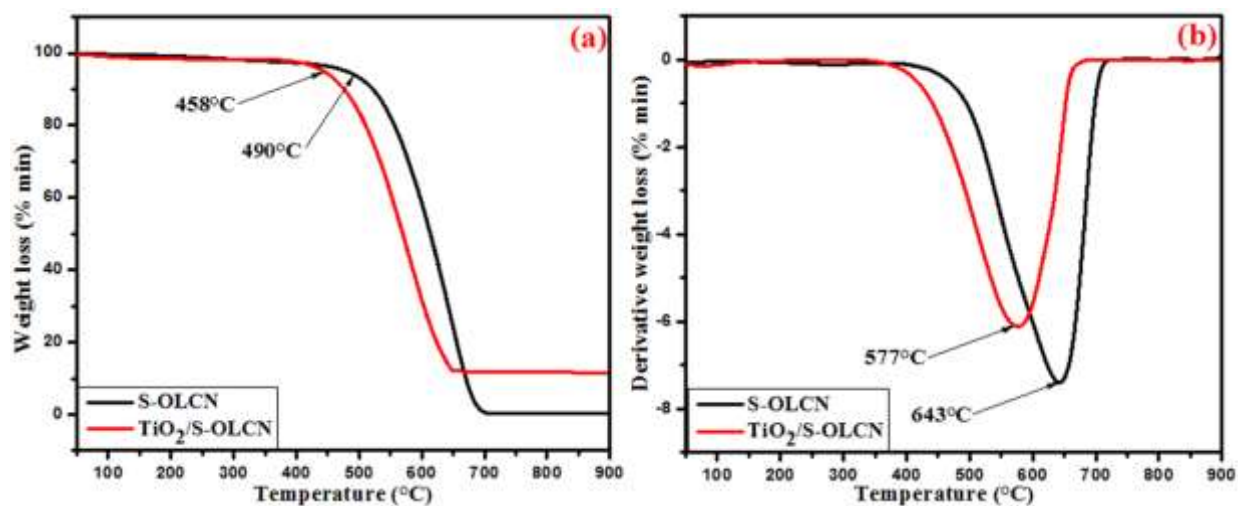


Fig. S4. (a) TGA profile and (b) TGA derivatives of S-OLCN and TiO₂/S-OLCN nanomaterials.

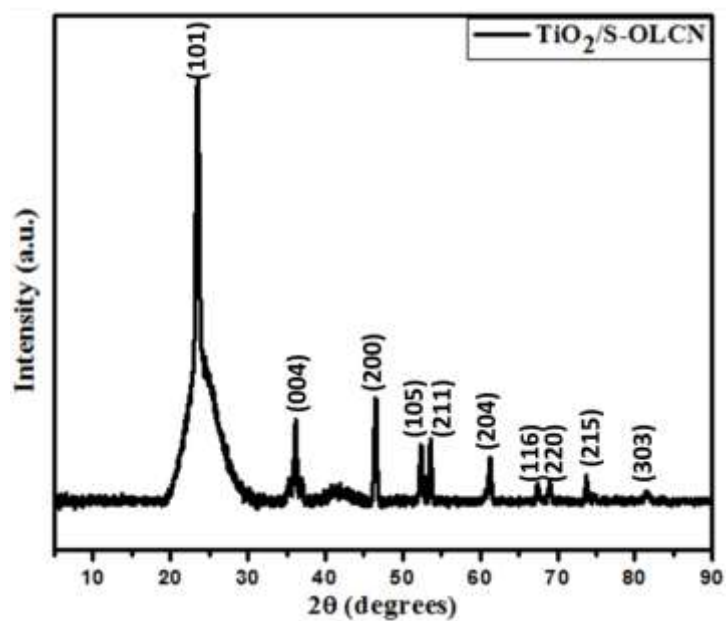


Fig. S5. X-ray diffractograms of TiO₂/S-OLCN nanomaterials.

2. Brunauer-Emmett-Teller Nitrogen adsorption (BET)

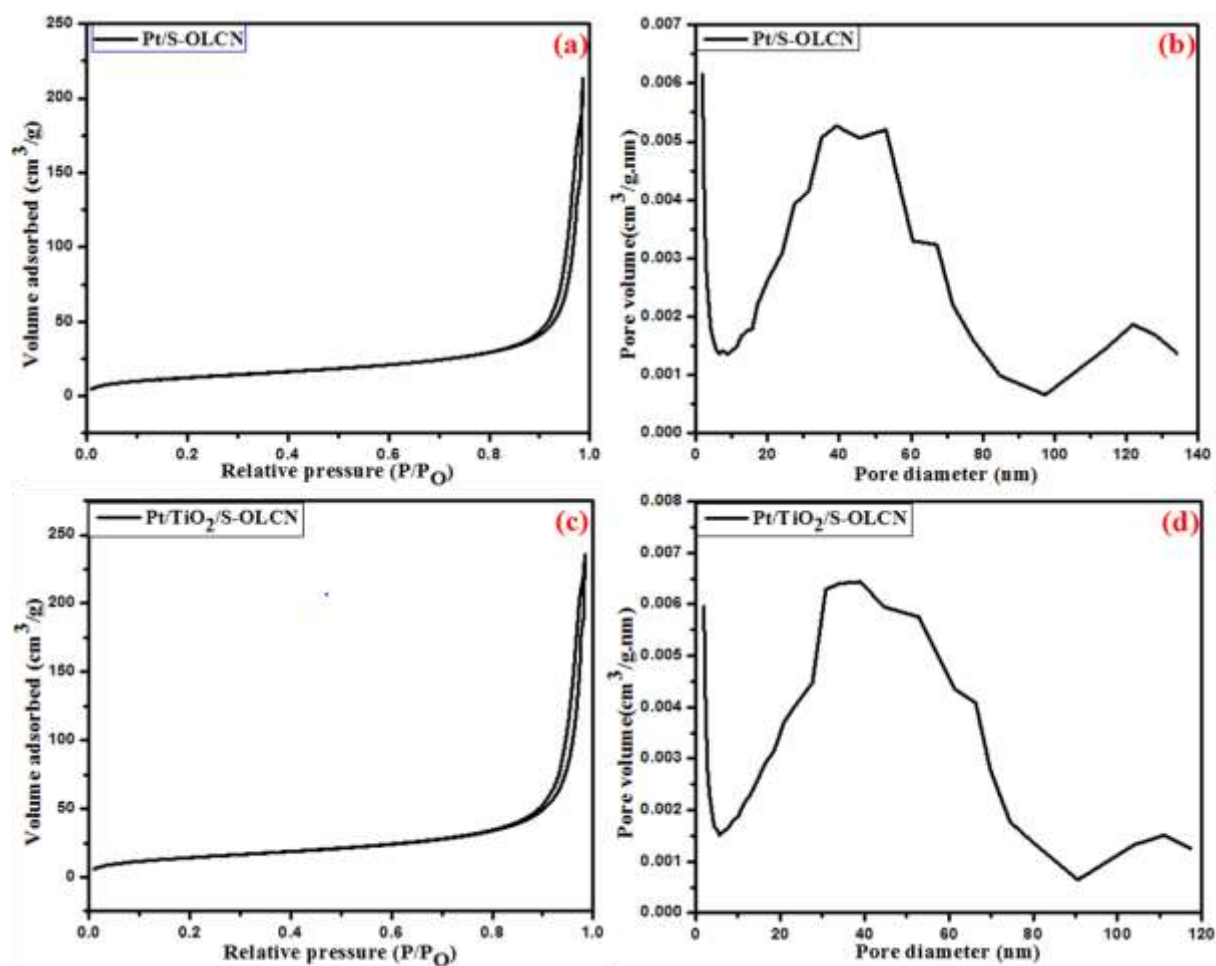


Fig. S6. (a and c) N₂ adsorption/desorption isotherms of Pt/S-OLCN and Pt/TiO₂/S-OLCN (b and d) Pore size distribution curve of Pt/S-OLCN and Pt/S-OLCN nanomaterial.

Chapter 6

1. Transmission electron microscopy

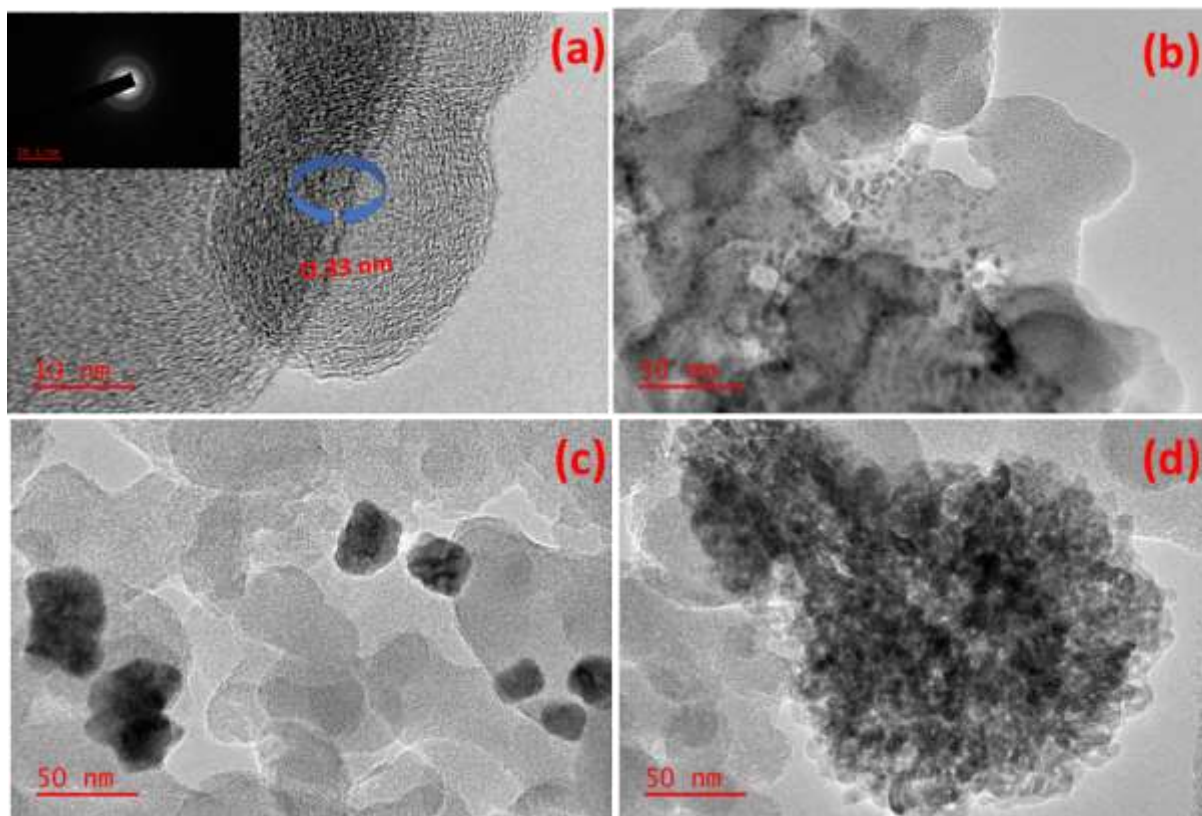


Fig. S1. TEM micrographs of (a) N-OLCN, (b) Pd/N-OLCN (c) Ag/N-OLCN and (d) Zn/N-OLCN nanomaterials

2. Thermogravimetric analysis (TGA)

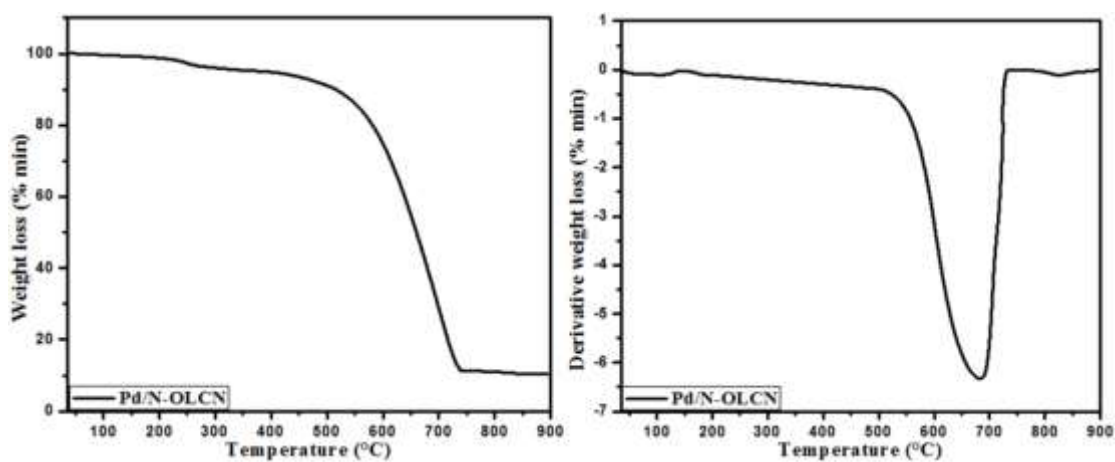


Fig. S2. (a) TGA profile and (b) TGA derivatives of Pd/N-OLCN nanomaterial.

3. X-ray diffraction spectroscopy (XRD)

Table S1: The measured peak positions, 2θ , of the Pd/Zn/N-OLCN, Pd/Ag/N-OLCN, Pd/N-OLCN crystalline planes from (111) to (222)

Sample name	Pd (111)	Pd (200)	Pd (220)	Pd (222)
Pd/Zn/N-OLCN	40.4	46.9	68.6	82.3
Pd/Ag/N-OLCN	39.8	46.1	67.7	81.6
Pd/N-OLCN	40.08	46.7	68.4	82.0 [26]

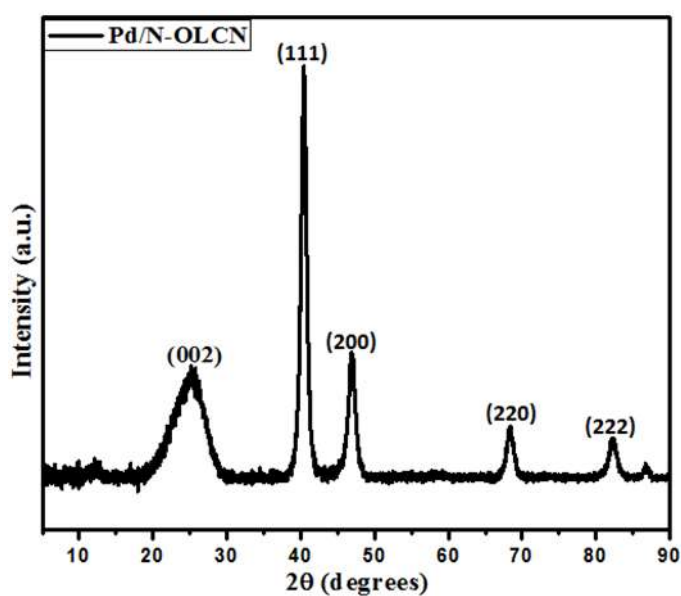


Fig. S3. X-ray diffractograms of Pd/N-OLCN nanomaterial.

4. X-ray photoelectron spectroscopy (XPS)

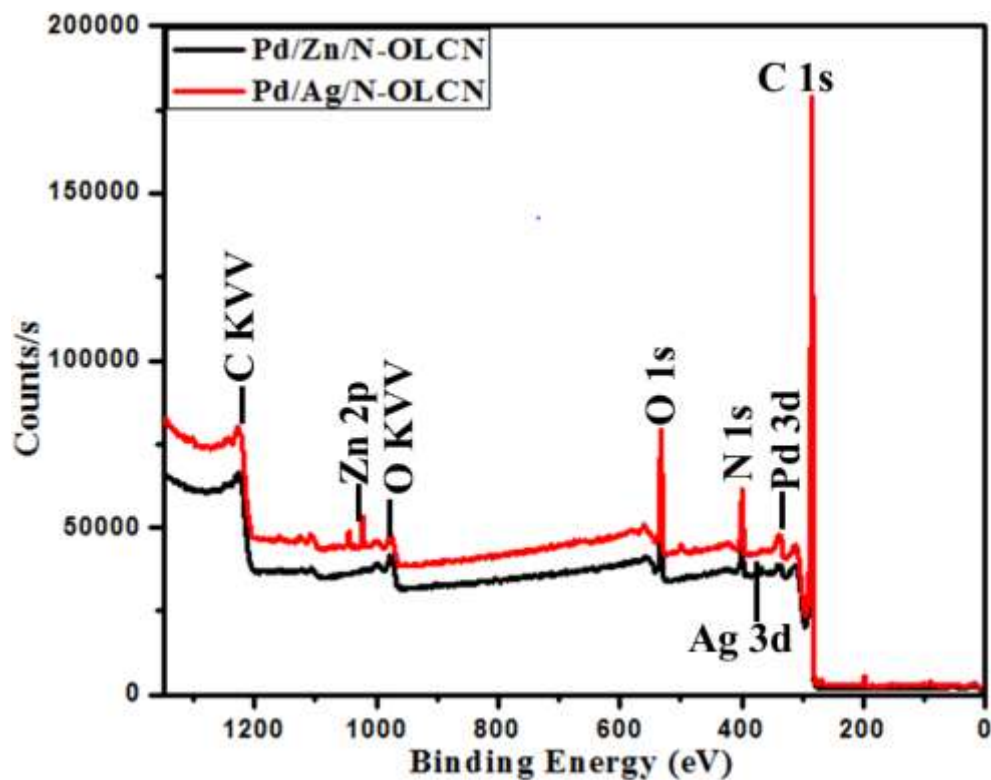


Fig. S4 (a). X-ray survey spectra of the Pd/Ag/N-OLCN and Pd/Zn/N-OLCN nanomaterials.

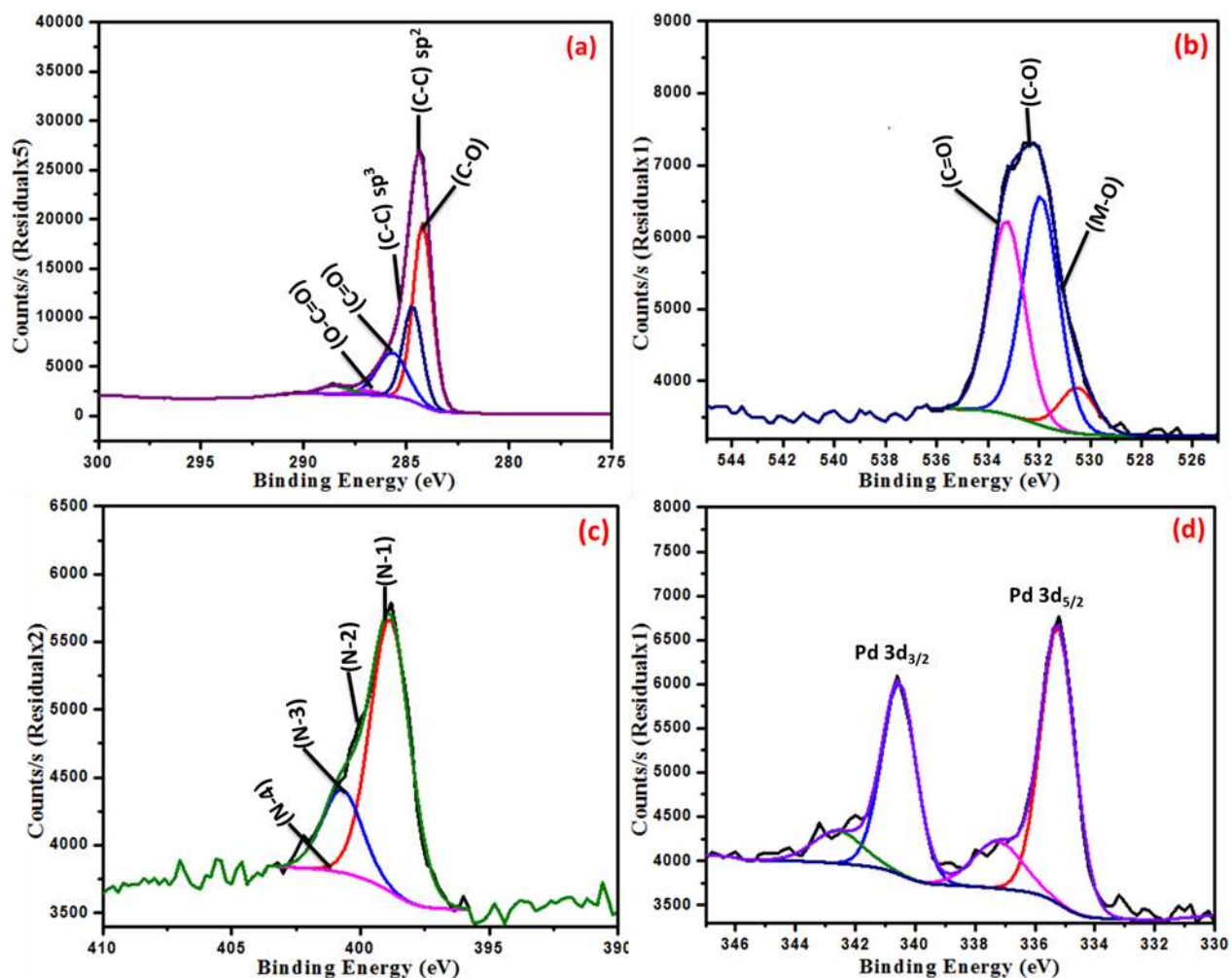


Fig. S 4 (b). XPS spectra of Pd/Ag/N-OLCN for (a) C 1s (b) O 1s, (c) N 1s, and (d) Pd 3d.

Table S2: Chemical identification and quantification data for the Pd/Zn/N-OLCN and Pd/Ag/N-OLCN nanomaterials

Pd/Zn/N-OLCN	Peak BE	Atomic %	Pd/Ag/N-OLCN	Peak BE	Atomic %
C1s (C-C) sp ²	284.2	30.7	C1s (C-C) sp ²	284.2	41.0
C1s (C-C) sp ³	284.7	28.2	C1s (C-C) sp ³	284.7	20.5
C1s (C-O)	285.7	18.2	C1s (C-O)	285.7	14.2
C1s (C=O)	287.1	2.4	C1s (C=O)	287.1	3.0
C1s (O-C=O)	288.7	2.3	C1s (O-C=O)	288.5	3.4
Pd3d (Pd0)	335.2	3.8	Pd3d (Pd0)	335.1	3.6
Pd3d (Pd20)	340.4	2.3	Pd3d (Pd20)	340.5	2.5
N 1s (pyridine-N)	397.5	1.4	Ag3d (Ag0)	367.4	2.8
N 1s (pyrrole-N)	400.3	1.2	Ag3d (Ag20)	373.1	1.4
N 1s (graphitic-N)	402.1	0.5	N 1s (pyridine-N)	398.5	1.2
N 1s (oxidized-N)	404.2	0.4	N 1s (pyrrole-N)	400.4	1.0
O 1s (Metal)	530.5	1.0	N 1s (graphitic-N)	402.1	0.6

Oxide)					
O 1s (Organic C-O)	532.0	1.8	N 1s (oxidized-N)	404.3	0.5
O 1s (Organic C=O)	533.4	1.5	O 1s (Metal Oxide)	530.5	1.1
Zn2p3 (ZnO)	1022.5	3.2	O 1s (Organic C-O)	531.9	1.9
Zn2p3 (metal Zn)	1045.5	1.2	O 1s (Organic C=O)	533.3	1.5

5. Cyclic voltammetry and Chronoamperometry

The voltammetry results performed at 1 M NaOH + 1 M CH₃OH at a scan rate of 50 mVs⁻¹ are displayed on Fig S3 (a). Both Ag/N-OLCN and Zn/N-OLCN electrocatalysts exhibit higher anodic current peak as compared to N-OLCN metal free catalyst in methanol oxidation reactions in alkaline media. The enhanced electrocatalytic activity is due to the incorporation of Ag and Zn on the surface of N-OLCN catalyst support material. The results in Fig S3 (b) indicate that the Ag/N-OLCN and Zn/N-OLCN catalysts exhibits a much better stability than the N-OLCN metal free catalyst in 1 M NaOH + 1 M CH₃OH solution for an applied of -0.30 V. This behavior of Ag/N-OLCN and Zn/N-OLCN catalysts appears to indicate that Ag and Zn on the nitrogen doped OLCN is effective in weakening the poisoning by CO_{ad} species.

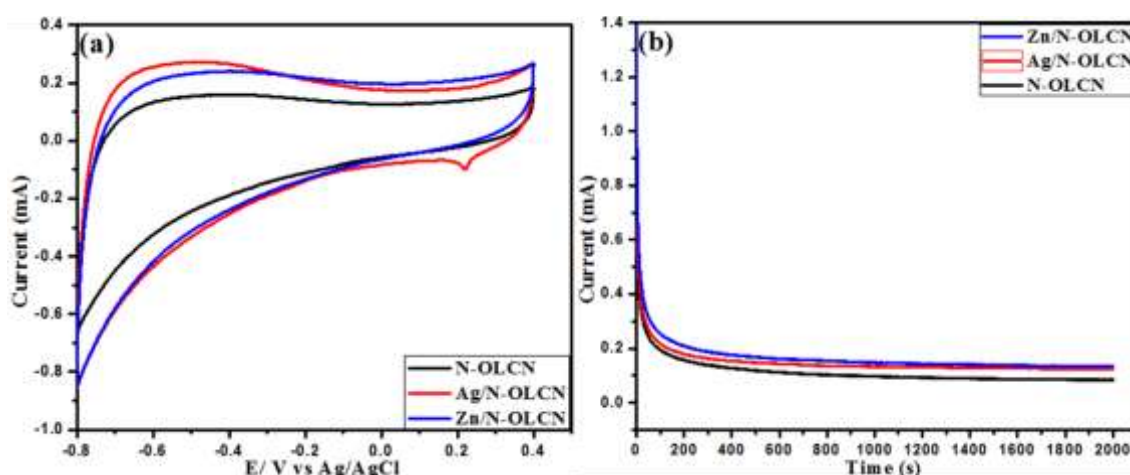


Fig. S5. (a) CV and (b) CA curves of N-OLCN, Ag/N-OLCN and Zn/N-OLCN electrocatalysts